Department of Neuroscience and Movement Sciences
University of Fribourg (Switzerland)

Neural population dynamics in premotor, motor and somatosensory cortices during locomotion in primates

THESIS
presented to the Faculty of Science and Medicine of the University of Fribourg
(Switzerland) in consideration for the award of the academic grade of
Doctor of Philosophy in Medical Sciences
(cluster in Neuroscience)

by

Simon Borgognon
from
Cugy, FR (CH)

Thesis No: 2226

UniPrint

2020

Accepted by the Faculty of Science and Medicine of the University of Fribourg (Switzerland) upon the recommendation of Professor Eric M. Rouiller, Professor Grégoire Courtine, Professor Gregor Rainer, Professor Carine Karachi and Professor Wolfgang Taube (President of the Jury).

Fribourg, the 24th of November 2020

Thesis supervisors:

Prof. Eric M. Rouiller

Eric M. Rouiller

Prof. Grégoire Courtine

Vice-Dean:

Prof. Michael Walch

“We can never go nowhere unless we share with each other.”
Tupac Shakur

ACKNOWLEDGMENT

I would like to express my gratitude to Professor Eric M. Rouiller who allowed me to pursue my PhD after my master in his laboratory. He conveyed to me his scientific vision and passion. I admire and am very grateful for his teaching and wisdom. All the years spent working alongside him forged my curiosity and scientific passion. I wish him a well-deserved retirement.

My sincere thanks go to Professor Grégoire Courtine for giving me the opportunity to perform my thesis in his laboratory. He allowed me to travel and opened the door of his group, thus widening my scientific background. Despite the scientific difficulties we encountered, his enthusiasm, faith, ambition, and energy were a source of inspiration that pushed me to never give up. Finally, it was always a pleasure to share collations and discussions.

I also thank my direct supervisors and friends, Professor Ismael Seáñez and Professor Marco Capogrosso, with whom I shared a lot over these years. Their critical minds and discernment always got me back on track when I strayed from the straight and narrow. It was my greatest pleasure to work with you and I hope we will continue to have scientific (and other) adventures together. I wish them good luck.

My thanks also go to Professor Jocelyne Bloch and Professor Stéphanie Lacour without whom the project would never have been accomplished. Although we were confronted with many challenges, their enthusiasm and motivation always helped find solutions.

A special thanks goes to Alexandra M. Hickey and Nicolò Macellari. Their precious collaboration and friendship strongly helped in the achievement of this project. Beyond their professionalism, their joy always ensures a good atmosphere. I wish y'all the best.

I would like to thank all the lab mates for providing a lot of encouragement, support, and fun: Aaron Brändli, Beatrice Barra, Dr. Sara Conti, Dr. Nathan Greiner, Dr. Matthew G. Perich, Dr. Tomislav Milekovic, Dr. Shiqi Sun, Dr. Elvira Pirondini, Dr. Luke Urban, Andreas Rowald, Maude Delacombaz, Fanny Demon, Dr. Florian Fallegger, Dr. Giuseppe Schiavone, Dr. Nicolas Vachicouras, Christopher M. Hitz, Dr. Florian Lanz, Dr. Eric Schmidlin, Dr. Michael Harvey, Dr. Sabry Barlatey, Dr. Quentin Barraud, Laetitia Baud, Dr. Léonie Asboth, Dr. Nicholas James, Newton Cho, Elodie Rey, Dr. Flavio Raschellà and Dr. Eduardo M. Moraud.

I also thank Laurent Bossy, Véronique Moret, André Gaillard, Andrea Francovich, Christine Roulin, David Michel, Laurent Monney, Jacques Maillard, Dr. Andrina Zbinden, Karine Schneuwly, Prof. Erwan Bézard, Dr. Li Qin, Dr. Daniel Ko, Li Hao, Peng Hao, Cheng Long, Yang Jianzhong, Soline Odouard, Arnaud Bichat, Katia Galan and Dr. Laura Batti for providing all the technical support.

My thanks go also to all my students: Margaux Di Natale, Rafael Ornelas Kobayashi, Elisabetta Pagliara, Damian Jandrasits, Lucas Zweili, Julie Martignoles, Audélia Mechti and Zulkaida Mamat.

Furthermore, I'd like to thank all my friends and family, who are far too numerous to be listed individually. You all supported me and stayed next to me in the happiest and saddest moment of the past few years.

Finally, my warmest thanks go to my beloved Marion, without whom nothing would have been possible. We are always going together through the storm to finally reach the illumination. Your presence and unconditional love are vital to me, and I am looking forward to pursuing our adventure together.

ABSTRACT

While movement may seem effortless, the underlying processes orchestrated by the nervous system are remarkably complex. From the central nervous system to the muscles, motor information must be well coordinated to elicit an appropriate movement. Although our knowledge of motor control has drastically increased, the precise role of cortical areas is still debated. For instance, locomotor gait (i.e. locomotion) is thought to be governed by automated neural circuitry residing within the spinal cord, or within the brain stem, while cortical areas may only adapt the adjustment of steps during walking on rugged terrain. In this context, it is important to better understand the role of different cortical area structures underlying the production of locomotor behavior. New findings could result in improving available treatments or in developing new therapeutic strategies to help patients with motor disabilities, such as spinal cord injury, stroke, or Parkinson's disease.

Nonhuman primates represent an adequate model to study the role of cortical areas during locomotion due to their advanced sensorimotor attributes which enable highly skilled capabilities. Moreover, recent advances in technology provide the opportunity to record large numbers of neurons from different areas simultaneously, together with whole-body 3D kinematics and muscular activity. We thus developed a technological framework for studying locomotion in freely-behaving monkeys. We first built a versatile setup accommodating locomotion on a treadmill, on a flat surface, on an uneven horizontal ladder, and over stairs and obstacles. We then trained the animals using positive reinforcement. In parallel, we built a wireless electrophysiological platform and designed the interface between the animals and the computers. This technological setup encompassed the assembly of hardware in percutaneous connectors as well as personalized surgical procedures.

To study cortical dynamics during locomotion, monkeys were implanted with intra-muscular electrodes, as well as multi-electrode arrays in the premotor, primary motor, and somatosensory cortices. The wide range of locomotor behaviors revealed specific neural dynamic patterns varying along the rostro-caudal axis: from premotor to somatosensory cortices. These neural dynamics were confined within a low-dimensional neural manifold: the locomotion subspace. The locomotion subspace can reliably predict locomotor-related events that could be used to trigger spinal cord stimulation at the lumbar segments in order to alleviate gait deficits after tetraplegia. We thus developed personalized spinal implants that specifically target different lumbar segments to elicit leg movements. The implants successfully elicited independent muscle synergy responses. However, their translation to clinical applications remains challenging, emphasizing the importance of validation in animal models from which such therapeutic strategies have emerged based on fundamental research.

RESUME

La production d'un mouvement semble triviale, cependant les processus sous-jacents orchestrés par le système nerveux sont remarquablement complexes. Du système nerveux central aux muscles, les informations motrices doivent être façonnées de manière à créer un mouvement approprié. Bien que nos connaissances sur le contrôle moteur aient considérablement augmenté, le rôle précis des aires corticales dans le contrôle moteur est toujours débattu. Par exemple, nous pensons que la marche locomotrice (c'est-à-dire la locomotion) est régie par des circuits neuronaux automatisés résidant dans la moelle épinière et/ou dans le tronc cérébral, tandis que les zones corticales pourraient uniquement adapter l'ajustement des pas pendant la marche sur un terrain accidenté. Dans ce contexte, il est important de mieux comprendre le rôle des différentes structures des aires corticales sous-jacentes à la production d'un comportement locomoteur. De nouvelles découvertes pourraient aboutir à l'amélioration des traitements disponibles ou à l'élaboration de nouvelles stratégies thérapeutiques pour aider les patients souffrant de troubles moteurs provoqués par les lésions médullaires, les accidents vasculaires cérébraux ou la maladie de Parkinson.

Les primates non-humains représentent un modèle adéquat pour étudier le rôle des aires corticales pendant la locomotion en raison de leurs attributs sensorimoteurs avancés fournissant une dextérité motrice fine. De plus, les récentes avancées technologiques permettent d'enregistrer un grand nombre de neurones de différentes zones simultanément avec la cinématique 3D du mouvement et l'activité musculaire. Nous avons ainsi développé un cadre technologique pour étudier la locomotion chez des primates non-humains. Nous avons d'abord construit une installation polyvalente permettant la locomotion sur un tapis roulant, sur une surface plane, sur une échelle horizontale, sur des escaliers et obstacles. Nous avons ensuite entrainé des animaux sur la base du renforcement positif. En parallèle, nous avons construit une plateforme électro-physiologique sans fil et conçu l'interface entre les animaux et les ordinateurs. Cette configuration technologique englobait l'assemblage de matériel dans des connecteurs percutanés ainsi que des procédures chirurgicales personnalisées, basées sur la morphologie de l'animal.

Pour étudier la dynamique corticale pendant la locomotion, des singes ont été implantés avec des électrodes intramusculaires ainsi que des champs d'électrodes dans les cortex pré-moteur, moteur primaire et somatosensoriel. La large gamme de comportements locomoteurs a révélé des motifs dynamiques neuronaux spécifiques variant le long de l'axe rostro-caudal: du cortex pré-moteur au cortex somatosensoriel. Ces dynamiques neuronales étaient confinées dans un espace neural de faible dimension: le sous-espace locomoteur. Le sous-espace locomoteur peut prédire de

manière fiable les événements liés à la locomotion qui pourraient être utilisés pour déclencher une stimulation de la moelle épinière au niveau des segments lombaires afin de réduire le déficit de marche après la tétraplégie. Nous avons ainsi finalement développé des implants rachidiens personnalisés qui ciblent spécifiquement différents segments lombaires pour provoquer des mouvements des jambes. Les implants ont suscité des réponses sous la forme de synergie musculaire indépendantes, toutefois sa translation clinique reste un défi relevant ainsi l'importance de la validation dans des modèles animaux à partir desquels différentes stratégies thérapeutiques ont été développées, basées sur des résultats issus de la recherche fondamentale.

LIST OF FIGURES AND TABLES

FIGURE 1.1 | SCHEMATIC REPRESENTATION OF MOTOR CORTICAL AREAS IN NHPS 23
FIGURE 1.2 | SCHEMATIC REPRESENTATION OF PRIMARY SOMATOSENSORY CORTEX IN NHPS 24
FIGURE 1.3 | HIERARCHICAL AND PARALLEL ORGANIZATION OF THE MOTOR CONTROL SYSTEM. 28
FIGURE 1.4 | THREE REPRESENTATIVE SPIKING ACTIVITY DURING MOVEMENT 29
FIGURE 1.5 | NEURONAL POPULATION CODING FOR MOVEMENT DIRECTION........ 31
FIGURE 1.6 | CONCEPTUAL ILLUSTRATION OF THE NEURAL MANIFOLD........ 33
FIGURE 1.7 | CONCEPTUAL PRINCIPLE OF THE DPCA 34
FIGURE 1.8| EXAMPLE OF LATENT ACTIVITIES AFTER PCA OR DPCA 35
FIGURE 1.9 | TWO SUCCESSIVE GAIT CYCLES........ 38
FIGURE 1.10 | MOTOR CORTEX ACTIVITY DURING WALKING 42

FIGURE 2.1 | LOCOMOTION LABORATORY SETUP 62
FIGURE 2.2 | BEHAVIORAL TRAINING PARADIGM 64
FIGURE 2.3 | 3D LEG KINEMATIC ACQUISITION 65
FIGURE 2.4 | DEEPLABCUT (DLC) OPTIMIZATION 65
FIGURE 2.5 | EXAMPLE OF KINEMATIC ANALYSIS 66
FIGURE 2.6 | COMMUNICATION BETWEEN THE EXPERIMENTAL ROOM AND THE CONTROL ROOM 67
FIGURE 2.7 | WIRELESS TRANSMITTER TECHNOLOGY 69
FIGURE 2.8 | PERSONALIZATION OF THE SURGICAL PROCEDURES 72
FIGURE 2.9 | TAILORED TITANIUM MESH METHODOLOGY FOR CHRONIC CRANIAL IMPLANT........ 76
FIGURE 2.10 | TITANIUM MESH, FOOT PLATE AND HEALING PLATE........ 77
FIGURE 2.11 | FOOT PLATE POSITIONING NOMENCLATURE 79
FIGURE 2.12 | ADVERSE EFFECTS 81
FIGURE 2.13 | POST-OP FOLLOWING-UP AFTER THE SURGERIES 82
FIGURE 2.14 | SUMMARY OF THE FREELY BEHAVING MONKEY PLATFORM IN UNTETHERED CONDITIONS........ 88

TABLE 2.1 | SUMMARY OF ALL THE ANIMALS FOLLOW-UP........ 84

FIGURE 3.1 | TASK AND HYPOTHESIS........ 97
FIGURE 3.2 | BEHAVIORAL RECORDINGS 99
FIGURE 3.3 | TIME-VARYING CORTICAL, MUSCLE, AND KINEMATIC SIGNALS USED FOR ANALYSIS 100
FIGURE 3.4 | CHANGES IN FIRING RATE AND MODULATION DEPTH WITH TASK COMPLEXITY 101
FIGURE 3.5 | NEURAL CORRELATES IN SINGLE NEURON ACTIVITY FAIL TO GENERALIZE BETWEEN RHYTHMIC AND PLANNED LOCOMOTION 103
FIGURE 3.6 | DIFFERENCES IN KINEMATICS AND MUSCLE ACTIVITY ACROSS LOCOMOTOR TASKS AND PHASE TUNING OF SINGLE NEURONS 103
FIGURE 3.7 | POPULATION ACTIVITY ACROSS TASKS IS MORE COMPLEX IN PREMOTOR AND MOTOR THAN IN SOMATOSENSORY CORTEX 105
FIGURE 3.8 | VARIANCE EXPLAINED BY NEURAL MANIFOLDS AND CONTRIBUTION OF EACH TASK TOWARDS INCREASE IN COMBINED DIMENSIONALITY 106
FIGURE 3. 9 | SIMILARITY ACROSS TASKS AND LOCOMOTION SUBSPACES FOR FOUR MONKEYS 107
FIGURE 3.10 | LOCOMOTION AND TASK-RELATED ACTIVITY OF SENSORIMOTOR CORTEX IN BASIC AND SKILLED LOCOMOTION 109
FIGURE 3. 11 | LATENT ACTIVITY IN TOP THREE NEURAL MODES 110
FIGURE 3.12 | DPCA CONTROLS........ 111
FIGURE 3.13 | ROBUST DECODING OF GAIT PARAMETERS ACROSS BASIC AND SKILLED LOCOMOTION........ 112

FIGURE 4.1 | BIOLOGICALLY REALISTIC NEURAL NETWORK OF MUSCLE SPINDLE FEEDBACK FOR TWO ANTAGONIST MUSCLES........ 134
FIGURE 4.2 | COMPARISON OF LUMBAR SPINAL CORD AND VERTEBRAL LENGTH BETWEEN TWO MACAQUE SPECIES 136
FIGURE 4.3 | VERTEBRAL LENGTH AND SPINAL CORD WIDTH IN ADULT FEMALE *FASCICULARIS* MONKEY 136
FIGURE 4.4 | COMPARISON BETWEEN TWO ADULT FEMALE *FASCICULARIS* MONKEY 137
FIGURE 4.5 | TAILORED LUMBAR SPINAL ARRAYS IN MK-KA 139
FIGURE 4.6 | SURGICAL PROCEDURE 140

Figure 4.7 | Muscle recruitment during EES 141
Figure 4.8 | Spatiotemporal map of the spinal cord during EES 142
Figure 4.9 | X-ray comparison 144
Figure 4.10 | Conceptual framework for the technology translation 145

Figure 5.1 | Hypothesis of shared information via communication subspaces during locomotion 152
Figure 5.2 | Histological preparation after Utah array implantation in leg M1 153
Figure 5.3 | Intersectional viral strategy specifically targeting the layer V projecting neurons to the lumbar spinal cord 155
Figure 5.4 | Synaptic connectome of the lumbar CST in the spinal cord 156
Figure 5.5 | Inhibition of the lumbar CST in rodents 158

Figure 6.1 | Synaptic density analysis pipeline 175

Table 6.1 | Viral vectors 173

TABLE OF CONTENT

ACKNOWLEDGMENT **7**

ABSTRACT **9**

RESUME **11**

LIST OF FIGURES AND TABLES **13**

TABLE OF CONTENT **15**

INTRODUCTION **19**

- 1.1. CONTEXT 21
- 1.2. GENERAL OVERVIEW OF THE MOTOR SYSTEM 22
  - *1.2.1. Cortical motor areas 22*
  - *1.2.2. Somatosensory areas 23*
  - *1.2.3. Sensorimotor system 25*
  - *1.2.4. Motor control organization 25*
    - 1.2.4.1. The basal ganglia 26
    - 1.2.4.2. The cerebellum 26
    - 1.2.4.3. The brain stem and its descending pathway 26
    - 1.2.4.4. The corticospinal tract and the spinal cord 27
- 1.3. NEURONAL BEHAVIOR 29
  - *1.3.1. Movement encoding 29*
  - *1.3.2. Neural population dynamics 31*
    - 1.3.2.1. Neural manifolds 32
  - *1.3.3. Signature for therapeutic application 36*
- 1.4. LOCOMOTION 37
  - *1.4.1. Non-cortical basis of locomotion 38*
    - 1.4.1.1. Spinal networks 38
    - 1.4.1.2. Basal ganglia and mesencephalic locomotor region 39
    - 1.4.1.3. The brain stem 39
  - *1.4.2. Cortical basis of locomotion 39*
    - 1.4.2.1. Primary motor cortex 40
    - 1.4.2.2. Premotor cortex 42
    - 1.4.2.3. Primary somatosensory cortex 43
- 1.5. SYNOPSIS AND AIMS 44
- 1.6. PERSONAL CONTRIBUTION 45
- 1.7. BIBLIOGRAPHY 46

FREELY BEHAVING MONKEY PLATFORM **59**

- 2.1. BEHAVIORAL SETUP IN UNTHETERED CONDITION 61
  - *2.1.1. Behavioral training 63*
  - *2.1.2. Leg kinematic during locomotion 64*
- 2.2. WIRELESS TECHNOLOGY 67
- 2.3. PERSONALIZED SURGICAL PROCEDURES 71
- 2.4. ADVERSE EFFECTS OF TAILORED CRANIAL IMPLANTS IN MACAQUE MONKEYS 73
  - *2.4.1. Abstract 73*
  - *2.4.2. Introduction 74*
  - *2.4.3. Material and Methods 77*
    - 2.4.3.1. Animals 77
    - 2.4.3.2. Titanium mesh, foot plate, healing plate and percutaneous connectors (pedestals) 77
    - 2.4.3.3. Computer tomography (CT) imaging, 3D reconstruction and mesh modeling 78
    - 2.4.3.4. Surgeries 79
    - 2.4.3.5. Adverse effect assessments 80
  - *2.4.4. Results 81*
  - *2.4.5. Discussion 84*

2.4.6. Acknowledgments ... *86*
2.5. CONCLUSION ... 87
2.6. BIBLIOGRAPHY ... 89

NEURAL POPULATION DYNAMICS ARE CORTEX-SPECIFIC IN PREMOTOR, MOTOR, AND SOMATOSENSORY CORTICES DURING LOCOMOTION ... 93

3.1. ABSTRACT ... 95
3.2. INTRODUCTION ... 96
3.3. RESULTS ... 98
3.3.1. Behavioral tasks and recordings ... *98*
3.3.2. Generalization of neural correlates in locomotion ... *101*
3.3.3. Similarity of neural manifolds across locomotor tasks ... *104*
3.3.4. Locomotion—and task-dependent—neural correlates in sensorimotor cortex. ... *107*
3.3.5. Generalized decoders with task-independent neural manifolds. ... *111*
3.4. DISCUSSION ... 113
3.4.1. Simplicity of cortical population activity for locomotion. ... *114*
3.4.2. Low contribution of somatosensory cortex towards voluntary gait modifications ... *114*
3.4.3. Neural manifolds in motor cortex across rhythmic and skilled locomotion ... *115*
3.4.4. Task-dependent subspaces for locomotion in premotor cortex ... *116*
3.4.5. Improvement in generalization and variance explained by task-independent components ... *116*
3.4.6. Locomotion-subspace for generalized control of neurotechnologies ... *117*
3.5. MATERIAL AND METHODS ... 119
3.5.1. Data pre-processing ... *119*
3.5.2. Single neuron correlates ... *120*
3.5.3. Dimensionality estimates for task-dependent neural manifolds ... *120*
3.5.4. Comparison of task-dependent neural manifolds ... *121*
3.5.5. Separation of neural activity into task-dependent and task-independent components ... *122*
3.5.6. Signal variance ... *123*
3.5.7. Decoding of gait events and generalization across tasks ... *123*
3.6. BIBLIOGRAPHY ... 125

TOWARDS PERSONALIZED NEUROPROSTHETICS FOR SPINAL CORD INJURY ... 131

4.1. INTRODUCTION ... 133
4.1.1. Spinal cord injury ... *133*
4.1.2. Epidural electrical stimulation mechanisms. ... *133*
4.2. VARIABILITY IN LUMBAR SPINAL CORD MORPHOLOGY ... 135
4.2.1. Inter-species variability ... *135*
4.2.2. Inter-individual variability ... *136*
4.3. LUMBAR SPINAL ARRAY PERSONALIZATION ... 138
4.3.1. Lumbar spinal array design ... *138*
4.3.2. Surgical procedure ... *139*
4.4. SPINAL CORD STIMULATION PROTOCOL DESIGN ... 141
4.5. LIMITATION AND CONCLUSION ... 143
4.6. BIBLIOGRAPHY ... 146

DISCUSSION AND PERSPECTIVE ... 149

5.1. NEURAL ENCODING ... 151
5.1.1. Further analysis ... *151*
5.1.2. Electrophysiological signature of cortical encoding at the cellular level ... *152*
5.1.3. Biological tool to perturb cortical encoding at the cellular level ... *154*
5.1.4. Technological limitations in single cell encoding ... *160*
5.1.5. Searching for the neural code by exploring the neural manifold ... *160*
5.2. NEUROPROSTHETICS FOR SPINAL CORD INJURY ... 162
5.2.1. Epidural electrical stimulation: a long clinical story ... *162*
5.2.2. Future directions: combinatorial therapies ... *162*
5.3. BIBLIOGRAPHY ... 164

APPENDIX **169**

6.1. APPENDIX 1 171
6.1.1. Animal models *171*
6.1.2. Surgeries *171*
6.1.3. Viral vectors *173*
6.1.4. DREADD-mediated inactivation experiments *174*
6.1.5. Kinematic and muscle activity recordings *174*
6.1.6. Perfusion and histological preparation *174*
6.1.7. Immunohistochemistry *174*
6.1.8. Synaptic connectome in the spinal gray matter analysis *175*
6.1.9. Bibliography *176*

CURRICULUM VITAE **177**

- PART 1 -

INTRODUCTION

1.1. CONTEXT

While a movement seems effortless, the underlying processes orchestrated by the nervous system are remarkably complex. From the central nervous system to the muscles, motor information must be well sculped to elicit an appropriate movement. Although our knowledge on motor control drastically increased, the precise role of cortical areas is still debated. For instance, locomotor gait (i.e. locomotion) is thought to be governed by automated neural circuitry residing within the spinal cord and/or within the brain stem, while cortical areas may only adapt the adjustment of steps during walking on a rugged terrain. In that context, it is important to better understand the role of different cortical area structures underlying the production of locomotor behavior. New findings could result in improving available treatments or in developing new therapeutic strategies helping people with motor disabilities such as spinal cord injury, stroke or Parkinson’s disease.

To study the role of cortical areas during locomotion, nonhuman primates (NHPs) represent an adequate model because of their advanced sensorimotor attributes, which provide higher skilled capabilities. Moreover, recent advances in technology give the opportunity to record large number of neurons from different areas simultaneously with whole-body 3D kinematics and muscular activity.

In this manuscript, I will first introduce the state-of-the-art of the motor system organization and function. I will then present the implementation of a wireless technological framework for studying neural activity from three different cortical areas in freely behaving NHPs. I will then present how neural population dynamics are cortex-specific across different locomotor behaviors. Later, I will present how this knowledge could potentially be used in a brain-machine interface paradigm with the development of personalized neuroprosthetics implanted in the dorsal aspect of the lumbar spinal cord. Finally, I will discuss the future perspectives of locomotor control.

1.2. GENERAL OVERVIEW OF THE MOTOR SYSTEM

One of the primary advantageous capabilities of the animal reign is the ability to move voluntarily. The quote of the pioneer scientist Charles Scott Sherrington : *"to move things is all that mankind can do, for such the sole executant is muscle, whether in whispering a syllable or in felling a forest*."[1] highlights the fundamental importance of the motor system. Many years of research have brought valuable knowledge on how the motor system is organized and how it communicates with other systems. One of the major structures involved in the control of the motor system is the cerebral cortex. In this section, I will provide an overview of the different anatomical regions within the cortex and how they differ in function towards the control of movement.

1.2.1. Cortical motor areas

The concept of a 'motor' cortex was first introduced by Fritsch and Hitzig after the observation of muscle contractions following the stimulation of dog's cerebral cortex (Fritsch and Hitzig 2009). Hughlings Jackson subsequently proposed a somatotopic arrangement of the motor cortex limited to one side of the body (Jackson 1873), which David Ferrier confirmed by conducting electrical stimulation experiments in NHPs and observing muscle responses (Ferrier 1873; Bennett and Hacker 2001). Early in the 20th century, Charles Scott Sherrington highlighted the role of the spinal cord in stepping and standing, notably the flexion-reflex (as a protective reflex) followed by an extension-reflex of the contralateral homologous limb. After suggesting there is a "…relation between the brain and the final common pathway", he was the first to describe a detailed somatotopic map of the primate motor cortex (Gruenbaum and Sherrington 1902; Bennett and Hacker 2001; Burke 2006).

The cortical motor areas are located in the frontal lobe and are composed by: (1) the primary motor cortex (M1 or F1 in NHPs; Brodmann's area (BA) 4); (2) the supplementary motor area (SMA, a part of BA 6) subdivided into pre-SMA (F6) rostrally and SMA-proper (F3) caudally; (3) the premotor cortex (PM, a part of BA 6) subdivided into a dorsal part (PMd, F2 and F7) and a ventral region (PMv, F4 and F5). As a generalization, SMA is thought to be responsible of initiating voluntary movement, whereas PM is involved for movement planning. M1 sends the final motor information to the motoneurons residing within the spinal cord through the corticospinal tract (CST). Interestingly, among the cortical motor areas, M1 represents about half of the corticospinal (CS) neurons, whereas ~10% of the CS neurons are found in PM and 20% in SMA. The remaining 20% CS neurons are found in the cingulate motor area (CMA, BA 6, 23 and 24) (**Figure 1.1**). M1 is further subdivided into a rostral region (old M1), that is common in many mammals, and a caudal region (new M1) unique to primate species (Rathelot and Strick 2009). Because of their interconnections, these motor cortical areas co-operate in order to generate an adequate movement. However, they also share reciprocal connections with many other brain structures (e.g. cerebellum, basal ganglia, parietal and prefrontal areas). Therefore, motor cortical areas are not solely responsible for creating appropriate motor output (e.g. for review: Lawrence and Kuypers 1968a; 1968b; Brinkman 1981; Matelli et al. 1985; Wiesendanger 1986; Dum and Strick 1991; Luppino et al. 1993; Rizzolatti et al. 1998; Rizzolatti and Luppino 2001; Dum and Strick 2002; Lemon 2008; Mendoza and Merchant 2014).

---

[1] Principles of Neural Science, 5th ed. (2013), E. R. Kandel, J. H. Schwartz, T. M. Jessell, S. A. Siegel-baum & A.J. Hudspeth. The McGraw-Hill Companies, Inc. *Part VI: Movement*, page 739.

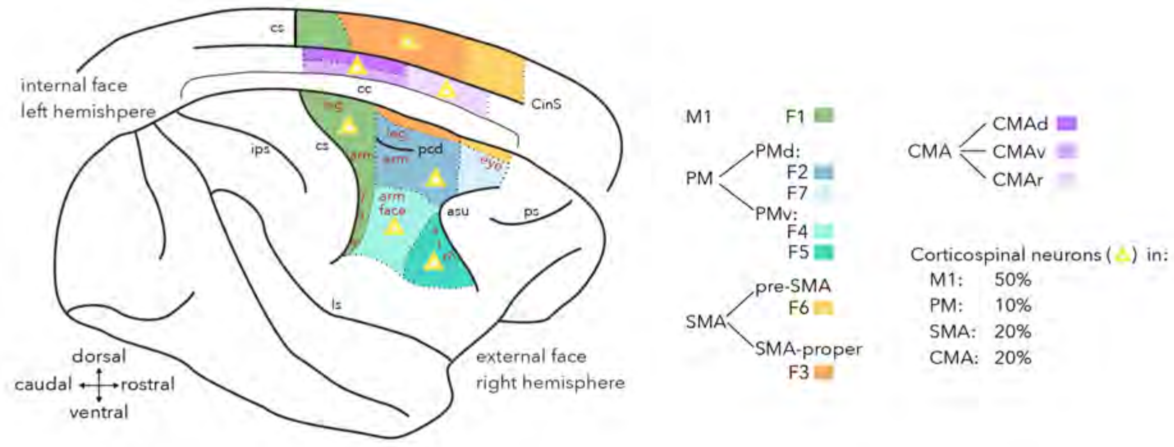

Figure 1.1 | Schematic representation of motor cortical areas in NHPs

The motor cortical areas are located rostrally to the central sulcus (cs) in the frontal lobe. The four principal motor cortical areas are depicted in different colors (green for M1, blue/turquoise for PM, orange for SMA and purple for CMA). The premotor cortex (PM) is subdivided into a ventral (PMv) and a dorsal (PMd) regions that are themselves further subdivided in two: the rostral part of PMd (PMd-r, F7) and the caudal part of PMd (PMd-c, F2). The same subdivision applies for PMv: rostral (PMv-r, F5) and caudal (PMv-c, F4) parts. Similarly, SMA is subdivided into a rostral part (pre-SMA, F6) and a caudal region (SMA-proper, F3). Finally, the cingulate motor area (CMA) is partitioned into three areas: the dorsal CMA (CMAd), the ventral (CMAv) and the rostral (CMAr) areas. The yellow triangles illustrate the corticospinal neurons in layer V. The percentage of the corticospinal neurons are based on (Dum and Strick 1991). Note that some CS neurons, also present in the parietal and somatosensory cortices, have not been considered here. Somatotopic organization is shown in red. cs=central sulcus; CinS= cingulate sulcus; cc=corpus callosum; ips=intraparietal sulcus; pcd=precentral dimple; asu= arcuate sulcus; ps=principal sulcus; ls=lateral sulcus. Modified from (Rizzolatti et al. 1998; Rouiller 2012).

1.2.2. Somatosensory areas

In early electrophysiological studies, somatosensory evoked-potentials to tactile stimuli have been recorded in clearly defined cortical regions in cats and monkeys. This region of the postcentral gyrus has thus been termed the primary somatosensory cortex (S1). Neuronal responses architectonically differ within S1 delineating four distinct sub-regions: area 3a, area 3b (proper S1), area 1 and area 2 of Brodmann. All the four areas are somatotopically organized and are summarized by the "homunculus", emphasizing the multiple body representations within S1. Each of the four areas tends to process a specialized type of information. As a generalization, area 3a is dominated by muscle receptor inputs, areas 3b and 1 mainly receive inputs from cutaneous receptors, and inputs to area 2 come from deep muscle and joint receptors. Cutaneous receptor responses are nevertheless found in all the 4 areas (Phillips et al. 1971; Whitsel et al. 1971; Hyvärinen and Poranen 1974; Merzenich et al. 1978; Tanji and Wise 1981; Pons et al. 1985; Gardner 1988) (**Figure 1.2**).

Touch and proprioception sensations are mediated by numerous types of mechanoreceptors (e.g. Pacinian corpuscle, Meissner corpuscle, Ruffini ending, muscle-spindle, Golgi tendon organ, etc). Both somatic sensations are conveyed by the medial lemniscus. The fibers ascend through the dorsal column of the spinal cord to the medulla, where the axons decussate. Finally, they project to the ventral posterior lateral (VPL) nucleus, ventral posterior inferior (VPI) nucleus and posterior nuclei group of the thalamus. A second ascending pathway, the anterolateral system, conducts mostly nociceptive, thermal and pressure information. The pathway decussates at the level of the spinal cord to finally reaches the VPL and to some extent the VPI, the centromedian, parafascicular complex and the intralaminar nuclei (De Vito and Simmons 1976; Berkley 1980; Dijkerman and de Haan 2007; Gardner & Johnson, 2013). Most of the somatic sensation information is relayed from VPL to S1. In addition, areas 3a and 2 receive projections from the ventroposterior superior nucleus (VPS). VPL and other thalamic nuclei also relay information to the secondary somatosensory (SII), posterior parietal, and insular cortices (Whitsel et al. 1969; Jones and Powell 1970; Burton and Jones 1976; Whitsel et al. 1978; Jones et al. 1979; Cusick et al. 1985; Friedman and Murray 1986).

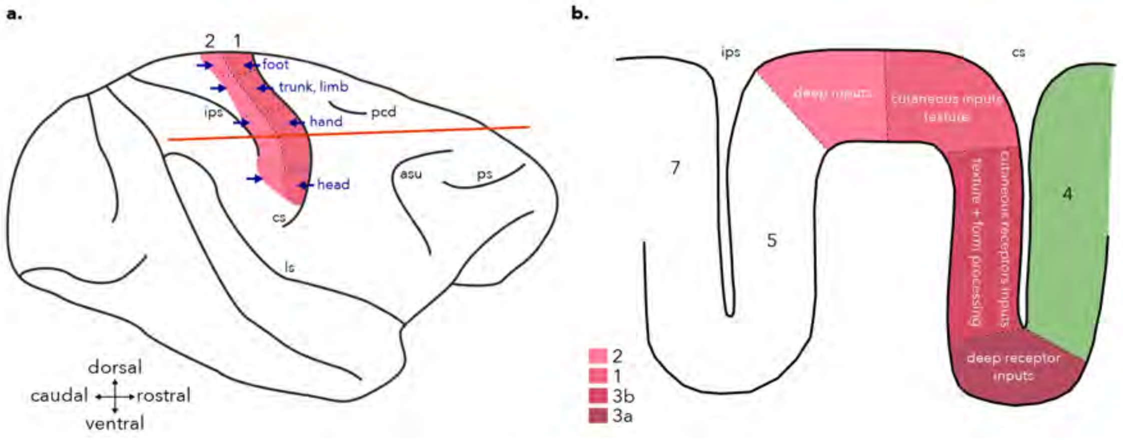

Figure 1.2 | Schematic representation of primary somatosensory cortex in NHPs

a. S1 is located caudally to the central sulcus (cs). Somatotopic organization is shown in blue. Note that the somatotopic organization is conserved along the medio-lateral axis between M1 and S1. **b.** Saggito-horizontal schematic view of a cross section in **a.** (red line). Four S1 areas are shown in red gradient colors. Area 3a is located in the deepest bank of the central sulcus and is a transition zone between BA 4 (M1, in green) and proper-S1 (area 3b). Area 1 and area 2 are located on the post-central gyrus before the transition with parietal cortex (BA 5 and BA 7). cs=central sulcus; ips=intraparietal sulcus; pcd=precentral dimple; asu= arcuate sulcus; ps=principal sulcus; ls=lateral sulcus. Modified from (Pons et al. 1985; 1987; James et al. 2007).

1.2.3. Sensorimotor system

In rodents and marsupial mammals, the sensorimotor cortex has been extensively documented (Ferezou et al. 2007; Petersen 2007; Diamond et al. 2008). In primates, the term of sensorimotor cortex may sound unusual because of M1 and S1 cytoarchitecture characteristics and macroscopic organization. However, the functional confinement representation within a strict cytoarchitecture boundaries is often impossible (Penfield and Boldrey 1937). Conceptually, it seems reasonable to assume a close collaboration between somatosensory and motor systems that would lead to motor behavior (Wiesendanger 1981). In fact, M1 and S1 share strong reciprocal connections. Usually, these connections keep a somatotopic organization (e.g. hand region of M1 receives projection from hand region of S1), although some heterotopic projections are also found (e.g. hand region of M1 projects to leg region of S1) (Jones and Powell 1970; Jones et al. 1978; Künzle 1978; Huerta and Pons 1990; Stepniewska et al. 1993; Tokuno and Tanji 1993; Burton and Fabri 1995; Kaas 2004; Liao et al. 2013). Interestingly, new M1 is more strongly connected with areas 3a and 1 than old M1. In contrast, old M1 has more projections to area 2 than new M1 (Stepniewska et al. 1993). Cutaneous inputs are also found in new M1 while old M1 mainly receives deep inputs (Strick and Preston 1978). Furthermore, electrophysiological studies support the sensorimotor system concept. For example: (1) in human patients, M1 stimulations lead to fingers sensations (Penfield and Boldrey 1937); (2) S1 stimulations evoke motor responses after a complete resection of M1 and SMA (Darling et al. 2011); (3) during movement preparation, the suppression of cutaneous evoked responses is exclusively restricted to M1 but not in PM and S1 (Seki and Fetz 2012).

Considering these anatomical and electrophysiological properties, the sensorimotor system integrates somatosensory information to produce an appropriate movement. This process is referred to as sensorimotor integration (Hatsopoulos and Suminski 2011; Pruszynski et al. 2011).

1.2.4. Motor control organization

The sensorimotor system does not rely only on the motor cortical and the somatosensory areas to control motor outputs, but incorporates all the afferents, efferents, and central integration processing from different structures. Those structures are organized in a hierarchical and parallel manner with the cerebral cortex in addition to the hierarchy (**Figure 1.3**) (Riemann and Lephart

2002). Some structures and their functions towards the control of movement are briefly described below.

1.2.4.1. The basal ganglia

The basal ganglia (BG) is composed by several nuclei located in the forebrain and the midbrain: the putamen, the caudate nucleus, the nucleus accumbens, the substantia nigra, the subthalamic nucleus and the globus pallidus. All BG structures are strongly interconnected for local processing of information. Virtually all the cerebral cortex projects to the BG and, in the form of a loop, the BG projects back the information to the cerebral cortex via the thalamus. The mechanism of BG structure functions are through a selection of adequate and inadequate responses. Inappropriate connectivity and/or disturbance within the BG can lead to disorders such as Parkinson's disease or Huntington's disease. (Nauta and Domesick 1984; Rouiller et al. 1994; Parent and Hazrati 1995; Haber 2003; Lanciego and Vázquez 2011).

1.2.4.2. The cerebellum

The cerebellum is principally involved in motor control by receiving information from several structures (cerebral cortex, BG, brain stem and the spinal cord). Generally, it adapts a movement by integrating information from the spinal cord and the cerebral cortex. With its direct connection with the brain stem, the cerebellum can directly influence and modulate a motor output (Ramnani 2006; Bostan et al. 2013; Lisberger and Thach, 2013).

1.2.4.3. The brain stem and its descending pathway

The brain stem encompasses many nuclei responsible in motor control and motor execution (Angeles Fernández-Gil et al. 2010). Those nuclei send projection via descending pathways to the spinal cord. Three main descending pathways can be listed as: (1) the ventromedial pathway (tectospinal tract, reticulospinal tract and vestibulospinal tract) contributing to the bilateral postural control (head, neck and trunk), respiration and proximal limb movements; (2) the dorsolateral pathway (rubrospinal tract and pontospinal tract) providing additional capacity to flexion movement in distal limb segments (elbow and wrist); and (3) the emotional motor system (raphespinal tract) including serotonin pathway that exerts influence on spinal reflexes and plays a role in specific motor activities (defensive reaction, cardiac change, …). The ventromedial pathway originates from reticular formation, superior colliculus and vestibular complex (Lemon 2008). The reticular formation is composed by several sub-structures such as the raphe nuclei; the pontine reticular nuclei and the gigantocellular nucleus; and the lateral reticular nucleus (Matsuyama and Drew 1997; Matsuyama et al.

1997; 1999; Lemon 2008; Sakai et al. 2009; Angeles Fernández-Gil et al. 2010). Interestingly, the superior colliculus plays also a role in sensorimotor integration, some neurons, located in the intermediate and deep layers, are indeed firing before the execution of a movement (Sparks and Hartwich-Young 1989; Sparks 1991; Gandhi and Katnani 2011).

1.2.4.4. The corticospinal tract and the spinal cord

As previously mentioned, the spinal cord receives information through descending pathways from the cortex. The tract that is mostly involved in the control of movement is the CST, present in all mammals. CST axons exit the cortex, travel though the internal capsule and cross the midline at the level of the pyramids (pyramidal decussation). They target the contralateral spinal cord gray matter via the dorsolateral and ventral pathways (note that a small proportion of axons, ~10%, project ipsilaterally) (Welniarz et al. 2016). In primates (and rodents), CS projections reach all spinal cord levels and innervate all regions of the spinal cord gray matter (Lemon 2008). CS neurons are found almost in all motor cortical areas (except F6 and F7, **Figure 1.1**), S1, parietal cortex and parietal operculum (Lemon 2008). Interestingly, in primates, the CST projects directly to the motoneurons located in the lamina IX of the spinal cord. This projection is called the corticomotoneuronal (CM) projection and confers fine control of movement (Courtine et al. 2005b; 2007; Lemon 2008; 2019). Interestingly, the CM projection is restricted to new M1 (caudal M1) and, remarkably, ~16% of CM neurons are found in area 3a of S1. The CM cells can bypass spinal cord mechanisms in order to shape new motor output patterns essential for highly skilled movements (Rathelot and Strick 2006; 2009).

The CST also contributes to other various domains: control of afferent inputs, control of spinal reflexes, plasticity of spinal cord circuits, etc. (e.g. for review: (Lemon 2008; 2019)). Certainly, motor commands are also sculpted through spinal reflexes (proprioception, H-relfex, etc) and possibly mediated within central pattern generators (CPGs), allowing the generation of automatic and rhythmic motor pattern, such as breathing or walking (Marder and Bucher 2001; Steuer and Guertin 2019).

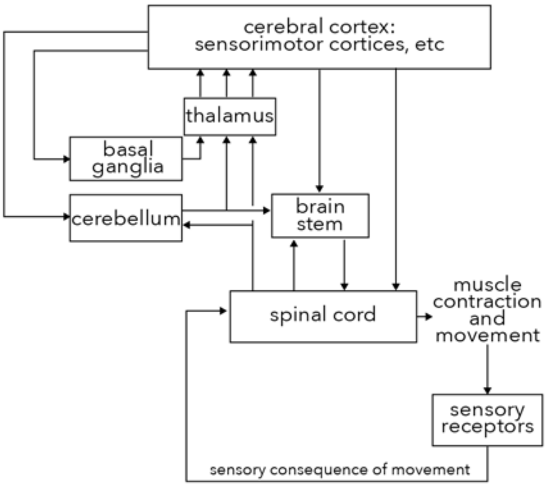
cerebral cortex:
sensorimotor cortices, etc
thalamus
basal ganglia
cerebellum
brain stem
spinal cord
muscle contraction and movement
sensory receptors
sensory consequence of movement

Figure 1.3 | Hierarchical and parallel organization of the motor control system.

Cerebral cortices send the final command to the muscle through the spinal cord for executing a movement. Information are locally processed in the basal ganglia and the cerebellum before sending it back to the cerebral cortex via the thalamus. Motor command information are also relayed and/or processed in the brain stem. Sensory feedback plays also a role in movement modulation. Note that for sake of clarity, the ascend somatosensory pathways as well as inputs from the visual and vestibular systems are not shown in the scheme.

1.3. NEURONAL BEHAVIOR

The wide range of nervous system structures involved in the production of movements indicates the complexity of the motor system. The primate sensorimotor cortex represents an adequate model to study the control of movement. In fact, numerous studies conducted on monkeys untangle how the cerebral cortex encodes motor outputs. A lot of knowledge have been acquired but numerous questions still remain open. A key question for executing a movement reside in the neuronal activity of the cerebral cortex, especially M1 that exhibits various neuronal patterns of activity while animals perform a variety of behaviors. This diversity of cell signaling is designated as neuronal behavior.

1.3.1. Movement encoding

A movement can be conceptualized as a model of three general hierarchical levels, from the highest level to the lowest: (1) extrinsic kinematics, which refers to the motion in space (target, movement path, direction); (2) intrinsic kinematics that define limb geometry during movement (joint angles) and (3) the intrinsic dynamics that are the causal force and muscle activity required for motor behavior (Kalaska and Crammond 1992). These parameters can be related (and / or correlated) with spiking activity of single neurons while a monkey perform a movement. As shown by Evarts (1968), the majority of pyramidal tract neurons (PTN) from M1 hand area are related to the variation of force output (intrinsic dynamic) generated by the wrist. The same neurons are secondary related to direction of displacement (extrinsic kinematics). However, some force-unrelated PTNs are related to the rough displacement. Along this line, numerous PTNs are related to the fine details of applied force only (Evarts 1968). However, other studies have highlighted other potential parameters that might be encoded by M1: (1) neurons discharging in relation to the pattern of muscular activity (intrinsic dynamic) and (2) neurons firing in relation to the wrist position and movement direction (extrinsic kinematics) (Thach 1978; Georgopoulos et al. 1982; Kakei et al. 1999) (**Figure 1.4**).

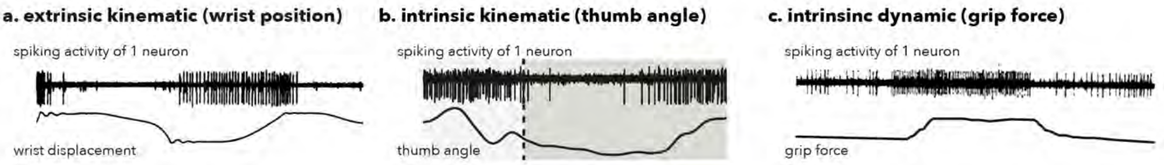

Figure 1.4 | Three representative spiking activity during movement

a. Neuron active during the flexion displacement of the wrist and silent during the extension displacement. Modified from (Evarts 1968). **b.** Neuron silent while the thumb adduction angle decreases (light gray = reaching; dashed vertical line =

grasping; dark gray = pulling). Modified from (Barra et al. 2019). **c.** Neuron activated during application of a grip force. Modified from (Smith et al. 1975).

Although, the three levels of the model can be correlated with spiking activity, the link between motor behavior, limb kinematics, and neural control remains poorly understood. Are the high-level features of behavior encoded by the cortical motor areas or is it the low-level features of the motor periphery? In other terms: do the cortical motor areas encode muscles or movements (Scott 2004)? The model cues answering this question by implying, in such a way, that a movement is represented at the single-cell level and that the nervous system must obey to the laws of motion by containing explicit representation of these parameters and controls the musculoskeletal system accordingly. Conceptually, this model seems a bit simplistic. Indeed, simple experiments in humans showed that a 3D reaching movement transforms the extrinsic kinematics to intrinsic kinematics using a non-linear approximation (Soechting and Flanders 1989; Flanders and Soechting 1990). In contrast, inaccurate reaching occurs when subjects implement a linear transformation suggesting that the nervous system uses linear approximations of the non-linear relation between limb angles and target location during the inaccurate movement execution (Soechting and Flanders 1989; Flanders and Soechting 1990; Kalaska and Crammond 1992). Moreover, the tuning property to movement covariates represents a small proportion of recorded neurons. For instance, ~35% of recorded neuron are tuned to the grip force (Smith et al. 1975) and ~40% are directionally tuned (Georgopoulos et al. 1982). Thus, some single neurons activity doesn't represent movement parameters (Fetz 1992; Scott 2004; Churchland and Shenoy 2007). Surprisingly, even some CM cells don't represent movement covariates (Fetz et al. 1989). Indeed, neuronal behavior is complex and heterogeneous therefore suggesting a causal role played by the recorded neurons in a larger network (Churchland and Shenoy 2007). Following this concept, Georgopoulos and colleagues had elegantly demonstrated that population of neurons encodes a direction of movement. In order to do so, they weighted the vectorial contribution of each cell (magnitude of the vector = change in cell discharge rate associated with the particular direction of movement; direction of the vector = preferred direction of that cell). The vector sum of these contributions is the neuronal population vector and points towards the direction of the movement in space before the movement onset (**Figure 1.5**) (Georgopoulos et al. 1988). Again, this population model accounts only the neurons representing the direction of movement and discards all other neuronal activity that does not represent this particular movement covariate.

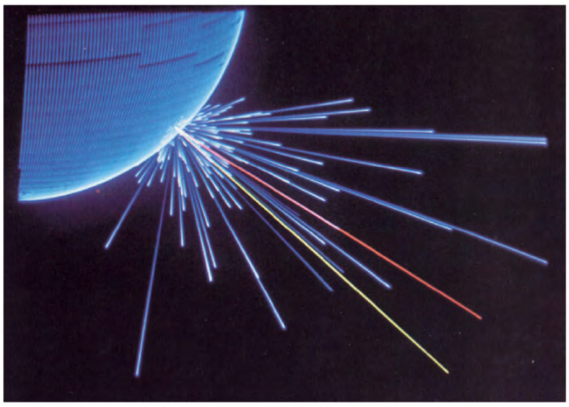

Figure 1.5 | Neuronal population coding for movement direction.
The vectorial contributions of individual neurons in the population (n=475 cells) are depicted with the blue lines. The population vector (vector sum) is shown in red while the direction of the movement is the yellow line (Georgopoulos et al. 1988).

In fact, by excluding some neurons, we may deviate from the understanding of the neural control of movement. As stated by Cisek: *"the role of the motor system is to produce movement, not to describe it"* (Cisek 2006). Thus, neural computations at the population level are based on the joint activity of interconnected neurons and therefore may reflect intrinsic dynamics comprising both the receiving inputs and the generated outputs (Sussillo et al. 2015). The results of population activity must therefore be constrained to the recorded network that includes inputs from other structures as well as the generated output (Shenoy et al. 2013). Thanks to the recent technological developments, it is now possible to record the activity of large numbers of neurons simultaneously with motor behavior. Furthermore, the statistical and modeling tools together with the computational power provide new methodological practice for analyzing neural population behavior (Gallego et al. 2017).

1.3.2. Neural population dynamics

Here, I will describe how we can conceptually explain the encoding paradigm and derive it to neural population dynamic system. The motor encoding paradigm described in the previous chapter attempts to explain most neural activity as tuning for movement parameters:

$$r_n(t) = f_n(param_1(t), param_2(t), \dots) \tag{1.1}$$

where $r_n(t)$ is the firing rate of the neuron n at time t; f_n is a tuning function and $param_1$, $param_2$ are the arguments such as joint angle, limb velocity, etc (Churchland et al. 2012). Certainly, the available parameters are so rich that models have to adjust some parameters. With such approach, the neural activity is understood in terms of representational functions. Instead, in a dynamical system (= system where the future state is a function of its current state, its input and maybe some noise), the nervous system generates a pattern of activity in order to achieve an adequate movement:

$$m(t) = G[r(t)] \tag{1.2}$$

where *m(t)* is a time varying vector of muscle activity, *r(t)* is a time varying vector of cortical activity and *G*[] is the mapping that captures the action that lies between the cortical and muscle activities; with the dimensions *m(t)* < *r(t)* (Shenoy et al. 2013). In equitation (1.2), the dynamical system must generate the firing pattern as *r(t)* has moved to the right side of the equation. Another way to describe the neural population activity is to express it with its derivative:

$$\dot{r}(t) = f\big(r(t)\big) + u(t) \tag{1.3}$$

where, *r(t)* is the firing rate, *ṙ(t)* its derivative, *f* an unknown function and *u(t)* other inputs (Churchland et al. 2012). Given equations (1.2) and (1.3), cortical function is therefore described through the activity at the population level, where the single-neuron activity is hardly separable. Certainly, the full dynamical system comprises millions of neurons receiving inputs, feedbacks and generating an output. Consequently, it is impossible to monitor the activity of the entire dynamical system. In order to tackle this issue, one may assume that the state of the population, even from few recorded cells (~100), evolves with time through a coordinated firing rate that engenders an output. If the encoded features are lower than the number of neurons, then, the population activity must capture relevant aspects in a lower dimensional space than the number of neurons. This property can be explained by the fact that neural population dynamics must be robust to achieve an adequate output regardless of the noise (e.g. neuronal death). Indeed, this noise would have only minimal impact on the map *G* in equation (1.2) and therefore, both *G* and the function *f* in equation (1.3) would probably pool the high dimensional neuronal activity of the vector *r* to a smaller meaningful low dimensional space. This lower dimensional space is embedded into all the possible patterns of activity. Thus, the function *f* in (1.3) must also be confined to this space because both the neural population dynamics and its influence on the muscles matter. Consequently, the application of dimensionality reduction techniques will capture low dimensional neural trajectories that summarize the whole population activity (Stopfer et al. 2003; Yu et al. 2009; Shenoy et al. 2013).

1.3.2.1. Neural manifolds

Population of neurons have been shown to have a common neural process that can be captured with dimensionality reduction methods. Dimensionality reduction methods find new explanatory variables from the high-dimensional data set. These new variables are called the *latent variables*. The latent variables capture the variance present in the original data set. Therefore, each neuron provides a shared neural process, prominent in the population, captured by the latent variables. The latent variables are therefore seen as a collective role of all recorded neurons as well as the unobserved neurons. Latent variable dynamics are confined within a low-dimensional space, designated as *neural manifold*. A neural manifold is characterized by independent patterns called *neural modes* describing the dynamics, or time evolution, of the latent variables. The dynamics of individual neurons is summarized by the following linear combination model (Gallego et al. 2017):

$$n_i(t) = \sum\nolimits_j u_{ij}\, L_j(t) + \varepsilon_i \tag{1.4}$$

where *n* is the activity of the *i*th neuron; L_j is the *j*th latent activity of the *j*th neural mode; u_{ij} is the coefficient that quantifies the contribution of the *j*th latent activity of the *i*th neuron; ε_i is the neural noise not accounted by the model (Cunningham and Yu 2014; Gallego et al. 2017) (**Figure 1.6**).

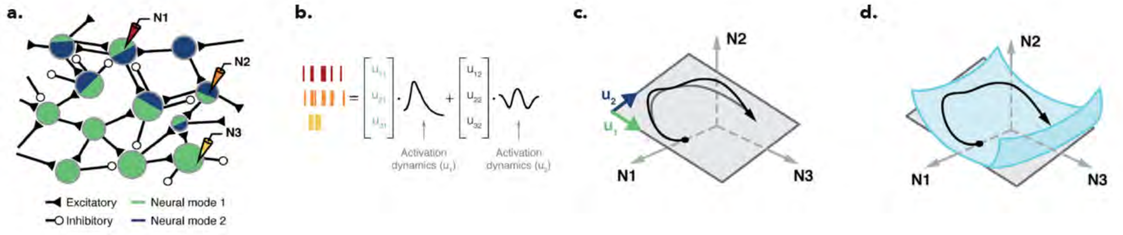

Figure 1.6 | Conceptual illustration of the neural manifold

a. The population activity is governed by latent variables. The magnitude contribution of the latent variable to the neuronal activity is shown by the relative size of the blue/green areas. **b.** the spiking activity of three recorded neurons (N1, N2 and N3) can be reconstructed with a linear combination of the two latent variables (black traces). The vectors [u_{11}, u_{21}, u_{31}] and [u_{12}, u_{22}, u_{32}] are the neural modes. **c.** Neural population activity (black curve) of the three neurons in the neural space [N1,N2,N3] is confined to a lower-dimension space, the neural manifold (gray plane) spanned by the two neural modes, u_1 and u_2. The gray curve represents the neural population activity projected to the neural manifold. **d.** A flat manifold (gray plane) can be extracted from a non-linear manifold (in blue) with linear approximation methods. Modified from (Gallego et al. 2017).

Common linear dimensionality reduction techniques, such as principal component analysis (PCA) provide the parameters of equation (1.4). Mathematically, PCA finds orthogonal eigenvectors (i.e. the neural modes) with the largest eigenvalues that best explain the spread in the data based on their covariance matrix (Cunningham and Yu 2014). Therefore, PCA is an unsupervised algorithm that extracts important features from unlabeled data. In contrast, supervised methods, such as linear discriminant analysis (LDA), classify labeled data of one or more dependent variables (e.g. stimulus identity, time index, …). Thus, LDA finds a low-dimensional space where the separation of the groups is optimized by identifying directions in which the between-group variance is maximized relative to the within-group variance (Cunningham and Yu 2014).

Although PCA extracts a complex picture of the population activity dominated by strong temporal dynamics, the neural modes can still include several mixed components that are related to specific parameters of the experiment, for example different tasks, types of stimuli, decisions, etc. The demixed PCA (dPCA) offers a solution to that issue by reducing the dimensionality of the data and decomposing the dependencies of neural activity onto the task parameters (**Figure 1.7**) (Kobak et al. 2016).

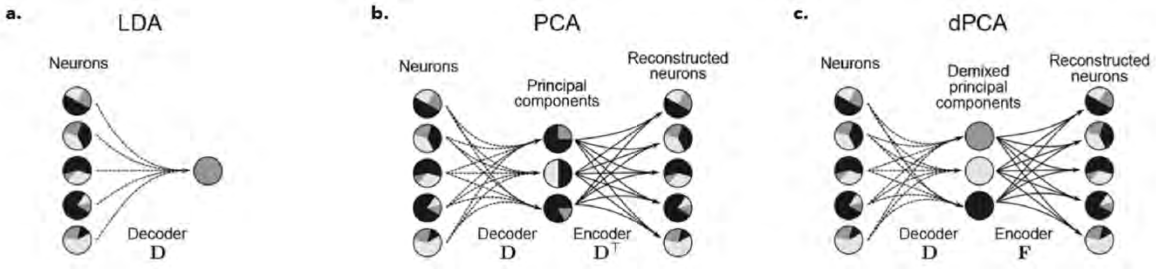

Figure 1.7 | **Conceptual principle of the dPCA**

a. LDA maps the neuronal firing rate to a latent component allowing to decode a task parameter of interest. The relative size of the shaded gray areas indicate the proportion of variance due to the task parameters (e.g. stimulus, time and decision). Neurons are therefore selectively mixed, whereas the LDA component is maximally demixed. **b.** PCA extracts components by minimizing the distances between the original data points and their projections to the low-dimensional space. However, the projected data into the PCA axis loss their mixed selectivity. A second linear transformation can reconstruct the original firing rates. **c.** the dPCA takes the advantage of the PCA and LDA by minimizing the projection distances and enforcing a demixing constraint on the latent variables. The original firing rates can also be reconstructed with linear transformations. Modified from (Kobak et al. 2016).

The key difference between PCA and dPCA resides in the computation of the decoder matrix. The PCA compresses the original data X with a decoder matrix D. An encoder matrix D^T can decompresses the resulting principal components to the original data X. The decoder matrix D is found by minimizing the squared error between X and the reconstructed data DD^TX:

$$L_{PCA} = \|X - D^T DX\|^2 \tag{1.5}$$

where, L_{PCA} is the loss function; X the original data (usually m rows of neurons and n samples in columns). The task parameters are not taken into account in the loss function, so the PCA is not able to decode nor demix theses parameters (Kobak et al. 2016). Instead, dPCA does not reconstruct the full firing rate X but the activity averaged over trials and over some task parameters, X_p. The flexibility of PCA is still preserved by keeping the decoder matrix D. The encoding and decoding matrices are obtained by minimizing the loss function:

$$L_{dPCA} = \sum_{p} \|X_p - F_p D_p X\|^2 \tag{1.6}$$

where, L_{dPCA} is the loss function; X the original data, X_p is the averaged data of a task parameters p; D the decoder matrix; and F the encoder matrix. Each row of D returns a demixed principal component. In contrast to classical PCA, the decoder and encoder axes of two different parameters p_1 and p_2 are found independently and therefore may not be orthogonal to each other (Kobak et al. 2016).

As an example, a monkey had to discriminate between two stimuli applied on the finger. The second stimulus (F2) comes 3 seconds after the first one (F1). Then, the monkey had to report which stimulus had a higher frequency by pressing one of the two buttons. When focusing on the neural representation of F1 and the decision, 12 different parameters are accounted (six different frequency of F1 and two different decisions) (**Figure 1.8a**). The peri-event time histogram (PETH, i.e. trial-averaged neuronal time-dependent firing rate), shows that neurons are tuned to F1, the decision or both; therefore, they are "mixed selective" (**Figure 1.8b**). After a PCA, the latent variables show similar pattern of activity across the different conditions (**Figure 1.8c**), whereas the dPCA demixes the experimental conditions and captures latent variables that are unrelated to the conditions, related to the stimulus, the decision or the interaction between both (**Figure 1.8d**) (Kobak et al. 2016).

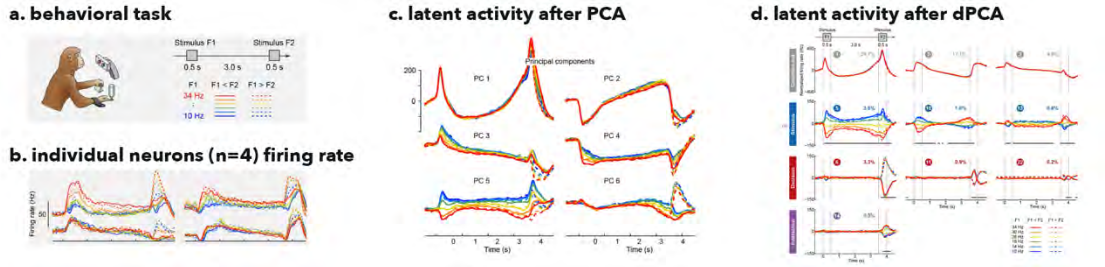

Figure 1.8| Example of latent activities after PCA or dPCA

a. After two tactile stimuli, the monkey reports what was the stimulus with higher frequency. **b.** PETH of four neurons showing their mixed selectivity. **c.** After a PCA, the latent activities are not demixed. **d.** The dPCA can demix the neural population activity into 4 components: (1) the independent-condition; (2) stimulus-dependent ; (3) decision-dependent and (4) the interaction-dependent. Modified from (Kobak et al. 2016).

In the example of **Figure 1.8**, the classic PCA does not offer a good solution for characterizing the neural population behavior. However, depending on the experimental conditions as well as the behavioral paradigm, PCA brings useful understanding about neural behavior. Indeed, latent variables during a reach-and-grasp movement to distinct target locations have different pattern of activation within non-similar neural manifolds orientation (i.e. angles between them) (Gallego et al. 2018). Neural manifolds are preserved in M1, PMd and S1 up to two years during consistent behavior, even though the recorded neurons were constantly changing (Gallego et al. 2019).

To summarize, recordings involving many neurons can be decomposed using dimensionality reduction techniques, such as PCA, that will recapitulate the firing rates to latent variable captured within a neural manifold. dPCA decomposes the neural manifold into *subspaces* capturing task-related and task-unrelated components providing detailed insights on the neural dynamic behaviors. For instance, a neural manifold can be decomposes to subspaces that are related to other manifolds, such as the output-potent subspace (Kaufman et al. 2014; Perich et al. 2018) or the communication subspace (Semedo et al. 2019).

1.3.3. Signature for therapeutic application

The wide variety of neural responses combined with the new advances of our understanding of neural dynamics affords a path for clinical application using brain-machine interfaces. In 2008, cortical patterns have been extracted to enable a monkey to move a robotic arm for self-feeding (Velliste et al. 2008). Monkeys were able to directly control muscles stimulation from M1 activity after a transient paralysis of the arm (Moritz et al. 2008; Ethier et al. 2012). Similarly in humans, tetraplegic patients were able to move a robotic arm or to control muscle stimulation in a brain-controlled fashion (Hochberg et al. 2012; Ajiboye et al. 2017). Close-looped stimulation of the spinal cord, also help the ability to move after spinal cord injury in monkeys (Zimmermann and Jackson 2014).

These examples show the extraordinary capability of BMIs to restore lost motor functions. However, most of these works, translational and fundamental, were performed in motor control of forelimbs movement paradigms, while hindlimbs movements, such as locomotion, remain explored to a lesser extent.

1.4. LOCOMOTION

Locomotion is defined as the ability to move from a place to another. In mammals, locomotor gait is constituted by a succession of stereotypic and repetitive limb movements through a complex sequences of muscular contractions orchestrated by the nervous system. In this manuscript, the term "locomotion" will mainly refer to as quadrupedal locomotor gait with a focus on the hindlimb (i.e. the legs) movements in quadrupeds. It is, nevertheless, important to notice that bipedal locomotion, as seen in humans, is also characterized by limb alternation while walking or running (Mann and Hagy 1980; Wannier et al. 2001). Thus, a good coordination of all limbs is crucial to achieve propulsion, balance and to adapt to the surrounding environment. Over-ground locomotion is characterized by a succession of gait cycles that are composed by a stance phase (when the foot is in contact with the ground) and a swing phase (when the foot is off the ground), both resulting from muscle contractions. The swing phase is subdivided into two phases: (1) the flexion and; (2) the early extension phase. In contrast the stance phase consists of two successive late extension phases. In order to initiate a swing phase, flexor muscles need to be engaged (e.g. from proximal to distal: iliopsoas (IL), semitendinosus (ST) and tibialis anterior (TA)). Then, extensor muscles activate for the stance phase (e.g. from proximal to distal: gluteus medius (GLU), medial gastrocnemius (MG) and flexor hallucis longus (FHL)) (**Figure 1.9b**) (Grillner 1975; Roy et al. 1991; Courtine and Schieppati 2003; Courtine et al. 2005a). Motoneurons located in the ventral horn of the spinal cord control the sequence to which the limbs and muscles are modulated. Interestingly, the spinal cord is able to produce a rhythmic and patterned activity without input from the cortex (Eidelberg et al. 1981; Grillner and Wallen 1985; Whelan 1996; Minassian et al. 2017) via the conceptual theory of the central pattern generators (CPGs), that provide activation of flexor and extensor motoneurons in the absence of sensory or descending inputs (Marder and Bucher 2001; McCrea and Rybak 2008). However, the fine-tuning of locomotion must be adapted through different inputs (CST, spinal interneurons, etc) (Lemon 2008; McCrea and Rybak 2008; Filli et al. 2019).

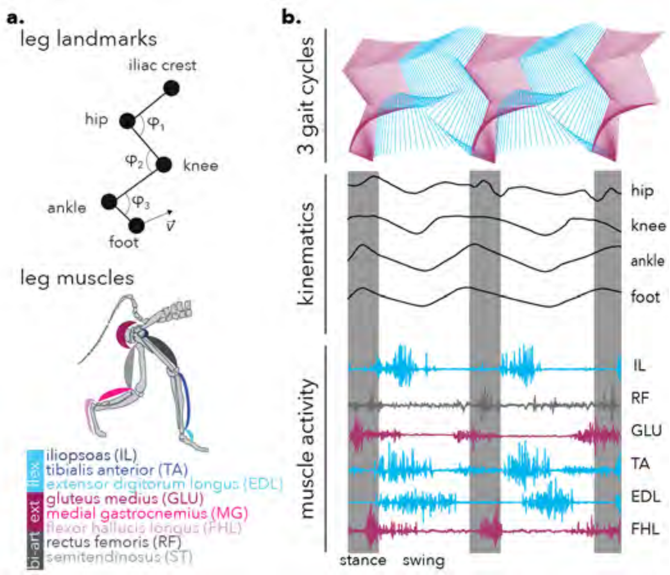
a.
leg landmarks
iliac crest
hip
φ1
φ2
knee
ankle
φ3
v
foot
leg muscles
flex
ext
bi-art
iliopsoas (IL)
tibialis anterior (TA)
extensor digitorum longus (EDL)
gluteus medius (GLU)
medial gastrocnemius (MG)
flexor hallucis longus (FHL)
rectus femoris (RF)
semitendinosus (ST)
b.
3 gait cycles
kinematics
muscle activity
hip
knee
ankle
foot
IL
RF
GLU
TA
EDL
FHL
stance
swing

Figure 1.9 | Two successive gait cycles

a. Body landmarks allow the 3D tracking of the right leg. Kinematics are subsequently computed. Here three joint angles are shown: hip angle (φ_1), knee angle (φ_2) and ankle angle (φ_3). Foot velocity is shown with the black arrow. Example of eight leg muscles (flexors in blue, extensors in red and bi-articular in gray). **b.** Two consecutive steps are depicted with a stick diagram (flexion in blue and extension in red). Cyclic pattern of kinematics and muscle activity are plotted during these three steps. The stance phase is shown with the gray rectangle.

1.4.1. Non-cortical basis of locomotion

As previously mentioned, motor behavior is elicited by a wide range of nervous system structures. The same is true during locomotion and event to a larger extent than voluntary forelimb movements.

1.4.1.1. Spinal networks

Spinal networks play a crucial role in the generation of locomotion pattern, as demonstrated by experiments where decerebrated cats could still walk on a treadmill (Whelan 1996). Remarkably, the limbs can even adapt to different treadmill belt speeds without input from the cortex. Therefore, the spinal cord itself generates rhythmic pattern activations of the motoneurons in the absence of supraspinal inputs. Yet, the gait pattern is disrupted and is not as ‘natural’ as in healthy animals (Forssberg et al. 1980; Barbeau and Rossignol 1987). Spinal networks also rely on afferent feedback from the periphery such as cutaneous afferents that carry mechanical, nociceptive, and thermal information as well as the proprioceptive afferents (Ia and II afferents from the muscle spindle and Ib afferents form the Golgi tendon organs) transmitting information of the limb position and movement. These afferents promote spinal flexion reflexes that are crucial for locomotor-related adaptation to the environment, such as the ability to walk on a ladder or climb over an obstacle (Eccles and Sherrington 1930; Zehr et al. 1997; Bouyer and Rossignol 2003; Takeoka et al. 2014). Interestingly, long bi-directional propriospinal connections connect the lumbar and cervical segments. These connections, homolateral and contralateral, are crucial for rhythmic alternation of motoneuron activation between the hindlimbs and forelimbs. Importantly, these connections receive supraspinal inputs, especially the cervico-lumbar propriospinal projections (Alstermark et al. 1987; Juvin et al. 2005; Dutton et al. 2006; Ruder et al. 2016).

1.4.1.2. Basal ganglia and mesencephalic locomotor region

As previously mentioned, supraspinal structures are crucial in locomotion. For instance, freezing of gait observed in Parkinson's disease patients is thought to be caused by a dysfunction of the cortico-subthalamic circuitry (Pozzi et al. 2019). Moreover, a key component of freezing of gait resides in the loss of cholinergic neurons in the pedunculopontine nucleus (PPN). Indeed, bilateral lesions of the PPN in monkeys leads to postural and locomotor deficits (Karachi et al. 2010). The PPN and the adjacent cuneiform nucleus form the mesencephalic locomotor region (MLR) that is part of the reticular formation. Although the MLR topography remains debated (Ryczko and Dubuc 2013; Sherman et al. 2015), its topography has nevertheless been demonstrated in primates (Karachi et al. 2012; Gay et al. 2020). One of its function is to initiate locomotion via glutamatergic cells, while receiving inputs from the BG (Lee et al. 2014; Roseberry et al. 2016) and sending output to the reticular formation.

1.4.1.3. The brain stem

The brain stem encompasses many nuclei involved in locomotion. Glutamatergic and serotoninergic neurons from the reticular formation (Hägglund et al. 2010; Cabaj et al. 2016) sends projection to the spinal cord through the reticulospinal tract (Matsuyama et al. 1999; Schepens and Drew 2004) and enable the control of postural muscle tone (Takakusaki et al. 2015). Among other nuclei, the red nucleus relays information from the cortex to the cerebellum and project fibers to the hindlimbs and forelimbs spinal cord segments (Liang et al. 2011). In rats, a lesion of the red nucleus impairs over-ground locomotion (Muir and Whishaw 2000). Finally, the vestibulospinal tract originating from the vestibular nuclei acts as a regulator of equilibrium and posture. It works closely with the cerebellum to maintain balance (Angelaki and Cullen 2008).

1.4.2. Cortical basis of locomotion

The motor cortical areas have been extensively studied for voluntary control of forelimb movements, nonetheless their roles in locomotion, especially in primates, remain uncertain (Barthélemy et al. 2011). In cats, pyramidotomyies show a modest effect on locomotion (Eidelberg and Yu 1981). Yet, stimulation of the cat motor cortex affects locomotor outputs. For instance: (1) stimulation during stance decreases extensor activity and in turn resets a gait cycle, while stimulation during swing increases flexor activity (Bretzner and Drew 2005) and (2) stimulations modify limb trajectories (Armstrong and Drew 1985). Similarly, in rodents, it is assumed that the motor cortex, therefore the CST, is not essential for the control of locomotion as demonstrated by moderate or nonexistent locomotor impairment after a bilateral motor cortex lesion or a pyramidotomy (Muir and Whishaw 1999; Asante et al. 2010; Kawai et al. 2015; Siegel et al. 2015). These results emphasize the important contribution of other structures. Yet, in primate, a thoracic CST lesion leads to significant impairment in foot grasping, but the animals walk without assistance on a treadmill (Courtine et al. 2005b). Thus, the motor cortex is believed to coordinate fine locomotor adaptation (DiGiovanna et al. 2016; Serradj et al. 2016) as well as the execution of skilled movements through sensorimotor integration mediated by the motor cortex (Serradj et al. 2014; Heindorf et al. 2018; Omlor et al. 2019).

To sum up, the brain stem, spinal cord, MLR, BG and the cerebellum contribute to locomotor initiation, posture and movement smoothness, while the motor cortical areas seem to take part in locomotor adaptation. Indeed, the cortical involvement seems to be enhanced during more difficult tasks, principally those that require visual feedback (Beloozerova and Sirota 1993; Armstrong and Marple-Horvat 1996; Drew et al. 2008). Since M1 gives rise to most of the CST fibers, it is assumed to exert more influence to motoneurons than the other CST-related cortices. Consequently, its neuronal activity might be essential during locomotor behavior.

1.4.2.1. Primary motor cortex

Neuronal activity in motor cortex is characterized by polyvalent responses to locomotion that are common through species. In rats, cortical activity is phase-locked during the gait cycle across different tasks. Moreover, an increase in firing rate is observed as the task complexity is enhanced (**Figure 1.10a**) (Rigosa et al. 2015). Similarly, detailed analyses in cat M1 (area 4γ) demonstrate that 80% of the neurons are tuned to different phases of the gait cycle (see example of one neuron **in Figure 1.10b**) and about 60% of the cells increase their firing rate during locomotion as compared to rest (Armstrong and Drew 1984). Similarly, in monkey, M1 neurons from the leg area modulate their activity depending on the gait cycle during bipedal locomotion in a treadmill (**Figure 1.10c**) (Mori et al. 2004; Fitzsimmons 2009; Yin et al. 2014). Furthermore, rat M1 engagement (firing rate and modulation depth) differs across tasks (**Figure 1.10d**) (DiGiovanna et al. 2016) likely through M1 neuronal sub-population that encode adjustment of the paw in a context-dependent manner (Omlor et al. 2019). Change in cortical activity is also seen in primate hand M1, where the multi-unit activity covaries with the step speeds in a treadmill (D Foster et al. 2014). Also, M1 cortical activity shows an increased depth of modulation during locomotor tasks requiring accurate positioning of the paw (Drew 1988; Beloozerova and Sirota 1993; Widajewicz et al. 1994; Beloozerova et al. 2010). Furthermore, change in M1 activity during postural correction characterizes the complexity of M1 responses to locomotion (Beloozerova et al. 2005; Karayannidou et al. 2009). Finally, subclasses of M1 rabbit neurons, such as the layer V projecting neurons and inhibitory interneurons, are modulated during normal locomotion and most of them change their tuning when overstepping obstacles. In contrast, ipsilateral and contralateral cortico-cortical neurons as well as the layer VI neurons (sending information to the thalamus) are not as active during locomotion. Altogether, this study suggests that layer V projecting neurons (i.e. CST) encode most of the final information for locomotion coordination in collaboration with the inhibitory interneurons (Beloozerova et al. 2003).

Despite its versatility in response to locomotion, M1 activity can be used in a decoder to predict: (1) leg kinematic in rats, while walking in a treadmill (Weiguo Song et al. 2009); (2) swing phase in rats during walking in a treadmill or climbing staircases (Bonizzato et al. 2018); and (3) foot-off and foot-strike in monkey during treadmill and over-ground locomotion (Capogrosso et al. 2016). In the two latter studies, the prediction was used online in a brain-spine interface paradigm to trigger epidural electrical stimulation of the lumbar spinal segments after a spinal cord injury in order to restore locomotion.

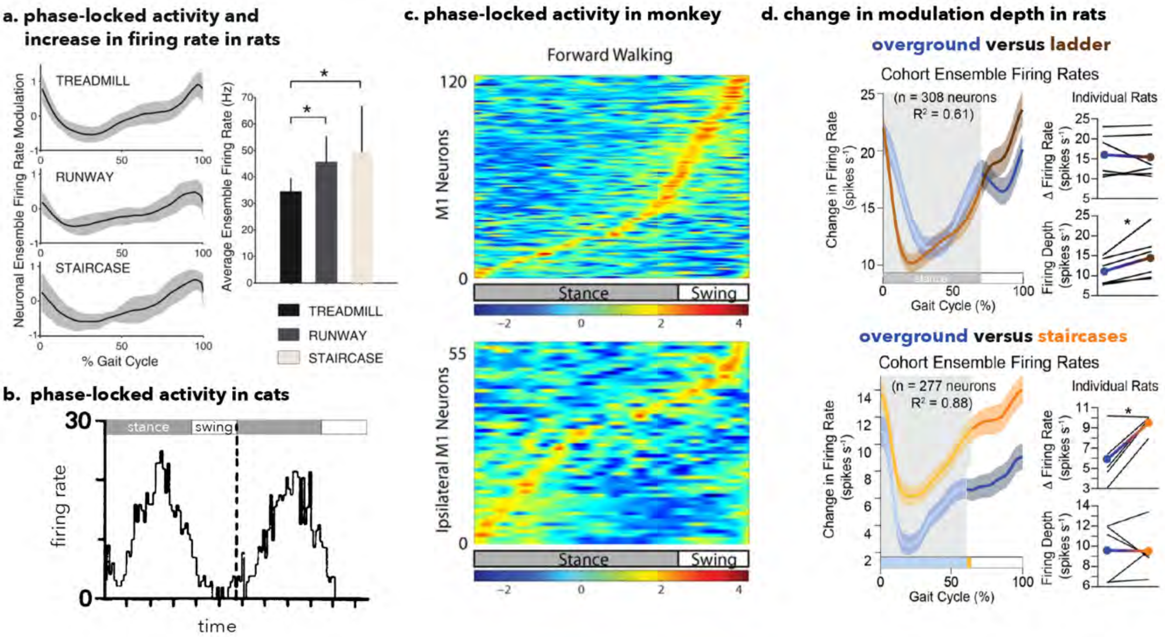

Figure 1.10 | **Motor cortex activity during walking**

a. Discharge timing remains relatively unchanged, while an increase in firing rate through locomotor behavior is observed Modified from (Rigosa et al. 2015). **b.** Example of one neuron in cat M1 recorded during a treadmill session. Modified from (Armstrong and Drew 1984). **c.** Perievent time histogram of neurons sorted according to their peak activity (red = high firing rate; blue = low firing rate). Modified from (Fitzsimmons 2009). **d.** Neuronal population activity in rats across different locomotor tasks. The modulation depth increases in ladder, while the firing rate remains constant. In contrast, the opposite is observed when comparing with the staircases. Modified from (DiGiovanna et al. 2016).

During locomotion on a treadmill, latent dynamics show rotational structure along the gait cycle suggesting a repetitive pattern of cortical contribution to locomotion (Churchland et al. 2012). Moreover, kinematic information can be decoded from neural manifolds in monkeys walking on a treadmill, along a corridor (over-ground walking) and across a horizontal ladder (Xing et al. 2019).

1.4.2.2. Premotor cortex

Little is known about the contribution of the premotor cortex during locomotion. Many studies lead to the general consensus that the rodent secondary motor cortex (M2) is akin to primate SMA due to its anatomical position and equivalent functions (Nachev et al. 2008; Yin 2009; Gremel and Costa 2013). However, one may consider that M2 is not restricted only to SMA but covers other primate frontal areas, including PM, because of its numerous characteristics (Barthas and Kwan 2016). In that context, specific chemogenetic inhibition of M2-M1 projecting neurons disrupts the learning ability of high precision grasping of ladder rungs. This indicates that M1 employs M2 information to adapt its motor output (Omlor et al. 2019). In parallel to M2-M1 projection, M2 sends glutamatergic (Hintiryan et al. 2016) and GABAergic fibers to the BG (Melzer et al. 2017). The photo-stimulation of the glutamatergic fibers increases locomotion (Magno et al. 2019), whereas the GABAergic projection photo-stimulation reduced locomotor activities (Melzer et al. 2017). These experiments show the large variability of M2 function therefore suggesting more diverse neuronal behavior than M1. Nevertheless, in monkeys, PM and S1 activities are essential for predicting motor outputs (e.g. muscle activity and kinematics) especially during natural whole-body movements (e.g. climbing, walking, etc) as compared to restricted forelimb movements. Indeed, their activities (high-gamma activity) during natural movement contribute to a larger extent than those during restricted forelimb movements (Umeda et al. 2019). Overall, those studies emphasize the importance of sensorimotor integration not only restricted to highly skilled forelimb movements but also during locomotion.

1.4.2.3. Primary somatosensory cortex

SI (or barrel cortex in rodents) is reflected by an increase in layer V neurons activity during locomotion through the layer II/III that continuously integrates tactile stimuli (Ayaz et al. 2019). Similarly to M1, areas 1 and 2 neurons are phase-locked during locomotion in both cats and monkeys (Fitzsimmons 2009; Favorov et al. 2015). In fact, depending on the neuronal nature, the moment when they are locked varies. Indeed, neurons with a proximal receptor field and fast conducting pyramidal neurons tend to fire at the middle of the swing phase, whereas slow conduction pyramidal neurons and distal receptor field neurons are characterized with a maximal peak at the transition between stance and swing phase (i.e. during foot-off) (Favorov et al. 2015). This characteristics is also valid in primate areas 1 and 2. Consequently, SI neurons contribute significantly to predict leg kinematics albeit less accurate than M1. Interestingly, no publication about SI neural dynamics can be found during primate locomotion.

1.5. SYNOPSIS AND AIMS

In this thesis, we seek to understand the cortical dynamics in the premotor, primary motor and somatosensory cortices in NHPs underlying different type of locomotor behaviors: from basic walking on a treadmill to climbing over staircases. The fundamental knowledge acquired from this understandings might help for developing new tools for accelerating the translational path for patients with neuromotor disorders.

The first challenge was to develop a technological framework for studying locomotion in freely-behaving monkeys. This began with building a versatile setup accommodating locomotion on a treadmill, over-ground, in a horizontal ladder, in stairs and obstacles. Then, the animal training based on positive reinforcement, followed in parallel with the setup of a wireless electrophysiological platform and the design of the interface between the animals and the computers. This technology development encompassed assembly of hardware in percutaneous connectors as well as personalized surgical procedures.

Once the data collection was performed, a detailed analysis on the neural dynamics from leg PMd (F2), leg M1 (F1) and leg S1 (area 1 and 2) revealed that population dynamics are preserved within a distinct neural manifold, namely the locomotion subspace. The neural variance accounted for by the locomotion subspace followed a rostro-caudal gradients: low in PMd and high in S1. This subspace can be used in order to train reliable decoders of locomotion-related events that are able to generalize to task that they were not trained for. Therefore, the locomotion subspace could be used in a brain-spine interface paradigm.

Finally, we developed personalized spinal implants that specifically target different lumbar segments to elicit leg movements. Although the implants showed remarkable specificity, the challenges of long-term durability persist.

1.6. PERSONAL CONTRIBUTION

The work presented in the present manuscript represents a collective team effort. It is thus crucial to highlight my personal contributions to this work.

In Part 2, I (i) chose (except the electrophysiological equipment) and ordered the hardware used in the locomotion laboratory; (ii) chose and ordered the surgical materials (instruments, surgical drill, sterilization equipment, etc); (iii) designed and developed the technological framework, which included: experimental and control room connections, different locomotor task design, percutaneous pedestals design and assembly, titanium mesh design and surgical approach design; (iv) trained the animals; (v) performed the *in-vivo* imaging; (vi) performed the titanium mesh surgeries in two animals; (vii) daily followed up the animals; (viii) analyzed the data; (ix) prepared the figures and (x) wrote the paper and chapter.

In Part 3, I (i) conceptualized the study; (ii) designed the surgical approach; (iii) assisted the surgeries in sterile condition; (iv) performed the experiment; (v) analyzed the data, except the decoding part; (vi) wrote the paper; (vii) generated the figures; (viii) planned and supervised the work performed by other team-members.

In Part 4, I (i) performed the *in-vivo* imaging; (ii) design the spinal arrays; (iii) designed the surgical approach; (iv) assisted the surgeries in sterile condition; (v) performed the experiment; (vi) analyzed the data; (vii) generated the figures; (viii) wrote the chapter.

In Part 5, I (i) designed and performed the surgeries in rodents and monkeys; (ii) supervised the animal training; (iii) designed and built the voluntary leg movement task in rodents; (iv) performed the experiments; (v) analyzed all the data; (vi) generated the figures (except Figure 5.2); (vii) wrote the chapter.

1.7. BIBLIOGRAPHY

Ajiboye AB, Willett FR, Young DR, Memberg WD, Murphy BA, Miller JP, et al. Restoration of reaching and grasping movements through brain-controlled muscle stimulation in a person with tetraplegia: a proof-of-concept demonstration. The Lancet. Elsevier; 2017;0(0).

Alstermark B, Kümmel H, Tantisira B. Monosynaptic raphespinal and reticulospinal projection to forelimb motoneurones in cats. Neuroscience Letters. 1987 Mar 9;74(3):286–90.

Angelaki DE, Cullen KE. Vestibular System: The Many Facets of a Multimodal Sense. Annu Rev Neurosci. 2008 Jul;31(1):125–50.

Angeles Fernández-Gil M, Palacios-Bote R, Leo-Barahona M, Mora-Encinas JP. Anatomy of the brainstem: a gaze into the stem of life. Semin Ultrasound CT MR. 2010 Jun;31(3):196–219.

Armstrong DM, Drew T. Discharges of pyramidal tract and other motor cortical neurones during locomotion in the cat. J Physiol (Lond). John Wiley & Sons, Ltd; 1984 Jan;346(1):471–95.

Armstrong DM, Drew T. Forelimb electromyographic responses to motor cortex stimulation during locomotion in the cat. J Physiol (Lond). John Wiley & Sons, Ltd; 1985 Oct;367(1):327–51.

Armstrong DM, Marple-Horvat DE. Role of the cerebellum and motor cortex in the regulation of visually controlled locomotion. Can J Physiol Pharmacol. 1996 Apr;74(4):443–55.

Asante CO, Chu A, Fisher M, Benson L, Beg A, Scheiffele P, et al. Cortical control of adaptive locomotion in wild-type mice and mutant mice lacking the ephrin-Eph effector protein alpha2-chimaerin. Journal of Neurophysiology. 2010 Dec;104(6):3189–202.

Ayaz A, Stäuble A, Hamada M, Wulf M-A, Saleem AB, Helmchen F. Layer-specific integration of locomotion and sensory information in mouse barrel cortex. Nat Commun. Springer US; 2019 Jun 7;:1–14.

Barbeau H, Rossignol S. Recovery of locomotion after chronic spinalization in the adult cat. Brain Research. 1987 May 26;412(1):84–95.

Barra B, Badi M, Perich MG, Conti S, Mirrazavi Salehian SS, Moreillon F, et al. A versatile robotic platform for the design of natural, three-dimensional reaching and grasping tasks in monkeys. J Neural Eng. 2019 Dec 5;17(1):016004.

Barthas F, Kwan AC. Secondary Motor Cortex: Where 'Sensory' Meets 'Motor' in the Rodent Frontal Cortex. Trends Neurosci. Elsevier Ltd; 2016 Dec 21;:1–13.

Barthélemy D, Grey MJ, Nielsen JB, Bouyer L. Involvement of the corticospinal tract in the control of human gait. Prog Brain Res. Elsevier; 2011;192:181–97.

Beloozerova IN, Farrell BJ, Sirota MG, Prilutsky BI. Differences in movement mechanics, electromyographic, and motor cortex activity between accurate and nonaccurate stepping. Journal of Neurophysiology. 2010 Apr;103(4):2285–300.

Beloozerova IN, Sirota MG. The role of the motor cortex in the control of accuracy of locomotor movements in the cat. J Physiol (Lond). John Wiley & Sons, Ltd; 1993 Feb;461(1):1–25.

Beloozerova IN, Sirota MG, Orlovsky GN, Deliagina TG. Activity of Pyramidal Tract Neurons in the Cat During Postural Corrections. Journal of Neurophysiology. 2005 Apr;93(4):1831–44.

Beloozerova IN, Sirota MG, Swadlow HA. Activity of different classes of neurons of the motor cortex during locomotion. J Neurosci. 2003 Feb 1;23(3):1087–97.

Bennett MR, Hacker P. The motor system in neuroscience: a history and analysis of conceptual developments. Prog Neurobiol. 2001 Dec 31;67(1):1–52.

Berkley KJ. Spatial relationships between the terminations of somatic sensory and motor pathways in the rostral brainstem of cats and monkeys. I. Ascending somatic sensory inputs to lateral diencephalon. J Comp Neurol. John Wiley & Sons, Ltd; 1980 Sep 1;193(1):283–317.

Bonizzato M, Pidpruzhnykova G, DiGiovanna J, Shkorbatova P, Pavlova N, Micera S, et al. Brain-controlled modulation of spinal circuits improves recovery from spinal cord injury. Nat Commun. Springer US; 2018 Jul 25;9(1):1–14.

Bostan AC, Dum RP, Strick PL. Cerebellar networks with the cerebral cortex and basal ganglia. Trends in Cognitive Sciences. Elsevier Ltd; 2013 May 1;17(5):241–54.

Bouyer LJG, Rossignol S. Contribution of Cutaneous Inputs From the Hindpaw to the Control of Locomotion. I. Intact Cats. Journal of Neurophysiology. 2003 Dec;90(6):3625–39.

Bretzner F, Drew T. Contribution of the Motor Cortex to the Structure and the Timing of Hindlimb Locomotion in the Cat: A Microstimulation Study. Journal of Neurophysiology. 2005 Jul;94(1):657–72.

Brinkman C. Lesions in supplementary motor area interfere with a monkey's performance of a bimanual coordination task. Neuroscience Letters. 1981 Dec;27(3):267–70.

Burke RE. Sir Charles Sherrington's The integrative action of the nervous system: a centenary appreciation. Brain. 2006 Nov 21;130(4):887–94.

Burton H, Fabri M. Ipsilateral intracortical connections of physiologically defined cutaneous representations in areas 3b and 1 of macaque monkeys: projections in the vicinity of the central sulcus. J Comp Neurol. John Wiley & Sons, Ltd; 1995 May 15;355(4):508–38.

Burton H, Jones EG. The posterior thalamic region and its cortical projection in New World and Old World monkeys. J Comp Neurol. John Wiley & Sons, Ltd; 1976 Jul 15;168(2):249–301.

Cabaj AM, Majczyński H, Couto E, Gardiner PF, Stecina K, Sławińska U, et al. Serotonin controls initiation of locomotion and afferent modulation of coordination via 5-HT 7receptors in adult rats. J Physiol (Lond). John Wiley & Sons, Ltd; 2016 Aug 8;595(1):301–20.

Capogrosso M, Milekovic T, Borton D, Wagner F, Moraud EM, Mignardot J-B, et al. A brain–spine interface alleviating gait deficits after spinal cord injury in primates. Nature. Nature Publishing Group; 2016 Nov 10;539(7628):284–8.

Churchland MM, Cunningham JP, Kaufman MT, Foster JD, Nuyujukian P, Ryu SI, et al. Neural population dynamics during reaching. Nature Publishing Group. Nature Publishing Group; 2012 Jun 27;487(7405):51–6.

Churchland MM, Shenoy KV. Temporal Complexity and Heterogeneity of Single-Neuron Activity in Premotor and Motor Cortex. Journal of Neurophysiology. 2007 Jun;97(6):4235–57.

Cisek P. Preparing for Speed. Focus on "Preparatory Activity in Premotor and Motor Cortex Reflects the Speed of the Upcoming Reach." Journal of Neurophysiology. 2006 Dec;96(6):2842–3.

Courtine G, Bunge MB, Fawcett JW, Grossman RG, Kaas JH, Lemon R, et al. Can experiments in nonhuman primates expedite the translation of treatments for spinal cord injury in humans? Nat Med. 2007 May;13(5):561–6.

Courtine G, Roy RR, Hodgson J, McKay H, Raven J, Zhong H, et al. Kinematic and EMG determinants in quadrupedal locomotion of a non-human primate (Rhesus). Journal of Neurophysiology. American Physiological Society; 2005a Jun;93(6):3127–45.

Courtine G, Roy RR, Raven J, Hodgson J, McKay H, Yang H, et al. Performance of locomotion and foot grasping following a unilateral thoracic corticospinal tract lesion in monkeys (Macaca mulatta). Brain. Oxford University Press; 2005b Oct;128(Pt 10):2338–58.

Courtine G, Schieppati M. Human walking along a curved path. II. Gait features and EMG patterns. Eur J Neurosci. John Wiley & Sons, Ltd; 2003 Jul;18(1):191–205.

Cunningham JP, Yu BM. Dimensionality reduction for large-scale neural recordings. Nat Neurosci. 2014 Aug 24;17(11):1500–9.

Cusick CG, Steindler DA, Kaas JH. Corticocortical and collateral thalamocortical connections of postcentral somatosensory cortical areas in squirrel monkeys: a double-labeling study with radiolabeled wheatgerm agglutinin and wheatgerm agglutinin conjugated to horseradish peroxidase. Somatosens Res. 1985;3(1):1–31.

D Foster J, Nuyujukian P, Freifeld O, Gao H, Walker R, I Ryu S, et al. A freely-moving monkey treadmill model. J Neural Eng. IOP Publishing; 2014 Jul 4;11(4):046020–15.

Darling WG, Pizzimenti MA, Morecraft RJ. Functional recovery following motor cortex lesions in non-human primates: experimental implications for human stroke patients. J Integr Neurosci. 2011 Sep;10(3):353–84.

De Vito JL, Simmons DM. Some connections of the posterior thalamus in monkey. Exp Neurol. 1976 May;51(2):347–62.

Diamond ME, Heimendahl von M, Knutsen PM, Kleinfeld D, Ahissar E. 'Where' and "what" in the whisker sensorimotor system. Nat Rev Neurosci. 2008 Aug;9(8):601–12.

DiGiovanna J, Dominici N, Friedli L, Rigosa J, Duis S, Kreider J, et al. Engagement of the Rat Hindlimb Motor Cortex across Natural Locomotor Behaviors. J Neurosci. Society for Neuroscience; 2016 Oct 5;36(40):10440–55.

Dijkerman HC, de Haan EHF. Somatosensory processes subserving perception and action. Behav Brain Sci. Cambridge University Press; 2007 Apr;30(2):189–201–discussion201–39.

Drew T. Motor cortical cell discharge during voluntary gait modification. Brain Research. 1988 Aug 2;457(1):181–7.

Drew T, Andujar J-E, Lajoie K, Yakovenko S. Cortical mechanisms involved in visuomotor coordination during precision walking. Brain Research Reviews. 2008 Jan;57(1):199–211.

Dum R, Strick P. Motor areas in the frontal lobe of the primate. Physiology & Behavior. 2002 Dec;77(4-5):677–82.

Dum RP, Strick PL. The origin of corticospinal projections from the premotor areas in the frontal lobe. Journal of Neuroscience. 1991 Mar;11(3):667–89.

Dutton RC, Carstens MI, Antognini JF, Carstens E. Long ascending propriospinal projections from lumbosacral to upper cervical spinal cord in the rat. Brain Research. 2006 Nov;1119(1):76–85.

Eccles JC, Sherrington CS. Reflex summation in the ipsilateral spinal flexion reflex. J Physiol (Lond). John Wiley & Sons, Ltd; 1930 Mar 17;69(1):1–28.

Eidelberg E, Walden JG, Nguyen LH. Locomotor control in macaque monkeys. Brain. 1981 Dec;104(Pt 4):647–63.

Eidelberg E, Yu J. Effects of corticospinal lesions upon treadmill locomotion by cats. Exp Brain Res. Springer-Verlag; 1981;43(1):101–3.

Ethier C, Oby ER, Bauman MJ, Miller LE. Restoration of grasp following paralysis through brain-controlled stimulation of muscles. Nature. Nature Publishing Group; 2012 May 9;485(7398):368–71.

Evarts EV. Relation of pyramidal tract activity to force exerted during voluntary movement. Journal of Neurophysiology. 1968 Jan;31(1):14–27.

Favorov OV, Nilaweera WU, Miasnikov AA, Beloozerova IN. Activity of somatosensory-responsive neurons in high subdivisions of SI cortex during locomotion. J Neurosci. 2015 May 20;35(20):7763–76.

Ferezou I, Haiss F, Gentet LJ, Aronoff R, Weber B, Petersen CCH. Spatiotemporal Dynamics of Cortical Sensorimotor Integration in Behaving Mice. Neuron. 2007 Dec;56(5):907–23.

Ferrier D. The Localization of Function in the Brain. Proceedings of the Royal Society of London 22, 228–232. 1873.

Fetz EE. Are movement parameters recognizably coded in the activity of single neurons? Behavioral and Brain Sciences. 1st ed. Cambridge University Press; 1992;(15):679–90.

Fetz EE, Cheney PD, Mewes K, Palmer S. Control of forelimb muscle activity by populations of corticomotoneuronal and rubromotoneuronal cells. Prog Brain Res. 1989;80:437–49–discussion427–30.

Filli L, Meyer C, Killeen T, Lörincz L, Göpfert B, Linnebank M, et al. Probing Corticospinal Control During Different Locomotor Tasks Using Detailed Time-Frequency Analysis of Electromyograms. Front Neurol. 2019 Jan 29;10:701–12.

Fitzsimmons NA. Extracting kinematic parameters for monkey bipedal walking from cortical neuronal ensemble activity. Front Integr Neurosci. Frontiers; 2009;3:1–19.

Flanders M, Soechting JF. Parcellation of sensorimotor transformations for arm movements. Journal of Neuroscience. 1990 Jul;10(7):2420–7.

Forssberg H, Grillner S, Halbertsma J, Rossignol S. The locomotion of the low spinal cat. II. Interlimb coordination. Acta Physiol Scand. 1980 Mar;108(3):283–95.

Friedman DP, Murray EA. Thalamic connectivity of the second somatosensory area and neighboring somatosensory fields of the lateral sulcus of the macaque. J Comp Neurol. John Wiley & Sons, Ltd; 1986 Oct 15;252(3):348–73.

Fritsch G, Hitzig E. Electric excitability of the cerebrum (Über die elektrische Erregbarkeit des Grosshirns). Epilepsy and Behavior. Elsevier Inc; 2009 Jun 1;15(2):123–30.

Gallego JA, Perich MG, Chowdhury RH, Solla SA, Miller LE. Long-term stability of cortical population dynamics underlying consistent behavior. Nat Neurosci. Springer US; 2019 Dec 20;:1–26.

Gallego JA, Perich MG, Miller LE, Solla SA. Neural Manifolds for the Control of Movement. Neuron. 2017 Jun 7;94(5):978–84.

Gallego JA, Perich MG, Naufel SN, Ethier C, Solla SA, Miller LE. Cortical population activity within a preserved neural manifold underlies multiple motor behaviors. Nat Commun. Springer US; 2018 Oct 6;9(1):1–13.

Gandhi NJ, Katnani HA. Motor Functions of the Superior Colliculus. Annu Rev Neurosci. 2011 Jul 21;34(1):205–31.

Gardner EP. Somatosensory cortical mechanisms of feature detection in tactile and kinesthetic discrimination. Can J Physiol Pharmacol. 1988 Apr;66(4):439–54.

Gay M, Belaid H, Rogers A, Pérez García F, Roustan M, Bardinet E, et al. Anatomo-functional mapping of the primate mesencephalic locomotor region using stereotactic lesions. Mov Disord. 2020 Jan 10;43(1):120–11.

Gardner, E.P. & Johnson, K.O. (2013) The Somatosensory System: Receptors and Central Pathways. In: Principles of neural science, ed. E. R. Kandel, J. H. Schwartz, T. M. Jessell, S. A. Siegelbaum & A.J. Hudspeth. The McGraw-Hill Companies, Inc

Georgopoulos AP, Kalaska JF, Caminit R, Massey JT. On the Relations Between the Direction of Two-Dimensional Arm Movements and Cell Discharge in Primate Motor Cortex. J Neurosci. 1982;2(11):1527–37.

Georgopoulos AP, Kettner RE, Schwartz AB. Primate motor cortex and free arm movements to visual targets in three- dimensional space. II. Coding of the direction of movement by a neuronal population. Journal of Neuroscience. Society for Neuroscience; 1988 Aug 1;8(8):2928–37.

Gremel CM, Costa RM. Premotor cortex is critical for goal-directed actions. Front Comput Neurosci. Frontiers; 2013;7:110.

Grillner S. Locomotion in vertebrates: central mechanisms and reflex interaction. Physiol Rev. 1975 Apr;55(2):247–304.

Grillner S, Wallen P. Central pattern generators for locomotion, with special reference to vertebrates. Annu Rev Neurosci. 1985.

Gruenbaum AS, Sherrington CS. Observations on the Physiology of the Cerebral Cortex of some of the Higher Apes (Preliminary Communication). Presented at the Proceedings of the Royal Society of London 69, 206–209. British Medical Association; 1902.

Haber SN. The primate basal ganglia: parallel and integrative networks. Journal of Chemical Neuroanatomy. 2003 Dec;26(4):317–30.

Hatsopoulos NG, Suminski AJ. Sensing with the Motor Cortex. Neuron. Elsevier Inc; 2011 Nov 3;72(3):477–87.

Hägglund M, Borgius L, Dougherty KJ, Kiehn O. Activation of groups of excitatory neurons in the mammalian spinal cord or hindbrain evokes locomotion. Nat Neurosci. Nature Publishing Group; 2010 Jan 17;13(2):246–52.

Heindorf M, Arber S, Keller GB. Mouse Motor Cortex Coordinates the Behavioral Response to Unpredicted Sensory Feedback. Neuron. The Author(s); 2018 Aug 15;:1–21.

Hintiryan H, Foster NN, Bowman I, Bay M, Song MY, Gou L, et al. The mouse cortico-striatal projectome. Nat Neurosci. Nature Publishing Group; 2016 Aug;19(8):1100–14.

Hochberg LR, Bacher D, Jarosiewicz B, Masse NY, Simeral JD, Vogel J, et al. Reach and grasp by people with tetraplegia using a neurally controlled robotic arm. Nature. Nature Publishing Group; 2012 May 9;485(7398):372–5.

Huerta MF, Pons TP. Primary motor cortex receives input from area 3a in macaques. Brain Research. 1990 Dec 24;537(1-2):367–71.

Hyvärinen J, Poranen A. Function of the parietal associative area 7 as revealed from cellular discharges in alert monkeys. Brain. 1974 Dec;97(4):673–92.

Jackson JH. On the Anatomical Investigation of Epilepsy and Epileptiform Convulsions. Br Med J. 1873 May 10;1(645):531–3.

James TW, Kim S, Fisher JS. The neural basis of haptic object processing. Can J Exp Psychol. 2007 Sep;61(3):219–29.

Jones EG, Coulter JD, Hendry SH. Intracortical connectivity of architectonic fields in the somatic sensory, motor and parietal cortex of monkeys. J Comp Neurol. John Wiley & Sons, Ltd; 1978 Sep 15;181(2):291–347.

Jones EG, Powell TP. Connexions of the somatic sensory cortex of the rhesus monkey. 3. Thalamic connexions. Brain. 1970;93(1):37–56.

Jones EG, Wise SP, Coulter JD. Differential thalamic relationships of sensory-motor and parietal cortical fields in monkeys. J Comp Neurol. John Wiley & Sons, Ltd; 1979 Feb 15;183(4):833–81.

Juvin L, Simmers J, Morin D. Propriospinal circuitry underlying interlimb coordination in mammalian quadrupedal locomotion. J Neurosci. 2005 Jun 22;25(25):6025–35.

Kaas JH. Evolution of somatosensory and motor cortex in primates. Anat Rec A Discov Mol Cell Evol Biol. 2004 Nov;281(1):1148–56.

Kakei, S., Hoffman, D. S., Strick, P. L. Muscle and movement representations in the primary motor cortex. Science. 1999 Sept 24;285, 2136–2139.

Kalaska JF, Crammond DJ. Cerebral cortical mechanisms of reaching movements. Science. American Association for the Advancement of Science; 1992 Mar 20;255(5051):1517–23.

Karachi C, André A, Bertasi E, Bardinet E, Lehéricy S, Bernard FA. Functional parcellation of the lateral mesencephalus. J Neurosci. Society for Neuroscience; 2012 Jul 4;32(27):9396–401.

Karachi C, Grabli D, Bernard FA, Tandé D, Wattiez N, Belaid H, et al. Cholinergic mesencephalic neurons are involved in gait and postural disorders in Parkinson disease. J Clin Invest. American Society for Clinical Investigation; 2010 Aug;120(8):2745–54.

Karayannidou A, Beloozerova IN, Zelenin PV, Stout EE, Sirota MG, Orlovsky GN, et al. Activity of pyramidal tract neurons in the cat during standing and walking on an inclined plane. J Physiol (Lond). John Wiley & Sons, Ltd; 2009 Jul 30;587(15):3795–811.

Kaufman MT, Churchland MM, Ryu SI, Shenoy KV. Cortical activity in the null space: permitting preparation without movement. Nat Neurosci. Nature Publishing Group; 2014 Feb 2;17(3):440–8.

Kawai R, Markman T, Poddar R, Ko R, Fantana AL, Dhawale AK, et al. Motor Cortex Is Required for Learning but Not for Executing a Motor Skill. Neuron. Elsevier Inc; 2015 Apr 14;:1–14.

Kobak D, Brendel W, Constantinidis C, Feierstein CE, Kepecs A, Mainen ZF, et al. Demixed principal component analysis of neural population data. Elife. 2016 Apr 12;5:9424.

Künzle H. Cortico-cortical efferents of primary motor and somatosensory regions of the cerebral cortex in Macaca fascicularis. Neuroscience. 1978 Jan;3(1):25–39.

Lanciego JL, Vázquez A. The basal ganglia and thalamus of the long-tailed macaque in stereotaxic coordinates. A template atlas based on coronal, sagittal and horizontal brain sections. Brain Struct Funct. 2011 Dec 18;217(2):613–66.

Lawrence DG, Kuypers HG. The functional organization of the motor system in the monkey. I. The effects of bilateral pyramidal lesions. Brain. 1968a Mar;91(1):1–14.

Lawrence DG, Kuypers HG. The functional organization of the motor system in the monkey. II. The effects of lesions of the descending brain-stem pathways. Brain. 1968b Mar;91(1):15–36.

Lee AM, Hoy JL, Bonci A, Wilbrecht L, Stryker MP, Niell CM. Identification of a Brainstem Circuit Regulating Visual Cortical State in Parallel with Locomotion. Neuron. Elsevier Inc; 2014 Jul 16;83(2):455–66.

Lemon R. Recent advances in our understanding of the primate corticospinal system. F1000Res. 2019;8.

Lemon RN. Descending Pathways in Motor Control. Annu Rev Neurosci. Annual Reviews; 2008 Jul;31(1):195–218.

Liang H, Paxinos G, Watson C. The red nucleus and the rubrospinal projection in the mouse. Brain Struct Funct. 3rd ed. 2011 Sep 17;217(2):221–32.

Liao C-C, Gharbawie OA, Qi H, Kaas JH. Cortical connections to single digit representations in area 3b of somatosensory cortex in squirrel monkeys and prosimian galagos. J Comp Neurol. 2nd ed. 2013 Sep 25;521(16):3768–90.

Lisberger, S.G. & Thach, W.T. (2013) The Cerebellum. In: Principles of neural science, ed. E. R. Kandel, J. H. Schwartz, T. M. Jessell, S. A. Siegelbaum & A.J. Hudspeth. The McGraw-Hill Companies, Inc

Luppino G, Matelli M, Camarda R, Rizzolatti G. Corticocortical connections of area F3 (SMA-proper) and area F6 (pre-SMA) in the macaque monkey. J Comp Neurol. 1993 Dec 1;338(1):114–40.

Magno LAV, Tenza-Ferrer H, Collodetti M, Aguiar MFG, Rodrigues APC, da Silva RS, et al. Optogenetic Stimulation of the M2 Cortex Reverts Motor Dysfunction in a Mouse Model of Parkinson's Disease. J Neurosci. Society for Neuroscience; 2019 Apr 24;39(17):3234–48.

Mann RA, Hagy J. Biomechanics of walking, running, and sprinting. Am J Sports Med. 1980 Sep;8(5):345–50.

Marder E, Bucher D. Central pattern generators and the control of rhythmic movements. Current Biology. 2001 Nov 27;11(23):R986–96.

Matelli M, Luppino G, Rizzolatti G. Patterns of cytochrome oxidase activity in the frontal agranular cortex of the macaque monkey. Behav Brain Res. 1985 Nov;18(2):125–36.

Matsuyama K, Drew T. Organization of the projections from the pericruciate cortex to the pontomedullary brainstem of the cat: a study using the anterograde tracer Phaseolus vulgaris-leucoagglutinin. J Comp Neurol. 1997 Dec 29;389(4):617–41.

Matsuyama K, Mori F, Kuze B, Mori S. Morphology of single pontine reticulospinal axons in the lumbar enlargement of the cat: a study using the anterograde tracer PHA-L. J Comp Neurol. 1999 Aug 2;410(3):413–30.

Matsuyama K, Takakusaki K, Nakajima K, Mori S. Multi-segmental innervation of single pontine reticulospinal axons in the cervico-thoracic region of the cat: anterograde PHA-L tracing study. J Comp Neurol. 1997 Jan 13;377(2):234–50.

McCrea DA, Rybak IA. Organization of mammalian locomotor rhythm and pattern generation. Brain Research Reviews. 2008 Jan;57(1):134–46.

Melzer S, Gil M, Koser DE, Michael M, Huang KW, Monyer H. Distinct Corticostriatal GABAergic Neurons Modulate Striatal Output Neurons and Motor Activity. CellReports. 2017 May 2;19(5):1045–55.

Mendoza G, Merchant H. Motor system evolution and the emergence of high cognitive functions. Prog Neurobiol. Elsevier Ltd; 2014 Sep 22;:1–21.

Merzenich MM, Kaas JH, Sur M, Lin CS. Double representation of the body surface within cytoarchitectonic areas 3b and 1 in “SI” in the owl monkey (Aotus trivirgatus). J Comp Neurol. John Wiley & Sons, Ltd; 1978 Sep 1;181(1):41–73.

Minassian K, Hofstoetter US, Dzeladini F, Guertin PA, Ijspeert A. The Human Central Pattern Generator for Locomotion: Does It Exist and Contribute to Walking? The Neuroscientist. 2017 Nov 5;23(6):649–63.

Mori F, Nakajima K, Tachibana A, Takasu C, Mori M, Tsujimoto T, et al. Reactive and anticipatory control of posture and bipedal locomotion in a nonhuman primate. Prog Brain Res. 2004;143:191–8.

Moritz CT, Perlmutter SI, Fetz EE. Direct control of paralysed muscles by cortical neurons. Nature. 2008 Dec 4;456(7222):639–42.

Muir GD, Whishaw IQ. Complete locomotor recovery following corticospinal tract lesions: measurement of ground reaction forces during over-ground locomotion in rats. Behav Brain Res. 1999 Aug;103(1):45–53.

Muir GD, Whishaw IQ. Red nucleus lesions impair over-ground locomotion in rats: a kinetic analysis. Eur J Neurosci. John Wiley & Sons, Ltd; 2000 Mar;12(3):1113–22.

Nachev P, Kennard C, Husain M. Functional role of the supplementary and pre-supplementary motor areas. Nat Rev Neurosci. 2008 Oct 9;9(11):856–69.

Nauta WJ, Domesick VB. Afferent and efferent relationships of the basal ganglia. Ciba Found Symp. 1984;107:3–29.

Omlor W, Wahl A-S, Sipilä P, Lütcke H, Laurenczy B, Chen I-W, et al. Context-dependent limb movement encoding in neuronal populations of motor cortex. Nat Commun. Springer US; 2019 Oct 15;10(1):1–16.

Parent A, Hazrati LN. Functional anatomy of the basal ganglia. I. The cortico-basal ganglia-thalamo-cortical loop. Brain Research Reviews. 1995.

Penfield W, Boldrey E. Somatic motor and sensory representation in the cerebral cortex of man as studied by electrical stimulation. Brain: A journal of neurology. 1937;60(4):389–443.

Perich MG, Gallego JA, Miller LE. A Neural Population Mechanism for Rapid Learning. Neuron. Elsevier Inc; 2018 Oct 16;100(4):1–21.

Petersen CCH. The Functional Organization of the Barrel Cortex. Neuron. 2007 Oct;56(2):339–55.

Phillips CG, Powell TP, Wiesendanger M. Projection from low-threshold muscle afferents of hand and forearm to area 3a of baboon's cortex. J Physiol (Lond). 1971 Sep;217(2):419–46.

Pons TP, Garraghty PE, Cusick CG, Kaas JH. The somatotopic organization of area 2 in macaque monkeys. J Comp Neurol. Wiley Subscription Services, Inc., A Wiley Company; 1985 Nov 22;241(4):445–66.

Pons TP, Garraghty PE, Friedman DP, Mishkin M. Physiological evidence for serial processing in somatosensory cortex. Science. American Association for the Advancement of Science; 1987 Jul 24;237(4813):417–20.

Pozzi NG, Canessa A, Palmisano C, Brumberg J, Steigerwald F, Reich MM, et al. Freezing of gait in Parkinson's disease reflects a sudden derangement of locomotor network dynamics. Brain. 2019 Jun 26;142(7):2037–50.

Pruszynski JA, Kurtzer I, Nashed JY, Omrani M, Brouwer B, Scott SH. Primary motor cortex underlies multi-joint integration for fast feedback control. Nature. Nature Publishing Group; 2011 Oct 10;478(7369):387–90.

Ramnani N. The primate cortico-cerebellar system: anatomy and function. Nat Rev Neurosci. 2006 Jul;7(7):511–22.

Rathelot J-A, Strick PL. Muscle representation in the macaque motor cortex: an anatomical perspective. Proc Natl Acad Sci USA. National Acad Sciences; 2006 May 23;103(21):8257–62.

Rathelot J-A, Strick PL. Subdivisions of primary motor cortex based on cortico-motoneuronal cells. Proc Natl Acad Sci USA. National Acad Sciences; 2009 Jan 20;106(3):918–23.

Riemann BL, Lephart SM. The sensorimotor system, part I: the physiologic basis of functional joint stability. J Athl Train. 2002 Jan;37(1):71–9.

Rigosa J, Panarese A, Dominici N, Friedli L, van den Brand R, Carpaneto J, et al. Decoding bipedal locomotion from the rat sensorimotor cortex. J Neural Eng. IOP Publishing; 2015 Aug 29;12(5):1–16.

Rizzolatti G, Luppino G. The cortical motor system. Neuron. 2001 Sep 26;31(6):889–901.

Rizzolatti G, Luppino G, Matelli M. The organization of the cortical motor system: new concepts. Electroencephalogr Clin Neurophysiol. 1998 Apr;106(4):283–96.

Roseberry TK, Lee AM, Lalive AL, Wilbrecht L, Bonci A, Kreitzer AC. Cell-Type-Specific Control of Brainstem Locomotor Circuits by Basal Ganglia. Cell. Elsevier Inc; 2016 Jan 28;164(3):526–37.

Rouiller EM. What can we learn from animal models? Routledge Handbook of Motor Control and Motor Learning. 2012.

Rouiller EM, Liang F, Babalian A, Moret V, Wiesendanger M. Cerebellothalamocortical and pallidothalamocortical projections to the primary and supplementary motor cortical areas: a multiple tracing study in macaque monkeys. J Comp Neurol. 1994 Jul 8;345(2):185–213.

Roy RR, Bodine-Fowler SC, Kim J, Haque N, de Leon D, Rudolph W, et al. Architectural and fiber type distribution properties of selected rhesus leg muscles: feasibility of multiple independent biopsies. Acta Anat (Basel). Karger Publishers; 1991;140(4):350–6.

Ruder L, Takeoka A, Arber S. Long-Distance Descending Spinal Neurons Ensure Quadrupedal Locomotor Stability. Neuron. Elsevier Inc; 2016 Nov 16;:1–17.

Ryczko D, Dubuc R. The multifunctional mesencephalic locomotor region. Curr Pharm Des. 2013;19(24):4448–70.

Sakai ST, Davidson AG, Buford JA. Reticulospinal neurons in the pontomedullary reticular formation of the monkey (Macaca fascicularis). Neuroscience. 2009 Nov 10;163(4):1158–70.

Schepens B, Drew T. Independent and Convergent Signals From the Pontomedullary Reticular Formation Contribute to the Control of Posture and Movement During Reaching in the Cat. Journal of Neurophysiology. 2004 Oct;92(4):2217–38.

Scott SH. Optimal feedback control and the neural basis of volitional motor control. Nat Rev Neurosci. Nature Publishing Group; 2004 Jul;5(7):532–45.

Seki K, Fetz EE. Gating of sensory input at spinal and cortical levels during preparation and execution of voluntary movement. J Neurosci. Society for Neuroscience; 2012 Jan 18;32(3):890–902.

Semedo JD, Zandvakili A, Machens CK, Yu BM, Kohn A. Cortical Areas Interact through a Communication Subspace. Neuron. Elsevier Inc; 2019 Apr 3;102(1):249–259.e4.

Serradj N, Agger SF, Hollis ER II. Corticospinal circuit plasticity in motor rehabilitation from spinal cord injury. Neuroscience Letters. Elsevier Ireland Ltd; 2016 Dec 10;:1–11.

Serradj N, Paixão S, Sobocki T, Feinberg M, Klein R, Kullander K, et al. EphA4-mediated ipsilateral corticospinal tract misprojections are necessary for bilateral voluntary movements but not bilateral stereotypic locomotion. J Neurosci. 2014 Apr 9;34(15):5211–21.

Shenoy KV, Sahani M, Churchland MM. Cortical Control of Arm Movements: A Dynamical Systems Perspective. Annu Rev Neurosci. 2013 Jul 8;36(1):337–59.

Sherman D, Fuller PM, Marcus J, Yu J, Zhang P, Chamberlin NL, et al. Anatomical Location of the Mesencephalic Locomotor Region and Its Possible Role in Locomotion, Posture, Cataplexy, and Parkinsonism. Front Neurol. Frontiers; 2015 Jun 24;6:1–13.

Siegel CS, Fink KL, Strittmatter SM, Cafferty WBJ. Plasticity of intact rubral projections mediates spontaneous recovery of function after corticospinal tract injury. J Neurosci. Society for Neuroscience; 2015 Jan 28;35(4):1443–57.

Smith AM, Hepp-Reymond MC, Wyss UR. Relation of activity in precentral cortical neurons to force and rate of force change during isometric contractions of finger muscles. Exp Brain Res. Springer-Verlag; 1975 Sep 29;23(3):315–32.

Soechting JF, Flanders M. Errors in pointing are due to approximations in sensorimotor transformations. Journal of Neurophysiology. 1989 Aug;62(2):595–608.

Sparks DL. Sensori-motor integration in the primate superior colliculus. Seminars in Neuroscience. 1991.

Sparks DL, Hartwich-Young R. The deep layers of the superior colliculus. Rev Oculomot Res. 1989;3:213–55.

Stepniewska I, Preuss TM, Kaas JH. Architectonics, somatotopic organization, and ipsilateral cortical connections of the primary motor area (M1) of owl monkeys. J Comp Neurol. John Wiley & Sons, Ltd; 1993 Apr 8;330(2):238–71.

Steuer I, Guertin PA. Central pattern generators in the brainstem and spinal cord: an overview of basic principles, similarities and differences. Rev Neurosci. 2019 Jan 28;30(2):107–64.

Stopfer M, Jayaraman V, Laurent G. Intensity versus Identity Coding in an Olfactory System. Neuron. 2003 Sep;39(6):991–1004.

Strick PL, Preston JB. Sorting of somatosensory afferent information in primate motor cortex. Brain Research. 1978 Nov 10;156(2):364–8.

Sussillo D, Churchland MM, Kaufman MT, Shenoy KV. A neural network that finds a naturalistic solution for the production of muscle activity. Nat Neurosci. 2015 Jun 15;18(7):1025–33.

Takakusaki K, Chiba R, Nozu T, Okumura T. Brainstem control of locomotion and muscle tone with special reference to the role of the mesopontine tegmentum and medullary reticulospinal systems. J Neural Transm. Springer Vienna; 2015 Oct 26;:1–35.

Takeoka A, Vollenweider I, Courtine G, Arber S. Muscle spindle feedback directs locomotor recovery and circuit reorganization after spinal cord injury. Cell. 2014 Dec 18;159(7):1626–39.

Tanji J, Wise SP. Submodality distribution in sensorimotor cortex of the unanesthetized monkey. Journal of Neurophysiology. 1981 Mar;45(3):467–81.

Thach WT. Correlation of neural discharge with pattern and force of muscular activity, joint position, and direction of intended next movement in motor cortex and cerebellum. Journal of Neurophysiology. 1978 May;41(3):654–76.

Tokuno H, Tanji J. Input organization of distal and proximal forelimb areas in the monkey primary motor cortex: a retrograde double labeling study. J Comp Neurol. John Wiley & Sons, Ltd; 1993 Jul 8;333(2):199–209.

Umeda T, Koizumi M, Katakai Y, Saito R, Seki K. Decoding of muscle activity from the sensorimotor cortex in freely behaving monkeys. Neuroimage. Elsevier Inc; 2019 Apr 20;197:1–75.

Velliste M, Perel S, Spalding MC, Whitford AS, Schwartz AB. Cortical control of a prosthetic arm for self-feeding. Nature. 2008 May 28;453(7198):1098–101.

Wannier T, Bastiaanse C, Colombo G, Dietz V. Arm to leg coordination in humans during walking, creeping and swimming activities. Exp Brain Res. 2001 Dec 1;141(3):375–9.

Weiguo Song, Ramakrishnan A, Udoekwere UI, Giszter SF. Multiple Types of Movement-Related Information Encoded in Hindlimb/Trunk Cortex in Rats and Potentially Available for Brain–Machine Interface Controls. IEEE Trans Biomed Eng. 2009 Oct 13;56(11):2712–6.

Welniarz Q, Dusart I, Roze E. The corticospinal tract: Evolution, development, and human disorders. Guthrie S, Chédotal A, editors. Devel Neurobio. John Wiley & Sons, Ltd; 2016 Oct 14;77(7):810–29.

Whelan PJ. Control of locomotion in the decerebrate cat. Prog Neurobiol. 1996 Aug;49(5):481–515.

Whitsel BL, Dreyer DA, Roppolo JR. Determinants of body representation in postcentral gyrus of macaques. Journal of Neurophysiology. 1971 Nov;34(6):1018–34.

Whitsel BL, Petrucelli LM, Werner G. Symmetry and connectivity in the map of the body surface in somatosensory area II of primates. Journal of Neurophysiology. 1969 Mar;32(2):170–83.

Whitsel BL, Rustioni A, Dreyer DA, Loe PR, Allen EE, Metz CB. Thalamic projections to S-I in macaque monkey. J Comp Neurol. 1978 Apr 1;178(3):385–409.

Widajewicz W, Kably B, Drew T. Motor cortical activity during voluntary gait modifications in the cat. II. Cells related to the hindlimbs. Journal of Neurophysiology. 1994 Nov;72(5):2070–89.

Wiesendanger M. Organization of Secondary Motor Areas of Cerebral Cortex. 2nd ed. John Wiley Sons, Inc., editor. Vol. 13. Hoboken, NJ, USA: Comprehensive Physiology; 1981. pp. 1121–47.

Wiesendanger M. Recent developments in studies of the supplementary motor area of primates. Rev Physiol Biochem Pharmacol. 1986;103:1–59.

Xing D, Aghagolzadeh M, Truccolo W, Borton D. Low-Dimensional Motor Cortex Dynamics Preserve Kinematics Information During Unconstrained Locomotion in Nonhuman Primates. Front Neurosci. Frontiers; 2019 Oct 4;13:555–12.

Yin H. The role of the murine motor cortex in action duration and order. Front Integr Neurosci. Frontiers; 2009;3:1–10.

Yin M, Borton DA, Komar J, Agha N, Lu Y, Li H, et al. Wireless neurosensor for full-spectrum electrophysiology recordings during free behavior. Neuron. 2014 Dec 17;84(6):1170–82.

Yu BM, Cunningham JP, Santhanam G, Ryu SI, Shenoy KV, Sahani M. Gaussian-Process Factor Analysis for Low-Dimensional Single-Trial Analysis of Neural Population Activity. Journal of Neurophysiology. 2009 Jul;102(1):614–35.

Zehr EP, Komiyama T, Stein RB. Cutaneous reflexes during human gait: electromyographic and kinematic responses to electrical stimulation. Journal of Neurophysiology. 1997 Jun;77(6):3311–25.

Zimmermann JB, Jackson A. Closed-loop control of spinal cord stimulation to restore hand function after paralysis. Front Neurosci. Frontiers; 2014;8(57):87.

- PART 2 -

FREELY BEHAVING MONKEY PLATFORM

2.1. BEHAVIORAL SETUP IN UNTHETERED CONDITION

The first aim was to set up a platform at which researchers could perform experiments involving electrophysiological and 3D kinematic recordings in freely behaving monkeys. The platform was required to be constructed in such a way that the experimenter would be able to quickly and easily switch between task conditions with minimal animal manipulation. Moreover, the platform setup had to be built with suitable dimensions for monkey experiments while still being able to fit in the available room. Based on the room size and our experiment purposes, a treadmill (N-mill, Motekforce Link, Netherlands) was acquired and a corridor was built. The corridor was required to be adaptable and versatile enough to enable the experimenter to quickly change from one task to another (see below). Thus, on either side of the corridor, we manufactured two independent resting boxes between which the animal could be transferred without requiring any manipulation. The treadmill, corridor, and resting boxes were all mounted on wheels. The locomotion room was split into two spaces: (1) a recording space and, (2) an animal preparation space. The recording space was surrounded by black walls on which a scaffold (item Industrietechnik Schweiz GmbH, Switzerland) was fixed, enabling the attachment of various equipment (e.g. cameras,…). The preparation space allowed the experimenters to prepare the animal for the recording session/for the experiment session and to store diverse materials (**Figure 2.1a**).

To prevent the monkey from escaping, the treadmill and the corridor were each surrounded by transparent Plexiglas enclosures, designed in CAD format with Solidworks. To enable the transfer of the monkey into the locomotor environment, a vertical sliding door was mounted on one side of the enclosure. The other side contained a small opening used to reward the animal with food during the task assessment (**Figure 2.1b**). The dimensions of the corridor and treadmill enclosures were: 200cm long, 40cm wide, and 93cm high; and 146cm long, 63cm wide and 80cm high, respectively (**Figure 2.1c,d**). The resting boxes measured 60cm long, 40cm wide, and 72cm high. The study of different locomotor behaviors required a removable polyvinyl chloride (PVC) board on top of the corridor, allowing for the rapid transition between over-ground walking and horizontal ladder. The ladder consisted of 10 plastics rungs (2.5cm in diameter) spaced apart by 16cm, 8cm, 46cm, 24cm, 24cm, 24cm, 16cm, 8cm, and 14cm. Furthermore, two additional tasks, constructed from wood, could easily and efficiently be added to, or removed from, the PVC board. These included a staircase (3 ascending and 3 descending steps; w:35cm, h:15cm), and two boxes of varying height (l:40cm, w:35cm, h:20cm and 30cm) which were termed, obstacles (**Figure 2.1e**). All of the above described equipment was custom-made, apart from the treadmill.

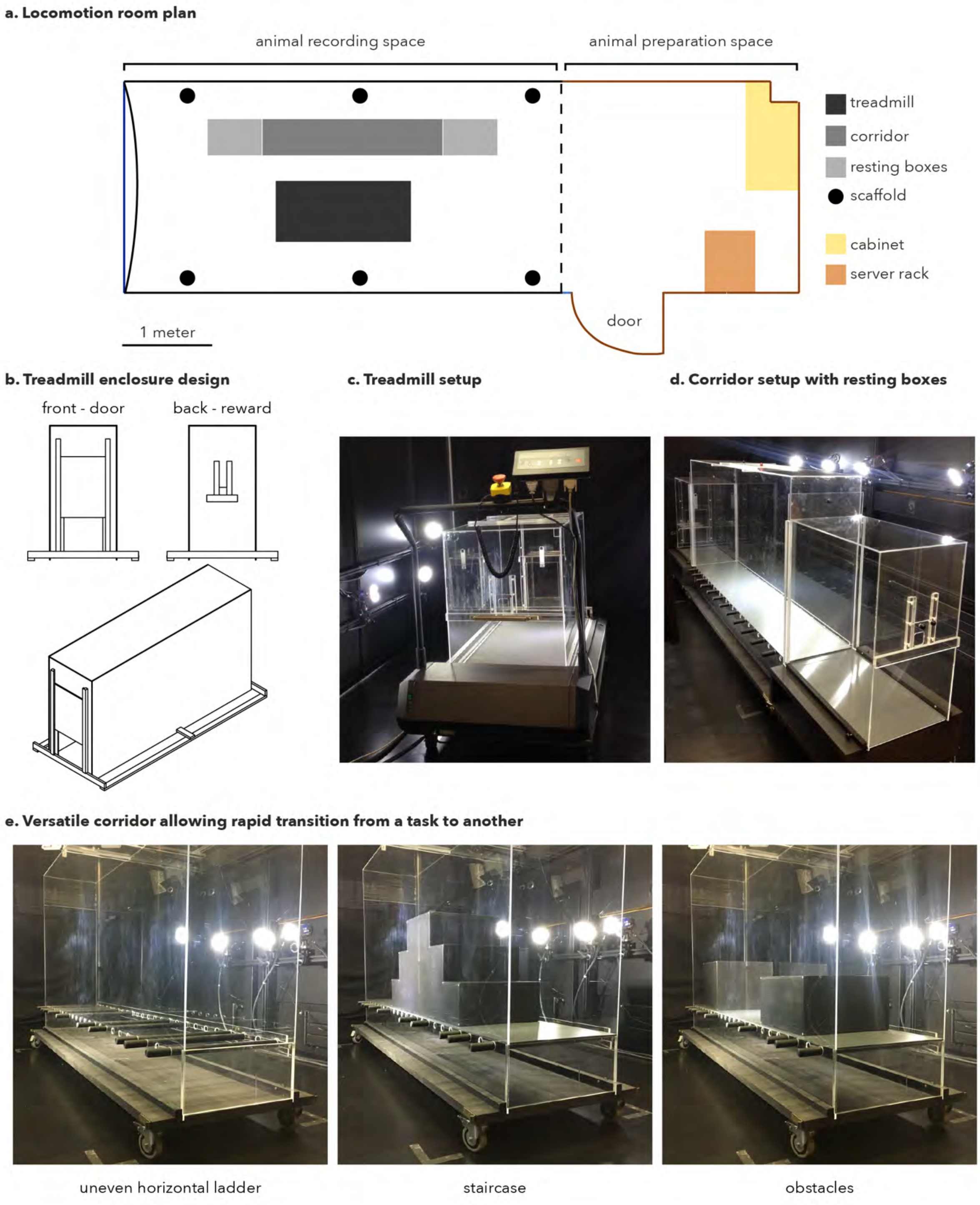
a. Locomotion room plan
animal recording space
animal preparation space
treadmill
corridor
resting boxes
scaffold
cabinet
server rack
door
1 meter
b. Treadmill enclosure design
front - door
back - reward
c. Treadmill setup
d. Corridor setup with resting boxes
e. Versatile corridor allowing rapid transition from a task to another
uneven horizontal ladder
staircase
obstacles

Figure 2.1 | Locomotion laboratory setup

a. The laboratory room was separated into two spaces: the animal preparation space and the animal recording space. The recording space was equipped with a scaffold (black circle) where equipment, such as cameras, could be attached. The treadmill, the corridor, and the resting boxes were mounted on wheels and surrounded by Plexiglas enclosures (see treadmill CAD example in **b.**). **c.** Treadmill setup mounted on wheels and surrounded by a custom made Plexiglas enclosure. **d.** The corridor setup consisted of a PVC board (gray surface) and was positioned between the two resting boxes. **e**. The corridor was built in such a way to allow the experimenter to easily and rapidly change between locomotor tasks. Note that the resting boxes are not shown in these pictures.

2.1.1. Behavioral training

The second aim was to train the animals to become accommodated to the different tasks. Four adult female macaque monkeys (*Macaca fascicularis*), aged 6 years and weighing between 3.4 and 4.6 kg, were involved in this study. They were kept in group at the animal house facility of the University of Fribourg in an enriched room of 45m^3 (as required by the Swiss law on animal protection) and an outdoor space of 15m^3 (not required by the law). The animals were able to interact with each other and were free to move. They had free access to water and they were not food deprived. All the experiments were approved by Federal and local veterinary authorities (veterinary authorization No 2016_09_FR). The monkey's identities were: Mk-Ka, Mk-Ek, Mk-Nt and Mk-Xn. After their arrival in February of 2016, they were habituated to the environment and the researchers working closely with them. They were trained using food rewards and positive reinforcement (associated with a clicker) to enter into a primate chair (Schmidlin et al. 2011; see also video: http://www.unifr.ch/neuro/rouiller/home/nhp). The learning phase of the chair varied among animals, sometimes requiring up to 2 months to master. After successful habituation to the chair, the monkeys were transferred to the experimental room for the locomotion tasks. At this stage, the animals were trained to wear a jacket. The jacket was initially intended to be used as a means of carrying various electronic devices involved in the recordings but was ultimately deemed unsuited to the task. This stage lasted from 2.5 to 10 weeks, until the monkey was comfortable wearing the jacket, determined by the lack of vocalization and acceptance of food with the jacket on. Then, the monkey was transferred to the treadmill. Initially, the animal was simply fed on the stationary treadmill. As the monkey grew more comfortable in the treadmill enclosure, the belt was intermittently turned on while food rewards continued to be provided. This gradual introduction was crucial for the animal to feel at ease in the treadmill environment. The animal was then trained to walk quadrupedally over 1.5 minute sessions at different speeds (1 to 5 km/h) with positive reinforcement. Food rewards were given immediately upon demonstration of the desired behavior (i.e. walking in a straight line on the treadmill). Up to 10 daily sessions were performed, typically 5 days a week. Two animals (Mk-Ka and Mk-Ek) learned the task quickly and therefore reached a plateau, whereas the remaining two animals (Mk-Xn and Mk-Nt) required more time to become accustomed to the treadmill (**Figure 2.2**). After successful habituation to the treadmill, the over-ground walking training phase began. To do so, the monkey was placed in one of the resting boxes on either side of the corridor. To encourage the monkey to walk across the corridor (~5-6 steps), a food reward was presented on the opposite side of the corridor, together with a verbal Go-cue. The monkey was considered to have reached a plateau after 20 crossings without any food refusal. The habituation to over-ground walking was usually fairly rapid (~2weeks). After becoming accustomed to the corridor, the same training procedure was used to habituate the monkey to the uneven ladder, the staircase, and the two obstacles. The number of crossings and variety of tasks performed on the same day was gradually increased. Typically, after a training period of 2-4 months, monkeys were able to successfully complete all tasks in about 1.5 hours within one session. After each training, the monkeys were returned to the animal facility where additional food (primate cereal croquettes) was provided, to comply with daily nutritional requirements.

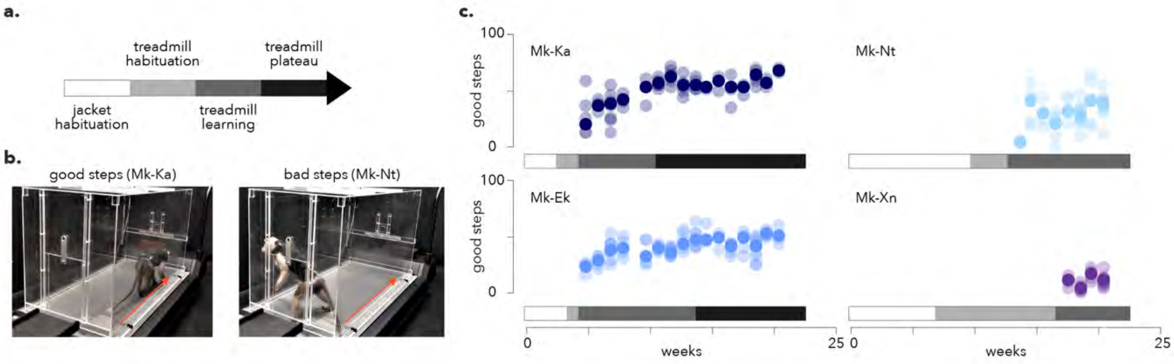

Figure 2.2 | **Behavioral training paradigm**

a. The training started with a jacket habituation phase (see text) followed by a treadmill habituation phase, during which the animal was acclimatized to the new environment. The treadmill belt was intermittently turned on. **b.** During the treadmill learning phase, the animal learned to walk straight (red arrows) with positive reinforcement. “Bad steps” occurred when the animal walked: (1) with an angle of more than 45° from the red arrow, (2) bipedally, and/or (3) while looking backwards **c**. The “good steps” were quantified over one daily session of 1.5 minutes at 2km/h and subsequently plotted (light color). The mean over days is shown in the darker color. The plot shows the interindividual variability of the time needed for animals to become accustomed to the task. Note that Mk-Nt and Mk-Xn eventually reached a plateau of performance not shown in this graph.

2.1.2. Leg kinematic during locomotion

Leg kinematics were recorded using 8 high-resolution cameras (SIMI Reality Motion Systems, GmbH, Germany) at 100 Hz. Prior to the recording, reflective markers (paint or stickers) were placed on body landmarks: iliac crest, greater trochanter (hip), lateral condyle (knee), lateral malleolus (ankle) and the 5th metatarsophalangeal joint (foot). 3D kinematic reconstruction was initially performed manually with SIMI (**Figure 2.3**).

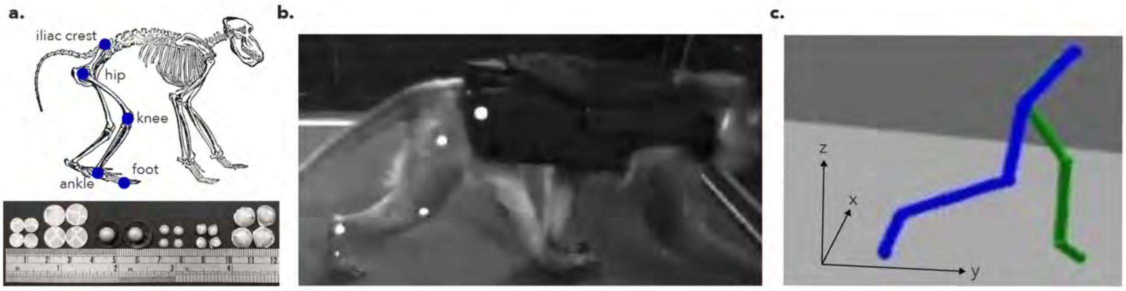

Figure 2.3 | 3D leg kinematic acquisition

a. Top panel: representation of the leg landmarks in a macaque monkey. Bottom panel: examples of various custom-made reflective marker designs. **b.** Frame screenshot during treadmill locomotion, taken by one SIMI camera. The five reflective markers of the right leg are easily identifiable. **c.** After tracking, 3D leg kinematics can be reconstructed for both legs (right leg in blue, left leg in green).

After the release of DeepLabCut (DLC) machine learning algorithm (Mathis et al. 2018), the kinematic 2D coordinates were obtained, then imported into SIMI and combined with a 3D calibration to obtain 3D coordinates of each marker. Various DLC networks were tested in order to obtain satisfying precision. The optimal procedure consisted of creating one network per animal, per task. The network was trained with all 8 camera recordings from 3 to 5 independent days. The joints (crest, hip, knee, ankle and foot for both legs) were manually labelled in 30 frames per camera as a basis. Training of the network lasted approximatively 24 hours, after which the 2D coordinates of the markers were extracted. In an effort to optimize tracking time, it was determined that increasing the number of frames simultaneously analyzed (= batch size) to the maximum (32) had no effect on labeling precision. Therefore, DLC significantly reduced the tracking time by approximately 200 times, as compared to manual tracking in SIMI (**Figure 2.4**).

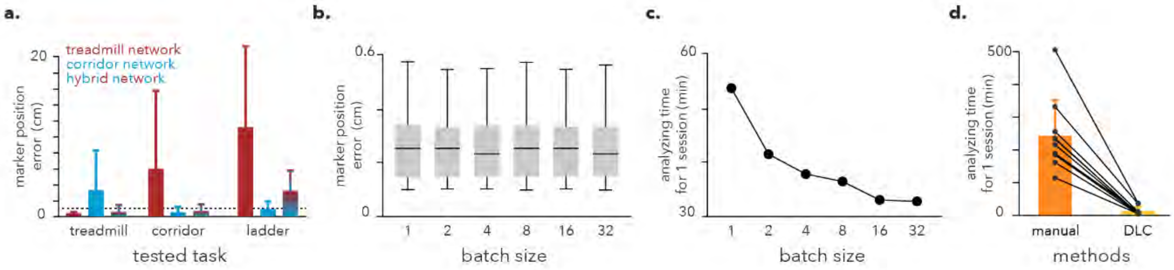

Figure 2.4 | DeepLabCut (DLC) optimization

a. Different tasks were tested with different networks. In this example, we see that the specialized network used to analyze the same task outperformed all the other combinations. The dashed line represents 1cm error. The bar plots show the mean ± SD. **b.** Increasing the batch size (the number of frames analyzed simultaneously) did not affect the precision of the pose estimation but significantly decreased the time needed to analyze videos (**c.**). **d.** The optimized DLC method decreased the time needed to analyze videos by about 200 times, as compared to manual tracking in SIMI (mean ± SD).

Once the 3D marker coordinates were extracted, all kinematic features (joint angles, speed, etc.) were computed in a time-wrapped gait cycle from foot strike to foot strike, forcing the foot-off to be at 60% of the gait cycle, as previously described (Courtine 2005, Capogrosso, 2016, 2018). As an example, 58 kinematic features, encompassing the following various parameters: (1) timing, (2) step dimensions, (3) endpoint control, (4) posture, (5) joint angles, (6) elevation angles, (7) oscillation amplitudes, and (8) joint oscillatory amplitudes, were computed in seven different tasks in monkey Mk-Nt on one day (**Figure 2.5**).

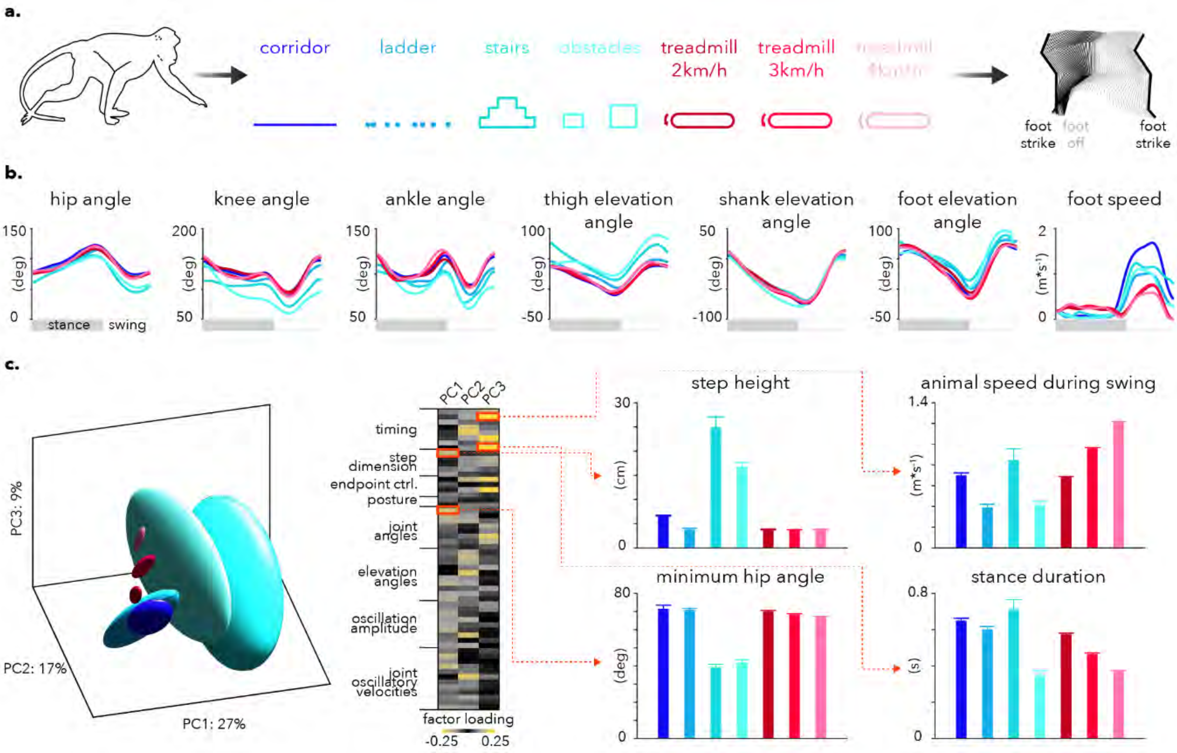

Figure 2.5 | Example of kinematic analysis

a. A monkey walked either across a corridor, on an uneven horizontal ladder, on a staircase, over obstacles, or in a treadmill at three different speeds. The 3D leg kinematics were extracted, and gait cycles manually marked from foot-strike to foot-strike. This allowed the comparison of kinematic features across tasks. **b.** Examples of seven kinematic features over one gait cycle (line=average across all steps for each of the seven tasks). **c.** Principal component analysis (PCA) performed on 58 kinematic features. The seven tasks are clustered in the PC space (PC1 explained 27 % of the variance in the data, PC2 17 % and PC3 9 %). However, steps on obstacles and stairs showed more variability. Factor loadings (negative and positive) identify kinematic features that contribute to the difference in the PC space, such as step height, minimum hip angle, stance duration, and the speed of the animal during the swing phase (mean ± S.E.M).

2.2. WIRELESS TECHNOLOGY

The laboratory needed electrophysiological technology for wireless data acquisition (electromyographic and brain). In order to achieve the platform's experimental goals, various equipment was purchased. The main components are listed below:

- Blackrock Microsystems (USA) for brain and muscle electrophysiology
    - Two Cerebus System Digital, 128-ch real-time data
    - CerePlex, W-Series, 16 Antenna, Digital wireless receiver
    - CerePlex, W-Series digital wireless transmitter, 96-ch
    - CerePlex, W-Series Exilis digital wireless transmitter, 96-ch
    - Inserter, System, Control unit, Wand assembly, trigger assembly and spacers
- Multichannel system (Germany) for muscle electrophysiology
    - W2100-System-AO
        - Wireless2100-RE-AO receiver
        - 5 antennas for signal reception
        - Interface board 3.0 multiboot

The equipment listed above, as well as the treadmill and the SIMI system, were stored in a rack server inside the experimental room (**Figure 2.1a**, orange square). The communication between the two rooms required additional equipment. The experimental setup was managed by a local network (**Figure 2.6**).

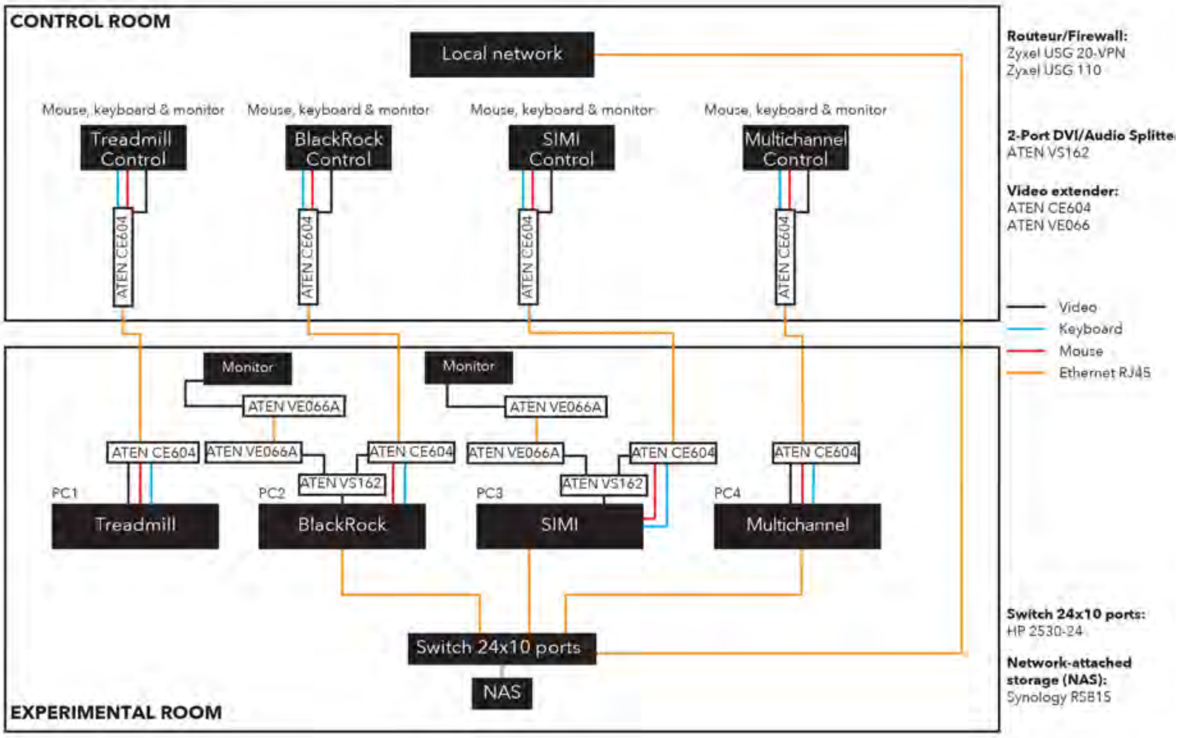
CONTROL ROOM
Local network
Mouse, keyboard & monitor
Treadmill Control
Mouse, keyboard & monitor
BlackRock Control
Mouse, keyboard & monitor
SIMI Control
Mouse, keyboard & monitor
Multichannel Control
ATEN CE604
ATEN CE604
ATEN CE604
ATEN CE604
Monitor
Monitor
ATEN VE066A
ATEN VE066A
ATEN CE604
ATEN VE066A
ATEN CE604
ATEN VE066A
ATEN CE604
ATEN CE604
ATEN VS162
ATEN VS162
PC1
PC2
PC3
PC4
Treadmill
BlackRock
SIMI
Multichannel
Switch 24x10 ports
NAS
EXPERIMENTAL ROOM
Routeur/Firewall:
Zyxel USG 20-VPN
Zyxel USG 110
2-Port DVI/Audio Splitte
ATEN VS162
Video extender:
ATEN CE604
ATEN VE066
Video
Keyboard
Mouse
Ethernet RJ45
Switch 24x10 ports:
HP 2530-24
Network-attached storage (NAS):
Synology RS815

Figure 2.6 | Communication between the experimental room and the control room

The control of the equipment inside the experimental room required connection via diverse additional equipment.

After the technology acquisition, the interface between the available wireless transmitters and the animal was designed. The implanted electrodes were interfacing connectors embedded into a percutaneous connector, referred to as pedestal. Blackrock microsystems provided a complete package, consisting of a wireless transmitter (Cereplex W) and a pedestal (Cereport), upon which the Cereplex W could safely be mounted and secured. A micro-electrode array (48 to 64 channel Utah array, 400µm pitch) was attached to the pedestal (**Figure 2.7a**). The available technology from Multichannel consisted of a transmitter with a 32 channel female Omnetics connector (A79023-001, Omnetics Corporation, USA). Therefore, the male component (A79022-001, Omnetics Corporation, USA) was embedded in a custom-made titanium pedestal, designed with Solidworks and manufactured at the EPFL workshop. The connector was sealed with silicone (Dowsil, 734 flowable sealant) and secured with custom-made inserters (plastic pieces inside the pedestal used for stabilization). The male 32 channel connector was attached to silicone-coated, stainless steel electrodes (38 AWG Cooner wires, Omnetics Corporation, USA) that were tunneled subcutaneously and implanted into specific muscles (see below). As the transmitter was simply plugged into the pedestal with no additional support, the system was dangerously fragile, especially given it was meant to withstand the curious hands of a freely moving macaque monkey. To protect the components, protective caps that encased both pedestal and transmitter were designed and 3D printed. The bottom half was screwed onto the pedestal, the transmitter plugged in, and the top half screwed onto the bottom, thereby enclosing the system securely. The design of the protective cap was performed in such a way the animal could not reach and unplug the transmitter. Moreover, the monkey was not able to unscrew the cap. These protective caps were essential for performing safe and productive recordings. In order to prevent moisture and debris from infiltrating the electronics in home cage of the animal facility, protective caps based on the Blackrock Cereport pedestal design were manufactured that fit the custom-made pedestal dimensions (**Figure 2.7b**). In 2018, Blackrock microsystem released a new wireless transmitter called Exilis. This transmitter consisted of 3 x 32 Omnetics channels arranged in row. The altered dimensions of the connectors necessitated the design of a new custom-made titanium pedestal, manufactured by a private company (Buri SA, La Chaux-de-Fonds, Switzerland). Following the same procedure as described above, the connectors were sealed into the pedestal with custom-made inserters. The system came with a 64 channel Utah array connected to two Omnetics connectors. The remaining Omnetics connector was therefore available for the silicone-coated, stainless steel electrodes for muscle implantation. Since the dimensions of the pedestal were bigger than the one of Multichannel, new protective caps were designed and 3D-printed, following the same procedures as described above. The Exilis system allowed brain and muscle recordings from the same transmitter (**Figure 2.7c**). Therefore, another pedestal consisting only of

Utah arrays could be implanted. Mk-Xn and Mk-Ka were the animals implanted first, with one Cereport pedestal and one Multichannel pedestal. Mk-Ek was then implanted with one Cereport pedestal and one Exilis pedestal. Finally, Mk-Nt was implanted with two Cereport pedestals (see next chapter for more details).

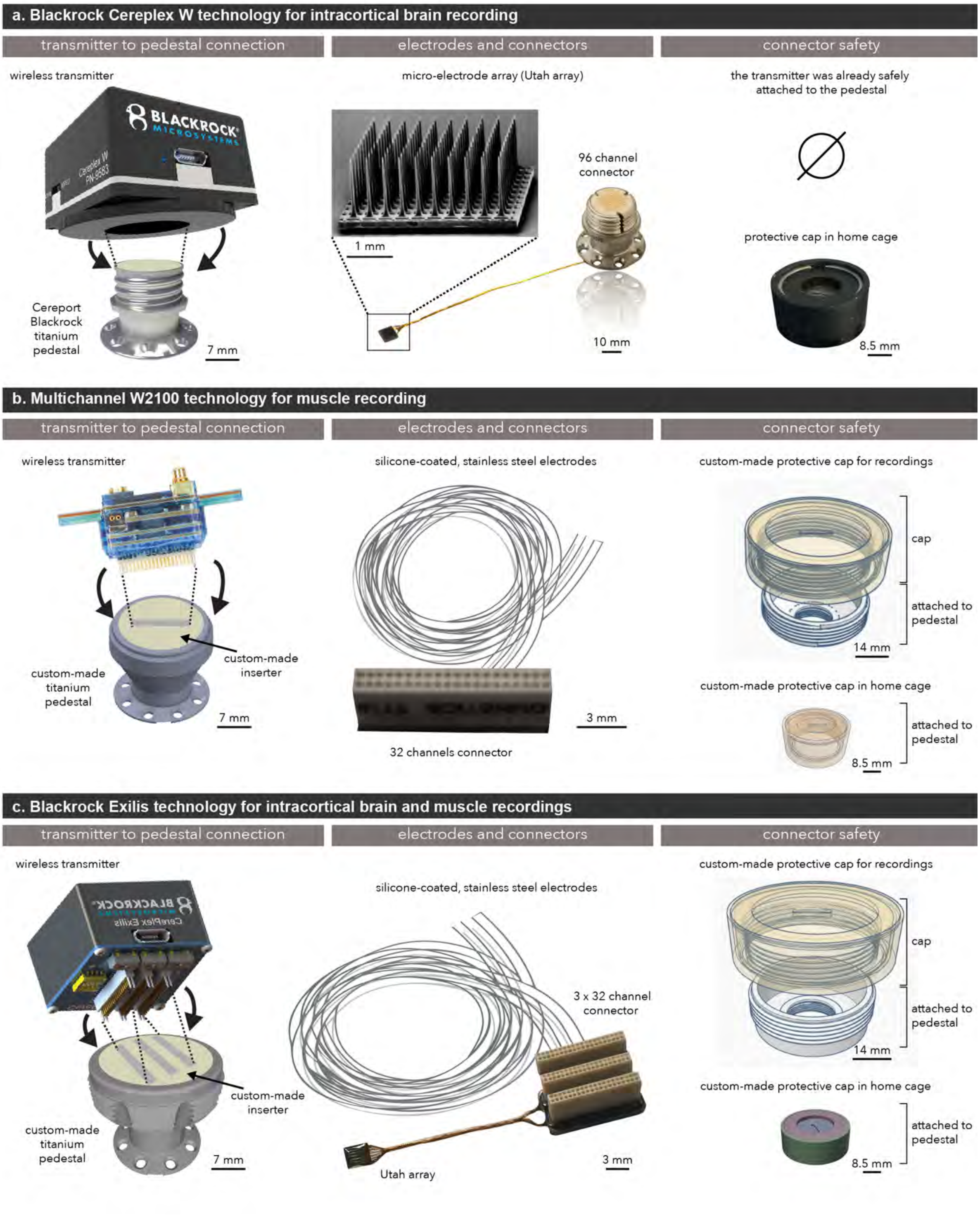
a. Blackrock Cereplex W technology for intracortical brain recording
transmitter to pedestal connection
electrodes and connectors
connector safety
wireless transmitter
BLACKROCK MICROSYSTEMS
Cereplex W
Cereport Blackrock titanium pedestal
7 mm
micro-electrode array (Utah array)
1 mm
96 channel connector
10 mm
the transmitter was already safely attached to the pedestal
∅
protective cap in home cage
8.5 mm
b. Multichannel W2100 technology for muscle recording
transmitter to pedestal connection
electrodes and connectors
connector safety
wireless transmitter
custom-made inserter
custom-made titanium pedestal
7 mm
silicone-coated, stainless steel electrodes
3 mm
32 channels connector
custom-made protective cap for recordings
cap
attached to pedestal
14 mm
custom-made protective cap in home cage
attached to pedestal
8.5 mm
c. Blackrock Exilis technology for intracortical brain and muscle recordings
transmitter to pedestal connection
electrodes and connectors
connector safety
wireless transmitter
BLACKROCK
CerePlex Exilis
custom-made inserter
custom-made titanium pedestal
7 mm
silicone-coated, stainless steel electrodes
3 x 32 channel connector
Utah array
3 mm
custom-made protective cap for recordings
cap
attached to pedestal
14 mm
custom-made protective cap in home cage
attached to pedestal
8.5 mm

Figure 2.7 | Wireless transmitter technology

a. Complete package of Blackrock, consisting of a wireless transmitter (Cereplex W), a pedestal (Cereport) embedding the connector with an intracortical array (Utah array), and a protective cap for connector safety. **b.** Multichannel provided a 32-female Omnetics connector, leading to the design of custom-made equipment. **c.** Blackrock Exilis technology allowed the combination of both muscle and brain recordings from the same transmitter.

2.3. PERSONALIZED SURGICAL PROCEDURES

For long-term durability of the implanted technology, the pedestals had to be securely attached to the skull. Surgical procedures, personalized for each animal, were developed in order to achieve the most successful attachment and subsequent osseointegration. The first step consisted of acquiring Computer Tomography (CT) and Magnetic Resonance Imaging (MRI) of the animal in order to extract the skull and brain in STL format for 3D printing proposes. A titanium mesh (TiMesh, Medtronic) was modeled on the 3D printed skull for each specific animal, and covered with hydroxyapatite (Medicoat AG, Zürich, Switzerland) to promote osseointegration. Two titanium foot plates (Buri SA, La Chaux-de-Fonds, Switzerland) were attached to the mesh and covered with titanium healing plates, used to prevent bacteria from invading any slots or openings on the foot plates. The mesh was then implanted with self-drilling screws (Medtronic, 1.6x3.5mm or 4mm). After a period of 2 to 3 weeks allotted for healing and recovery, the muscle and brain surgeries took place. The healing plates were removed, and the pedestals were screwed to the foot plates with 8 titanium M1.6 screws (Buri SA, La Chaux-de-Fonds, Switzerland). The mesh modeling was formatted in such a way that access via craniotomy to the leg primary motor (M1, F1), leg dorsal premotor (PMd, F2) and leg primary somatosensory (SI, area 1 and 2) cortices was preserved. In order to validate the localization of the craniotomy (and therefore determine the shape of the mesh) the skull was co-registered with the corresponding brain and a practice craniotomy was performed, in which plastic rectangles with the dimensions of the Utah arrays were placed on the surface of the model brain. The silicone-coated, stainless steel electrodes were prepared according to the targeted leg muscles. Typically, two muscles per joint were chosen: (1) iliopsoas (IL), (2) tibialis anterior (TA), (3) extensor digitorum longus (EDL), (4) gluteus medius (GLU), (5) medial gastrocnemius (MG), (6) flexor hallucis longus (FHL), (7) rectus femoris (RF) and (8) semitendinosus (ST).

After a skin incision, a craniotomy on the left side (~4-5cm^2) was made above the leg areas of PMd, M1, and SI cortices. The dura mater was opened with a surgical blade to expose the brain. Based on anatomical landmarks of the sulci, and with the help of the 3D printed brain, we chronically implanted the Utah arrays using a pneumatic impactor (Blackrock microsystem, USA). The number of channels varied per animal and cortex: PMd (48 channels in all 4 animals, 1mm electrode tip length, except in Mk-Nt: 1.5mm), M1 (48 channels in all 4 animals, except in Mk-Nt: 64 channels, 1.5mm electrode tip length), S1 (64 channels with 1.5mm electrode tip length in Mk-Ek and 32 channels with 1mm electrode tip length in Mk-Nt) . Note that Mk-Nt was also implanted with a 48-channel array (1.5mm electrode tip length) in the posterior parietal cortex. After securing the array, the dura mater was sutured back together and the bone flap was fixed in place, closing the skull. The muscles of the scalp were sutured back together and the skin sutured closed. Next, the muscle electrodes were tunneled subcutaneously from the pedestal to the abdomen, at which point two of these electrodes were taken and implanted longitudinally into the muscle for bipolar recordings. Moreover, one reference and one ground electrode were placed in the back. Finally, the muscles and skin were sutured back into place.

Post-mortem evaluation confirmed the correct localization of the Utah arrays, apart from the first implanted animal, Mk-Xn. In this particular animal, the mesh was not designed properly, leading to the implementation of the refined methods of mesh design for the following three animals, as described above (**Figure 2.8**). Detailed procedures for animal preparation, mesh surgery, post-operative care and *in-vivo* imaging are described in the next chapter.

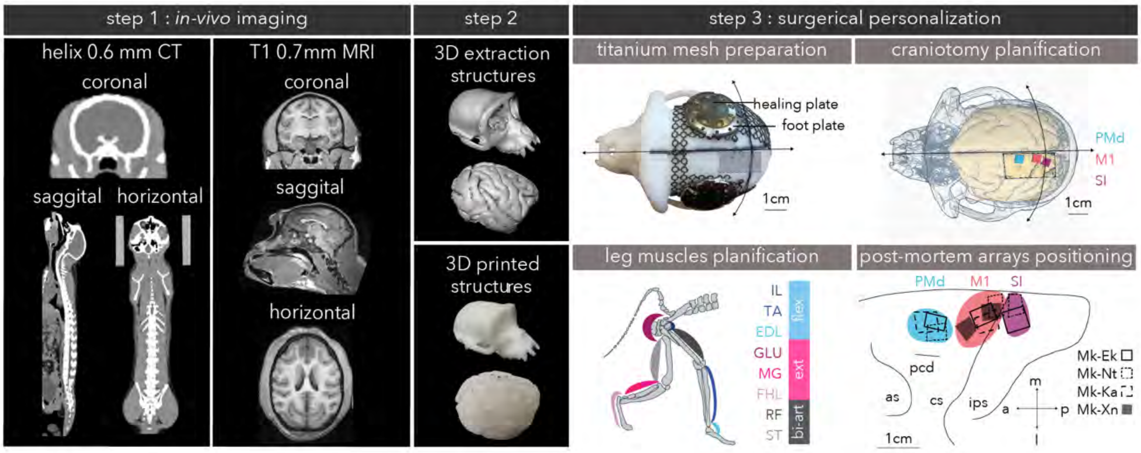
step 1 : in-vivo imaging
helix 0.6 mm CT
coronal
saggital
horizontal
T1 0.7mm MRI
coronal
saggital
horizontal
step 2
3D extraction structures
3D printed structures
step 3 : surgical personalization
titanium mesh preparation
healing plate
foot plate
1cm
craniotomy planification
PMd
M1
SI
1cm
leg muscles planification
IL
TA
EDL
GLU
MG
FHL
RF
ST
flex
ext
bi-art
post-mortem arrays positioning
PMd
M1
SI
pcd
as
cs
ips
m
a
p
l
1cm
Mk-Ek
Mk-Nt
Mk-Ka
Mk-Xn

Figure 2.8 | Personalization of the surgical procedures

The first step consisted of performing *in-vivo* imaging to extract and reconstruct the skull from CT scans and the brain from MRI scans. A titanium mesh was modeled, based on the shape of the skull (Mk-Ek shown as an example). Foot and healing plates were fixed to the mesh, allowing robust attachment of the pedestals. Co-registration of the brain and the skull enabled the planning of the craniotomy and the positioning of Utah arrays. (Mk-Ek as an example). Bipolar electrodes were prepared according to the target leg muscles. Post-mortem array positioning confirmed the correct localization of the array, apart from Mk-Xn (see text). In Mk-Ka, the Blackrock Exilis technology was not available yet. Therefore, only PMd and M1 were implanted. PMd = leg dorsal premotor cortex (F2), M1 = leg primary motor cortex (F1) and SI = leg primary somatosensory cortex (area 1 and 2), IL = iliopsoas, TA = tibialis anterior, EDL = extensor digitorum longus, GLU = gluteus medius, MG = medial gastrocnemius, FHL = flexor hallucis longus, RF = rectus femoris and ST = semitendinosus.

While the titanium mesh did, in fact, contribute greatly to the stability of the pedestals, adverse side effects, technical challenges, and the cost of the procedures put the utility of the titanium mesh into question. A retrospective report on 14 animals who have undergone the procedures is described in the next chapter.

2.4. ADVERSE EFFECTS OF TAILORED CRANIAL IMPLANTS IN MACAQUE MONKEYS

The content of this chapter was adapted from a manuscript in preparation: ***Adverse effects of tailored cranial implants in macaque monkeys***. Simon Borgognon#, Alexandra Hickey, Ismael Seáñez, Marion Badi, Nicolò Macellari, Sara Conti, Beatrice Barra, Aaron Braendli, Elvira Pirondini, Silvestro Micera, Jonas Zimmerman, Alain Woodtli, Eric M. Rouiller, Jocelyne Bloch, Grégoire Courtine & Marco Capogrosso#.

# *corresponding authors.*

Personal contributions: performed the *in-vivo* imaging, planned the surgical approaches, designed the titanium mesh and foot plate positioning, performed the surgery in two animals, provided the post-operative cares, analyzed the data, wrote the paper.

2.4.1. Abstract

In primate neuroscience research, scientists often use skull-mounted pedestals for brain recording. In an effort to reduce the incidence of post-operative complications, recent studies have proposed the implementation of subject-personalized pedestals. At our institution, we recently conducted experiments requiring the implantation of two skull-mounted pedestals in 14 animals. Therefore, we performed *in-vivo* medical imaging (i.e. magnetic resonance imaging (MRI) and computer tomography (CT) scans) enabling the 3D reconstruction of the brain and skull of each specific animal. We molded a titanium mesh based on a 3D printed replicate of the skull of the living monkey. We then coated the mesh with hydroxyapatite to promote bone adhesion, and fixed titanium foot plates onto the mesh for pedestal anchoring. We positioned the foot plates and cut the mesh based on MRI data so that access to the brain region of interest would not be impeded. In a first surgery, we implanted the titanium mesh and the foot plates. After waiting a period of a few weeks to promote osseointegration of the mesh, a second surgery was performed on the animal, in which the pedestals were implanted. The benefits of the refined methodology was evidenced by the remarkable stability of the pedestals. However, 55% of the subjects had complications (mostly swelling of the face), one even leading to the mesh explantation due to major infection. After the pedestal surgery, 85% of the animals showed adverse effects, such as skin recession, hole formation on the scalp and/or infection. We conclude that the best minimization of risk for a pedestal implantation is to integrate pedestal feet to the base that are flexible. Ideally, a fully-implantable system without percutaneous connectors would be a better solution.

2.4.2. Introduction

In primate neuroscience research, scientists often use implantable devices for recording or for electrical stimulation (Nicolelis et al. 2003; Jackson and Fetz 2007; Wyss et al. 2013; Schwarz et al. 2014; Zimmermann and Jackson 2014). Currently, the most adopted method is an implantable device that is mounted on the skull of the animal. Termed a recording chamber, this unique device offers the remarkable possibility to access deep and superficial brain structures by inserting an electrode. Spatial and temporal recordings can therefore be performed under diversified behavioral conditions. Once the recording is completed, the experimenter can close the chamber and thus protect the brain from the external environment (Evarts 1968; Adams et al. 2011; McAndrew et al. 2012; Lanz et al. 2013). More recently, a method consisting of implanting a transcranial, multi-electrode array connected to a skull-mounted pedestal has been implemented for multi-cellular recordings. An interface directly connected to the pedestal allows communication with external computers (Barrese et al. 2013; Yin et al. 2014; Capogrosso et al. 2016). However, both methods require percutaneous implants that can lead to several complications, such as bacterial contaminations, skull softening, and excessive bleeding. These complications may jeopardize the well-being of the animals, as well as the experimenters in cases of zoonotic bacterial infection. The refinement of surgical procedures is thus highly recommended, especially for long-term experiments (Johnston et al. 2016).

In an effort to reduce the incidence of such complications, recent studies have proposed the implementation of subject-personalized pedestals and chambers. Prior to each surgery, the experimenters of the study perform *in-vivo* medical imaging, such as magnetic resonance imaging (MRI) and computer tomography (CT) scans. This enables the 3D reconstruction of the brain and skull of each specific animal. The experimenter is then better able to plan the positioning of the implant, which in turn significantly improves the post-operative outcomes. Additionally, molding the implant based on the cranial shape of the specific subject facilitates a more secure anchoring of the implant to the skull (Lanz et al. 2013; Johnston et al. 2016; Chen et al. 2017; Ortiz-Rios et al. 2018). This refinement leads to many advantages: (1) decreasing the gap size between the bone and the implant base, thereby minimizing the space available for bacteria to proliferate; (2) avoiding the process of scoring the bone for implant fitting, thus maintaining the robust bone surface for fixation, and (3) reducing the granulation tissue around the skin margin.

In order to increase the longevity of the implant, the experimenter has the option to coat the part of the implant that comes into contact with the bone in a natural mineral form of calcium apatite, known as hydroxyapatite. The mineral helps create a strong connection between the foreign material and the host bone. Hydroxyapatite offers a good solution for long-term experiments and where increased durability of the implant stability is concerned (Cook et al. 1992). Moreover, hydroxyapatite eliminates the need for dental acrylic cement, whose exothermic reaction during the sealing process can damage the bone and underlying brain tissue (Lanz et al. 2013; Chen et al. 2017; Ortiz-Rios et al. 2018).

At our institution, we recently conducted different experiments requiring the implantation of two skull-mounted pedestals. Taking the refined techniques described above into consideration, we implemented an unreported methodology. This method consisted of molding a titanium mesh based on a 3D printed replicate of the skull of the living monkey. We then coated the mesh with hydroxyapatite to promote bone adhesion, and fixed titanium foot plates onto the mesh. The foot plates served as an anchor for the pedestals. We positioned the foot plates and cut the mesh based on MRI data so that access to the brain region of interest would not be impeded. Once the material was sterilized, we implanted the mesh in the initial surgery. After waiting a period of 2 to 32 weeks to ensure proper healing and promote osseointegration of the mesh, a second surgery was performed on the animal, in which the pedestals were implanted (**Figure 2.9**). The benefits of the refined methodology was evidenced by the remarkable stability of the pedestals; however, we reported adverse effects that put into question the utility of this procedure. In this report, we describe the mesh methodology and the adverse effects encountered in 14 adult macaque monkeys.

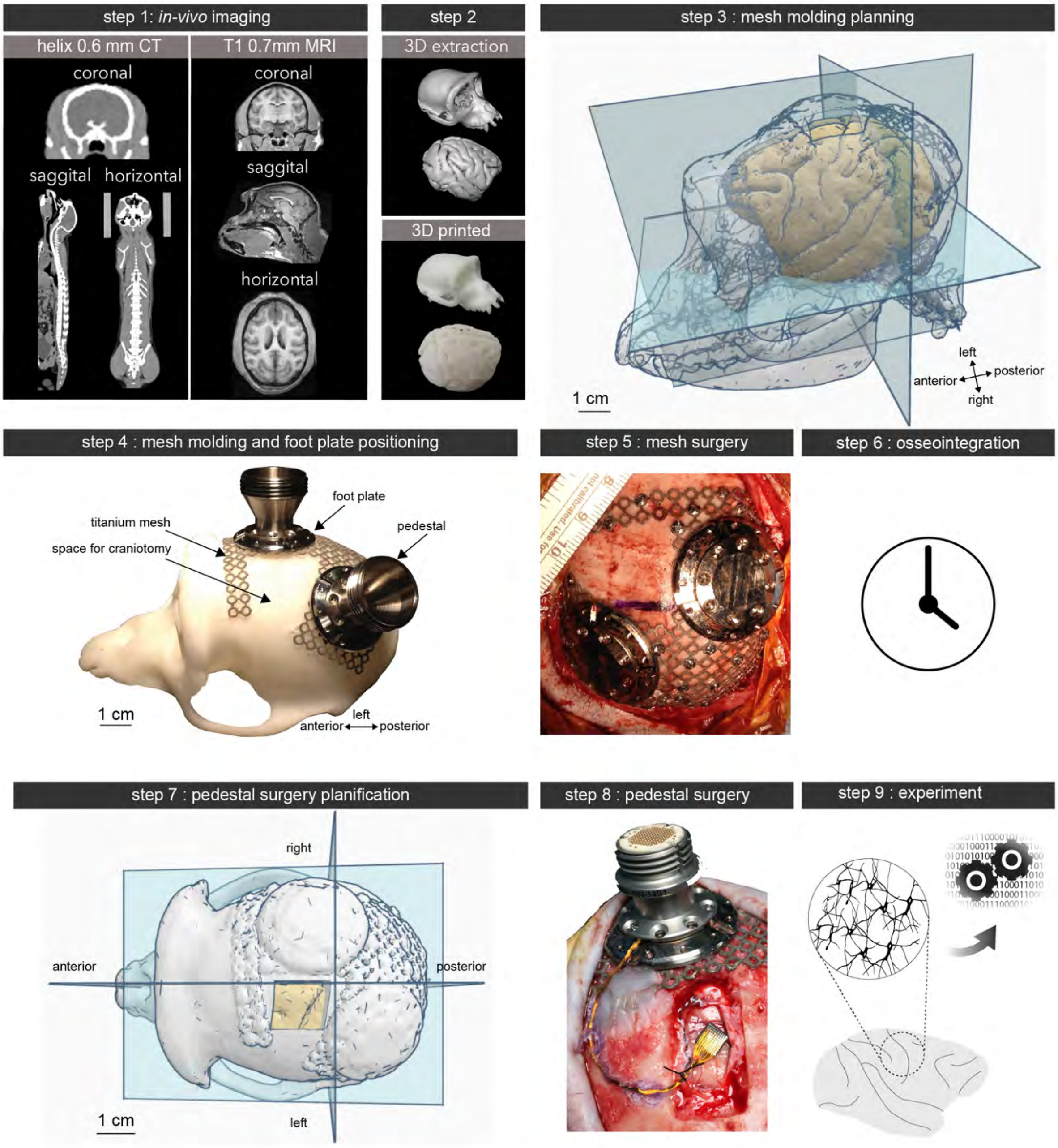
step 1: *in-vivo* imaging
helix 0.6 mm CT
T1 0.7mm MRI
coronal
saggital
horizontal
coronal
saggital
horizontal
step 2
3D extraction
3D printed
step 3 : mesh molding planning
left
anterior
posterior
right
1 cm
step 4 : mesh molding and foot plate positioning
foot plate
titanium mesh
pedestal
space for craniotomy
1 cm
left
anterior
posterior
step 5 : mesh surgery
step 6 : osseointegration
step 7 : pedestal surgery planification
right
anterior
posterior
1 cm
left
step 8 : pedestal surgery
step 9 : experiment

Figure 2.9 | Tailored titanium mesh methodology for chronic cranial implant

The first steps consisted of extracting and 3D printing a replicate of the living monkey based on MRI and CT scans. Next, we molded a titanium mesh according to the cranial shape and the experimental purpose. In this example, we targeted the motor cortical areas of the leg region. We then coated the mesh with hydroxyapatite, and, in sterile conditions, assembled the mesh with foot plates (pedestal anchor, see **Figure 2.10**). After the mesh surgery, a period of 2 to 32 weeks was given to promote osseointegration of the mesh. The pedestal surgery was then planned based on the MRI of the subject. Finally, we performed the pedestal surgery. Here is an example of one micro-electrode arrays implanted in two motor cortical areas of the leg.

2.4.3. Material and Methods

2.4.3.1. Animals

14 adult (5.9 ± 2.4 years old) female macaque monkeys (*Macaca fascicularis*) weighing 3.7 ± 0.6 kg were involved in this report. They were housed in the animal facility of the University of Fribourg (Switzerland) in groups of 2 to 5 animals in 45m^3 enriched rooms, as required by the Swiss law on animal protection. In addition, the group had access to an outdoor space of 15m^3. They had free access to water and were not food deprived. All the animals underwent micro-electrode array (Utah array, Blackrock microsystem, USA) implantation of the motor cortical areas (leg or hand). Therefore, the connectors were embedded in a percutaneous connector, referred to as pedestal. A second pedestal containing another Utah array connector, a custom-made electromyographic connector, a custom-made epidural electrical stimulation connector, and/or a custom-made peripheral intraneural stimulation connector was implanted in all animals except Mk-PD. All the experimental procedures were approved by the Federal and local veterinary authorities under the veterinary license numbers 2016_09_FR, 2017_03_FR, 2017_04E_FR and 2017_22_FR.

2.4.3.2. Titanium mesh, foot plate, healing plate and percutaneous connectors (pedestals)

We implanted a titanium mesh (TiMesh, Medtronic) in each animal. The mesh was soft and malleable, enabling smooth reshaping and forming without any external device. We designed the foot and healing plates (Buri SA, La Chaux-de-Fonds, Switzerland) based on the dimension of the Blackrock CerePort pedestal basis. The foot plate contained 8 holes to fix the healing plate, and later, the pedestal, with M1.6 titanium screws (Buri SA, La Chaux-de-Fonds, Switzerland) (**Figure 2.10**). The mesh was modeled in such a way that access to the brain for multi-electrode arrays implantations was not impeded (**Figure 2.9**). Depending on the scientific purpose of the project, we implanted various mesh designs with varying locations of the foot plates (**Figure 2.11**).

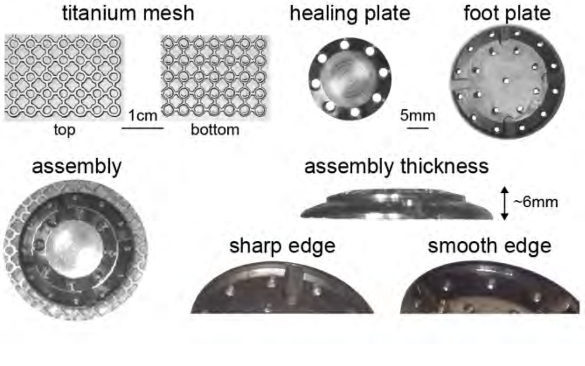

Figure 2.10 | Titanium mesh, foot plate and healing plate

Magnification of the malleable titanium mesh. The foot plate was attached to the top view, whereas the bottom part was in contact with the bone. The assembly (mesh, foot and healing plates) was about 6mm thick. Two foot plates were designed : with sharp or with smooth edge.

2.4.3.3. Computer tomography (CT) imaging, 3D reconstruction and mesh modeling

The animal was slightly sedated with a mixture of ketamine (ketasol-100, 10mg/kg, intramuscular) and midazolam (Dormicum, 0.1mg/kg, intramuscular) and brought to the computer tomography (CT) facility of the hospital of Fribourg (HFR). At the HFR site, the animal was anesthetized with a mixture of ketamine (ketasol-100, 4 mg/kg, intramuscular) and medetomidine (Dorbene, 0.04 mg/kg, intramuscular). The animal was then placed in a prone position within a stereotactic frame (ear bars were covered with Lidohex, a local anesthetic). An oxygen tube (3L/min) was placed in front of the monkey. Latex gloves filled with hot water and a bubble wrap sheet were placed around the animal in order to prevent body temperature from dropping. The electrocardiogram (ECG) as well as oxygen saturation (SO_2) were monitored and recorded every 5 minutes. After the acquisition, the animal received an intramuscular dose of atipamezole (Alzane, 0.2mg/kg) and was brought back to the animal facility where we closely monitored its condition until it was fully awake. Finally, after ensuring the animal's health and confirming the lack of post-anesthesia complications, the animal was fed, hydrated, and returned to the group. The CT parameters of the acquisition were a 0.6mm helicoidal low dose CT on a Philips Ingenuity TF machine. The 3D surface rendering (from the original DICOM files) was obtained in OsiriX (v.3.0.2), then exported in STL format and finally cleaned in blender (v.2.78) to be 3D printed. We molded the titanium mesh based on the 3D printed skull of each animal. The mesh was then covered with hydroxyapatite (Medicoat AG, Zürich, Switzerland) to promote osseointegration in all apart from three animals. The sterilization procedures were performed in a 3 step fashion: (1) the screws, foot plates, healing plates, mesh, and 3D printed skull were sterilized at a low temperature (55°C) with vaporized H_20_2 plasma (PlazMax Line P50, Tuttnauer, Switzerland); (2) in sterile conditions, we attached the foot and healing plates to the mesh and confirmed the mesh shape and positioning on the 3D printed skull and (3) the mounted mesh was sterilized again with vaporized H_2O_2 plasma. The meshes of Mk-LE and Mk-PD were additionally autoclaved. In Mk-JO, we performed the same procedure but with only autoclave sterilization.

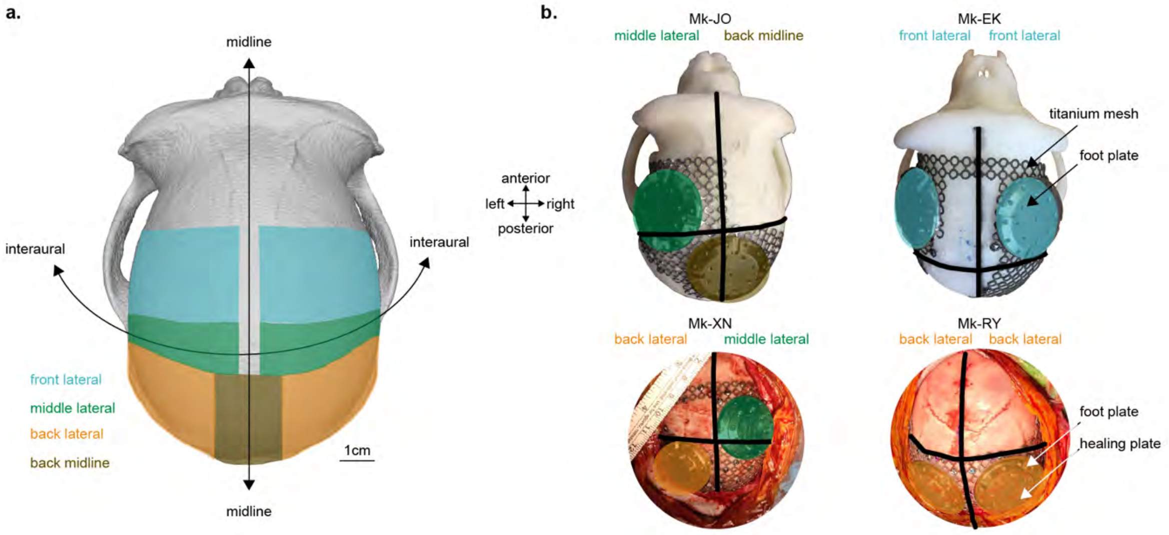
a.
midline
interaural
interaural
front lateral
middle lateral
back lateral
back midline
1cm
midline
b.
anterior
left
right
posterior
Mk-JO
middle lateral
back midline
Mk-EK
front lateral
front lateral
titanium mesh
foot plate
Mk-XN
back lateral
middle lateral
Mk-RY
back lateral
back lateral
foot plate
healing plate

Figure 2.11 | **Foot plate positioning nomenclature**

a. The foot plate was placed in 4 different regions of the skull, highlighted by the different colors. This nomenclature is further used in **Table 2.1**. **b.** Examples of four representative monkeys during the mesh shaping (top panel) or the during the surgery (bottom panel).

2.4.3.4. Surgeries

On the day prior to the surgery, the animal was anesthetized following the imaging protocol described above. Then, the skull was shaved and the animal received a dose of amoxicillin antibiotics (Noroclav, 30mg/kg, subcutaneously). Additionally, if a brain surgery was planned, an injection of dexamethasone (Dexadreson, 0.3mg/kg, intramuscularly) was given to help prevent the risk of vasogenic edema. The day of the surgery, the animal was sedated using an intramuscular mixture of ketamine (ketasol-100, 10mg/kg), midazolam (Dormicum, 0.1mg/kg) and methadone (Methadon, 0.2mg/kg). The animal received amoxicillin antibiotics (see above), dexamethasone (see above), analgesic carprofen (Rimadyl, 4mg/kg, subcutaneously) and atropine (atropine, 0.05mg/kg, intramuscular). The monkey was then anesthetized with a continuous infusion of propofol 1% and ringer-lactate (dilution 1:1, intravenously) and placed in a prone position within a stereotaxic frame. Moreover, the animal received a continuous warmed infusion of ringer-lactate (intravenously) and analgesia opioid (Fentanyl, diluted 1:1 in saline). ECG, SO_2, rectal temperature, and respiration rate were closely monitored and recorded every 5 minutes during the entire surgical protocol. The delivery rate of propofol, ringer-lactate and opioid were adjusted as needed by a trained professional monitoring the animal's vital signs. A local analgesic (Rapidocain 10 mg/ml) was injected subcutaneously before the initial skin incision. All the surgical procedures described below were performed in standard sterile conditions.

After a skin incision (midline and/or lateral), the mesh was implanted with ~20 self-drilling screws (Medtronic, 1.6x3.5mm or 4mm). Finally, the muscles were sutured back together and the skin sutured closed. After a period to allow for osseointegration (between 3 and 32 weeks, **Table 2.1**: Timing: integration time), the animal underwent the next surgery as described in (Capogrosso et al 2016). Importantly, the healing plates were removed and the pedestals were screwed to the footplates with the 8 titanium M1.6 screws. Note that in five animals (Mk-NT, Mk-LE, Mk-IG, Mk-PD and Mk-OL), we implanted the mesh and the pedestal(s) within the same surgery. Mk-BR underwent the mesh implantation twice, as a severe infection following the initial implantation required explantation of the mesh. In the five animals operated last, we covered the craniotomy and the connection cables with dental cement. This was performed to prevent any wires from becoming exposed after possible hole formations and/or skin retraction as observed in the previous animals.

2.4.3.5. Adverse effect assessments

Changes in group hierarchy following a surgical intervention are not an uncommon occurrence. Depending upon the initial rank of the operated animal, its weakened state and changes in appearance due to implanted material create an opportunity for other ambitious group members to rise in rank. In order to prevent such fights for dominance and ensure proper recovery, we isolated the monkey in a nursery within the animal facility for a period of 1 to 3 days. We gave doses of dexamethasone (Dexadreson, 0.3mg/kg, intramuscularly), analgesic carprofen (Rimadyl, 4mg/kg, subcutaneously or per os), and amoxicillin antibiotics (Noroclav, 30mg/kg, subcutaneously), for three, four, and ten days after the surgery, respectively. We removed the stitches approximately 10 days after the surgery. If necessary, we performed an antibiogram in order to adjust antibiotic medication. Depending on the antibiogram results, we administered a daily dose of amoxicillin/ clavulanic acid (Synulox or Clavubactin, 30mg/kg, subcutaneous or per os, respectively), gentamicin (Pargenta, 4mg/kg, subcutaneous), enrofloxacin (Baytril, 5mg/kg, subcutaneous), or a weekly dose of ceftiofur sodium (Naxcel, 20mg/kg, subcutaneous). We monitored the well-being and recovery of the animals based on a standardized score sheet used to evaluate behavior, posture, appearance, respiration, food/drink/digestion, body weight, body condition, and the surgery wound. The experimenters, who worked with the animal daily, reported the adverse effects. In **Table 2.1**, we reported all the observed adverse effects and classified the animal in one of 4 levels of severity : (1) severe adverse effects (complications that led to explantation); (2) middle adverse effects (at least two complications were present); (3) low adverse effects (only one complication was present) and (4) no observed adverse effect.

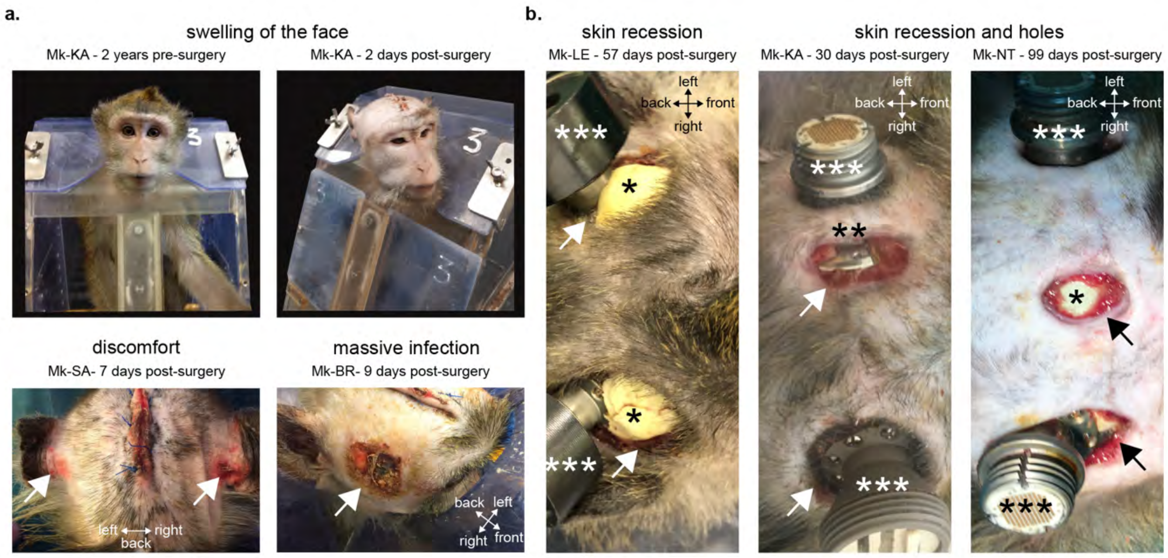
a.
swelling of the face
Mk-KA - 2 years pre-surgery
Mk-KA - 2 days post-surgery
discomfort
Mk-SA- 7 days post-surgery
left ⟷ right
back
massive infection
Mk-BR- 9 days post-surgery
back left
right front
b.
skin recession
Mk-LE - 57 days post-surgery
skin recession and holes
Mk-KA - 30 days post-surgery
Mk-NT - 99 days post-surgery
left
back front
right
***
*
**

Figure 2.12 | **Adverse effects**

a. Titanium mesh post-operative adverse effects. Swelling of the face example in Mk-KA before and after the mesh surgery. After the mesh surgery, Mk-SA obsessively scratched the ear area leading to inflammation (bottom left panel, large arrows). 9 days after the surgery, a massive infection (bottom right panel, big arrow) occurred in Mk-BR. **b.** Pedestal post-operative adverse effects. The most common adverse effect was skin recession around the basis of the pedestal. Most of the time, this was accompanied by the formation of a hole, either at the edge of the foot plate (middle panel) or elsewhere (right panel). A local infection was also present most of the time. * dental cement; ** foot plate edge; *** pedestals.

2.4.4. Results

This procedure showed remarkable stability of the pedestals; none of the animals lost their pedestals over the course of the experiment. Post-mortem analysis confirmed the correct location of the micro-electrode arrays. Moreover, the mesh was well-integrated to the bone as a result of the hydroxyapatite, which was impossible to remove during dissection.

In general, the mesh surgery itself did not lead to major complications. 78% of the animals showed no or low adverse effects (**Figure 2.13**). The most common adverse effect was swelling of the face that soon receded, without any medication. One animal (Mk-SA) compulsively scratched the ear area in possible discomfort, but after few weeks this behavior disappeared (**Figure 2.12a**). This animal was also considered to have low adverse effect. One animal (Mk-RY) had both a swollen face and a small infection that receded with the administration of antibiotics. Thus, Mk-RY was in the middle adverse effect group. In Mk-BR, a major infection appeared and we had to explant the titanium mesh to facilitate the animal's recovery (**Figure 2.12a**). This animal received a new mesh and pedestal together in the same surgery 27 weeks after the first mesh explantation (**Table 2.1**).

After the pedestal implantations, the most common adverse effect was skin recession around the pedestals, present in 69% of the animals (**Figure 2.12b**, **Table 2.1**). Infection and formation of holes in the skin were present in 62% of the animals (**Figure 2.12b**, **Table 2.1**). Two (Mk-BR and Mk-EK) out of 13 animals had multi-resistant bacterial infections that required pedestal explantation. However, since the mesh was osseointegrated due to the hydroxyapatite, it was not possible to explant the mesh and the infection could not be properly treated, resulting in the termination of the two animals a few weeks later. To summarize, 54% of the animals exhibited middle adverse effects while only 30% had low or no adverse effects (**Figure 2.13**).

No positive correlation was found between the integration time (i.e. time between the mesh and the pedestal implantation) and the severity of the mesh post-operative complications (data not shown). A slight positive correlation was observed between duration of time after the pedestal surgery and complication severity (data not shown), although exceptionally, just 9 weeks after the pedestal implantation surgery, Mk-BR was terminated due to severe complications.

Finally, neither the position of the foot plate nor the dental cement applications seemed to have a negative or positive effect on the post-operative outcomes (**Table 2.1**). Nevertheless, the edges of the foot plates in both designs was routinely observed to have created a hole in the skin at this location (**Figure 2.12b**)

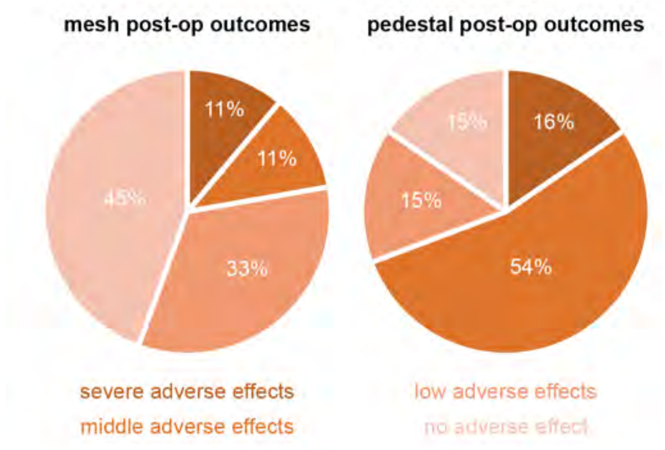

Figure 2.13 | Post-op following-up after the surgeries

After the titanium mesh implantation (left panel), only 45% of the animals showed no adverse effects, whereas 33% showed low adverse effects, such as swelling of the face. 11% of them had middle complications, including infection requiring antibiotics. The last 11% had major complications, leading to the explantation of the mesh. After the percutaneous implantations (right panel), 54% of the animals showed holes in the skin accompanied by local infections and skin recessions. 16% of the animals had to be explanted due to massive infections.

	ANIMAL INOFRMATION		MESH INOFRMATION			OTHER INFORMATION	
	Age (years)	Weight (kg)	Hydroxyapatite	Foot plates	Foot plates positions	Sterilization procedure	Dental cement with antibiotic
Mk-BR	3	3.4	yes	2	middle lateral / back midline	3 steps plasma	yes
Mk-EK	7	4.6	yes	2	front lateral / front lateral	3 steps plasma	-
Mk-NT	7	4	yes	2	front lateral / front lateral	3 steps plasma	yes
Mk-RY	4	2.9	yes	2	back lateral / back lateral	3 steps plasma	-
Mk-KA	7	4.3	yes	2	front lateral / front lateral	3 steps plasma	-
Mk-LE	5	3.8	-	2	back lateral / back lateral	3 steps plasma + autoclave	yes
Mk-SA	9	4	yes	2	front lateral / back lateral	3 steps plasma	-
Mk-IG	3	2.9	yes	2	middle lateral / back midline	3 steps plasma	yes
Mk-XN	7	4.1	yes	2	back lateral / middle lateral	3 steps plasma	-
Mk-CS	9	4	yes	2	middle lateral / back lateral	3 steps plasma	-
Mk-PD	5	3.4	-	1	back midline	3 steps plasma + autoclave	yes
Mk-JO	10	3.6	yes	2	middle lateral / back midline	3 steps plasma	-
Mk-AY	3	3.2	yes	2	back lateral / back lateral	3 steps plasma	-
Mk-OL	4	2.9	-	1	back lateral	3 steps autoclave	-

	MESH POST-OP FOLLOW-UP					PEDESTAL POST-OP FOLLOW-UP						TIMING (weeks)		
	Explantation	Infection	Discomfort	Swelling of the face	**Adverse effects**	Explantation	Infection	Holes	Skin recession	Other effects	**Adverse effects**	Intergration time	Time after pedestal	Total time
Mk-BR	yes	yes	-	-	**severe**	yes	yes	yes	yes	-	**severe**	0**	9	9***
Mk-EK	-	-	-	-	**-**	yes	yes	yes	yes	-	**severe**	8	47	55
Mk-NT					**&**	-	yes	yes	yes	swelling of the face*	**middle**	0	27	27
Mk-RY	-	yes	-	yes	**middle**	-	yes	yes	yes	-	**middle**	10	27	37
Mk-KA	-	-	-	yes	**low**	-	yes	yes	yes	-	**middle**	8	30	38
Mk-LE					**&**	-	yes	-	yes	-	**middle**	0	43	43
Mk-SA	-	-	scratching ear area	-	**low**	-	-	yes	yes	-	**middle**	3	30	43
Mk-IG					**&**	-	-	yes	yes	-	**middle**	0	9	9
Mk-XN	-	-	-	-	**-**	-	yes	yes	-	-	**middle**	18	7	25
Mk-CS	-	-	-	-	**-**	-	-	-	yes	-	**low**	7	13	19
Mk-PD					**&**	-	yes	-	-	-	**low**	0	27	27
Mk-JO	-	-	-	-	**-**	-	-	-	-	-	**-**	32	4.5	36.5
Mk-AY	-	-	-	yes	**low**						**&&**	8	0	8
Mk-OL					**&**	-	-	-	-	-	**-**	0	9	9

Table 2.1 | **Summary of all the animals follow-up**

All the reported animals were female macaque monkeys (*Macaca fascicularis*). All 14 animals, apart from two, received a titanium mesh, coated with hydroxyapatite, to which 2 foot plates were attached . The positioning of the footplates varied depending on the project (see example in **Figure 2.11**). The sterilization procedures are described in the Material & Methods. Five out of 14 animals underwent both mesh and pedestal(s) implantation in the same surgery. In these animals, the *integration time* (i.e. the time between the mesh and pedestal implantation) is thus 0 weeks. *The time after pedestal* refers to the duration of time from the pedestal implantation surgery to the sacrifice of the animal. The complications after the mesh or the pedestal surgery were assessed by the experimenters working with the animal daily. Here, we reported all the adverse effects and classified the animal in a level of adverse effect severity. An animal was in the severe adverse effect level when we had to explant the mesh and/or the pedestals. The middle adverse effects indicate when at least two complications occurred. Low adverse effect group include animals with only one side effect observed.

* might be due to the mesh.

** considering the second mesh implantation. Mk-BR underwent two mesh implantation surgeries.

*** from the first implantation : 36 weeks

& These animals underwent the mesh and the pedestal(s) implantation during the same surgery. Therefore, this assessment was not possible.

&& This animal died few hours after the surgery due to respiratory failure. Therefore, this assessment was not possible.

2.4.5. Discussion

Here we described a new method for cranial implantation surgery in nonhuman primates. This method consisted of first implanting a titanium mesh, manually molded based on the 3D cranial replicate of the monkey. The titanium mesh was then coated with hydroxyapatite to promote osseointegration. Moreover, two titanium foot plates were attached to the mesh. In a second surgery, we implanted a pedestal containing micro-electrode arrays and a second pedestal housing either another micro-electrode array, or an electromyographic or stimulation connector. The two pedestals were anchored to the foot plates. This method facilitated impressive pedestal stability: none of the monkey lost their pedestals over the course of the experiment. Additionally, MRI-guided planning of the second surgery ensured successful positioning of the micro-electrode arrays. However, while this method seemed efficient and was in many ways beneficial, it must be said that the post-operative complications we encountered considerably weakened its reliability.

After the mesh surgery, some animals showed low adverse effects, such as swelling of the face that gradually receded after a few days. However, another animal developed a massive infection that was so severe it required explantation of the mesh. While explantation is indeed a last resort and less commonly seen, the symptom of edema is not surprising, as facial swelling is an adverse effect seen also in human patients after titanium cranioplasty surgery, a reparative surgery of the skull (Tattersall 1984; Huang et al. 2013; Tong et al. 2015; Martini et al. 2017). A recent retrospective study in human patients who underwent titanium cranioplasty surgery (plate or mesh), showed that the overall complication rate was 26% and plate removal rate 10%. Infection occurred in 69% of the plate removal cases (Mukherjee et al. 2014). In contrast, 55% of the subjects in our study had complications, one even leading to explantation. Overall, we advise against the implantation of titanium mesh in macaque monkeys.

After the pedestal surgery, only 15% of the animals did not show adverse effects. This may be explained by the fact the experiment lasted a maximum of 9 weeks. Of course, the longer the experiment lasts, the more likely it is for complications to occur, such as skin recession and the formation of holes in the skin (**Table 2.1**).

Almost all the animals developed skin recession after the pedestal implantation, to varying degrees of severity. We tried different post-operative care routines, such as weekly shaving the skin margin, applying dermal cream, etc. None of this techniques prevented the skin from retracting from the implant. This complication was often accompanied by the formation of holes at the edge of the footplate, or in the middle of the head. The dual foot plate designs often lead to more extreme skin recession. However, we observed that the further from the midline the footplates were positioned, the less likely a hole in the skin was to form. In addition to the increased risk of infection, the holes in the skin and the skin recession presented another problem that placed the experiment in jeopardy: as the skin retracted, wires and electronics feeding out of the pedestals were exposed and at risk for damage. Therefore, in the last animals we added the step of application of dental acrylic cement on top of the wires, to protect them. It is known that dental cement has a detrimental effect (skin recession) and is prone to infection (Lanz et al. 2013; Johnston et al. 2016; Ortiz-Rios et al. 2018). Consequently, its application did not solve the problem.

Skin recession and hole formation may have happened for two reasons. First, the animals were relatively small. Indeed, our long-tail female macaque monkeys (*Macaca fascicularis*) were approximately 2.5 times lighter than the rhesus macaque monkeys (*Macaca mulatta*) used in (Chen et al. 2017; Ortiz-Rios et al. 2018) and 2.2 times lighter than male *fascicularis* in (Lanz et al. 2013). In those studies, they did not report any hole formation or skin resection (<0.5 cm). Thus, in our study, the available skin on the scalp might have been too little. Consequently, skin tension was likely too high. Indeed, in human patients, thin scalp skin and skin tension during suturing are two considerations to be addressed in order to ensure a positive post-operative outcome after a cranioplasty surgery (Di Rienzo et al. 2016; Mikami et al. 2017; Sheng et al. 2017). Second, scalp vascularization might have been weakened after the first surgery with the mesh implantation and hydroxyapatite bone assimilation. Proper blood supply was even more challenging after the second surgery, especially with percutaneous connectors (Steiner et al. 2018; Wolff et al. 2019). Therefore, favorable conditions for skin healing were most likely not met.

The major consideration was the bacterial infection present in almost all animals. The fact that the animals lived in group of 2 to 5 certainly favored bacterial proliferation via grooming and other forms of social contact. Knowing this, we regularly performed antibiograms for antibiotic medication adjustment. An extremely disturbing trend observed was that the longer the experiment lasted, the higher the risk was for developing dangerous multi-resistant bacteria. In two cases where this exact scenario occurred in our study, the resistant infection became so severe that the well-being of the animal deteriorated to a point where the pedestals required explantation. Unfortunately, the advanced stage of infection around the osseo-integrated mesh could not be resolved and the animals were terminated a few weeks later. To reduce overall experiment time duration and therefore reduce the risk of multi-resistant infection, we combined the first and second surgery in the last five animals. In three of them, we directly implanted an uncoated mesh, followed by the pedestal, during the same surgery. We noticed that the stability of the implant did not change. To summarize, removing the step of coating with hydroxyapatite had three advantages: (1) decreasing the number of surgeries and the risks associated with them; (2) maintaining the possibility of mesh explantation in case of complications and (3) the financial gain of sparing the cost of coating. We conclude that the best minimization of risk for a pedestal implantation would be to integrate pedestal feet to the base. However, these feet must have the practicality and flexibility of the mesh and cannot be rigid. The implantation of such a pedestal must be performed in one surgery. Moreover, we recommended a period of isolation during the experiment in order to avoid contamination across animals.

Unfortunately, implant-associated infections occur in about 3-15% of surgeries in the US (Conen et al. 2020). In people with percutaneous pedestals, antibiotics have to be frequently applied to reduce infection (https://www.newyorker.com/magazine/2018/11/26/how-to-control-a-machine-with-your-brain). Consequently, in a clinical application for a brain-machine interface, achieving total minimization of risks involves the implementation of a fully implantable system, such as NeuralLink system.

2.4.6. Acknowledgments

The authors thank Laurent Bossy, Jacques Maillard and Dr. Mélanie Kaeser for their valuable daily collaboration for the care of the monkeys in the animal facility. We also thank Dr. Eric Schmidlin, Dr. Florian Lanz and Dr. Mélanie Kaeser for their anesthesia expertise during the surgeries. Finally, our thanks go also to Jean-Daniel Niederhaeuser for 3D printing the skull and brain replicates.

2.5. CONCLUSION

The newly renovated platform allowed studies of untethered, free behavior in nonhuman primates. Custom-built plexiglass enclosures allowed the interchanging of ground surfaces so that monkeys could perform various tasks, such as walking on a treadmill, through a corridor, and over a ladder, obstacles and stairs (**Figure 2.14, top**). Three systems have been linked in synchronicity to record behavior and neurophysiological data in freely behaving monkeys. A Cereplex W lightweight wireless digital headstage was connected to a pedestal on the monkey's head to transmit intracortical neural data to a neural signal processor. The start of the recording on the Blackrock system triggered data collection of the electromyographic system. The W2100 Multichannel System wireless headstage was connected to a second pedestal on the monkey's head to transmit wireless EMG recordings to a computer and to the Blackrock neural signal processor. A high quality 8-video camera system was used to track reflective markers placed on anatomical landmarks on the legs (**Figure 2.14, left**). The start of the recording on the SIMI system sent a trigger pulse to the Blackrock neural signal processor and the Multichannel interface board. This pulse was used to align the data collected by the three systems. A pipeline intended to personalize the surgical implantation protocols according to subject-specific anatomical features was established. CT and MRI scans enabled the skull and brain to be converted into 3D models and 3D printed. Co-registration of the skull and brain allowed personalization of the shape and position of a titanium mesh screwed onto the skull that ensured the longevity of the head connectors. The 3D registration also facilitated the identification of the precise locations of the brain regions within which intracortical arrays were inserted. It also allowed for the optimization of the craniotomy location. 3D printed anatomical models were used during the surgery as references to ensure accurate device placement and ease of navigation. Following this protocol, monkeys were implanted with intracortical multielectrode arrays and bipolar electrodes for muscle recordings. Neuronal firing rate was computed for each channel and synchronized with the muscle activity, kinematics, and gait events (**Figure 2.14, middle**). These recordings were used to extract single unit spike activity and compute a spatiotemporal map of motor neuron pool activation in the spinal cord (**Figure 2.14, right**).

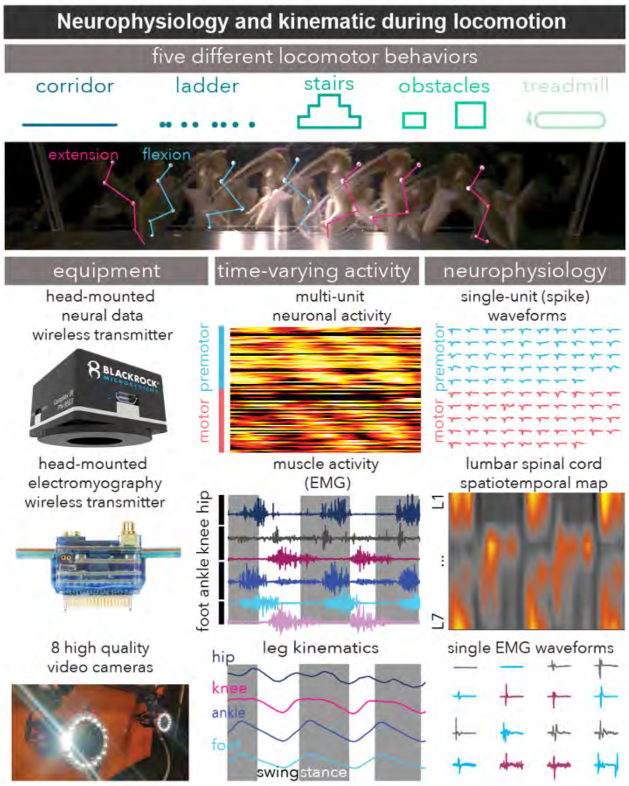
Neurophysiology and kinematic during locomotion
five different locomotor behaviors
corridor
ladder
stairs
obstacles
treadmill
extension
flexion
equipment
time-varying activity
neurophysiology
head-mounted neural data wireless transmitter
multi-unit neuronal activity
single-unit (spike) waveforms
motor
premotor
head-mounted electromyography wireless transmitter
muscle activity (EMG)
lumbar spinal cord spatiotemporal map
foot ankle knee hip
L1
L7
8 high quality video cameras
leg kinematics
hip
knee
ankle
foot
swing
stance
single EMG waveforms

Figure 2.14 | Summary of the freely behaving monkey platform in untethered conditions
Top: schematic representation of the five locomotor behavior conditions. Plexiglas enclosure allowing NHPs to behave without constraints in various tasks. The chronography illustrates kinematic recordings with overlaid stick diagrams on Mk-Xn walking across the corridor. Left: commercial recording equipment for neural signals, EMG, and kinematics. Middle: synchronized spiking activity from M1 and premotor cortex, EMG, and leg joint angles. Right: Spikes extracted from intracortical array recordings, spatiotemporal map of motor neuron pool activation in the lumbar spinal cord, and single EMG responses.

Taking into consideration the fact that the brain control of movement remains poorly understood, especially in case of locomotion, this newly renovated platform allowed the exploratorily neurophysiological study of locomotion in primates. In the next chapter, I will describe the sensorimotor neural dynamic patterns seen during five locomotor tasks, namely, the corridor (over-ground walking), uneven horizontal ladder, stairs, obstacles and the treadmill and I will also discuss how these dynamics differed across premotor, primary motor and somatosensory cortices.

2.6. BIBLIOGRAPHY

Adams DL, Economides JR, Jocson CM, Parker JM, Horton JC. A watertight acrylic-free titanium recording chamber for electrophysiology in behaving monkeys. Journal of Neurophysiology. 2011 Sep;106(3):1581–90.

Barrese JC, Rao N, Paroo K, Triebwasser C, Vargas-Irwin C, Franquemont L, et al. Failure mode analysis of silicon-based intracortical microelectrode arrays in non-human primates. J Neural Eng. IOP Publishing; 2013 Nov 12;10(6):066014–24.

Capogrosso M, Milekovic T, Borton D, Wagner F, Moraud EM, Mignardot J-B, et al. A brain–spine interface alleviating gait deficits after spinal cord injury in primates. Nature. Nature Publishing Group; 2016 Nov 10;539(7628):284–8.

Chen X, Possel JK, Wacongne C, van Ham AF, Klink PC, Roelfsema PR. 3D printing and modelling of customized implants and surgical guides for non-human primates. J Neurosci Methods. Elsevier B.V; 2017 Jul 15;286:38–55.

Conen A, Raabe A, Schaller K, Fux CA, Vajkoczy P, Trampuz A. Management of neurosurgical implant-associated infections. Swiss Med Wkly. EMH Media; 2020 Apr 24;150(1718):1–14.

Cook SD, Thomas KA, Dalton JE, Volkman TK, Whitecloud TS, Kay JF. Hydroxylapatite coating of porous implants improves bone ingrowth and interface attachment strength. J Biomed Mater Res. John Wiley & Sons, Ltd; 1992 Aug;26(8):989–1001.

Di Rienzo A, Pangrazi P, Riccio M, Colasanti R, Ghetti I, Iacoangeli M. Skin flap complications after decompressive craniectomy and cranioplasty: Proposal of classification and treatment options. Surg Neurol Int. 2016;7(29):737–9.

Evarts EV. Relation of pyramidal tract activity to force exerted during voluntary movement. Journal of Neurophysiology. 1968 Jan;31(1):14–27.

Huang Y-H, Yang T-M, Lee T-C, Chen W-F, Yang K-Y. Acute autologous bone flap infection after cranioplasty for postinjury decompressive craniectomy. Injury. Elsevier Ltd; 2013 Jan 1;44(1):44–7.

Jackson A, Fetz EE. Compact Movable Microwire Array for Long-Term Chronic Unit Recording in Cerebral Cortex of Primates. Journal of Neurophysiology. 2007 Nov;98(5):3109–18.

Johnston JM, Cohen YE, Shirley H, Tsunada J, Bennur S, Christison-Lagay K, et al. Recent refinements to cranial implants for rhesus macaques (Macaca mulatta). Nature Publishing Group. Nature Publishing Group; 2016 May 1;45(5):180–6.

Lanz F, Lanz X, Scherly A, Moret V, Gaillard A, Gruner P, et al. Refined methodology for implantation of a head fixation device and chronic recording chambers in non-human primates. J Neurosci Methods. 2013 Oct 15;219(2):262–70.

Martini M, Röhrig A, Reich RH, Messing-Jünger M. Comparison between piezosurgery and conventional osteotomy in&nbsp;cranioplasty with fronto-orbital advancement. Journal of Cranio-Maxillofacial Surgery. Elsevier Ltd; 2017 Mar 1;45(3):395–400.

Mathis A, Mamidanna P, Cury KM, Abe T, Murthy VN, Mathis MW, et al. DeepLabCut: markerless pose estimation of user-defined body parts with deep learning. Nat Neurosci. Springer US; 2018 Aug 27;21(9):1–12.

McAndrew RM, VanGilder JLL, Naufel SN, Tillery SIH. Individualized recording chambers for non-human primate neurophysiology. J Neurosci Methods. Elsevier B.V; 2012 May 30;207(1):86–90.

Mikami T, Miyata K, Komatsu K, Yamashita K, Wanibuchi M, Mikuni N. Exposure of titanium implants after cranioplasty: A matter of long-term consequences. Interdisciplinary Neurosurgery: Advanced Techniques and Case Management. The Authors; 2017 Jun 1;8(C):64–7.

Mukherjee S, Thakur B, Haq I, Hettige S, Martin AJ. Complications of titanium cranioplasty—a retrospective analysis of 174 patients. Acta Neurochir. Springer Vienna; 2014 Mar 11;156(5):989–98.

Nicolelis MAL, Dimitrov D, Carmena JM, Crist R, Lehew G, Kralik JD, et al. Chronic, multisite, multielectrode recordings in macaque monkeys. PNAS. National Academy of Sciences; 2003 Sep 16;100(19):11041–6.

Ortiz-Rios M, Haag M, Balezeau F, Frey S, Thiele A, Murphy K, et al. Improved methods for MRI-compatible implants in nonhuman primates. J Neurosci Methods. Elsevier; 2018 Oct 1;308:377–89.

Schmidlin E, Kaeser M, Gindrat A-D, Savidan J, Chatagny P, Badoud S, et al. Behavioral assessment of manual dexterity in non-human primates. J Vis Exp. 2011;(57).

Schwarz DA, Lebedev MA, Hanson TL, Dimitrov DF, Lehew G, Meloy J, et al. Chronic, wireless recordings of large-scale brain activity in freely moving rhesus monkeys. Nat Meth. Nature Publishing Group; 2014 Jun;11(6):670–6.

Sheng H-S, Shen F, Wang M-D, Lin J, Lin F-C, Yin B, et al. Titanium mesh implants exposure after cranioplasty in two children: involvement of osteogenesis? Chinese Neurosurgical Journal. Chinese Neurosurgical Journal; 2017 Jan 17;:1–4.

Steiner D, Horch RE, Eyüpoglu I, Buchfelder M, Arkudas A, Schmitz M, et al. Reconstruction of composite defects of the scalp and neurocranium—a treatment algorithm from local flaps to combined AV loop free flap reconstruction. World Journal of Surgical Oncology; 2018 Nov 6;:1–11.

Tattersall MP. Massive swelling of the face and tongue. A complication of posterior cranial fossa surgery in the sitting position. Anaesthesia. 34 ed. John Wiley & Sons, Ltd; 1984 Oct;39(10):1015–7.

Tong JW, Emelin JK, Wong R, Meltzer HS, Cohen SR. Subgaleal Drain Placement Improves Surgical Outcomes After Primary Cranioplasty in Craniosynostosis Patients. Journal of Craniofacial Surgery. 2015 Sep;26(6):1963–6.

Wolff AY, Santiago GF, Belzberg M, Manson PN, Huang J, Brem H, et al. Full-Thickness Skin Grafting for Local Defect Coverage Following Scalp Adjacent Tissue Transfer in the Setting of Cranioplasty. Journal of Craniofacial Surgery. 2019;30(1):115–9.

Wyss AF, Hamadjida A, Savidan J, Liu Y, Bashir S, Mir A, et al. Long-term motor cortical map changes following unilateral lesion of the hand representation in the motor cortex in macaque monkeys showing functional recovery of hand functions. Restor Neurol Neurosci. 2013 Jan 1;31(6):733–60.

Yin M, Borton DA, Komar J, Agha N, Lu Y, Li H, et al. Wireless neurosensor for full-spectrum electrophysiology recordings during free behavior. Neuron. 2014 Dec 17;84(6):1170–82.

Zimmermann JB, Jackson A. Closed-loop control of spinal cord stimulation to restore hand function after paralysis. Front Neurosci. Frontiers; 2014;8(57):87.

- PART 3 -

NEURAL POPULATION DYNAMICS ARE CORTEX-SPECIFIC IN PREMOTOR, MOTOR, AND SOMATOSENSORY CORTICES DURING LOCOMOTION

The content of this chapter was adapted from a manuscript in preparation: ***Population dynamics in premotor, motor and somatosensory cortices during locomotion***. Ismael Seáñez*, Simon Borgognon*, Nicolò Macellari, Alexandra M. Hickey, Matthew G. Perich, Rafael E. Ornelas Kobayashi, Luke S. Urban, Christopher Hitz, Florian Fallegger, Stéphanie P. Lacour, Eric M. Rouiller, Tomislav Milekovic, Jocelyne Bloch, Grégoire Courtine#

**equally contribution*

# corresponding author

Personal contributions: conception and technological framework, performed experiments, analyzed the data apart from the decoder, generated the figures, wrote the paper

3.1. ABSTRACT

Cortical activity is believed to coordinate the adjustment of leg movements associated with volitional modifications of gait, yet the relative contribution of different cortical regions within the sensorimotor cortex remains unknown. We investigated whether preservation of structure and dynamics commonly observed in primary motor cortex (M1) neural population activity were also present in dorsal premotor (PMd) and primary somatosensory (S1) areas. We recorded from populations of neurons as monkeys walked on a treadmill, along corridors, uneven ladders, obstacles, and stairs. S1 displayed robust neural activation patterns across tasks. Neural population activity for different tasks resided within aligned subspaces of the neural manifold, and most neural variance was associated with locomotion-dependent parameters. In contrast, neural activation patterns in PMd differed across tasks, resided within distinct task-dependent subspaces, and neural variance was equally associated with task-dependent and locomotion-dependent parameters. Neural population activity in M1 also resided within task-dependent subspaces. However, like in S1, most of the neural variance was captured by locomotion-dependent parameters. Interestingly, locomotion-dependent parameters allowed an improvement in decoder generalization for locomotor tasks requiring different patterns of muscle and single unit activity in PMd and M1, but had no apparent effect in S1.

3.2. INTRODUCTION

Different brain regions play a unique yet complementary function in the generation and control of movement. One of the remaining fundamental questions in neuroscience is how different brain circuits effectively modulate their behavior to allow the generation of a rich repertoire of movements. In this study, we ask how different cortical regions within the sensorimotor cortex mediate the adaptation of behavior to the requirements of various types of related movements.

Studies of neural behavior during locomotion have shown that cortical neurons in premotor (PMd), primary motor (M1), and somatosensory (S1) cortices have increased activity during rhythmic locomotion (Armstrong and Drew 1984a; 1984b; Fukuyama et al. 1997; Ayaz et al. 2019; Karadimas et al. 2019), are time-locked to different phases of the gait cycle (Armstrong and Drew 1984a; 1984b; Beloozerova et al. 2003; Fitzsimmons 2009; D Foster et al. 2014; Favorov et al. 2015; McCrimmon et al. 2017), and can be used to predict kinematics and muscle activity (Fitzsimmons 2009; Weiguo Song et al. 2009; Yin et al. 2014; Rigosa et al. 2015). Although descending pathways in the corticospinal tract (CST) are not essential for basic, rhythmic locomotion in rats and cats (Beloozerova and Sirota 1993; Muir and Whishaw 1999), they do contribute towards the precise control of paw placement or limb trajectory (Drew et al. 2002). In primates, the CST plays an even larger role in motor control (Lemon 2008), and studies in human and nonhuman primates with damage to the CST demonstrate that it is crucial for the control of gait (Courtine et al. 2005b; Barthélemy et al. 2011). However, although a majority of descending projections in the corticospinal tract originate in the motor cortex (Dum and Strick 1991), a considerable percentage of fibers have been shown to originate in PMd (Dum and Strick 1991) and S1 (Rathelot and Strick 2006; Karadimas et al. 2019). Therefore, the relative contribution of different cortical regions within the sensorimotor cortex towards voluntary modifications in locomotor behavior remains unknown.

Recent studies in neural control of movement have reported that while multiple motor behaviors require different patterns of muscle and single unit activity in M1, the structure and activity of the low dimensional components is preserved across tasks (Gallego et al. 2018; Lara et al. 2018). Here, we ask whether PMd and S1 obey similar or different population-level dynamics as M1 across locomotor tasks requiring coordinated adjustment of leg movements. To answer this question, we recorded neural population activity from leg PMd, M1, and S1 cortical regions during several locomotor tasks (**Figure 3.1a**). We then identified and studied the cortex-specific subspaces of the neural manifold where neural population activity for each task resided (**Figure 3.1b**). While neural population activity may reside within similarly aligned subspaces of the neural manifold for multiple motor behaviors, activity of neurons involved in proactive modifications of the gait pattern may reside within distinct, task-dependent subspaces. Visually guided locomotor tasks that require fine control of the legs require preparatory or planning activity, which has been shown to be prevalent in PMd, somewhat less prevalent in M1, and essentially absent in the muscles (Prut and Fetz 1999; Fetz et al. 2002; Kaufman et al. 2014). We expect task-dependent planning activity to be reflected in the task-dependent population structure and dynamics. Therefore, we hypothesize that neural activity for different tasks will reside within distinct subspaces in PMd, somewhat more aligned in M1, and within highly aligned subspaces in S1 (**Figure 3.1b**).

Despite a strong relationship between single neuron activity and behavior for individual tasks, we observed lower stability in neural correlates across locomotor tasks in PMd compared to M1. In contrast, activity from populations of neurons in S1 remained stable across tasks. We found a rostro-caudal increase (from PMd to M1, to S1) in the alignment of the neural manifolds across tasks. This observation was further supported by the amount of neural variance that could be explained by the neural modes whose activity was dependent on each task. The different neural dynamics and types of information carried by population activity within each cortex, argue that PMd, M1, and S1 contribute in a unique but complementary manner to allow the sensorimotor cortex to make adjustments necessary to perform a rich repertoire of locomotor behaviors

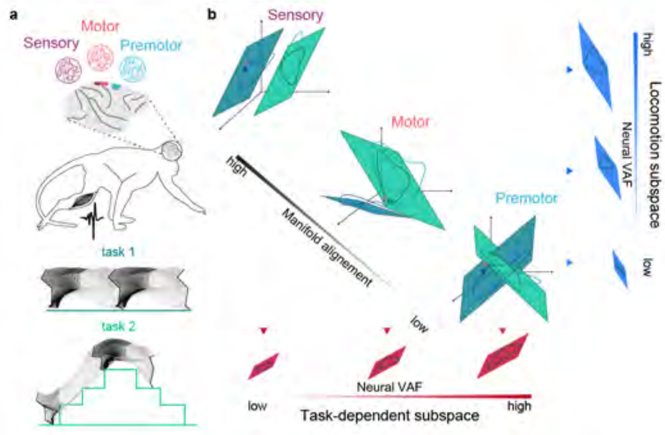

Figure 3.1 | Task and hypothesis

a. Is neural activity in the different regions of the sensorimotor cortex stable across locomotor tasks requiring coordinated adjustment of leg movements? To answer this question, three monkeys were implanted with micro-electrode arrays in PMd, M1 cortices, and an additional array S1 cortex in two of them. **b**. Hypothesis: a rostro-caudal gradient in alignment of neural manifolds across varied locomotor behaviors.

3.3. RESULTS

3.3.1. Behavioral tasks and recordings

We trained adult female *Macaca fascicularis* monkeys to perform five types of locomotor activities in the same session. These tasks included walking over a corridor, an unevenly spaced ladder, a three-step stair, two obstacles, and on a motorized treadmill (**Figure 3.2a**). We recorded hindlimb kinematics, and muscle activity (EMG) patterns of the right leg as monkeys performed each task. To study sensorimotor cortex behavior during locomotion, we recorded neural activity using microelectrode arrays chronically implanted in the leg area of left premotor (PMd, F2), primary motor (M1, F1), and somatosensory (S1, area 1/2). Electrode location verified post-mortem is shown in **Figure 2.8** (Note that Mk-Xn was excluded in this study as the two arrays were in M1). We extracted single-neuron responses that remained stable across the whole session from PMd (118, 110, and 252 single neurons respectively for Mk-Ek, Mk-Nt, and Mk-Ka), M1 (170, 58, and 221 neurons) and S1 (89 and 81 neurons for Mk-Ek and Mk-Nt). We aligned kinematics, EMG profiles, and single neuron firing rates at foot-strike and foot-off, concatenated time-warped trials, and averaged them to allow comparison between tasks with different durations of the gait cycle (Armstrong and Drew 1984b; T. Drew 1993; Courtine, Roy, Hodgson, et al. 2005; Fitzsimmons NA, Lebedev MA, Peikon ID 2009) (**Figure 3.2b-d**, time-based signals in **Figure 3.3**). Single neurons are organized by the timing of their peak firing rate for the corresponding task of each column. The peak firing gait phases of all neurons were evenly distributed over the entire gait cycle in PMd (**Figure 3.4**). In contrast, a greater proportion of neurons in M1 were phase-locked to foot-strike (Mk-Ek) and late stance (Mk-Ek and Mk-Nt) compared to early stance and swing. In S1, a majority of single neurons had peak firing at foot-strike (Mk-Ek and Mk-Nt).

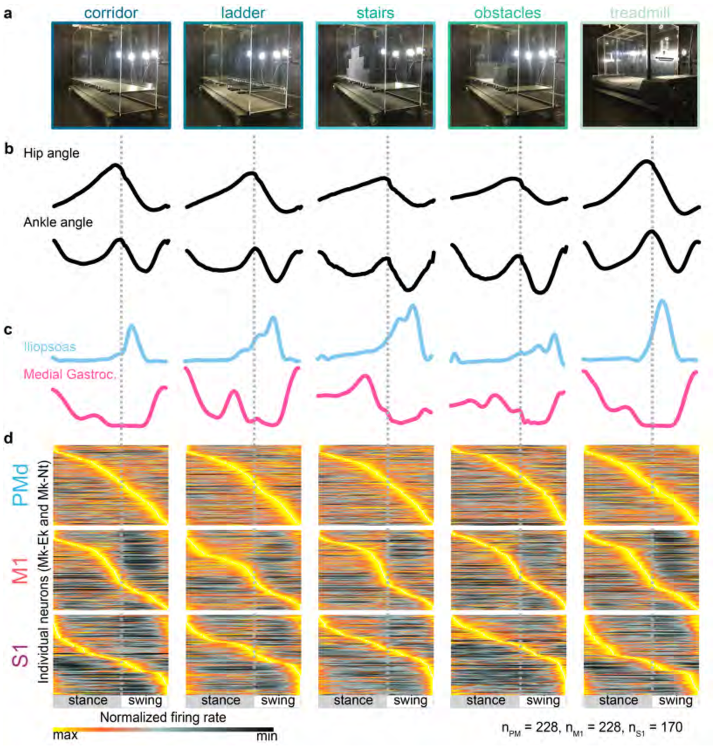

Figure 3.2 | Behavioral recordings

a. Animals were trained to walk over-ground on a corridor, on a horizontal ladder, over a staircase, over obstacles and on a treadmill (3km/h). We performed synchronized recordings of hindlimb kinematics, EMGs (8 muscles), and intracortical recordings of the sensorimotor cortex. **b.** Representative example of averaged kinematic features in Mk-Nt over the gait cycle (295, 312, 124, 208 and 256 steps for corridor, ladder, stairs, obstacles and treadmill, respectively) aligned at stance and swing onset. **c.** Examples of flexor and extensor EMG activity averaged over the gait cycle in Mk-Ek (140, 197, 176, 66 and 320 for corridor, ladder, stairs, obstacles and treadmill, respectively). **d.** Average normalized PMd, M1, and S1 neuronal firing rates along the gait cycle aligned at swing and stance onset for all sessions in monkeys Mk-Ek and Mk-Nt. Individual neurons (rows) are sorted by the timing of peak firing on each task. White dots indicate the phase of peak firing for each neuron in that task.

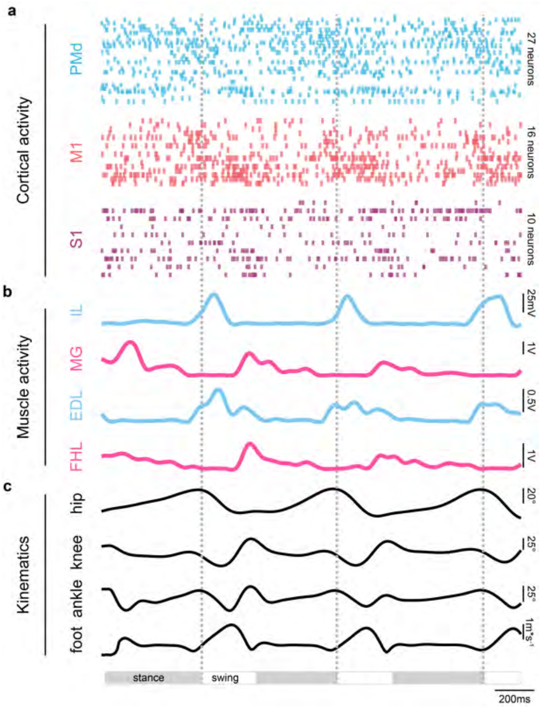

Figure 3.3 | Time-varying cortical, muscle, and kinematic signals used for analysis

Example of a real-time recording in Mk-EK on a treadmill (3km/h) in untethered condition. **a**. Raster plot of 53 single neurons isolated from 3 microelectrode arrays implanted in dorsal premotor cortex (PMd, F2), in primary motor cortex (M1, F1, leg area) and in primary somatosensory cortex (S1, area 1/2). **b**. Example of 4 muscle activity (extensors in pink and flexors in blue) using a chronically implanted recording system. **c.** Kinematic examples of 3 joint angles (hip, knee and ankle) and foot velocity acquired with 8 HD video camera system. Gait phases (stance and swing) were manually marked. IL, iliopsoas; MG, medial gastrocnemius; EDL, extensor digitorum longus; FHL, flexor hallucis longus.

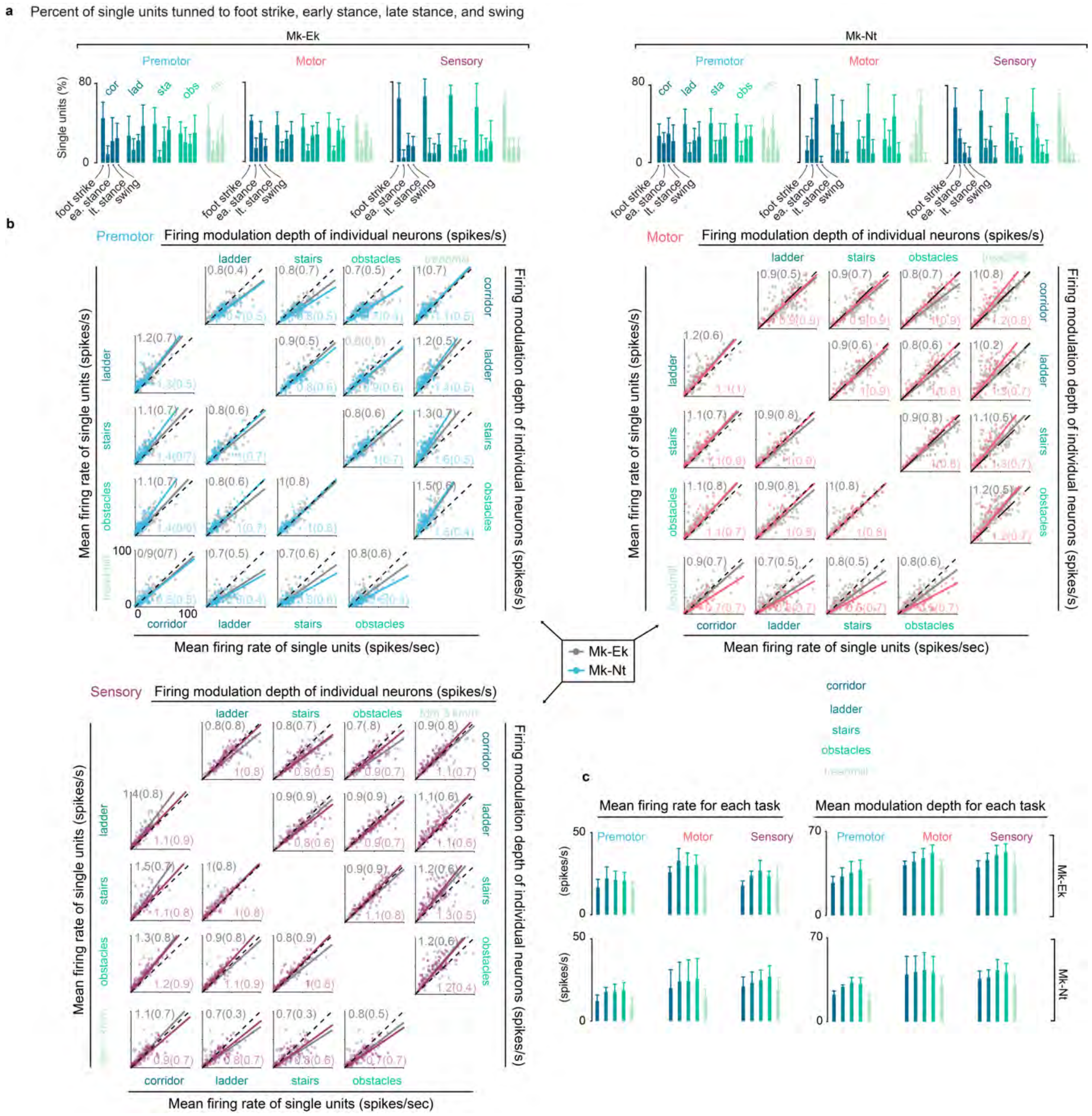

Figure 3.4 | Changes in firing rate and modulation depth with task complexity

a. Percent of all identified single neurons tuned to each four gait phases in PMd, M1, and S1 cortices. **b**. Comparisons in mean firing rate and modulation depth for each single neuron in all task combinations. The black dashed line represents a 1 to 1 relationship between both conditions. The gray and cortex-colored solid lines represent the linear regression line between tasks. The regression coefficient *m* and its respective R^2 value for each monkey's regression line are shown in the bottom-right and top-left corners of each panel $m(R^2)$. **c**. Average firing rate and modulation depth across tasks. Bars: mean ± S.D. across days.

3.3.2. Generalization of neural correlates in locomotion

We studied whether patterns of single-neuron responses were consistent across locomotor tasks. If a cortical region has a high involvement in the planning for the adjustment of task-specific leg movements, we would expect that neural activation patterns identified for locomotor tasks that involve steady locomotion would not translate to planned locomotion tasks. If correct, our hypothesis predicts that the synchronized order of neuronal activation would be conserved when the monkey performed self-paced locomotion along a corridor vs stepping on a treadmill, but not when the monkey walked over ladders, stairs, or obstacles. Moreover, we would expect this observation to be more apparent in cortical regions that are highly involved in planning or preparatory activity (Churchland et al. 2010; Vyas et al. 2018).

We sorted single neurons by the timing of their peak firing in the corridor task and used that same order in the panels for the other tasks, so that each neuron appears in the same vertical position for all panels in **Figure 3.5a**. The order of single-neuron activation was moderately conserved between locomotion along the corridor and the treadmill in M1 and S1 cortices. However, we observed a substantial change in firing rate patterns when the monkey performed locomotor tasks requiring voluntary modifications to stepping as in the ladder, stairs, and obstacles tasks: some neurons that had peak firing at foot-strike on the corridor had peak firing at foot-off during the ladder, and vice-versa. Substantial changes in patterns of neuronal activation across locomotor tasks were more common in PMd.

To quantify observations of changes in neuronal tuning to the gait phase, we computed the correlation coefficient (r) between the average firing rate across each pair of tasks (5 tasks, 10 comparisons per session). For each session, we averaged all neurons within a brain region to generate a mean value for the correlation in neuronal population responses across tasks (**Figure 3.5b**). There was a rostro-caudal increase in average correlation of single neuron activity across tasks. Neuronal responses were significantly less correlated across tasks in PMd than in M1 and S1. For a reference in behavior, the distribution of correlation in kinematics and muscle activity across tasks is shown in **Figure 3.6**. To further understand the amount of change in neuronal tuning across tasks, we identified each neuron's average preferred gait phase during each task and computed the circular standard deviation in preferred gait phase across tasks (**Figure 3.5c**). Similar to correlation, variability in preferred gait phase was higher in PMd than M1 and S1 (no significance for M1 in Mk-Nt).

In agreement with reports by several groups on the increase in firing rate and modulation depth for locomotor tasks requiring accurate control paw placement or limb trajectory (Drew 1988; Beloozerova and Sirota 1993; Widajewicz et al. 1994; Beloozerova et al. 2010; DiGiovanna et al. 2016), we observed both to be higher during planned compared to rhythmic locomotion tasks (**Figure 3.4b**). Firing rate and modulation depth were both higher in M1 and S1 than in PMd (**Figure 3.4c**).

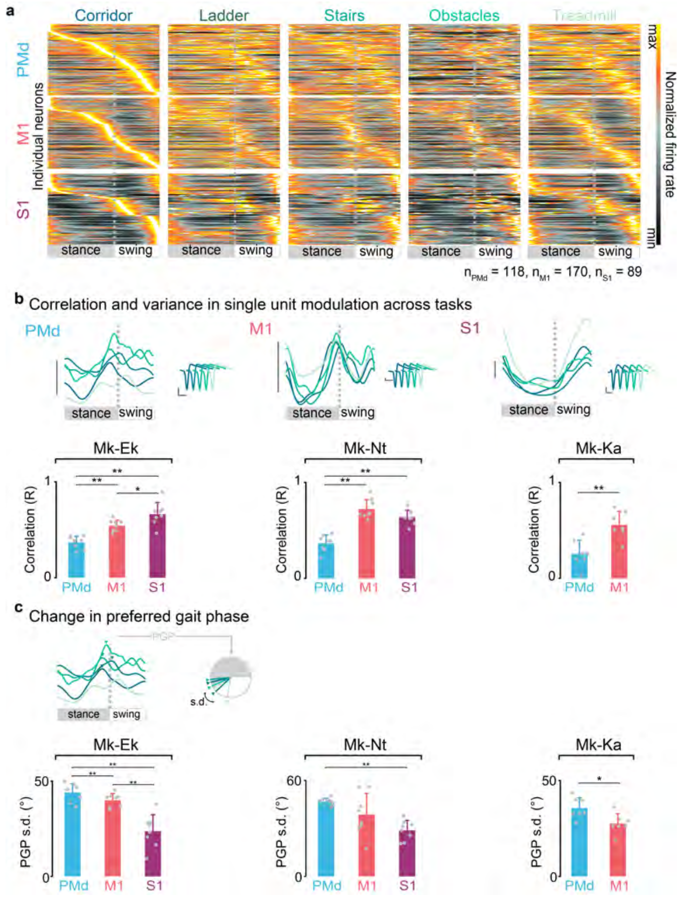

Figure 3.5 | Neural correlates in single neuron activity fail to generalize between rhythmic and planned locomotion

a. Normalized neuronal firing rates aligned at stance and swing onsets and sorted by the timing of peak firing on the corridor task for one monkey (Mk-Ek). Note the substantial changes in neural activity, reflected in changes of gait phase tuning on each neuron. **b**. We computed the Pearson's linear correlation coefficient across tasks. **c**. We identified each neuron's preferred gait phase for each task and computed the circular standard deviation in preferred gait phase across locomotor tasks. Bars: mean ± s.d.. Wilcoxon signed rank test.

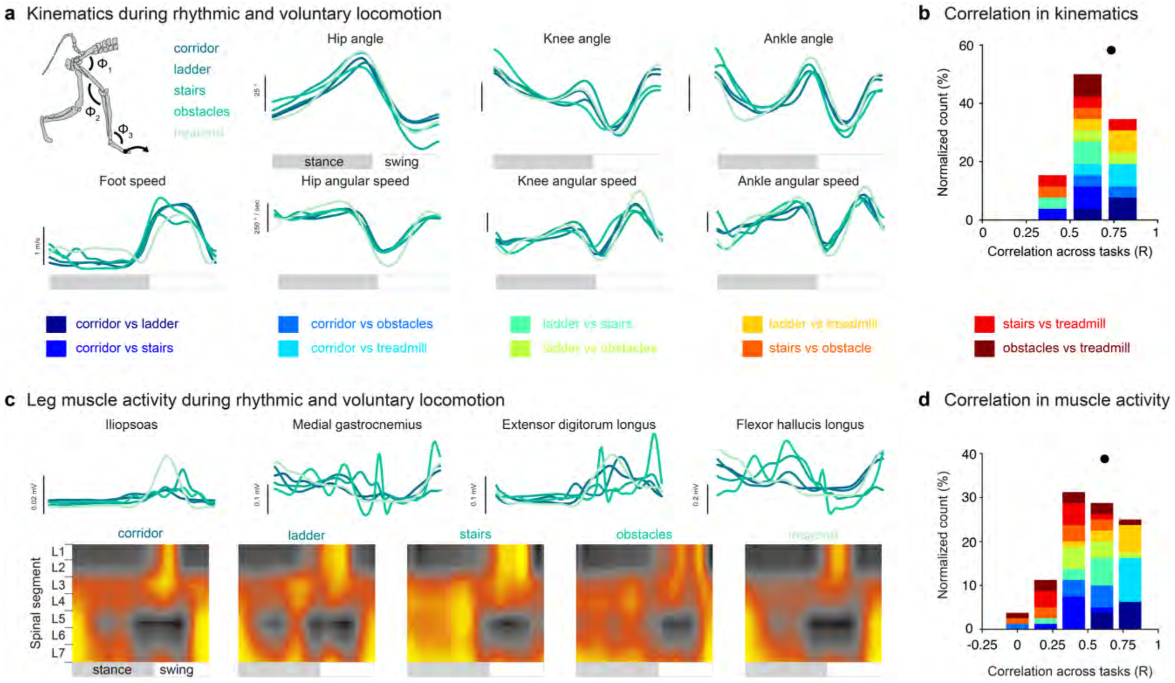

Figure 3.6 | Differences in kinematics and muscle activity across locomotor tasks and phase tuning of single neurons

a. Leg joint angles, angular speed, and foot speed for basic and skilled locomotion tasks. **b**. We computed the Pearson's linear correlation coefficient for each kinematic parameter across two different conditions and averaged correlation coefficients for all parameters to generate the mean correlation between kinematics across two tasks. The gray dotted vertical line indicates the average correlation coefficient when all kinematic parameters are normalized by their within-task correlation. **c**. Leg muscle and spinal segment activity during basic and skilled locomotor tasks. **d**. Analogous analysis for EMG profiles as in **b.**

3.3.3. Similarity of neural manifolds across locomotor tasks

Changes in single neuron correlates across locomotor behaviors revealed differences in the robustness of neural correlates across locomotor tasks. However, the heterogeneity of single-neuron responses can make these results difficult to interpret, and neural inputs to muscle activity and behavior are more likely to be a weighted combination of these neuron responses (Mazor and Laurent 2005; Churchland et al. 2010; Cunningham and Yu 2014). We used dimensionality reduction methods to better understand neural mechanisms that may involve coordination of responses across neurons. For neural population activity and multi-dimensional analyses, we identified neural units through threshold crossings on each electrode. We refer to these as neural units.

To estimate the dimensionality of the neural manifolds for each locomotor task and all tasks combined, we used the method developed by Machens et al. (Machens et al. 2010). We first estimate the variance that can be explained by noise by performing PCA on the estimates of trial-to-trial-variability selecting 1000 random pairs of trials (**Figure 3.7a, 1-2**, Methods). We then performed PCA on the trial-averaged firing rates and subtracted the variance that could be explained by noise (**Figure 3.7a, 3**); thus keeping only the amount of variance that can be attributed to signal. Finally, the number *m* of neural modes needed to explain 95% of the explainable variance was taken as the dimensionality of the dataset (**Figure 3.7a, 4**).

We compared the dimensionality estimates between neural manifolds for individual tasks and those where all tasks during a session were combined (**Figure 3.7b**). We hypothesized that if activity within a cortical area takes place along uniquely aligned neural manifolds for each locomotor task, the dimensionality estimates of datasets with combined tasks should be larger than that of individual tasks. Single-task dimensionalities were relatively low for neural manifolds in all three cortical regions (**Figure 3.7c**, **Figure 3.8**). However, there was a rostro-caudal decrease in the difference between dimensionality estimates of single or combined locomotor tasks (**Figure 3.7d**). Generally, tasks that may require planning (ladder, stairs, obstacles) had a greater contribution towards this increase in dimensionality than steady locomotion tasks (corridor and treadmill, **Figure 3.8b**). Our results suggest that although neural manifolds are low-dimensional for a given task and may reflect the simplicity of locomotor tasks (Gao and Ganguli 2015), PMd and M1 may employ flexible combinations of these neural modes to generate the appropriate gait modifications for each task.

If neural manifolds within a cortical area are well-preserved to generate appropriate movement for a variety of tasks, they would have similar orientations across tasks (Gallego et al. 2018). We tested this theory in the three cortical regions by computing the principal angles (Björck and Golub 1973) between the m-dimensional manifolds for all pairs of tasks during each session (**Figure 3.7f**, Methods). The hypothesis, as postulated by Gallego et al. (Gallego et al. 2018), is that if neural manifolds are similarly oriented across locomotor tasks, the angles between them will be small. In contrast, if a cortex recruits neurons through arbitrary combinations, the neural manifolds for different tasks would not be similarly oriented, and thus, the principal angles between them would not be small.

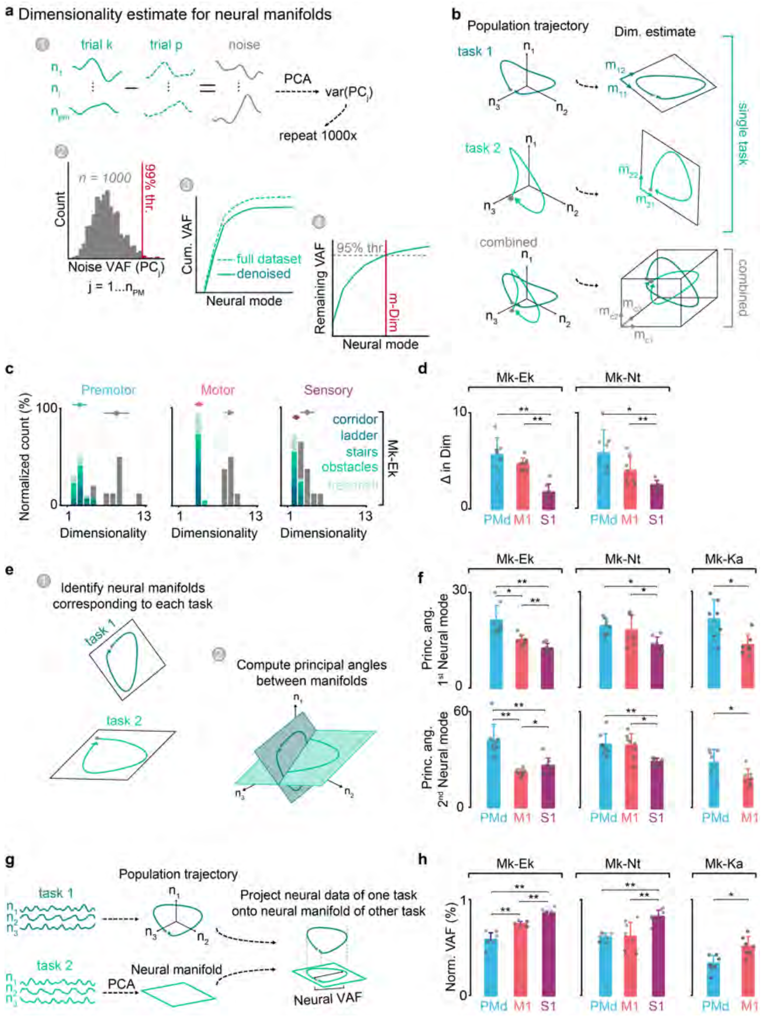

Figure 3.7 | Population activity across tasks is more complex in premotor and motor than in somatosensory cortex

a. Computation of dimensionality estimates for neural manifolds. For each neural mode, we estimated the amount of variance that can be explained by noise and subtracted it from the explained variance for that mode. The dimensionality of a dataset was taken as the number of dimensions needed to explain 95% of the remaining variance. **b.** We compared dimensionality estimates of individual tasks to dimensionality of all tasks combined. We hypothesized that if neural population activity occurs along neural manifolds with different orientations for each task, then the dimensionality of the combined data sets would be greater than that of single tasks. **c**. Dimensionality estimates for individual and combined task datasets for representative monkey Mk-Ek. **d**. Dimensionality estimates for neural population activity in combined datasets. **e**. We computed the principal angles between neural manifolds corresponding to two tasks. **f**. The two leading principal angles between neural manifolds for 5 tasks across 8 days (10 task comparisons each day). **g**. We computed the variance accounted for (VAF) by projecting the neural activity of one task onto the neural manifold of another task. **h**. VAF of normalized by projecting the neural activity of the same task onto its corresponding manifold. Bars: mean ± s.d.

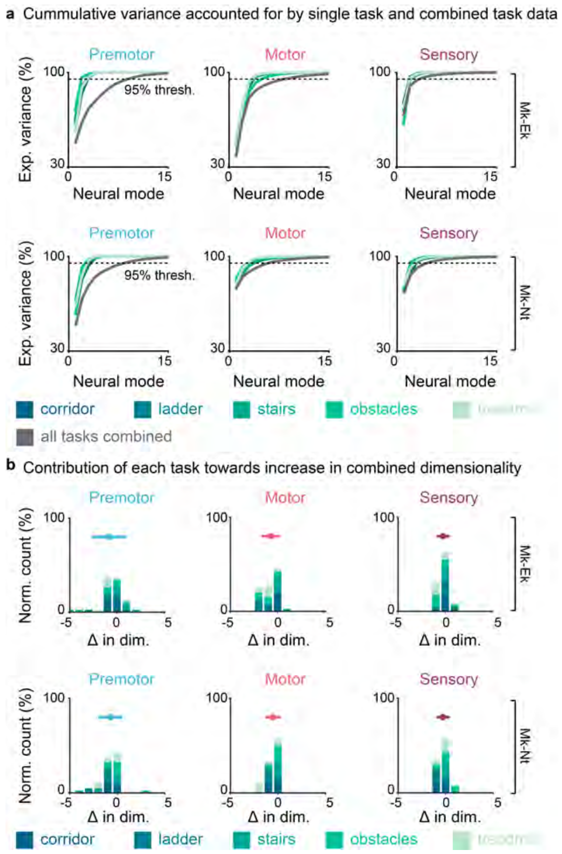

Figure 3.8 | Variance explained by neural manifolds and contribution of each task towards increase in combined dimensionality

a. Cumulative variance explained by principal modes of neural data during five locomotion tasks and all tasks combined. The dimensionality of a dataset was taken as the number of neural modes necessary to explain 95 percent of the explainable (noise removed) variance. **b**. We calculated the dimensionality of the combined conditions after removing one condition from the dataset. We then compared the difference in dimensionality from this reduced dataset to the original dataset with all five conditions.

The two leading principal angles between ten pairs (5 tasks) of task-dependent, *m*-dimensional manifolds averaged across days (gray circles) and sessions (bars) are shown in **Figure 3.7g**. The *m* number of dimensions to compare was determined by the neural manifold of the task with the lowest dimensionality. Neural population activity for different tasks resided within aligned subspaces of the neural manifold in S1. In contrast, neural activation patterns resided within distinct task-dependent subspaces in PMd and, to a lesser extent in M1. As an additional test, we computed the 15 principal angles between the 15-D manifolds (maximum number of combined dimensionality in **Figure 3.7c** except for one day) for all pairs of tasks and compared them to the distribution of angles obtained from a null hypothesis generated with the tensor maximum entropy method (Elsayed et al.

2016) (**Figure 3.9**). Across all sessions, a majority of leading principal angles were below the surrogate significance threshold (dashed line). Note that principal angles in S1 are consistently small across leading neural modes.

To better understand the degree of similarity across manifolds corresponding to different tasks, we projected the neural activity of one task onto the *m*-dimensional neural manifold of another task (**Figure 3.7g**). We then computed the neural variance accounted for (VAF) by this projection and divided it over the VAF of the same neural activity projected onto its corresponding neural manifold (Gallego et al. 2018). There was a rostro-caudal increase in the amount of across-task VAF, with S1 explaining the most VAF across tasks (**Figure 3.7h**).

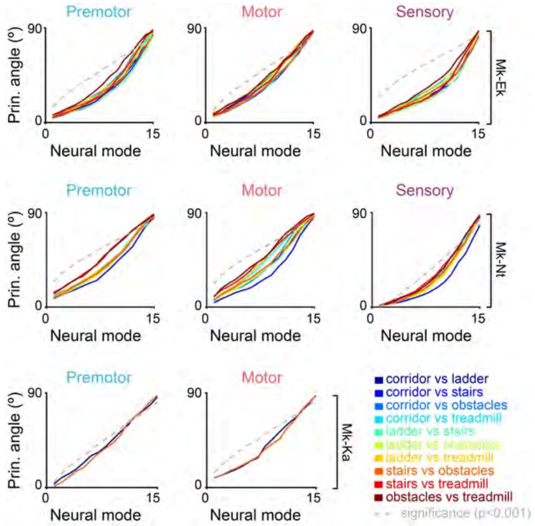

Figure 3. 9 | Similarity across tasks and locomotion subspaces for four monkeys

Average principal angles in motor, premotor, and somatosensory cortices for all locomotor sessions of three monkeys performing more than one task on the same day

3.3.4. Locomotion—and task-dependent—neural correlates in sensorimotor cortex

The rostro-caudal increase in neural correlates' generalization and similarity of neural correlates across tasks may reflect the contribution of each cortical region towards adapting the behavior. Therefore, we expect that there will be a rostro-caudal decrease in the proportion of neural activity that covaries specifically with each task. To test this theory, we used demixed PCA (Kobak et al. 2016) (dPCA) to separate neural population activity into parameter specific averages: a task-independent part that is obtained by averaging the full data over the tasks, and a task-dependent part that is obtained by averaging over the gait cycle (**Figure 3.10a**, Methods). Our hypothesis predicts that a large percentage of neural variance in PMd would be explained by task-dependent information whereas neural variance in M1 and S1 would have a greater contribution from task-independent information.

The time-dependent activation, or latent activity, corresponding to the six leading dPCs for each locomotor task in one representative session of M1 in monkey Mk-Ek is shown in **Figure 3.10b**. The top row shows the latent activity within neural modes that captured task-dependent activity. For example, the sixth dPCA neural mode captures a task-dependent offset between corridor, and treadmill, and stairs and obstacles. This task-dependent offset is present at the stance and swing phases, and may represent some aspect of movement adaptation required for the task. The bottom row in **Figure 3.10b** shows neural modes that capture modulations of the neural activity throughout the gait cycle, irrespective of the locomotor task. Throughout this paper, we refer to these neural modes as the locomotion-related components. Latent activities for the three cortical regions during a representative session are shown in **Figure 3.11**.

Demixed neural modes within each cortex covaried partly with task and locomotion-related components (**Figure 3.10c**). This representation allowed us to highlight several general features of the population activity in the sensorimotor cortex (see 'signal variance' in Methods). A larger amount of variance was captured by condition-independent components in M1 and S1 compared to PMd. For the two monkeys performing 5 tasks in the same day, task-independent activity in PMd only captured about half of the total neural variance (50.7±10.0% for Mk-Ek and 55.1±8.0% for Mk-Nt). The amount of variance captured by task-dependent components depended on the amount of tasks being compared. As a control, we repeated the dPCA analysis in those two monkeys by comparing only corridor vs ladder and stairs vs obstacles. Indeed, the amount of variance captured by task-independent components with only two tasks was higher in PMd, but it was still lower than that captured in M1 and S1 (**Figure 3.12b**). To quantify the amount of task-dependent variance that could be explained by trial-to-trial variability within a task, we performed dPCA on two sets where we randomly selected trials of the same task (**Figure 3.12c**). Task-dependent components in the three cortices explained less than 10% of neural variance.

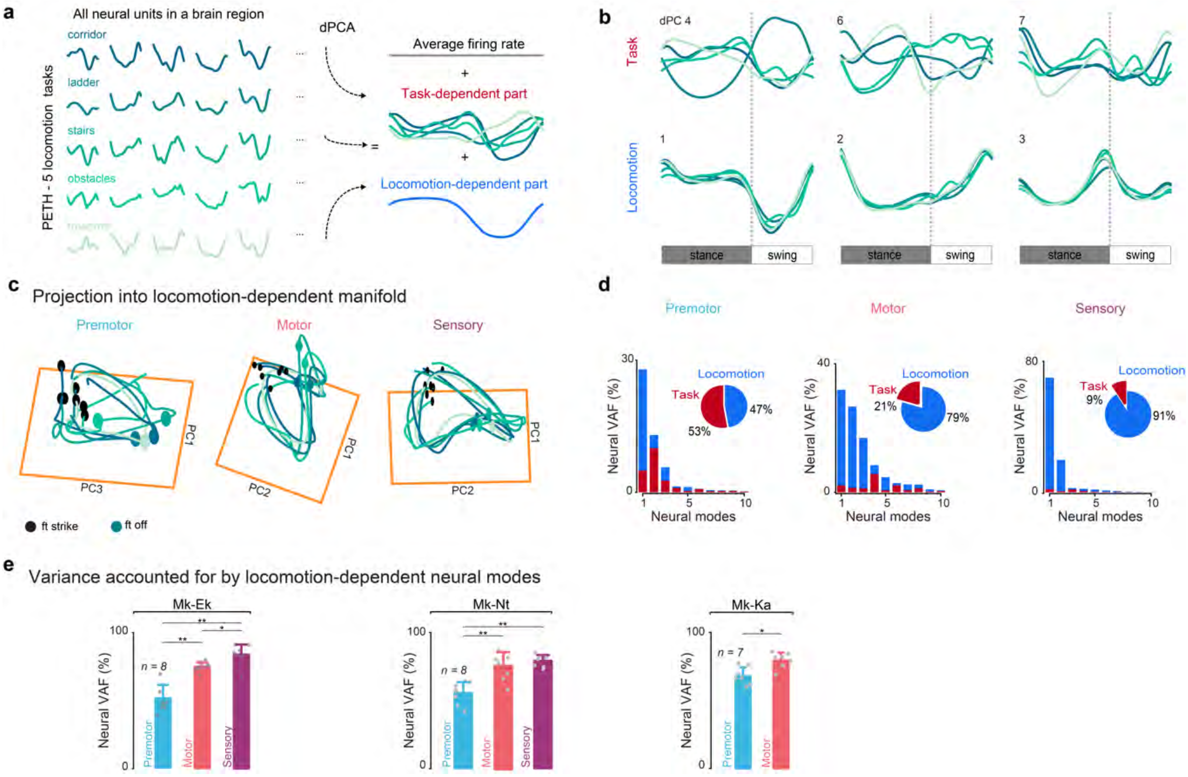

Figure 3.10 | Locomotion and task-related activity of sensorimotor cortex in basic and skilled locomotion

a. Decomposing population activity of one session into task-dependent and task-independent components (dPCA). **b**. Activity of six dPC neural components for each brain region, grouped by the parameter they are most strongly associated with (task-related or locomotion-related). The number of the top left of each panel indicates the ranking of that neural component in terms of VAF. Scale is arbitrary. **c**. Average population trajectories in locomotion-dependent subspace. **d**. Neural variance accounted for (VAF) by each dPC in one session of monkey Mk-Ek. Pie charts indicate how the total variance for one session is split between task and locomotion-dependent parameters. **e**. Total VAF for task and locomotion-dependent parameters, averaged over all sessions. Wilcoxon signed rank test; Bars: mean ± s.d.

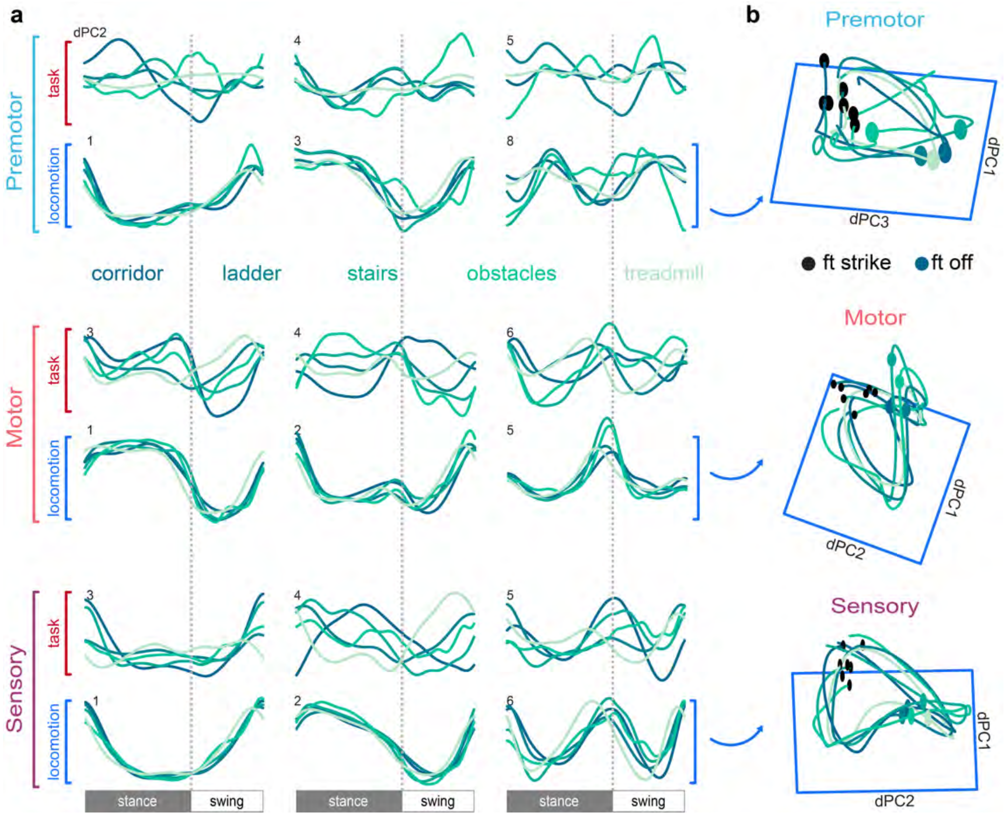

Figure 3. 11 | **Latent activity in top three neural modes**

a. Latent activity in the three task and locomotion-dependent neural modes explaining the highest amounts of variance for a representative session in monkey Mk-Ek. Latent activities are aligned at foot-strike and foot-off. Neural modes, indicated by the number on the top-left corner of each panel, are numbered by descending magnitudes of explained variance. **b**. Three-dimensional projections of neural population trajectories for five locomotor tasks in the locomotion subspace.

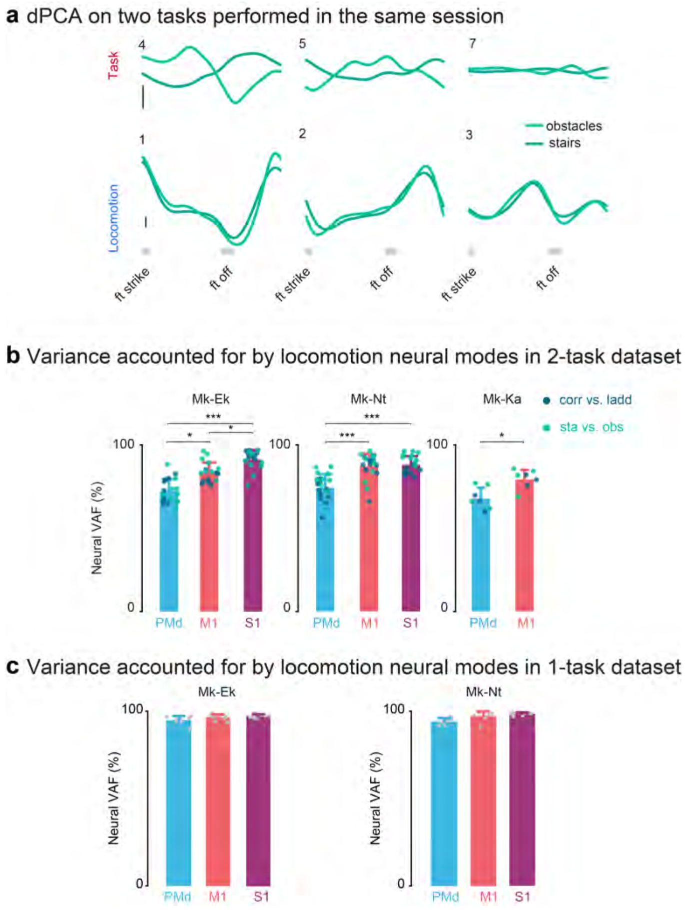

Figure 3.12 | dPCA controls

a. We repeated the dPCA decomposition into task and locomotion related neural components when the three monkeys performed two tasks: stairs and obstacles or corridor and ladder. Activity of first three task-dependent and locomotion-dependent dPCA neural components in motor cortex for monkey Mk-Ka. **b**. Total variance accounted for by locomotion-dependent components, averaged over all two-task sessions for monkeys Mk-Ek, Mk-Nt, and Mk-Ka. **c**. We created surrogate datasets of the same task where trials of the same task were randomly selected and computed the variance that could be accounted for by the locomotion-dependent components. Two-sided Wicoxon's rank-sum test; bars: mean ± s.d.

The strong similarity in the neural activity and orientation of the neural manifolds suggests that S1 structure is well preserved across rhythmic and skilled locomotor tasks. In contrast, PMd may generate unique dynamics for each task, as evidenced by low correlations in single unit activity across tasks, increased dimensionality estimates in the combination of tasks, and an equal amount of variance explained by task and locomotion-related components.

3.3.5. Generalized decoders with task-independent neural manifolds.

Muscle activity and kinematics can be reasonably well predicted based on brain-decoding algorithms that are trained on the same task that they are to be tested (Fitzsimmons 2009; Weiguo Song et al. 2009; Rigosa et al. 2015; Xing et al. 2019). However, decoding performance may degrade for locomotion tasks that require substantially different patterns of cortical activity (**Figure 3.2a**). Latent activity in the locomotion-dependent subspace for all three cortical regions remained stable across conditions (**Figure 3.11**) and appeared to resemble EMG and kinematic activity during locomotion (**Figure 3.6 a-c**). We first asked whether this type of locomotion-dependent activity captured valuable contributions of neural activity to behavior and if so, whether it remained stable across locomotor tasks. For each cortical region, we build a linear discriminant analysis (LDA) based classifier

(Capogrosso et al. 2016) to predict the occurrence of foot-strike and foot-off gait events in 'real time' (**Figure 3.13a**, Methods). Our hypothesis predicts that if neural activity within a cortical region captures robust, task-independent contributions of neural activity onto behavior, decoding performance in generalization may be improved by projecting neural activity of a single task onto the low-dimensional locomotion-dependent subspace for decoding training and testing. Decoding generalization performance in PMd and M1 was higher when using the locomotion-dependent subspace projection compared to using the full neural space or the task-independent projection (**Figure 3.13b**). These results suggest the locomotion manifolds in PMd and M1 carry important information about behavior that remains stable across tasks.

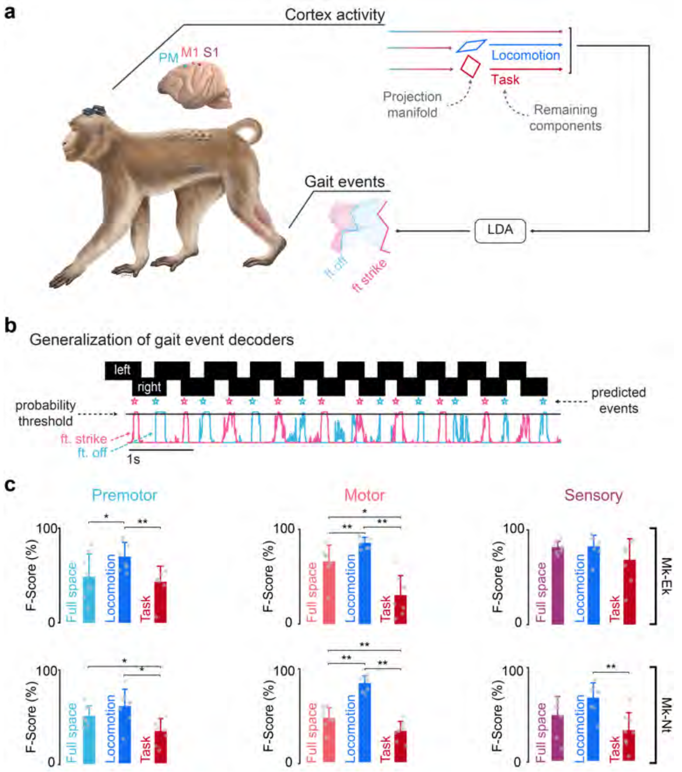

Figure 3.13 | Robust decoding of gait parameters across basic and skilled locomotion

a. We trained decoders to predict foot-strike and foot-off gait events. We compared the decoding performance of decoders using the full neural space or a projection onto the locomotion-dependent or task-dependent manifolds **b**. Real and predicted foot-strike and foot-off gait events. **c**. F-scores in generalization of gait event predictors for decoders trained on a single task and tested on all other tasks. Wilcoxon signed rank test; Bars: mean ± s.d.

3.4. DISCUSSION

The role of the sensorimotor cortex in the control of gait is assumed to play a larger role in humans than in quadrupedal mammals (Eidelberg 1981; Fedirchuk et al. 1998; Nielsen 2003). Understanding how the different areas within the cortex interact towards the natural control of gait remains therefore a significant question in neuroscience. Previous studies of cortical control of locomotion have shown that cortical neuronal activity in PMd (Fitzsimmons 2009; Churchland et al. 2012; Nakajima et al. 2019; Nordin et al. 2019), M1 (Armstrong and Drew 1984b; Beloozerova et al. 2003; D Foster et al. 2014; Yin et al. 2014; DiGiovanna et al. 2016; Xing et al. 2019), and S1 (Fitzsimmons 2009; Favorov et al. 2015; Ayaz et al. 2019; Karadimas et al. 2019) covaries with different parameters during locomotion. These regions in the sensorimotor cortex are believed to be crucial for the coordinated adjustment of leg movements associated with volitional modifications of gait such as controlling speed (Armstrong and Drew 1984a; D Foster et al. 2014; Xing et al. 2019), walking along uneven terrain (Beloozerova et al. 2005; Rigosa et al. 2015; DiGiovanna et al. 2016), or avoiding obstacles (Drew 1988; Beloozerova and Sirota 1993; Widajewicz et al. 1994; Drew et al. 2002; Nakajima et al. 2019; Nordin et al. 2019). Indeed, we observed that single neurons were phase-locked to the different phases of gait in all locomotor tasks (**Figure 3.2d**), and in agreement with previous studies, there was an overall, although modest, increase in firing rate and modulation depth of single unit activity for skilled compared to rhythmic tasks (**Figure 3.4b**). However, as apparent in this figure and previously observed by other groups, as the number of tasks and recorded neurons increases, it becomes increasingly difficult to extract meaningful, interpretable structure from the activity of individual neurons (Cunningham and Yu 2014). Moreover, the initial difference in firing rate between distinct cortical areas for the same task (**Figure 3.4c**) makes understanding their relative contributions towards the voluntary control of locomotion by comparing single unit firing rates across cortices quite challenging.

Rather than attempting to determine the independent encoding of functions by the activity of single neurons (Thach 1978; Kakei et al. 1999), we studied how populations of neurons in the sensorimotor cortex behave during rhythmic and skilled locomotion. We extracted the low-dimensional portions of the full neural space explored by the neural populations for individual tasks, and measured whether the structure of these neural manifolds is preserved across tasks. We reported the first comparison across neural manifolds in the sensorimotor cortex associated with a variety of locomotion tasks. Our results suggest that dorsal premotor, primary motor, and somatosensory cortices perform unique neural computations with distinct levels of contributions towards the volitional modification of the gait cycle: neural manifolds in S1 were largely preserved across tasks; although population activity in M1 resided within task-dependent subspaces, most of the neural variance was captured by neural modes whose activity was virtually the same regardless of task; neural activation patterns in PMd also resided within task-dependent subspaces, however the amount of neural variance that was specific for each task and the amount that remained the same were virtually the same.

The different cortical regions in the sensorimotor cortex may play unique yet complementary roles towards the proactive modification of the gait cycle. Based on our results and previous reports on the role of each region towards cortical control of movement, we believe that M1 takes an active part in the generation and control of the rhythmic activation of spinal locomotor circuits to generate movement (Christensen et al. 2000), PMd plays a large role in the task-specific planning—and M1 in the execution—of gait modifications (Nakajima et al. 2019; Nordin et al. 2019), and S1 integrates peripheral information about the locomotor state (Christensen et al. 2000). These results provide new insight into how planned locomotion is generated by the different regions within the sensorimotor cortex.

3.4.1. Simplicity of cortical population activity for locomotion

A significant portion of the variability in the activity of populations of neurons is captured by a set of low-dimensional neural modes (Gallego et al. 2017) that can be obtained through dimensionality reduction methods (Mazor and Laurent 2005; Shenoy et al. 2013). We found that population activity in PMd, M1, and S1 occupied low-dimensional neural manifolds during both rhythmic and skilled locomotion tasks (2 to 4 dimensions, **Figure3.7c**, **Figure3.8a**). For comparison, dimensionality estimates for PMd and M1 during center-out reaching in *Macaca mulatta* monkeys have previously been reported as 14 and 8.5 dimensions respectively (Perich et al. 2018). The theory that limiting behavior complexity constraints the dimensionality of neural manifolds (Gao and Ganguli 2015) highlights the simplicity of locomotor tasks compared to upper-arm reaching in terms of cortical input.

3.4.2. Low contribution of somatosensory cortex towards voluntary gait modifications

Walking in ever-changing environments requires the continuous integration of proprioceptive, mechanical, cutaneous, and motor output information by the somatosensory cortex (Phillips et al. 1971; Whitsel et al. 1971; Merzenich et al. 1978; Tanji and Wise 1981; Pons et al. 1985; Gardner 1988; Umeda et al. 2019). Although S1 has direct corticospinal pathways to excitatory neurons that modulate the lumbar locomotion networks independently from other supra-spinal centers in mice

(Karadimas et al. 2019), its role in modulating locomotion in primates remains an open question in neuroscience. We found that unlike PMd and M1 where phase-locking of neurons was evenly distributed across the gait cycle, a great proportion of neurons in S1 seem to be tuned to key moments where the gait cycle transitions from stance to swing or vice versa (**Figure 3.2d**, **Figure 3.4a**). Patterns of single neuron activity in S1 were more likely to be preserved (**Figure 3.5**), and the neural manifolds for individual tasks had a high degree of alignment and similarity compared to PMd and M1. Most of the neural variance in S1 was captured by locomotion-dependent components (**Figure 3.10d,e**). However, the lack of improvement in decoder generalization by the projection of S1 activity onto the locomotion-dependent neural modes makes it difficult to whether these neural modes captured relevant contributions of neural activity onto behavior.

Together, our results suggest that S1 plays a small role towards the voluntary adjustment of muscle activity patterns required for gait modification. Somatosensory feedback is nonetheless crucial for the accurate execution of movement by the cortex (Sainburg et al. 1995; Scott et al. 2015). One possibility for this discrepancy is that modifications of gait in response to the requirements of the 5 locomotor tasks are proactive in nature, and probably originate in the central nervous system (Barthélemy et al. 2011). In contrast, we may expect S1 to have a higher involvement in reactive modifications of gait that originate from activation to the peripheral nervous system by the environment, for example during changes in balance (Safavynia and Ting 2013) or terrain friction, or during unexpected movement errors (Perich et al. 2020).

3.4.3. Neural manifolds in motor cortex across rhythmic and skilled locomotion

Related behaviors with distinct muscle activity patterns may be generated by the motor cortex through flexible combinations of a set of well-preserved neural modes (Shenoy et al. 2013; Gallego et al. 2017; 2018; Lara et al. 2018). We observed lower similarities in orientation of the neural manifolds corresponding to the different locomotor tasks in M1 compared to S1 (**Figure 3.7**), indicating that the structure of the neural modes employed during these tasks is less preserved. However, the total neural variance was mostly explained by task-independent neural modes (**Figure 3.10e**). This suggests that although neural population activity in M1 resides within task-dependent neural manifolds across locomotor tasks, there must be a portion of the task-dependent neural manifolds that is shared across all tasks. Conceptually, this would be analogous to two orthogonal planes with a shared axis. While there is a high number of aligned neural modes in S1 as evidenced by the low principal angles in the leading modes (**Figure 3.9a**), the principal angles for the first (leading) neural modes in M1 are small but quickly rise for increasing modes. Our results show that M1 generates the necessary adjustments to the locomotor pattern through flexible activations of neural modes that are mostly preserved across locomotor tasks.

3.4.4. Task-dependent subspaces for locomotion in premotor cortex

Proactive modifications of the gait cycle originate in the central nervous system (Schubert et al. 1999; Bonnard et al. 2002; Farrell et al. 2015; Nordin et al. 2019). However, due the small number of studies in human and non-human primates performed on this topic, much remains to be learned regarding the neural mechanisms underlying proactive gait control (Barthélemy et al. 2011). The activity of single neurons in PMd was strongly task-dependent, as evidenced by their low correlations and high variabilities across tasks (**Figure 3.5**). Neural population activity in PMd resided within low-dimensional neural manifolds that had different orientations for each locomotor task (**Figure 3.7**). Our dPCA analysis revealed that a considerable amount of total variance in PMd was related to neural activity that was specific to each locomotor tasks. These modes therefore likely reflect inputs and outputs to and from PMd, rather than the generic temporal features of locomotion that are present regardless of the task (Perich et al. 2018) (**Figure 3.11**). We believe the high variance captured by task-dependent components might reflect preparatory activity (Churchland et al. 2010; Vyas et al. 2018) by premotor cortex to adjust the locomotion cycle. This interpretation would be in agreement with previous observations that premotor cortex contributes towards the temporal evolution of a planning process to avoid obstacles (Nakajima et al. 2019; Nordin et al. 2019). A remaining open question is how the premotor cortex shares this information with M1 and S1 in order to adjust the gait cycle.

3.4.5. Improvement in generalization and variance explained by task-independent components

We expected that the extraction of task-independent neural activity would lead to an improvement in the decoding generalization performance of the three cortices. However, although projection of neural activity into the locomotion-dependent subspace had a significant improvement in generalization performance for M1, PMd and S1 showed only a slight, sometimes minimal improvement (**Figure 3.13c**). The improvement in generalization might be a reflection of the stability of population activity across locomotor tasks. Compared to M1 and S1, a lower amount of neural variance in PMd was explained by locomotion-dependent components (**Figure 3.10e**). This may explain the lower generalization performance in PMd compared to the other cortices, and the lack of improvement after projection in the locomotion-dependent subspace, which explained only half of the total variance. In contrast, most of the neural variance in S1 was explained by locomotion-dependent components (**Figure 3.10e**), probably due to consistent activation during foot-strike and food-off across tasks (**Figure 3.5a**, **Figure 3.4a**). Therefore, the generalization performance of foot-strike and foot-off events with the full S1 population activity was already quite high, leaving small room for improvements after projection onto the locomotion-dependent subspace. Generalization performance of the full M1 population lies in the middle of PMd and S1, and benefited from a projection onto the low-dimensional locomotion-dependent subspace.

3.4.6. Locomotion-subspace for generalized control of neurotechnologies

Although neural correlates with behavioral parameters during locomotion can be used to train decoders that accurately predict the parameters on the tasks they have been trained on (Fitzsimmons 2009; Weiguo Song et al. 2009; Yin et al. 2014; Rigosa et al. 2015; Xing et al. 2019), decoding models of one type of behavior have not been able to be generalized to other types of behaviors (Umeda et al. 2019). Therefore, it remains difficult to determine whether the neural correlates of a single locomotor task truly capture the fundamental building blocks of the neural activity that control locomotion and whether they differ from the ones that contribute towards the voluntary adjustment to behavior across a wide variety of locomotor tasks (Sussillo et al. 2015; Gallego et al. 2017; Russo et al. 2018). Recorded population activity may include intrinsic computations as well as responses to inputs from other cortical regions or the periphery. In this work, we used dPCA to identify a set of neural modes with robust latent activity across different types of rhythmic and skilled locomotion. These locomotion-dependent neural manifolds likely captured the global temporal evolution (Churchland et al. 2012; Sussillo et al. 2015; Russo et al. 2018) of each cortical region during different types of locomotion. Projecting neural activity onto the locomotion-dependent neural manifold improved decoding performance in tasks that decoders were not explicitly trained on. Although the extraction of this locomotion-dependent neural manifold that can be used to improve generalization performance required monkeys to perform the 5 tasks in the same session, an analysis of what combination of 2 tasks provides significant improvements in generalization may already facilitate the development of decoders that can be used to control neurotechnologies in a variety of non-trained tasks.

Neurotechnologies used to restore function in patients with neuromotor disorders (Ethier et al. 2012; Bouton et al. 2016; Donati et al. 2016; Seanez-Gonzalez et al. 2016; 2017; Biasiucci et al. 2018; Wagner et al. 2018) will need to adapt to the changing environment of everyday life (Shenoy and Carmena 2014). Having a clear understanding of the complex activity patterns of neurons in the different regions of the sensorimotor cortex, and the mechanisms by which their populations of neurons can generate a rich repertoire of behaviors, will allow the development of user-controlled neurotechnologies that can adapt to the ever-changing environments of daily life.

3.5. MATERIAL AND METHODS

All the surgical and behavioral training procedures were described in chapter 2.1, 2.3 and 2.4.

3.5.1. Data pre-processing

Gait events, namely foot-off and foot strike, were manually marked by visual video inspection in MATLAB (Mathworks, USA). Gait cycles were rejected if the duration of the step was longer than 1.5 seconds, and based on gait cycle duration and stance duration relative to the gait cycle with an outlier detection algorithm. Outliers in step and stance duration were detected as exceeding 1.5 times the 75th and 25th interquartile range. In total, there were 295, 312, 124, 208 and 256 steps for corridor, ladder, stairs, obstacles and treadmill at 3km/h, respectively in Mk-Nt, 140, 197, 176, 66 and 320 in Mk-Ek, and 74, 64, 110, and 68, in Mk-Ka. Mk-Ka performed the treadmill task on a separate session. Therefore, Mk-Ka treadmill trials are not included in this analysis.
Kinematic 2D coordinates were obtained using DeepLabCut (Mathis et al. 2018), a pose estimation method based on transfer learning with deep neural networks. Pixel coordinates were then imported into SIMI and combined with a 3D calibration to obtain 3D coordinates of each marker. All kinematic features (joint angles, speed, etc…) were computed as previously described (Courtine et al. 2005a; Capogrosso et al. 2016). EMG signals were band-pass filtered (Butterworth filter at 50-450 Hz, 4th order), rectified, and then low-pass filtered (Butterworth filter at 10 Hz, 4th order) to obtain the EMG profiles. To extract the spike events, we first concatenated the data streams of all trials of the 5 conditions and sorted using Offline Sorter (Plexon, Dallas, USA) to identify putative single neurons. Throughout this paper we refer to these as single neurons. For neural population activity and multidimensional analyses (see below), we identified neural units through threshold crossings (-4x RMS) on each electrode. These could include well-isolated single units as well as multi-units. Throughout this paper we refer to these as neural units. For both, single and neural units, we counted the number of spikes occurring in 10ms bins matching the 100 Hz kinematic data and finally we converted them to an instantaneous firing rate by convolution with a Gaussian kernel (50ms standard deviation) to compute a smooth firing rate. Both EMG profiles and firing rates were down-sampled to 1KHz for storing purposes.

We computed the average firing rate of single neurons for each task by normalizing the time of each step as a percentage of the gait cycle. Steps from foot-strike to foot-strike were resampled to a uniform length of 100 samples using the MATLAB function *interp1*. Foot-off events were forced to be at 60% of the gait cycle. This procedure creates firing rate vectors that can be averaged across steps of different durations and can be defined as the discharge rate of the 'average neuron' in the sample during the step (Armstrong and Drew 1984b; Capogrosso et al. 2016). Note that the alignment of firing rate to normalized time does not change peak firing rate or modulation depth. As a precaution, we confirmed that the distribution of foot-off was centered at 60% of the gait cycle for the different conditions (data not shown). The same procedure was used to align and average multiunit activity, kinematics and EMGs.

3.5.2. Single neuron correlates

We computed the preferred gait phase of each neuron was as the time (percent) of peak in average firing rate. Neurons were ordered by their preferred gait phase on each task for plotting in **Figure 3.2d**, so that neurons that fired immediately after foot-strike appear at the top on the panel. In **Figure 3.5a**, neurons were ordered by their preferred gait phase on the corridor task, and the same order was kept on the panels of the other tasks.

For each pair of tasks (5 tasks, 10 comparisons), we computed the correlation coefficient (r) between average neuronal responses measured in each task to obtain a distribution of r across all neurons in a cortex for each day. To compare the change in preferred gait phase across tasks for each cortical region, we computed the circular standard deviation (Zar 1999) using the Circular Statistics Toolbox for MATLAB. Each procedure created a distribution of neural correlates for each cortical region in one session. The average of this distribution represents each gray circle in **Figure 3.5c**. Comparisons across cortical regions were performed by computing the average across sessions (bars ± s.d.) and performing a Wilcoxon signed rank test.

3.5.3. Dimensionality estimates for task-dependent neural manifolds

We estimated the dimensionality of neural manifolds based on the conceptual framework developed by Machens et al (Machens et al. 2010) and then adapted by Perich et al (Perich et al. 2018). We sought to estimate an upper bound of the variance that could be explained by noise using trial-to-trial variation in each unit's firing rate. We first subtracted the activity of a random pair of steps and performed Principal Component Analysis (PCA) on the residuals. We iterated this process 1000 times to build a distribution of eigenvalues for each principal component. The noise-related variance was estimated by a 99% threshold on the obtained distributions. We estimated the dimensionality of the dataset as the number of components needed to explain 95% of the remaining variance after having removed the variance that could be explained by noise (**Figure 3.7a**).

3.5.4. Comparison of task-dependent neural manifolds

To assess whether neural manifolds from the different tasks were similar to each other, we compared the dimensionality estimates of individual tasks to the dimensionality of the 5 tasks combined (**Figure 3.7b**). We performed dimensionality estimates for individual tasks within a session (color bars in **Figure 3.7c**) and all tasks within a session combined (gray bars). To rule out the possibility that the increase in dimensionality was driven by a single task of high dimensionality compared to the others, we performed a control experiment where we computed the dimensionality of the combined-task dataset when a single task was excluded. This method allowed us to understand the contribution of each task towards the increase in dimensionality of the combined dataset (**Figure 3.8b**).

Principal angles (Björck and Golub 1973) are a measure of similarity between two linear subspaces, thus giving an estimate of the linear independence of the two. We computed principal angles between two m-dimensional neural manifolds as implemented by Gallego et al (Gallego et al. 2018). In this process, basis vectors are sequentially ordered from the smallest angle to the biggest. Those basis were computed to minimize the principal angles between the two manifolds. To compute the principal angles between two m dimensional manifolds, we can consider two $m\,x\,t$ matrices A and B with orthonormal basis of their latent space $\boldsymbol{W_a}$, $\boldsymbol{W_b}$ of size $n\,x\,m$, we defined the principal angles as the cos^{-1} of the diagonal elements of matrix C, such that:

$$\boldsymbol{W_a}^{\boldsymbol{T}}\boldsymbol{W_b} = \boldsymbol{P_a}\boldsymbol{C}\boldsymbol{P_b}^{\boldsymbol{T}} \tag{3.1}$$

where $\boldsymbol{P_a}$ and $\boldsymbol{P_b}$ of size $m\,x\,m$ are a new basis of the low-dimensional subspaces minimizing the principal angles. In this example, *m* is the number of dimensions, *n* is the number of recorded neural units, t is the number of time samples. For each comparison of two manifolds, the m number of dimensions being compared was equal to the dimensionality of the task manifold with the lowest dimensionality. As control, we estimated principal angles between all tasks where we set the manifold dimensionalities *m* to be 15 (**Figure 3.9**). This somewhat arbitrary selection of the number of *m* dimensions does not affect the results in principal angles (Gallego et al. 2018). To establish whether these principal angles were significantly small, we generated 10,000 surrogate datasets according to the Tensor Maximum Entropy (TME) method of Elsayed et al (Elsayed and Cunningham 2017). We considered principal angles to be significantly small (with a probability P < 0.001) if they were lower than a threshold defined by the 0.1th percentile of the distributions of principal angles between surrogate datasets. We computed principal angles between real and surrogate datasets in 10 possible combinations of the five tasks.

As an additional method to assess whether two task-dependent manifolds were similarly oriented, we measured how much of the neural variance of one task could be accounted for when we projected the data of that task onto the neural manifold of a different task (Elsayed et al. 2016). We computed the variance accounted for (VAF) when projecting the data of task 1 onto the neural manifold of task 2, and compared it to the VAF when data from task 1 was projected onto the neural manifold of task 1. If the two task-dependent manifolds have almost identical orientations, we would expect the ratio of the two VAF to be close to one. Variance accounted for was computed in terms of the corresponding reconstruction error as described in Gallego et al (Gallego et al. 2018):

$$\boldsymbol{VAF_m} = \frac{||\boldsymbol{X}||^2 - ||\boldsymbol{X} - \boldsymbol{D_m E_m X}||^2}{||\boldsymbol{X}||^2} \tag{3.2}$$

where the *n* by *t* data matrix $\boldsymbol{X}$ matrix contains the trial-averaged data, and matrices $\boldsymbol{E_m}$ and $\boldsymbol{D_m}$ are the encoding and decoding matrices respectively. The $\boldsymbol{E_m}$ matrix projects the original neural data onto the *m*-dimensional neural manifold, and the $\boldsymbol{D_m}$ matrix optimally reconstructs the original neural data from the latent activity.

3.5.5. Separation of neural activity into task-dependent and task-independent components

We used dPCA (Kobak et al. 2016), a linear dimensionality reduction technique, to understand the role of neural activity in the generation of movement across and within locomotor tasks. This approach decomposes neural population activity within each cortical region into parameter specific averages: a task-dependent part that is obtained by averaging population responses for different tasks over the gait cycle, and a task-independent part, obtained by averaging the responses over tasks. The ability to identify a single task-independent neural manifold for all tasks within a session is possible when there is a strong similarity in orientation of the corresponding task-dependent manifolds (Gallego et al. 2018) (**Figure 3.10c**).

We begin by concatenating mean-subtracted, trial-averaged, neural data into a 3-dimensional matrix $\boldsymbol{X}$ of size $n\,x\,p\,x\,100$ where n is the number of channels per cortex, p the number of tasks and 100 the length of the time-wrapped average firing rate for each condition. This matrix $\boldsymbol{X}$ is decomposed into a sum of matrices describing $\boldsymbol{X_\theta}$ behavioral parameters, plus measurement noise $\boldsymbol{X_{noise}}$:

$$\boldsymbol{X} = \boldsymbol{\Sigma_\theta X_\theta} + \boldsymbol{X_{noise}} \tag{3.3}$$

Given the decomposition in (3.3), the loss function of dPCA is given by:

$$\boldsymbol{L_\theta} = \left|\left|\boldsymbol{X_\theta} - \boldsymbol{F_\theta D_\theta X}\right|\right|^2 \tag{3.4}$$

where decoder matrix $\boldsymbol{D_\theta}$ and encoder matrix $\boldsymbol{F_\theta}$ are two distinct linear maps, and the activity to be reconstructed is the one demeaned with respect to one of the parameters. In our case, we have only two behavioral parameters $\boldsymbol{\theta}$: the time (percent of gait) along the trial, and the task. After this marginalization where neural activity is decomposed into parameter-specific averages, it becomes possible to extrapolate the activity related to one parameter by subtracting the average activity of the other parameter. The remaining activity represents the activity related to only one parameter. A detailed description of dPCA for neural population data has been given by Kobak et al (Kobak et al. 2016).

3.5.6. *Signal variance*

Using the decomposition in (3.3), we can split the fraction of explained variance of each dPCA component into the additive contributions of each marginalization. To compute the fraction of variance explained by each dPCA component, we use:

$$\boldsymbol{R^2} = \sum_{\boldsymbol{\theta}} \frac{\left|\left|\boldsymbol{X_\theta}\right|\right|^2 - \left|\left|\boldsymbol{X_\theta} - \mathbf{FD}\boldsymbol{X_\theta}\right|\right|^2}{\left|\left|\boldsymbol{X}\right|\right|^2} \tag{3.5}$$

We used this decomposition to show how the variance explained by each dPCA component is split between each marginalization in **Figure 3.10d**. The pie charts in **Figure 3.10d** show the amount of total variance explained by each marginalization. A detailed description of the estimation of the amount of variance in different marginalizations with subtracted estimated contributions of the residual noise variance has been given by Kobak et al (Kobak et al. 2016).

3.5.7. *Decoding of gait events and generalization across tasks*

To assess whether the locomotion-dependent neural components captured valuable contributions of neural activity to behavior, and whether these remained stable across locomotor tasks, we compared the predictions of decoders based on the full neural space to the predictions of decoders that used as inputs the neural activity projected onto the locomotion-dependent or the task-dependent neural modes. Decoders were trained on the neural and gait event data from the corridor task and evaluated for generalization performance on the 4 other tasks.

We built neural decoders that predicted gait-related motor states from neural activity based on a multiclass regularized linear discriminant analysis (rLDA) (Friedman 1989) decoding model as previously described by our group (Milekovic et al. 2013; Capogrosso et al. 2016).We used the timings of the manually-marked right hindlimb foot-strike (FS) and foot-off (FO) gait events to identify sets of neuronal features that could be used to calibrate the decoders. We derived three motor state classes of neural features based on these two gait events and no event. The amount of neural data taken before each gait event (feature length), the number of bins within it (feature dimension), and the regularization coefficient for each decoder were determined based on a measure of mutual information by cross-validation as previously described by our group (Milekovic et al. 2013). The three motor state classes of optimized neural features were then used to calibrate the rLDA decoder model. We computed the probability of every feature vector in the test dataset to belong to either class using the trained decoder. When one of the motor state probabilities crossed an 80% threshold, that motor state was 'predicted'. There was a refractory period 100ms after a motor state was predicted where it could not be predicted again. Decoding performance was quantified by the mutual information as described by MacKay et al (MacKay-Lyons et al. 2013) and used previously by our group (Milekovic et al. 2013; Capogrosso et al. 2016).

3.6. BIBLIOGRAPHY

Armstrong DM, Drew T. Discharges of pyramidal tract and other motor cortical neurones during locomotion in the cat. J Physiol (Lond). John Wiley & Sons, Ltd; 1984a Jan;346(1):471–95.

Armstrong DM, Drew T. Locomotor-related neuronal discharges in cat motor cortex compared with peripheral receptive fields and evoked movements. J Physiol (Lond). John Wiley & Sons, Ltd; 1984b Jan;346(1):497–517.

Ayaz A, Stäuble A, Hamada M, Wulf M-A, Saleem AB, Helmchen F. Layer-specific integration of locomotion and sensory information in mouse barrel cortex. Nat Commun. Springer US; 2019 Jun 7;:1–14.

Barthélemy D, Grey MJ, Nielsen JB, Bouyer L. Involvement of the corticospinal tract in the control of human gait. Prog Brain Res. Elsevier; 2011;192:181–97.

Beloozerova IN, Farrell BJ, Sirota MG, Prilutsky BI. Differences in movement mechanics, electromyographic, and motor cortex activity between accurate and nonaccurate stepping. Journal of Neurophysiology. 2010 Apr;103(4):2285–300.

Beloozerova IN, Sirota MG. The role of the motor cortex in the control of accuracy of locomotor movements in the cat. J Physiol (Lond). John Wiley & Sons, Ltd; 1993 Feb;461(1):1–25.

Beloozerova IN, Sirota MG, Orlovsky GN, Deliagina TG. Activity of Pyramidal Tract Neurons in the Cat During Postural Corrections. Journal of Neurophysiology. 2005 Apr;93(4):1831–44.

Beloozerova IN, Sirota MG, Swadlow HA. Activity of different classes of neurons of the motor cortex during locomotion. J Neurosci. 2003 Feb 1;23(3):1087–97.

Biasiucci A, Leeb R, Iturrate I, Perdikis S, Al-Khodairy A, Corbet T, et al. Brain-actuated functional electrical stimulation elicits lasting arm motor recovery after stroke. Nat Commun. Springer US; 2018 Jun 14;:1–13.

Björck Å, Golub GH. Numerical methods for computing angles between linear subspaces. Math Comp. 1973;27(123):579–94.

Bonnard M, Camus M, Coyle T, Pailhous J. Task-induced modulation of motor evoked potentials in upper-leg muscles during human gait: a TMS study. Eur J Neurosci. John Wiley & Sons, Ltd; 2002 Dec;16(11):2225–30.

Bouton CE, Shaikhouni A, Annetta NV, Bockbrader MA, Friedenberg DA, Nielson DM, et al. Restoring cortical control of functional movement in a human with quadriplegia. Nature Publishing Group. Nature Publishing Group; 2016 May 1;533(7602):247–50.

Capogrosso M, Milekovic T, Borton D, Wagner F, Moraud EM, Mignardot J-B, et al. A brain–spine interface alleviating gait deficits after spinal cord injury in primates. Nature. Nature Publishing Group; 2016 Nov 10;539(7628):284–8.

Christensen LOD, Johannsen P, Sinkj r T, Petersen N, Pyndt HS, Nielsen JB. Cerebral activation during bicycle movements in man. Exp Brain Res. Springer-Verlag; 2000 Oct 16;135(1):66–72.

Churchland MM, Cunningham JP, Kaufman MT, Foster JD, Nuyujukian P, Ryu SI, et al. Neural population dynamics during reaching. Nature Publishing Group. Nature Publishing Group; 2012 Jun 27;487(7405):51–6.

Churchland MM, Yu BM, Cunningham JP, Sugrue LP, Cohen MR, Corrado GS, et al. Stimulus onset quenches neural variability: a widespread cortical phenomenon. Nature Publishing Group. Nature Publishing Group; 2010 Feb 21;13(3):369–78.

Courtine G, Roy RR, Hodgson J, McKay H, Raven J, Zhong H, et al. Kinematic and EMG determinants in quadrupedal locomotion of a non-human primate (Rhesus). Journal of Neurophysiology. American Physiological Society; 2005a Jun;93(6):3127–45.

Courtine G, Roy RR, Raven J, Hodgson J, McKay H, Yang H, et al. Performance of locomotion and foot grasping following a unilateral thoracic corticospinal tract lesion in monkeys (Macaca mulatta). Brain. Oxford University Press; 2005b Oct;128(Pt 10):2338–58.

Cunningham JP, Yu BM. Dimensionality reduction for large-scale neural recordings. Nat Neurosci. 2014 Aug 24;17(11):1500–9.

D Foster J, Nuyujukian P, Freifeld O, Gao H, Walker R, I Ryu S, et al. A freely-moving monkey treadmill model. J Neural Eng. IOP Publishing; 2014 Jul 4;11(4):046020–15.

DiGiovanna J, Dominici N, Friedli L, Rigosa J, Duis S, Kreider J, et al. Engagement of the Rat Hindlimb Motor Cortex across Natural Locomotor Behaviors. J Neurosci. Society for Neuroscience; 2016 Oct 5;36(40):10440–55.

Donati ARC, Shokur S, Morya E, Campos DSF, Moioli RC, Gitti CM, et al. Long-Term Training with a Brain-Machine Interface-Based Gait Protocol Induces Partial Neurological Recovery in Paraplegic Patients. Sci Rep. Nature Publishing Group; 2016 Jul 25;6(1):1–16.

Drew T. Motor cortical cell discharge during voluntary gait modification. Brain Research. 1988 Aug 2;457(1):181–7.

Drew T, Jiang W, Widajewicz W. Contributions of the motor cortex to the control of the hindlimbs during locomotion in the cat. Brain Res Brain Res Rev. 2002 Oct;40(1-3):178–91.

Dum RP, Strick PL. The origin of corticospinal projections from the premotor areas in the frontal lobe. Journal of Neuroscience. 1991 Mar;11(3):667–89.

Elsayed GF, Cunningham JP. Structure in neural population recordings: an expected byproduct of simpler phenomena? Nat Neurosci. 2017 Aug 7;20(9):1310–8.

Elsayed GF, Lara AH, Kaufman MT, Churchland MM, Cunningham JP. Reorganization between preparatory and movement population responses in motor cortex. Nat Commun. Nature Publishing Group; 2016 Oct 27;7(1):13239–15.

Ethier C, Oby ER, Bauman MJ, Miller LE. Restoration of grasp following paralysis through brain-controlled stimulation of muscles. Nature. Nature Publishing Group; 2012 May 9;485(7398):368–71.

Farrell BJ, Bulgakova MA, Sirota MG, Prilutsky BI, Beloozerova IN. Accurate stepping on a narrow path: mechanics, EMG, and motor cortex activity in the cat. Journal of Neurophysiology. 2015 Nov;114(5):2682–702.

Favorov OV, Nilaweera WU, Miasnikov AA, Beloozerova IN. Activity of somatosensory-responsive neurons in high subdivisions of SI cortex during locomotion. J Neurosci. 2015 May 20;35(20):7763–76.

Fetz EE, Perlmutter SI, Prut Y, Seki K, Votaw S. Roles of primate spinal interneurons in preparation and execution of voluntary hand movement. Brain Res Brain Res Rev. 2002 Oct;40(1-3):53–65.

Fitzsimmons NA. Extracting kinematic parameters for monkey bipedal walking from cortical neuronal ensemble activity. Front Integr Neurosci. Frontiers; 2009;3:1–19.

Friedman JH. Regularized Discriminant Analysis. Journal of the American Statistical Association. 1989 Mar;84(405):165–75.

Fukuyama H, Ouchi Y, Matsuzaki S, Nagahama Y, Yamauchi H, Ogawa M, et al. Brain functional activity during gait in normal subjects: a SPECT study. Neuroscience Letters. 1997 Jun 13;228(3):183–6.

Gallego JA, Perich MG, Miller LE, Solla SA. Neural Manifolds for the Control of Movement. Neuron. 2017 Jun 7;94(5):978–84.

Gallego JA, Perich MG, Naufel SN, Ethier C, Solla SA, Miller LE. Cortical population activity within a preserved neural manifold underlies multiple motor behaviors. Nat Commun. Springer US; 2018 Oct 6;9(1):1–13.

Gao P, Ganguli S. ScienceDirect On simplicity and complexity in the brave new world of large-scale neuroscience. Current Opinion in Neurobiology. Elsevier Ltd; 2015 Jun 1;32:148–55.

Gardner EP. Somatosensory cortical mechanisms of feature detection in tactile and kinesthetic discrimination. Can J Physiol Pharmacol. 1988 Apr;66(4):439–54.

Kakei S, Hoffman DS, Strick PL. Muscle and movement representations in the primary motor cortex. Science. American Association for the Advancement of Science; 1999 Sep 24;285(5436):2136–9.

Karadimas SK, Satkunendrarajah K, Laliberte AM, Ringuette D, Weisspapir I, Li L, et al. Sensory cortical control of movement. Nature Publishing Group. Springer US; 2019 Dec 18;:1–24.

Kaufman MT, Churchland MM, Ryu SI, Shenoy KV. Cortical activity in the null space: permitting preparation without movement. Nat Neurosci. Nature Publishing Group; 2014 Feb 2;17(3):440–8.

Kobak D, Brendel W, Constantinidis C, Feierstein CE, Kepecs A, Mainen ZF, et al. Demixed principal component analysis of neural population data. Elife. 2016 Apr 12;5:9424.

Lara AH, Cunningham JP, Churchland MM. Different population dynamics in the supplementary motor area and motor cortex during reaching. Nat Commun. Nature Publishing Group; 2018 Jul 16;9(1):14–6.

Lemon RN. Descending Pathways in Motor Control. Annu Rev Neurosci. Annual Reviews; 2008 Jul;31(1):195–218.

Machens CK, Romo R, Brody CD. Functional, But Not Anatomical, Separation of "What" and “When” in Prefrontal Cortex. Journal of Neuroscience. 2010 Jan 6;30(1):350–60.

MacKay-Lyons M, McDonald A, Matheson J, Eskes G, Klus M-A. Dual Effects of Body-Weight Supported Treadmill Training on Cardiovascular Fitness and Walking Ability Early After Stroke. Neurorehabilitation and Neural Repair. 7 ed. 2013 Apr 4;27(7):644–53.

Mathis A, Mamidanna P, Cury KM, Abe T, Murthy VN, Mathis MW, et al. DeepLabCut: markerless pose estimation of user-defined body parts with deep learning. Nat Neurosci. Springer US; 2018 Aug 27;21(9):1–12.

Mazor O, Laurent G. Transient Dynamics versus Fixed Points in Odor Representations by Locust Antennal Lobe Projection Neurons. Neuron. 2005 Nov;48(4):661–73.

McCrimmon CM, Wang PT, Heydari P, Nguyen A, Shaw SJ, Gong H, et al. Electrocorticographic Encoding of Human Gait in the Leg Primary Motor Cortex. Cereb Cortex. 5 ed. 2017 Jul 11;28(8):2752–62.

Merzenich MM, Kaas JH, Sur M, Lin CS. Double representation of the body surface within cytoarchitectonic areas 3b and 1 in “SI” in the owl monkey (Aotus trivirgatus). J Comp Neurol. John Wiley & Sons, Ltd; 1978 Sep 1;181(1):41–73.

Milekovic T, Ball T, Schulze-Bonhage A, Aertsen A, Mehring C. Detection of Error Related Neuronal Responses Recorded by Electrocorticography in Humans during Continuous Movements. Foffani G, editor. PLoS ONE. 2013 Feb 1;8(2):e55235–20.

Muir GD, Whishaw IQ. Complete locomotor recovery following corticospinal tract lesions: measurement of ground reaction forces during over-ground locomotion in rats. Behav Brain Res. 1999 Aug;103(1):45–53.

Nakajima T, Fortier-Lebel N, Drew T. Premotor Cortex Provides a Substrate for the Temporal Transformation of Information During the Planning of Gait Modifications. Cerebral Cortex. 5 ed. 2019 Mar 16;504:17–27.

Nordin AD, Hairston WD, Ferris DP. Human electrocortical dynamics while stepping over obstacles. Sci Rep. Springer US; 2019 Mar 8;9(1):1–12.

Perich MG, Conti S, Badi M, Bogaard A, Barra B, Wurth S, et al. Motor cortical dynamics are shaped by multiple distinct subspaces during naturalistic behavior. bioRxiv. Cold Spring Harbor Laboratory; 2020 Aug 3;94:2020.07.30.228767.

Perich MG, Gallego JA, Miller LE. A Neural Population Mechanism for Rapid Learning. Neuron. Elsevier Inc; 2018 Oct 16;100(4):1–21.

Phillips CG, Powell TP, Wiesendanger M. Projection from low-threshold muscle afferents of hand and forearm to area 3a of baboon's cortex. J Physiol (Lond). 1971 Sep;217(2):419–46.

Pons TP, Garraghty PE, Cusick CG, Kaas JH. The somatotopic organization of area 2 in macaque monkeys. J Comp Neurol. 1985 Nov 22;241(4):445–66.

Prut Y, Fetz EE. Primate spinal interneurons show pre-movement instructed delay activity. Nature. Nature Publishing Group; 1999 Oct 7;401(6753):590–4.

Rathelot J-A, Strick PL. Muscle representation in the macaque motor cortex: an anatomical perspective. Proc Natl Acad Sci USA. National Acad Sciences; 2006 May 23;103(21):8257–62.

Rigosa J, Panarese A, Dominici N, Friedli L, van den Brand R, Carpaneto J, et al. Decoding bipedal locomotion from the rat sensorimotor cortex. J Neural Eng. IOP Publishing; 2015 Aug 29;12(5):1–16.

Russo AA, Bittner SR, Perkins SM, Seely JS, London BM, Lara AH, et al. Motor Cortex Embeds Muscle-like Commands in an Untangled Population Response. Neuron. Elsevier Inc; 2018 Feb 21;97(4):953–8.

Safavynia SA, Ting LH. Sensorimotor feedback based on task-relevant error robustly predicts temporal recruitment and multidirectional tuning of muscle synergies. Journal of Neurophysiology. 2013 Jan 1;109(1):31–45.

Sainburg RL, Ghilardi MF, Poizner H, Ghez C. Control of limb dynamics in normal subjects and patients without proprioception. Journal of Neurophysiology. 1995 Feb;73(2):820–35.

Schubert M, Curt A, Colombo G, Berger W, Dietz V. Voluntary control of human gait: conditioning of magnetically evoked motor responses in a precision stepping task. Exp Brain Res. Springer-Verlag; 1999 Jun;126(4):583–8.

Scott SH, Cluff T, Lowrey CR, Takei T. Feedback control during voluntary motor actions. Current Opinion in Neurobiology. 2015 Aug;33:85–94.

Seanez-Gonzalez I, Pierella C, Farshchiansadegh A, Thorp E, Wang X, Parrish T, et al. Body-Machine Interfaces after Spinal Cord Injury: Rehabilitation and Brain Plasticity. Brain Sciences. Multidisciplinary Digital Publishing Institute; 2016 Dec;6(4):61–19.

Seanez-Gonzalez I, Pierella C, Farshchiansadegh A, Thorp EB, Abdollahi F, Pedersen JP, et al. Static Versus Dynamic Decoding Algorithms in a Non-Invasive Body-Machine Interface. IEEE Trans Neural Syst Rehabil Eng. 2017 Jul;25(7):893–905.

Shenoy KV, Carmena JM. Combining Decoder Design and Neural Adaptation in Brain-Machine Interfaces. Neuron. Elsevier Inc; 2014 Nov 19;84(4):665–80.

Shenoy KV, Sahani M, Churchland MM. Cortical Control of Arm Movements: A Dynamical Systems Perspective. Annu Rev Neurosci. 2013 Jul 8;36(1):337–59.

Sussillo D, Churchland MM, Kaufman MT, Shenoy KV. A neural network that finds a naturalistic solution for the production of muscle activity. Nat Neurosci. 2015 Jun 15;18(7):1025–33.

Tanji J, Wise SP. Submodality distribution in sensorimotor cortex of the unanesthetized monkey. Journal of Neurophysiology. 1981 Mar;45(3):467–81.

Thach WT. Correlation of neural discharge with pattern and force of muscular activity, joint position, and direction of intended next movement in motor cortex and cerebellum. Journal of Neurophysiology. 1978 May;41(3):654–76.

Umeda T, Koizumi M, Katakai Y, Saito R, Seki K. Decoding of muscle activity from the sensorimotor cortex in freely behaving monkeys. Neuroimage. Elsevier Ltd; 2019 Aug 15;197:512–26.

Vyas S, Even-Chen N, Stavisky SD, Ryu SI, Nuyujukian P, Shenoy KV. Neural Population Dynamics Underlying Motor Learning Transfer. Neuron. Elsevier Inc; 2018 Mar 7;97(5):1177–1186.e3.

Wagner FB, Mignardot J-B, Le Goff-Mignardot CG, Demesmaeker R, Komi S, Capogrosso M, et al. Targeted neurotechnology restores walking in humans with spinal cord injury. Nature Publishing Group. Springer US; 2018 Oct 24;563(7729):1–29.

Weiguo Song, Ramakrishnan A, Udoekwere UI, Giszter SF. Multiple Types of Movement-Related Information Encoded in Hindlimb/Trunk Cortex in Rats and Potentially Available for Brain–Machine Interface Controls. IEEE Trans Biomed Eng. 2009 Oct 13;56(11):2712–6.

Whitsel BL, Dreyer DA, Roppolo JR. Determinants of body representation in postcentral gyrus of macaques. Journal of Neurophysiology. 1971 Nov;34(6):1018–34.

Widajewicz W, Kably B, Drew T. Motor cortical activity during voluntary gait modifications in the cat. II. Cells related to the hindlimbs. Journal of Neurophysiology. 1994 Nov;72(5):2070–89.

Xing D, Aghagolzadeh M, Truccolo W, Borton D. Low-Dimensional Motor Cortex Dynamics Preserve Kinematics Information During Unconstrained Locomotion in Nonhuman Primates. Front Neurosci. Frontiers; 2019 Oct 4;13:555–12.

Yin M, Borton DA, Komar J, Agha N, Lu Y, Li H, et al. Wireless neurosensor for full-spectrum electrophysiology recordings during free behavior. Neuron. 2014 Dec 17;84(6):1170–82.

Zar JH. Biostatistical Analysis. Pearson Education India. 1999.

– PART 4 –

TOWARDS PERSONALIZED NEUROPROSTHETICS FOR SPINAL CORD INJURY

4.1. INTRODUCTION

In the context of brain-machine interfaces (BMIs), fundamental knowledge described in the previous chapter might be useful for building brain decoders that predict behavioral parameters. Such approach has already been carried out in a nonhuman primate (NHP) model of spinal cord injury (SCI) by our laboratory (Capogrosso et al. 2016). Brain signals were recorded from M1 and used to train a decoder to predict foot off and foot strike. The gait event detection triggered spatio-temporal spinal stimulation via a dorsal epidural spinal array located below the injury. Therefore, the information, which were normally conveyed by the spinal cord, digitally bypassed the lesion for alleviating gait deficit after SCI (Capogrosso et al. 2016). Along this line, we already built a potential applicable brain decoder (see chapter 3.3.5); however spinal array technology specific to our animals was missing. The available spinal array was designed for other macaque monkey species (Capogrosso et al. 2016) but in an universal fashion (i.e. not subject-specific). We therefore took the advantage of MRI and CT scan facilities access to build personalized neuroprosthetics targeting the lumbosacral spinal cord in a subject-specific manner. In this part, I will describe our effort to develop lumbar spinal cord array in the context of SCI.

4.1.1. Spinal cord injury

Spinal cord injury (SCI) interrupts the communication between the brain and the spinal circuits. The descending cortico-spinal tract and ascending sensory fibers are damaged, leading to the loss of motor function, sensation and autonomic function of body parts innervating by circuits located below the injury. However, the spinal circuits below the injury remain intact and therefore conserve the ability to generate rhythmic motor output (Forssberg et al. 1980; Barbeau and Rossignol 1987). The dormant spinal circuits (Rossignol and Frigon 2011) can nevertheless be reactivated, thus restoring a connection with supraspinal command. This can be achieved by different therapeutic strategies: (1) locomotor training (De Leon et al. 1999); (2) pharmacological treatments (Edgerton et al. 2008); (3) epidural electrical stimulation (EES) of the spinal cord below the injury (Courtine et al. 2008; 2009; van den Brand et al. 2012; Asboth et al. 2018) and (4) combination of the above. EES has already been applied in human patients with stroke or SCI and showed improvement in upper-limb function (Cioni et al. 1989) and locomotion (Wagner et al. 2018).

4.1.2. Epidural electrical stimulation mechanisms

Computational and experimental studies have demonstrated that EES of the spinal cord recruits large diameter afferent fibers carrying proprioceptive information (Capogrosso et al. 2013;

Moraud et al. 2016). These fibers enter the spinal cord via the dorsal roots and their activation modulates the local spinal circuits in accordance with the natural activity from muscle spindle feedback (**Figure 4.1**). Thanks to the local spinal cord circuits, motor output can be appropriately shaped during EES (Courtine et al. 2009; van den Brand et al. 2012; Wenger et al. 2014; Moraud et al. 2016; Wenger et al. 2016).

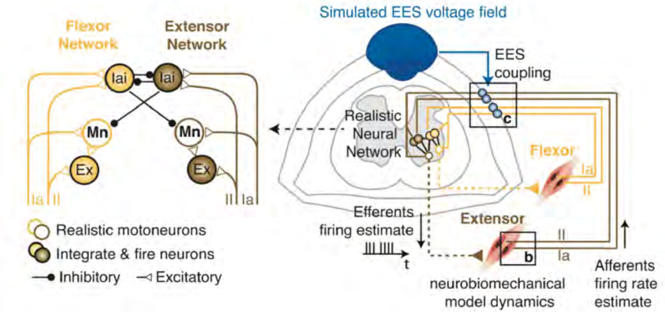
Flexor Network
Extensor Network
Iai
Iai
Mn
Mn
Ex
Ex
Ia
II
II
Ia
Realistic motoneurons
Integrate & fire neurons
Inhibitory
Excitatory
Simulated EES voltage field
EES coupling
c
Realistic Neural Network
Flexor
Ia
II
Efferents firing estimate
t
Extensor
II
b
Ia
neurobiomechanical model dynamics
Afferents firing rate estimate

Figure 4.1 | Biologically realistic neural network of muscle spindle feedback for two antagonist muscles

An electrical current applied on the dorsal aspect of the spinal cord recruits large proprioceptive afferent (Ia). Thanks to the local circuits of the spinal cord, the Ia modulation via EES will generate appropriate motor outputs. Modified from (Moraud et al. 2016).

In clinic, EES can been delivered via commercial epidural arrays (Medtronic) commonly used for the treatment of chronic pain. While this technology showed remarkable effect in human with SCI (Wagner et al. 2018), their efficiency could be improved with tailored array manufactured based on the patient's own morphology (Borton et al. 2013; Kibleur et al. 2020). Since EES recruits preferentially large proprioceptive afferents via the dorsal roots, an electrode placed laterally achieves better selectivity of motoneurons (Greiner et al. 2020). Taken together, we piloted an experiment in nohuman primate to assess the feasibility of personalized lumbar spinal array for EES.

4.2. VARIABILITY IN LUMBAR SPINAL CORD MORPHOLOGY

To ensure a successful experiment, the spinal array must be designed in accordance with the animal size. Based on previous NHPs spinal cord stimulation experiment in our laboratory (Capogrosso et al. 2016), we performed measurements of lumbar spinal cord of rhesus and long-tailed macaque monkeys and assessed their variability.

4.2.1. Inter-species variability

Generally, rhesus macaque monkeys (*Macaca mulatta*) are bigger than long-tailed macaque monkeys (*Macaca fascicularis*) (see chapter 2.4). As our animals were adult female *fascicularis* monkeys, we carried out morphological analysis in four other adult female *fascicularis* monkeys involved in another studies (Borgognon et al. 2017; 2019). After the sacrifice of these animals, the spinal cords were extracted and stored in PFA 4%. First, the longitudinal vertebral lengths (from caudal to rostral dorsal root exit points) were measured with an electronic caliper (150mm, Tesa shop-cal, Tesa Technology). Then, the length of each segment, defined as the root attachment length plus the upper inter-root length (Ko et al. 2004), was measured. Three different experimenters performed the measurements four times. Then, we computed the average among the 12 measures. Finally, the average of the length across monkeys as well as the relation between segmental and vertebral length were plotted. Based on previous data from our laboratory (Capogrosso et al. 2016), we performed the same analysis in order to compare the length of lumbar spinal cord from both species. As expected, the length of the lumbar spinal cord is smaller in *fascicularis* than in *mulatta* monkeys. Moreover, there was a gradual mismatch between the spinal cord segment and the vertebrae as the cauda equina started between L4 and L5 (**Figure 4.2**). Consequently, we could not implant the same array as previously used in (Capogrosso et al. 2016).

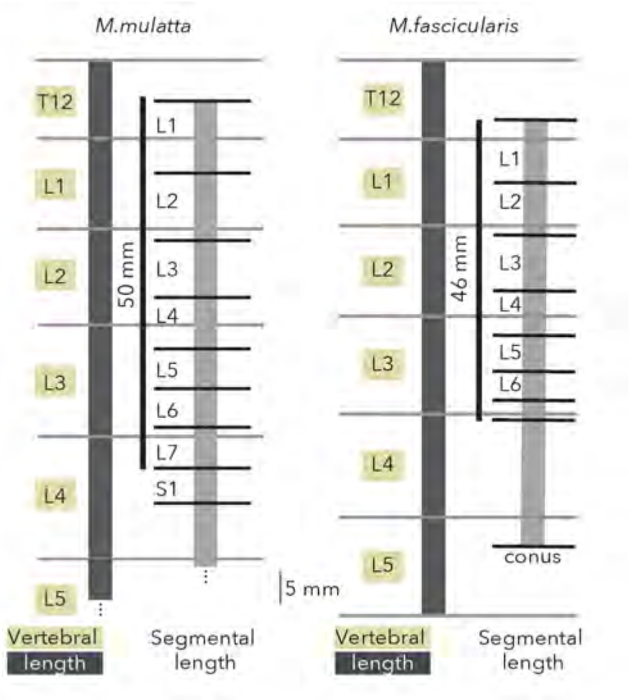

Figure 4.2 | Comparison of lumbar spinal cord and vertebral length between two macaque species

The vertebral length (from caudal to rostral dorsal root exit points) is represented with the black rectangles. The spinal cord segments with the gray rectangles. Left panel: representation of vertebral and spinal segment lengths in rhesus macaque monkeys (*Macaca mulatta*). Right panel: representation of vertebral and spinal segment lengths in long-tailed macaque monkeys (*Macaca fascicularis*). Note the that only the rostro-caudal length is scaled in this graph. The width proportions do not reflect the real size.

4.2.2. Inter-individual variability

The first idea was to develop an universal spinal array for *fascicularis* monkeys. We thus acquired MRI and CT scans as previously described in chapter 2.4 of our animals. We measured the ventral vertebral length in the longitudinal (i.e. sagittal) axis and the horizontal spinal cord width (**Figure 4.3**).

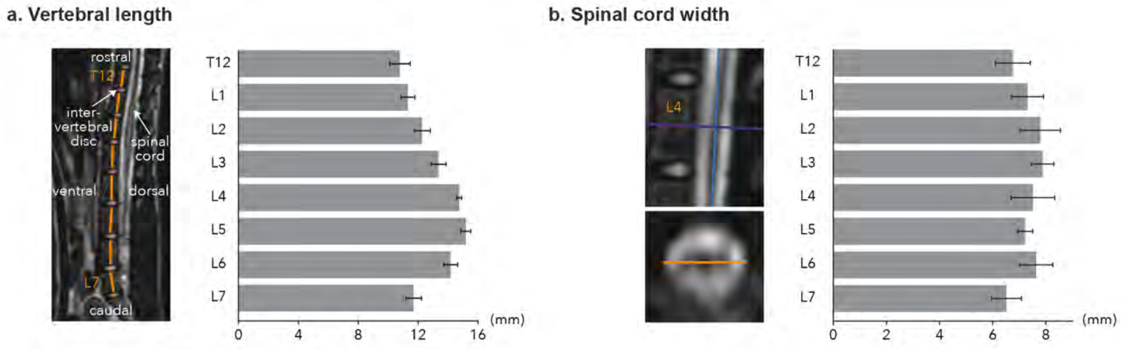
a. Vertebral length

b. Spinal cord width

Figure 4.3 | Vertebral length and spinal cord width in adult female *fascicularis* monkey

a. Left panel: the vertebral length (orange lines) was measured in a T2 MRI scan for each animal (Mk-EK as an example). Right panel: bar plots showing the means ± standard deviations of all our animals. **b.** Left panel: for each segment, the horizontal width (orange line) was taken at the middle of the corresponding vertebrae (purple line). Right panel: means ± standard deviations of all our animals.

Additionally, 3D replicate of the lumbar vertebral column was 3D printed from CT scan following the procedures described in chapter 2.4 and compared with a dissected vertebral column from another adult female *fascicularis* monkey (Mk-CA) from the laboratory (see above). Mk-CA dissection confirmed the global morphology of **Figure 4.2**. However, after aligning both specimens at T12 vertebra, a gradual misalignment occurred and finally reached a shift of 2.5 cm at L7 vertebra (**Figure 4.4**).

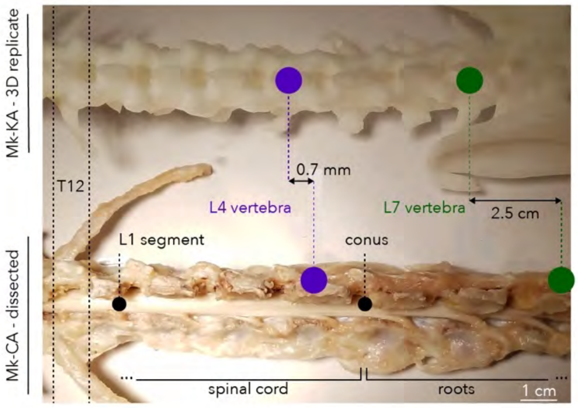

Figure 4.4 | Comparison between two adult female *fascicularis* monkey

On top, Mk-KA 3D replicate of the lumbar vertebral column. On the bottom, dissected lumbar vertebral column of Mk-CA. T12 vertebra was easily identifiable as it is the last vertebra with a rib. Both specimens were aligned at T12. Gradually, a shift took place. At the last lumbar vertebra (L7, green dots), the misalignment reached approximatively 2.5 cm.

The small variability in vertebral length in **Figure 4.3** indicated the possibility to use universal *fascicularis* lumbar spinal arrays. However, the direct comparison between two animals (same species and same gender) favored the design of tailored implants. For safety reason, we chose the second option. Indeed, personalized spinal array would better fit specific subject properties such as the uniqueness of SCI and lumbar morphology. The therapy can also be adjust depending on the subject's needs (Borton et al. 2013).

4.3. LUMBAR SPINAL ARRAY PERSONALIZATION

Variability in lumbar vertebral column and spinal cord dimensions across species and individuals advocated designing personalized lumbar spinal cord implant. The implants must be soft enough avoiding any compression or damage of the spinal cord. They were thus made of polydimethylsiloxane (PDMS) silicone. The activate sites, namely the electrodes, were made of platinum interfacing chromium, gold stack for current conductivity. Therefore, the lumbar spinal arrays offered a good elasticity and biocompatibility. The lumbar spinal arrays were manufactured in the Laboratory for Soft BioElectronic Interface (LSBI) of Professor Stephanie P. Lacour at EPFL (Minev et al. 2015; Schiavone et al. 2020). The lumbar spinal arrays were interfacing with an implantable pulse generator (IPG, Activa RC, Medtronic) through wired connectors of 2x8 stimulation sites. Because of this limitation and the softness of the array, we designed two lumbar spinal arrays (8 electrodes per array), namely the rostral lumbar spinal array and the caudal lumbar spinal array. They covered the entire lumbar vertebral column.

4.3.1. Lumbar spinal array design

EES recruits large proprioceptive fibers within the dorsal roots (Capogrosso et al. 2013; Moraud et al. 2016). Thus, electrodes targeting the dorsal root entry points within the spinal canal would offer an optimal selectivity. We used 3D anatomical reconstructions from CT scans to develop two personalized lumbar spinal arrays designed according to the size of vertebral bodies of an individual monkey (Mk-Ka). The length of the lumbar spinal array was chosen in order to reach dorsal roots of interest (L1 to L6 roots), while the electrode placement was distributed among its length. By adopting this strategy, the lumbar spinal arrays covered the proximal and distal muscles of the leg (Capogrosso et al. 2016). We discarded the midline electrodes as we observed unspecific elicited movement from these electrodes (Capogrosso et al. 2016). Therefore, we maximized our chances to recruit dorsal afferents with only lateral electrodes (**Figure 4.5**). The lumbar spinal arrays were connected to the IPG allowing wireless stimulation via a stimulator programmer.

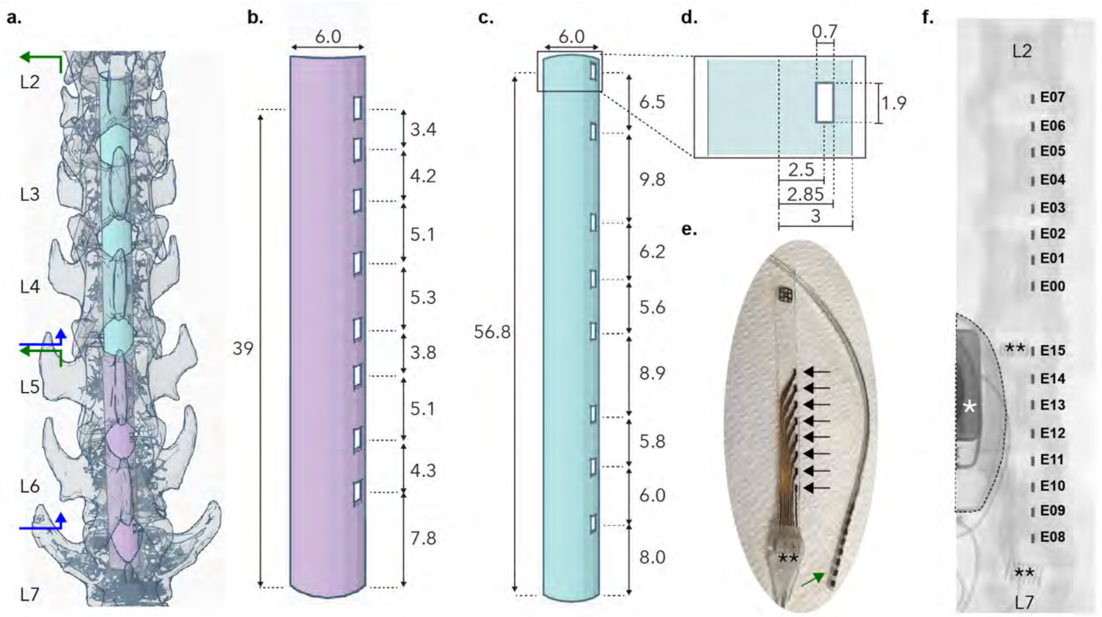

Figure 4.5 | Tailored lumbar spinal arrays in Mk-Ka

a. Overlay between 3D reconstructed lumbar vertebral column and lumbar spinal arrays. This procedures allowed the proper design of the arrays. The entry point of the caudal array was between vertebrae L6-L7 (bottom blue arrow) and the exit point between vertebrae L4-L5 (bottom green arrow). The entry point of the rostral array was therefore between vertebrae L4-L5 and the exit point between vertebrae L1-L2. **b.** Design of the caudal spinal array in mm. The white rectangles represent electrodes that deliver the electric current. **c.** Design of the rostral spinal array in mm. **d.** Electrode layout dimension in mm. **e.** Manufactured caudal spinal array. The 8 black arrows show the electrodes. ** shows the spinal array connector. The green arrow shows the interface between the array and the IPG connector. **f.** X-ray in Mk-Ka right after the surgery showing the implanted lumbar spinal arrays: caudal spinal array from electrode 08 (E08) to 15 (E15); rostral spinal array from electrode 0 (E00) to 07 (E07). * shows the IPG. ** shows the array connectors located outside the spinal canal.

4.3.2. Surgical procedure

Once the lumbar spinal arrays manufactured, we performed the surgery (anesthesia and post-operative care protocols are described in chapter 2.4) that consisted of first performing a dorsal longitudinal skin incision. We pushed the muscle aside in order to expose the dorsal aspect of the vertebral column. After vertebra identification, we performed a laminectomy at the entry and exit points (**Figure 4.5a**). The spinal array was then attached to a passing elevator allowing its insertion within the spinal canal as it was more rigid than the lumbar spinal arrays. We then inserted the passing elevator in the entry point and slid it until the exit point located more rostrally. The passing elevator was pulled out. The lumbar spinal array slid within the spinal canal by gently pulling on the passing elevator. We adjusted the spinal arrays location by electrically stimulating and assessing the leg responses. Once correctly placed, we secured the spinal array to the spinal process. Then, the connector cable (interface with the IPG, green arrow in **Figure 4.5e**) was tunneled to the abdomen. We performed a pocket into the abdomen in order to place the IPG for wireless stimulation. We plugged in connector to the IPG, suture the muscles and the skin. More detailed about surgical procedures are found in (Capogrosso et al. 2016; 2018). All the surgical procedures were performed by a trained functional neurosurgeon (**Figure 4.6**).

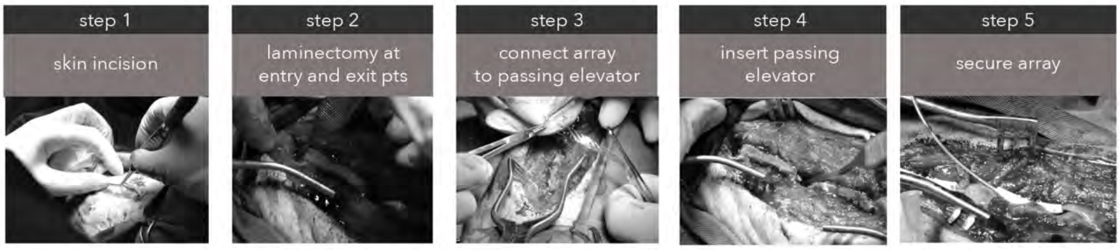
step 1
skin incision
step 2
laminectomy at entry and exit pts
step 3
connect array to passing elevator
step 4
insert passing elevator
step 5
secure array

Figure 4.6 | **Surgical procedure**

Step1: longitudinal skin incision. Step 2: laminectomy at the entry points (L6-L7 and L4-L5 for caudal and rostral spinal arrays, respectively) and at exit points (L4-L5 and L1-L2 for caudal and rostral spinal arrays, respectively). Step 3: connect the spinal array to a passing elevator. Step 4: insert passing elevator in entry point and push it until reaching the exit point. Then, insert spinal array by pulling on the passing elevator. Step 5: secure the spinal array by attaching the connector to the spinal process (Capogrosso et al. 2016; 2018).

4.4. SPINAL CORD STIMULATION PROTOCOL DESIGN

A custom-made stimulation protocol (MATLAB_R2017b) prompted a stimulator unit (IZ2H, Tucker Davis Technologies) for delivering biphasic cathodic-first current pulses (1Hz) of 300µs duration and increasing current intensities ranging from sub-threshold to a saturation value of the recorded muscle activation for the electrode being tested. The muscle activity was amplified (1000x, PZ5, Tucker Davis Technologies), filtered (50 Hz notch and 10-5000 Hz bandpass) and acquired at 12 kHz via a processor (RZ2, Tucker Davis Technologies) for offline analysis. We stimulated each electrode with four repetitions of 10 current steps. The average peak-to-peak amplitude of the evoked muscle response was used to analyze the relationship between the muscle activity and the stimulation intensity, namely the recruitment curves. The muscle activities were normalized to their maximal amplitude obtained during the experiment. This experiment was performed right after the surgery while the animal was still under propofol anesthesia (Barra et al. 2018) (**Figure 4.7**).

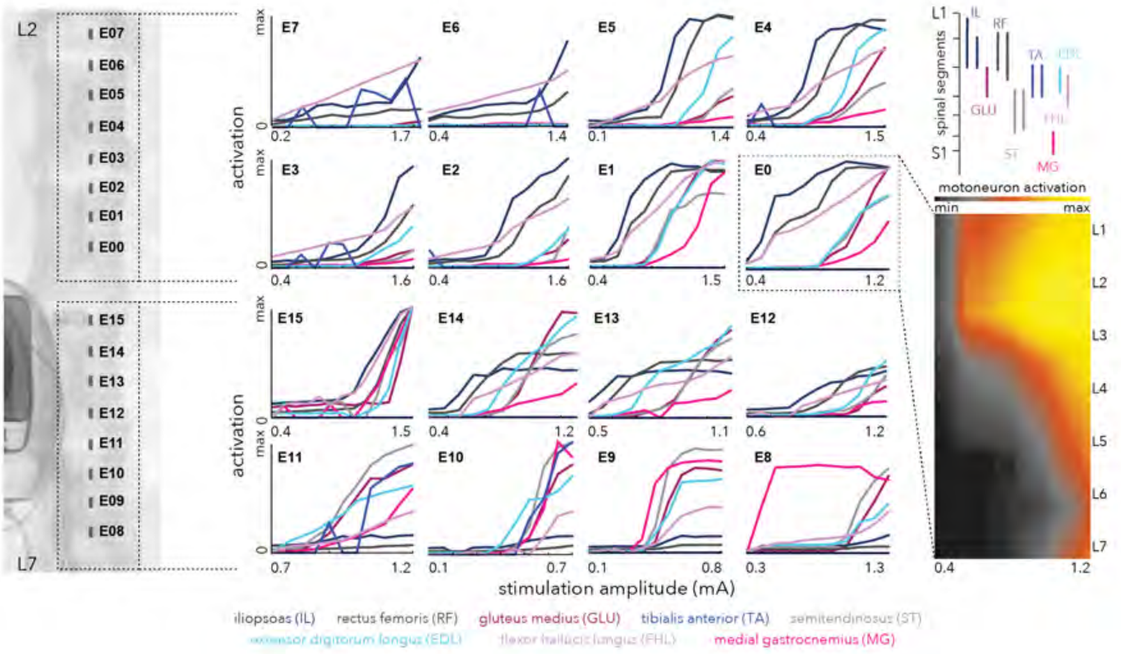

Figure 4.7 | Muscle recruitment during EES

Left panel: X-ray taken right after the surgery showing the location of the electrodes. Middle panel: level of muscle activation while stimulating with different amplitude for each electrode. Top right panel: motoneurons location within the spinal cord. Modified from (Capogrosso et al. 2016). Bottom right panel: muscle activity projection of electrode 0 (E0) to the anatomical location of the corresponding motoneurons.

The recruitment curves computed for the different electrodes showed the spatial selectivity suggesting good location of the spinal arrays. Given their good selectivity, we therefore designed a stimulation protocol that reproduced the normal pattern activation during locomotion. We first identified the spatiotemporal motoneuron recruitment pattern underlying healthy locomotion on a treadmill of the same animal. To this aim, we back projected the muscle activity to the anatomical location of the corresponding motoneuron over a normal gait cycle (average of 30 steps) (**Figure 4.8, top panel**). We then developed an algorithm that reproduced the spatiotemporal map in a time window of 50ms for each electrode at 10 different amplitudes (the range was obtained by the recruitment curve analysis). Each obtained spatiotemporal map was compared (Euclidean distance) with the cropped original map during natural gait (window size= 50ms). The electrode and amplitude giving the smallest Euclidean distance was chosen as the optimal configuration to reproduce that specific muscle activity. This was then repeated 20 times to cover the entire gait cycle of 1 second. Finally, the reconstructed spatiotemporal map of the spinal cord was plotted (**Figure 4.8, bottom panel**) with the corresponding electrode and given current amplitude (**Figure 4.8 middle panel**).

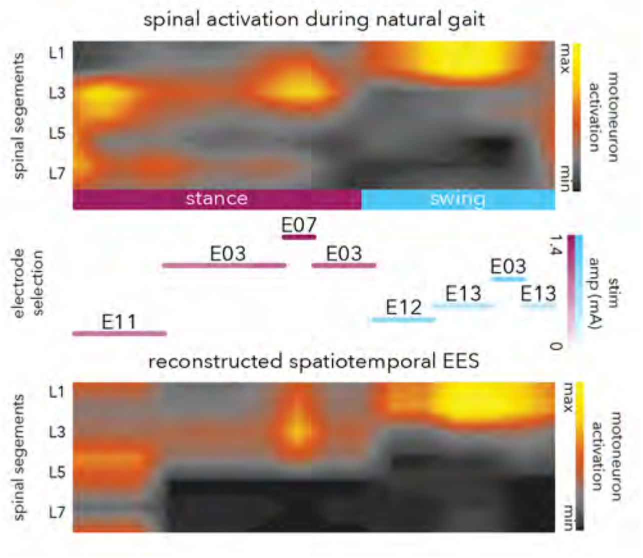

Figure 4.8 | Spatiotemporal map of the spinal cord during EES

Top panel: spatiotemporal map of the spinal cord during natural gait in a treadmill in Mk-Ka (average of n=30 steps). Middle panel: selection of different available electrodes implanted in Mk-Ka (see **Figure 4.7**) at a given amplitude. Bottom panel: optimal selection of electrodes allowed to reconstruct a theoretical spatiotemporal map.

Spatiotemporal maps of motoneuron activation showed a successive activation of hotpots during natural gait. This natural spatiotemporal motoneuron activation can be reproduced by targeting the dorsal roots with EES through the personalized lumbar spinal arrays. Amplitude, duration, and electrodes can be finely tuned to recreate motoneuron pool activation and therefore find the most suited EES parameters. Personalized neuroprosthetics (i.e. lumbar spinal array) can be safely tailored to individual anatomy and potentially help to regain function after SCI.

4.5. LIMITATION AND CONCLUSION

Personalized lumbar spinal arrays showed good selectivity and could theoretically reproduce natural patterns of spinal cord activation through fine tuning of stimulation parameters. Nevertheless, three considerations must be discussed.

First, the surgical procedure is highly challenging. Every step must carefully be reviewed prior to the surgery and inventory of suitable instruments made accordingly. For instance, the commercial available passing elevator (Medtronic, step 4 in **Figure 4.6**) cannot be used in adult female *fascicularis* monkeys as it is designed for humans, and is therefore too large. Its insertion within the spinal canal could compress the spinal cord and thus create irreversible damage. Thanks to the advance in *in-vivo* imaging and 3D printing technologies (Ploch et al. 2016; Choy et al. 2017), this problem can easily be tackled before any surgical intervention by designing a passing elevator that fits the spinal canal of small animals, and has the appropriate stiffness to pass through the spinal canal without causing damage to the spinal cord (Schiavone et al. 2020). The risk of surgical failure is thereby minimized.

Second, the reconstructed spatiotemporal map showed in **Figure 4.8** was made within a time range of 50ms. In other words, every 50ms, a stimulation should be delivered to reproduce the natural spatiotemporal map. Therefore, the chosen IPG must meet this requirement with the smallest stimulation delay as possible. Moreover, the IPG must be upgraded with wireless communication modules that enabled real-time control of EES parameters of pre-programmed sequences of stimulations (Capogrosso et al. 2016; Wagner et al. 2018). Finally, the described experiment was performed under anesthesia. During walking, the stimulation would certainly not affect the muscle responses in the same manner (Gerasimenko et al. 2006). Therefore, the re-evaluation of EES during walking in healthy condition must be performed (Capogrosso et al. 2016).

Third, the spinal array needs to fulfill various requirements such as robustness, elasticity and biocompatibility. Therefore, the manufacture of such arrays is highly challenging, especially for long-term application. Indeed, 20 days post-surgery, the implanted array in Mk-Ka showed mechanical failure (**Figure 4.9**).

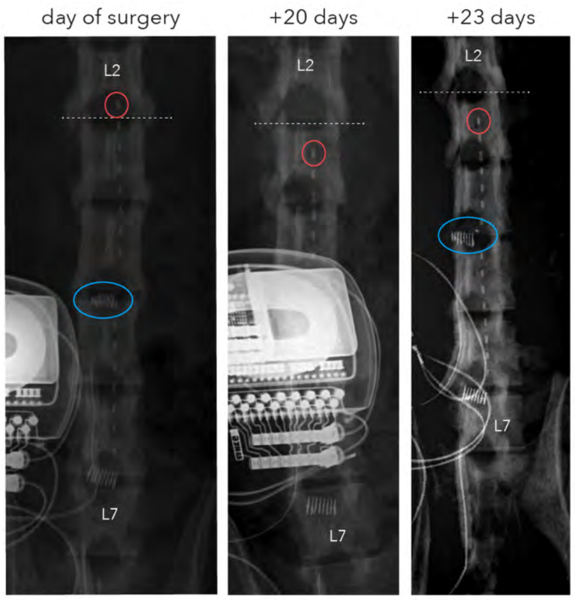

Figure 4.9 | X-ray comparison

Left picture: same as **Figure 5f** but with another contrast. The most rostral electrode (red circle) was located at vertebra L2 delimited with the white dashed line. The array connector (blue circle) was aligned to the vertebral column. Middle picture: 20 days post-surgery, the most rostral electrode was located at vertebra L3 (red circle below the white dashed line). The state of the connector was not assessable due to the IPG that move medially. Right picture: we thus explanted the IPG three days later and noticed that the spinal array connector was probably broken (blue circle).

The experience with Mk-Ka helped us to design a conceptual framework of neurotechnology validation (Schiavone et al. 2020). The validation of neurotechnology translation from the laboratory to clinical applications can be conceptualized in four steps: (1) tailored design; (2) manufacturing; (3) *in-vitro* validation and (4) *in-vivo* evaluation. Those steps must be re-iterated for optimizing proof-of-concept prototypes to translational study (**Figure 4.10**). In our case, we did not test the arrays *in-vitro* (step 3); therefore, the risk of failure was high. If we have had tested them, they would most likely have failed. Therefore, we would have built more robust spinal array before any surgical intervention.

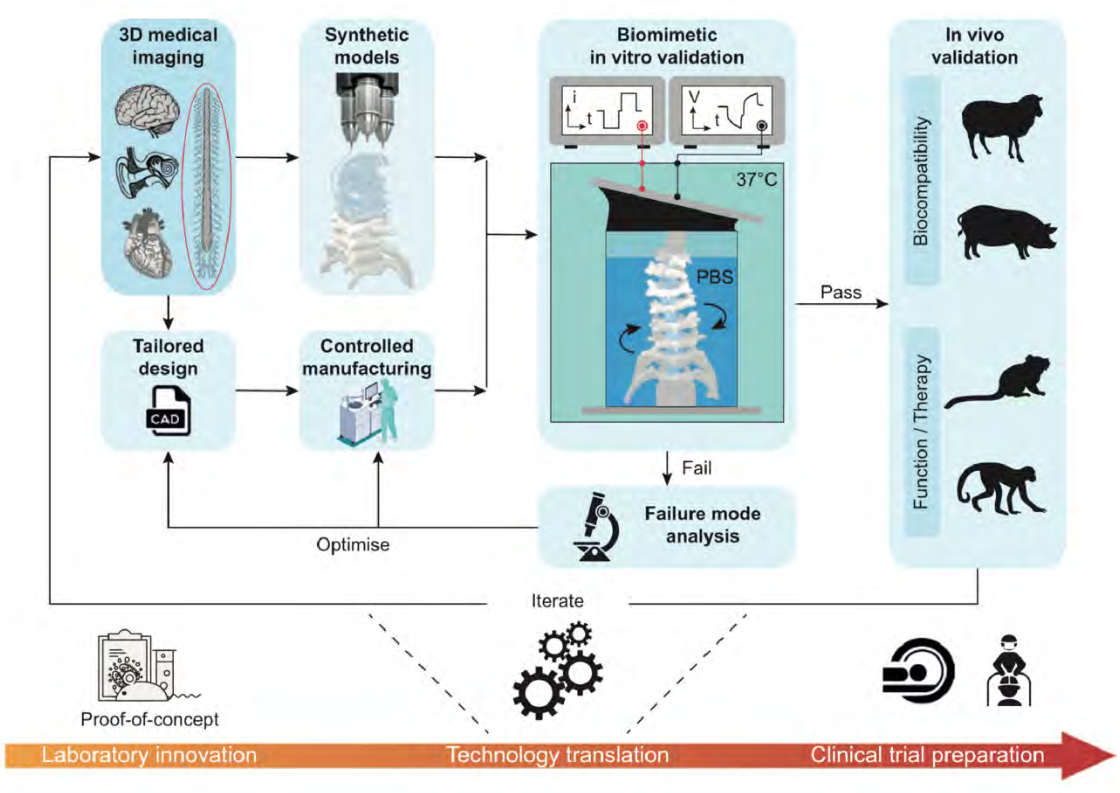
3D medical imaging
Synthetic models
Biomimetic in vitro validation
In vivo validation
37°C
PBS
Pass
Biocompatibility
Function / Therapy
Tailored design
CAD
Controlled manufacturing
Fail
Failure mode analysis
Optimise
Iterate
Proof-of-concept
Laboratory innovation
Technology translation
Clinical trial preparation

Figure 4.10 | **Conceptual framework for the technology translation**

The translational path between innovative technology in laboratory to clinic represents 4 consecutive steps of development: (1) design of tailored neuroprosthesis based on *in-vivo* medical imaging; (2) manufacture of the technology; (3) *in-vitro* validation in biomimetic environment and (4) functional and biocompatibility assessments in animal models. Modified from (Schiavone et al. 2020).

To summarize, tailored neuroprosthetics represented a promising, yet challenging approach for SCI. Before any *in-vivo* intervention, the technology must be tested following the conceptual framework. Assuming that this approach successfully passes the framework, it may provide a practical path to establish a similar framework for clinical applications in humans.

4.6. BIBLIOGRAPHY

Asboth L, Friedli L, Beauparlant J, Martinez-Gonzalez C, Anil S, Rey E, et al. Cortico–reticulo–spinal circuit reorganization enables functional recovery after severe spinal cord contusion. Nat Neurosci. Springer US; 2018 Mar 19;:1–19.

Barbeau H, Rossignol S. Recovery of locomotion after chronic spinalization in the adult cat. Brain Research. 1987 May 26;412(1):84–95.

Barra B, Roux C, Kaeser M, Schiavone G, Lacour SP, Bloch J, et al. Selective Recruitment of Arm Motoneurons in Nonhuman Primates Using Epidural Electrical Stimulation of the Cervical Spinal Cord. Conf Proc IEEE Eng Med Biol Soc. IEEE; 2018 Jul;2018:1424–7.

Borgognon S, Cottet J, Moret V, Chatagny P, Carrara L, Fregosi M, et al. Fine Manual Dexterity Assessment After Autologous Neural Cell Ecosystem (ANCE) Transplantation in a Non-human Primate Model of Parkinson's Disease. Neurorehabilitation and Neural Repair. 2019 Jun 6;33(7):1545968319850133–567.

Borgognon S, Cottet J, Moret V, Chatagny P, Ginovart N, Antonescu C, et al. Enhancement of Striatal Dopaminergic Function Following Autologous Neural Cell Ecosystems (ANCE) Transplantation in a Non-Human Primate Model of Parkinson's Disease. J Alzheimers Dis Parkinsonism. 2017;7(5):1–11.

Borton D, Micera S, Millán JDR, Courtine G. Personalized neuroprosthetics. Sci Transl Med. American Association for the Advancement of Science; 2013 Nov 6;5(210):210rv2–210rv2.

Capogrosso M, Milekovic T, Borton D, Wagner F, Moraud EM, Mignardot J-B, et al. A brain–spine interface alleviating gait deficits after spinal cord injury in primates. Nature. Nature Publishing Group; 2016 Nov 10;539(7628):284–8.

Capogrosso M, Wagner FB, Gandar J, Moraud EM, Wenger N, Milekovic T, et al. Configuration of electrical spinal cord stimulation through real-time processing of gait kinematics. Nature Protocols. Nature Publishing Group; 2018 Sep 6;13(9):2031–61.

Capogrosso M, Wenger N, Raspopovic S, Musienko P, Beauparlant J, Luciani LB, et al. A Computational Model for Epidural Electrical Stimulation of Spinal Sensorimotor Circuits. Journal of Neuroscience. Society for Neuroscience; 2013 Dec 4;33(49):19326–40.

Choy WJ, Mobbs RJ, Ben Wilcox, Phan S, Phan K, Sutterlin CE III. Reconstruction of Thoracic Spine Using a Personalized 3D-Printed Vertebral Body in Adolescent with T9 Primary Bone Tumor. World Neurosurgery. Elsevier Inc; 2017 Sep 1;105:1032.e13–7.

Cioni B, Meglio M, Zamponi A. Effect of spinal cord stimulation on motor performances in hemiplegics. Stereotact Funct Neurosurg. Karger Publishers; 1989;52(1):42–52.

Courtine G, Gerasimenko Y, van den Brand R, Yew A, Musienko P, Zhong H, et al. Transformation of nonfunctional spinal circuits into functional states after the loss of brain input. Nat Neurosci. Nature Publishing Group; 2009 Oct 1;12(10):1333–42.

Courtine G, Song B, Roy RR, Zhong H, Herrmann JE, Ao Y, et al. Recovery of supraspinal control of stepping via indirect propriospinal relay connections after spinal cord injury. Nat Med. 2008 Jan;14(1):69–74.

De Leon RD, Hodgson JA, Roy RR, Edgerton VR. Retention of hindlimb stepping ability in adult spinal cats after the cessation of step training. Journal of Neurophysiology. 1999 Jan;81(1):85–94.

Edgerton VR, Courtine G, Gerasimenko YP, Lavrov I, Ichiyama RM, Fong AJ, et al. Training locomotor networks. Brain Research Reviews. 2008 Jan;57(1):241–54.

Forssberg H, Grillner S, Halbertsma J, Rossignol S. The locomotion of the low spinal cat. II. Interlimb coordination. Acta Physiol Scand. 1980 Mar;108(3):283–95.

Gerasimenko YP, Lavrov IA, Courtine G, Ichiyama RM, Dy CJ, Zhong H, et al. Spinal cord reflexes induced by epidural spinal cord stimulation in normal awake rats. J Neurosci Methods. 2006 Oct;157(2):253–63.

Greiner, N., Barra, B., Schiavone, G., James, N., bioRxiv, F. F., et al. Recruitment of Upper-Limb Motoneurons with Epidural Electrical Stimulation of the Primate Cervical Spinal Cord. 2020. Biorxiv.org

Kibleur P, Tata SR, Greiner N, Conti S, Barra B, Zhuang K, et al. Spatiotemporal Maps of Proprioceptive Inputs to the Cervical Spinal Cord During Three-Dimensional Reaching and Grasping. IEEE Trans Neural Syst Rehabil Eng. 2020 Jul;28(7):1668–77.

Ko H-Y, Park JH, Shin YB, Baek SY. Gross quantitative measurements of spinal cord segments in human. Spinal Cord. 2004 Jan;42(1):35–40.

Minev IR, Musienko P, Hirsch A, Barraud Q, Wenger N, Moraud EM, et al. Biomaterials. Electronic dura mater for long-term multimodal neural interfaces. Science. 2015 Jan 9;347(6218):159–63.

Moraud EM, Capogrosso M, Formento E, Wenger N, DiGiovanna J, Courtine G, et al. Mechanisms Underlying the Neuromodulation of Spinal Circuits for Correcting Gait and Balance Deficits after Spinal Cord Injury. Neuron. Elsevier Inc; 2016 Feb 17;89(4):814–28.

Ploch CC, Mansi CSSA, Jayamohan J, Kuhl E. Using 3D Printing to Create Personalized Brain Models for Neurosurgical Training and Preoperative Planning. World Neurosurgery. Elsevier Inc; 2016 Jun 1;90(C):668–74.

Rossignol S, Frigon A. Recovery of Locomotion After Spinal Cord Injury: Some Facts and Mechanisms. Annu Rev Neurosci. 2011 Jul 21;34(1):413–40.

Schiavone G, Fallegger F, Kang X, Barra B, Vachicouras N, Roussinova E, et al. Soft, Implantable Bioelectronic Interfaces for Translational Research. Adv Mater. John Wiley & Sons, Ltd; 2020 Mar 16;24:1906512–10.

van den Brand R, Heutschi J, Barraud Q, DiGiovanna J, Bartholdi K, Huerlimann M, et al. Restoring voluntary control of locomotion after paralyzing spinal cord injury. Science. American Association for the Advancement of Science; 2012 Jun 1;336(6085):1182–5.

Wagner FB, Mignardot J-B, Le Goff-Mignardot CG, Demesmaeker R, Komi S, Capogrosso M, et al. Targeted neurotechnology restores walking in humans with spinal cord injury. Nature Publishing Group. Springer US; 2018 Oct 24;563(7729):1–29.

Wenger N, Moraud EM, Gandar J, Musienko P, Capogrosso M, Baud L, et al. Spatiotemporal neuromodulation therapies engaging muscle synergies improve motor control after spinal cord injury. Nat Med. 2016 Jan 18;22(2):138–45.

Wenger N, Moraud EM, Raspopovic S, Bonizzato M, DiGiovanna J, Musienko P, et al. Closed-loop neuromodulation of spinal sensorimotor circuits controls refined locomotion after complete spinal cord injury. Sci Transl Med. American Association for the Advancement of Science; 2014 Sep 24;6(255):255ra133–3.

- PART 5 -

DISCUSSION AND PERSPECTIVE

5.1. NEURAL ENCODING

The work presented in this thesis first describes the setup of a reliable technological framework for studying freely behaving monkey in untethered condition. This setup encompassed recent technologies allowing the simultaneous recording of multiple brain areas, muscle activities and whole-body 3D kinematics. Additionally, surgeries have been performed in a subject-specific manner based on the anatomy of each animal ensuring the successful positioning of intracortical microelectrode arrays. Finally, the percutaneous connectors were anchored to an implanted titanium mesh integrated to the skull of the animals. This surgical approach led to long term stability of the implants allowing the recording of the animals for months in several locomotor behaviors.

The animals were trained to perform multiple locomotor tasks (walking in a treadmill, overground walking on a corridor, crossing an uneven horizontal ladder, climbing stairs and obstacles) while we recorded the neural activity of the dorsal premotor (PMd), primary motor (M1) and primary somatosensory (S1) cortices. Our hypothesis stated that (1) single unit activity showed different phase-locked patterns across tasks and; (2) neural population activity is confined to a preserved neural manifold referred to as locomotion subspace. These two hypothesis were tested and confirmed. Interestingly, neural dynamic patterns varied along the rostro-caudal axis: from PMd to S1. In the context of brain-machine interfaces, these patterns of neural dynamics reliably predict locomotor-related events across tasks.

Although this neural analysis at the population level revealed cortico-specific patterns that can potentially underlie neuronal mechanisms, the question on how the sensorimotor cortex encodes movement remains (Lebedev et al. 2019). Here I will discuss different limitations and future points than can be assessed.

5.1.1. Further analysis

Cortico-specific neural population dynamics describe how the brain is active during locomotion, but did not portray its causal role with movement (see more details about causality in chapter 5.1.5). Different extended analysis could potentially improve our knowledge about sensorimotor cortex involvement during locomotion. First, predictive analysis between neuronal modulations and movement (kinematic or muscle activity) can be used with Granger causality (Wang et al. 2016) or cross-correlation methods (Fitzsimmons 2009). In the latter, correlation peaks for lags in firing rate of a neuron preceding the muscle activity (negative lags) could indicate a causal link (Fitzsimmons 2009). However, this method does not take into account biological properties (e.g. fiber lengths, synaptic delay, etc) of the recorded neuron and the downstream motoneuron; therefore the lags of a recorded neuron have to be arbitrary assumed (Mulliken et al. 2008; Takei et al. 2018). Second, at the population level, cortical activity can be captured in an output-null (= population activity that can be modulated without affecting downstream target) or output potent subspaces (= population activity modulating downstream target) (Kaufman et al. 2014; Perich et al. 2018). M1 and PMd employ an output-null subspace before the movement occurrence, whereas the output-potent subspace functionally maps the downstream activity (i.e. muscle activity). In our case, we could therefore compare (e.g. principal angles, correlation, etc) the output-potent subspace with the locomotion subspace to further assess their similarity. The hypothesis would be that the locomotion subspace is more similar to an output potent subspace than to an output-null subspace. If so, the locomotion subspace would encompass neuronal mechanisms related to downstream activities. Finally, interaction between cortices through communication subspaces might reveal interesting insights on the routing of population signals between areas (Semedo et al. 2019; Perich et al. 2020). Is the sensorimotor activity compartmentalized within distinct communication subspaces during locomotion? Assuming that such communication subspaces exist, are the shared information more related to the locomotion or task subspaces ? Since PMd plays a role in motor planning (Cisek and Kalaska 2005), the hypothesis is that its receiving information from M1 and S1 are equally related to their locomotion and task subspaces, whereas the other shared information are more related to the locomotion subspace (**Figure 5.1**). If true, PMd might thus process task-related information that needs to be properly integrated for preparatory purposes. Therefore, the other shared information might reflect temporal features driving locomotion.

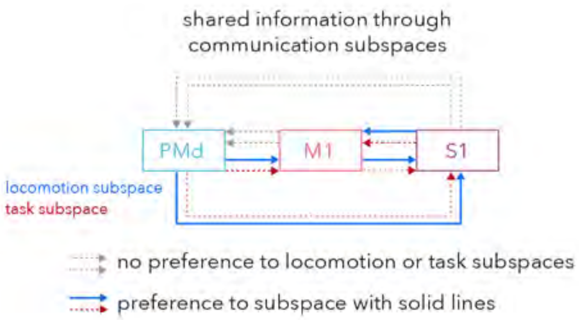
shared information through communication subspaces
PMd
M1
S1
locomotion subspace
task subspace
no preference to locomotion or task subspaces
preference to subspace with solid lines

Figure 5.1 | Hypothesis of shared information via communication subspaces during locomotion

Assuming that communication subspaces reside within the sensorimotor cortex, converging information to PMd could be equally related to both the task and locomotion subspaces of the source cortex (M1 and S1). This would reflect preparatory information needed to output an adequate locomotor behavior for a given environment.

5.1.2. Electrophysiological signature of cortical encoding at the cellular level

Depending on the Utah array electrodes location, captured putative neurons are located in the superficial layers (receiving information from other brain region) or deep layers (containing long corticofugal neurons) (Donoghue and Wise 1982; Rathelot and Strick 2009; Gerfen et al. 2016;

Ninomiya et al. 2019) (**Figure 5.2**). The signals are thus coming from myriad of neurons making difficult to surely define the neural source of the signal. Some studies addressed this issue by classifying waveform shape to distinguish cell types (Mountcastle et al. 1969; Chaisanguanthum et al. 2017). Paravalbumin-positive (PV+) interneurons, morphologically basket cells, show fast spiking and narrow waveform profile. In contrast, broad waveform and regular low spiking rate likely correspond to pyramidal cells (Trainito et al. 2019). One possible extended analysis is therefore to assess the dynamics of distinct neural classes with the hypothesis that pyramidal neurons are more responsible for creating dynamics seen in the locomotion subspace. This analysis would nonetheless require huge amount of neurons. Unfortunately, we could not perform the same analysis on sorted units identifying putative neurons as their number was sometimes to low (<7) per sessions.

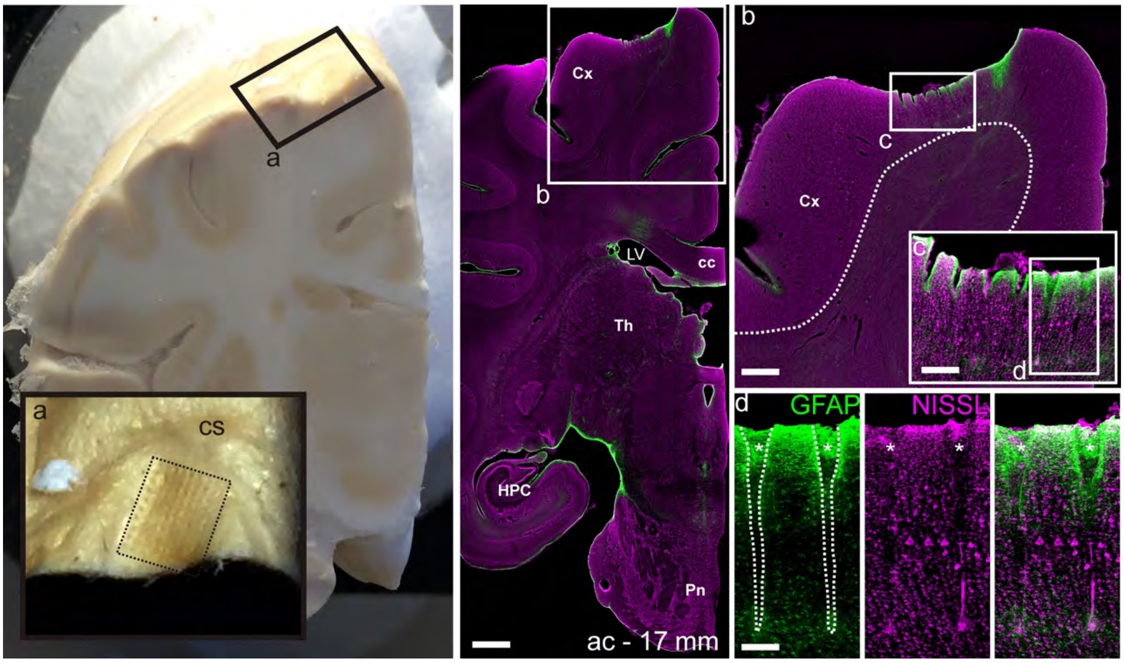

Figure 5.2 | Histological preparation after Utah array implantation in leg M1

Left panel: frozen left hemisphere block before cutting in a cryostat. **a.** Location of the Utah array (dashed rectangle). cs = central sulcus. Middle panel: overview of an histological section after Nissl in magenta and GFAP (astrocytes) in green immunostaining. Cx = cortex; LV = lateral ventricle ; cc = corpus callosum; Th = thalamus; HPC = hippocampus ; Pn = Pontine nucleus; ac = anterior commissure as reference. Scale bar = 1mm. Right panel: **b**. Magnification of leg M1. Cx = cortex. Scale bar = 500µm. **c.** Magnification of the Utah array localization. Scale bar = 250µm. **d**. Magnification of two Utah array electrodes (dashed lines, *). Scale bar = 200µm. Note that this animal was involved in another study (Capogrosso et al. 2016). By the courtesy of Dr. Quentin Barraud.

Traditionally, pyramid tract neurons (PTN) have been identified as corticospinal neurons by their antidromic responses to stimulation of the pyramidal tract (Evarts 1964; 1968). PTNs fired before movement onset, and their discharge frequencies are correlated with movement. Moreover, some of these PTNs make direct connections to the spinal motoneurons and are therefore in position to modulate or generate a movement (Rathelot and Strick 2006; Lemon and Kraskov 2019). Taken these two considerations, PTNs are eminent candidate as 'command' neurons (Lemon and Kraskov 2019). One may thereby assume that specific inhibition or excitation of PTNs projecting to the lumbar region may unveil the possible causality link between neural activity and movements. Indeed, the dynamical systems framework recapitulates neural responses during movement, but does not attempt to ignore the complex features of single-neuron modulation. This complexity might be explained by underlying dynamics at the population level (Shenoy et al. 2013). Thus, one remaining question is: what is the underlying neuronal circuit that produces these dynamics (Shenoy et al. 2013)? One could answer this question by perturbating observed dynamical structures by inhibition or excitation of specific neural sub-populations (Shenoy et al. 2013). The identification of single neurons would help for the understanding of neural encoding. In the next chapter, I will thus present a pilot experiment conducted on rodents and primates assessing the feasibility and outcome of specific neural inhibition.

5.1.3. Biological tool to perturb cortical encoding at the cellular level

Recent advances in molecular engineering allow researchers to specifically target neurons (Sheikh et al. 2018; Wang et al. 2018) by co-injecting a retrograde adeno-associated viral (AAV) vector carrying cre-recombinase and an AAV cre-dependent vectors (Asboth et al. 2018; Omlor et al. 2019). Thus, the genetic material carried by the AAV cre-dependent vector is only expressed if the cre protein is transduced. AAV vectors can carry optogenetic, chemogenetic, synaptophysin marker or axonal markers transgenes (Galvan et al. 2017). Chemogenetic approach seems more suitable than optogenetic in term of surgical, post-operative following-up and technological challenges, especially in nonhuman primates. We therefore piloted a chemogenetic study in rodents and monkeys where we specifically targeted the layer V corticospinal neurons projecting to the lumbar spinal cord (**Figure 5.3**). To this aim, we injected leg M1 with a cre-dependent AAV carrying the human muscarinic type 4 (hM4Di) designer receptors exclusively activated by designer drugs (DREADDs). During the same surgery, we injected a retrograde AAV-cre vector in the ventral horn of the spinal cord at the lumbar level. Additionally, the same surgical procedure was performed with anatomical transgenes for synaptic quantification along the rostro-caudal axis of the spinal cord. The material and methods of this work are summarized in chapter 6.1.

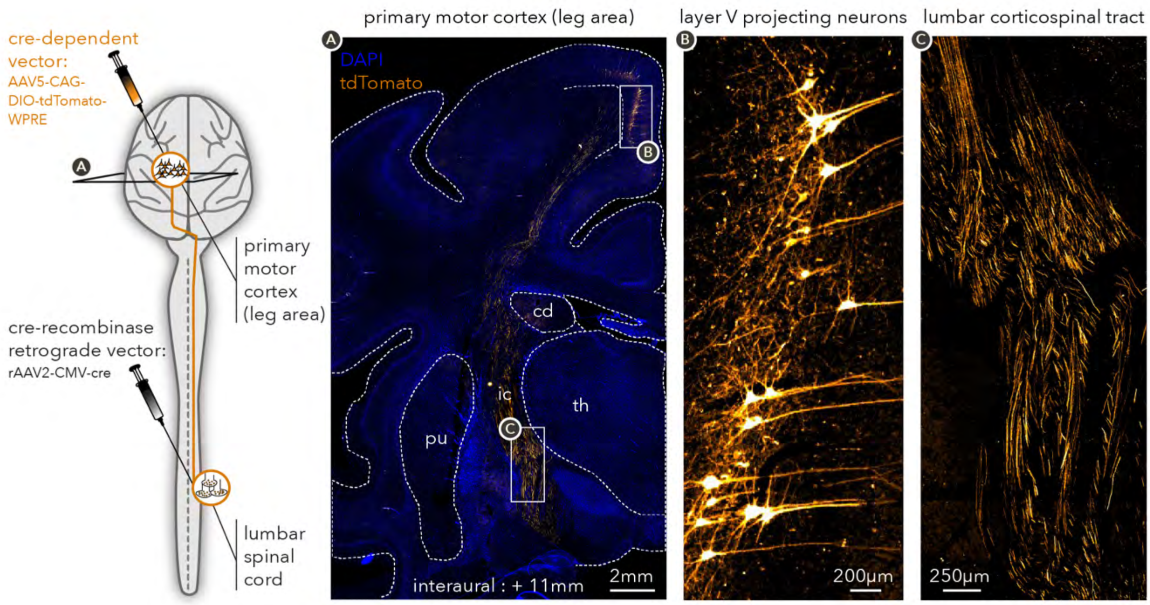
cre-dependent
vector:
AAV5-CAG-
DIO-tdTomato-
WPRE
A
primary
motor
cortex
(leg area)
cre-recombinase
retrograde vector:
rAAV2-CMV-cre
lumbar
spinal
cord
primary motor cortex (leg area)
A
DAPI
tdTomato
B
cd
ic
th
pu
C
interaural : + 11mm
2mm
layer V projecting neurons
B
200µm
lumbar corticospinal tract
C
250µm

Figure 5.3 | Intersectional viral strategy specifically targeting the layer V projecting neurons to the lumbar spinal cord

In this example, the monkey was injected with a retrograde cre-vector (rAAV2-CMV-cre) in the ventral horn of the lumbar spinal cord. During the same surgery, a cre-dependent vector (AAV5-DIO-tdTomato) was injected in the leg area of M1. After a waiting period allowing viral transduction, only the layer V projecting neurons expressed the axonal marker tdTomato. cd = caudate nucleus, pu = putamen, th = thalamus, ic = internal capsule.

Our hypothesis was that the layer V lumbar corticospinal tract (CST) neurons (**Figure 5.3**) are mainly engaged for voluntary leg movement, while during normal locomotion their inhibition would affect the behavior to a lesser extent. Our motivation came from the fact that an increase of firing rate is observed during complex locomotor tasks as compared to treadmill (see chapter 3.3.1) (Drew 1988; Beloozerova and Sirota 1993; DiGiovanna et al. 2016). Moreover, an inhibitory effect would be more pronounced in nonhuman primates than rodents (Lemon 2008; Friedli et al. 2015). In order to better understand the extent of a possible inhibition, we first characterize the synaptic density of the lumbar CST in both species (**Figure 5.4**).

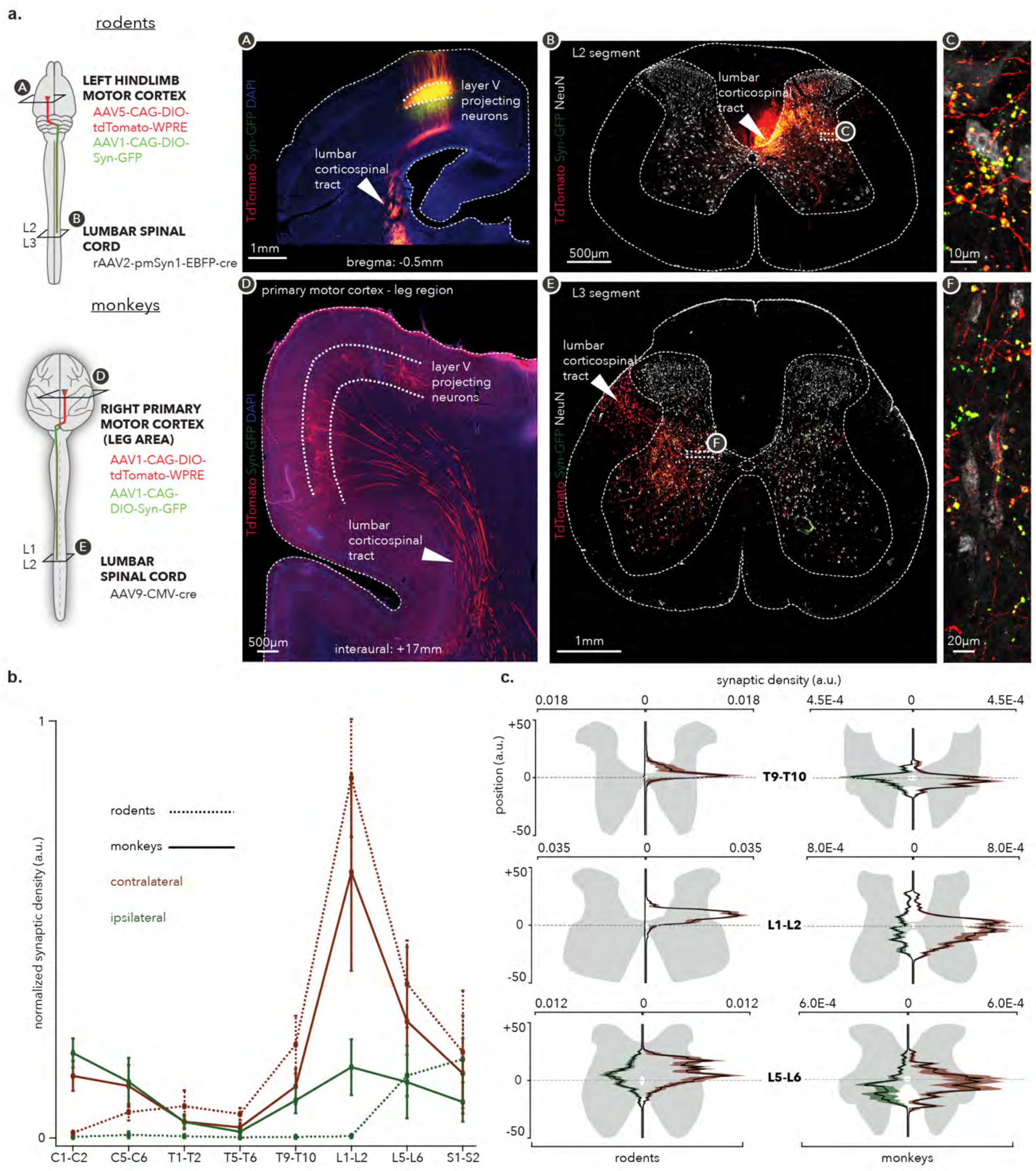
a.
rodents
A
LEFT HINDLIMB MOTOR CORTEX
AAV5-CAG-DIO-tdTomato-WPRE
AAV1-CAG-DIO-Syn-GFP
L2
L3
B
LUMBAR SPINAL CORD
rAAV2-pmSyn1-EBFP-cre
monkeys
D
RIGHT PRIMARY MOTOR CORTEX (LEG AREA)
AAV1-CAG-DIO-tdTomato-WPRE
AAV1-CAG-DIO-Syn-GFP
L1
L2
E
LUMBAR SPINAL CORD
AAV9-CMV-cre
A
TdTomato Syn-GFP DAPI
layer V projecting neurons
lumbar corticospinal tract
1mm
bregma: -0.5mm
B
L2 segment
TdTomato Syn-GFP NeuN
lumbar corticospinal tract
C
500µm
C
10µm
D
primary motor cortex - leg region
TdTomato Syn-GFP DAPI
layer V projecting neurons
lumbar corticospinal tract
500µm
interaural: +17mm
E
L3 segment
TdTomato Syn-GFP NeuN
lumbar corticospinal tract
F
1mm
F
20µm
b.
1
0
normalized synaptic density (a.u.)
rodents
monkeys
contralateral
ipsilateral
C1-C2
C5-C6
T1-T2
T5-T6
T9-T10
L1-L2
L5-L6
S1-S2
c.
synaptic density (a.u.)
0.018
0
0.018
4.5E-4
0
4.5E-4
+50
0
-50
position (a.u.)
T9-T10
0.035
0
0.035
8.0E-4
0
8.0E-4
+50
0
-50
L1-L2
0.012
0
0.012
6.0E-4
0
6.0E-4
+50
0
-50
L5-L6
rodents
monkeys

Figure 5.4 | Synaptic connectome of the lumbar CST in the spinal cord

a. Intersectional viral strategy for targeting the lumbar CST in rodents (top panel) and monkeys (bottom panel). The axons (tdTomato) are depicted in red, the synapses (Syn-GFP) in green and the neurons (NeuN) in white. **b.** Quantification of synaptic density along the spinal rostro-caudal axis normalized by the maximal density value of all the histological slices per species. Mean± sd. **c.** Dorsoventral distribution of synapse density along the spinal cord gray matter in three different spinal levels. Mean±sem.

The synaptic density of the lumbar CST is located more ventrally in nonhuman primates compared to rodents, which might lay emphasis on the corticomotoneuronal projection (Lemon 2019).

Moreover, higher density of collaterals at cervical level in nonhuman primates suggest a stronger lumbar CST involvement for movement.

To further asses the involvement of the lumbar CST in rodents, we specifically inhibited with clozapine-N-oxide (CNO) (Roth 2016) the lumbar CST transfected with hM4Di DREADDs receptors. The rats were trained to walk over-ground on a flat surface, across an uneven ladder and to flex the leg after a vocal go-signal. Therefore, the level of task complexity, from the less complex to the most complex task, could be assumed to be as followed: 1) over-ground walking, 2) uneven ladder crossing and 3) voluntary leg flexion. After a baseline recording, the rats were injected with CNO (5mg/kg, intraperitoneal) and were tested on the same tasks 50 minutes after the injection. Behavioral performances were assessed with principal component analysis (PCA) performed on 20 kinematic features and electromyographic (EMG) activities of four muscles, namely iliopsoas (IL), medial gastrocnemius (MG), semitendinosus (ST) and tibialis anterior (TA). Furthermore, the leg of the animal was attached to a force sensor during the voluntary leg flexion task. After the behavioral recordings, the animals were sacrificed and the tissue (brain and spinal cord) collected for histological verification of the viral transfection. Note that only the swing phase (from foot-off to foot strike) was considered in the locomotor tasks (i.e. over-ground and uneven ladder) as no proper stance phase was present in the voluntary leg flexion task. Therefore, leg movements across the three different tasks were comparable.

The viral transfection was effective and impressive in rats. The level of transfection was qualitatively similar to this observed in a previous study from our laboratory (Asboth et al. 2018) (**Figure 5.5a**). After CNO administration, the rats encountered difficulties to lift the leg during the voluntary leg flexion task resulting in a decrease of the generated flexion force (**Figure 5.5b**, p-value ≤ 0.01, note that the force was normalized with the maximal peak amplitude for each rat in order to account for variability across animals). During over-ground walking, no behavioral change was observed. Thus, both kinematic and muscle trajectories (baseline and CNO) in the PC space as well as the hindlimb length were overlapping. Furthermore, EMG activity of tibialis anterior (computed as the area under the curve (AUC) normalized with the maximal area for each rat) pre-post CNO administration was statistically non-significant (p-value > 0.05) (**Figure 5.5c**, top panel). In the uneven ladder, similar results were observed, albeit with less pronounced overlap in the PC space as well as the limb length (**Figure 5.5c**, middle panel). Interestingly, during the voluntary leg flexion task, two distinct trajectories were seen in the PC space. The same was true for the length of the leg during the time course of the movement. A decrease in EMG activity of the tibialis anterior was present after the CNO administration (p-value ≤ 0.01) (**Figure 5.5c**, bottom panel).

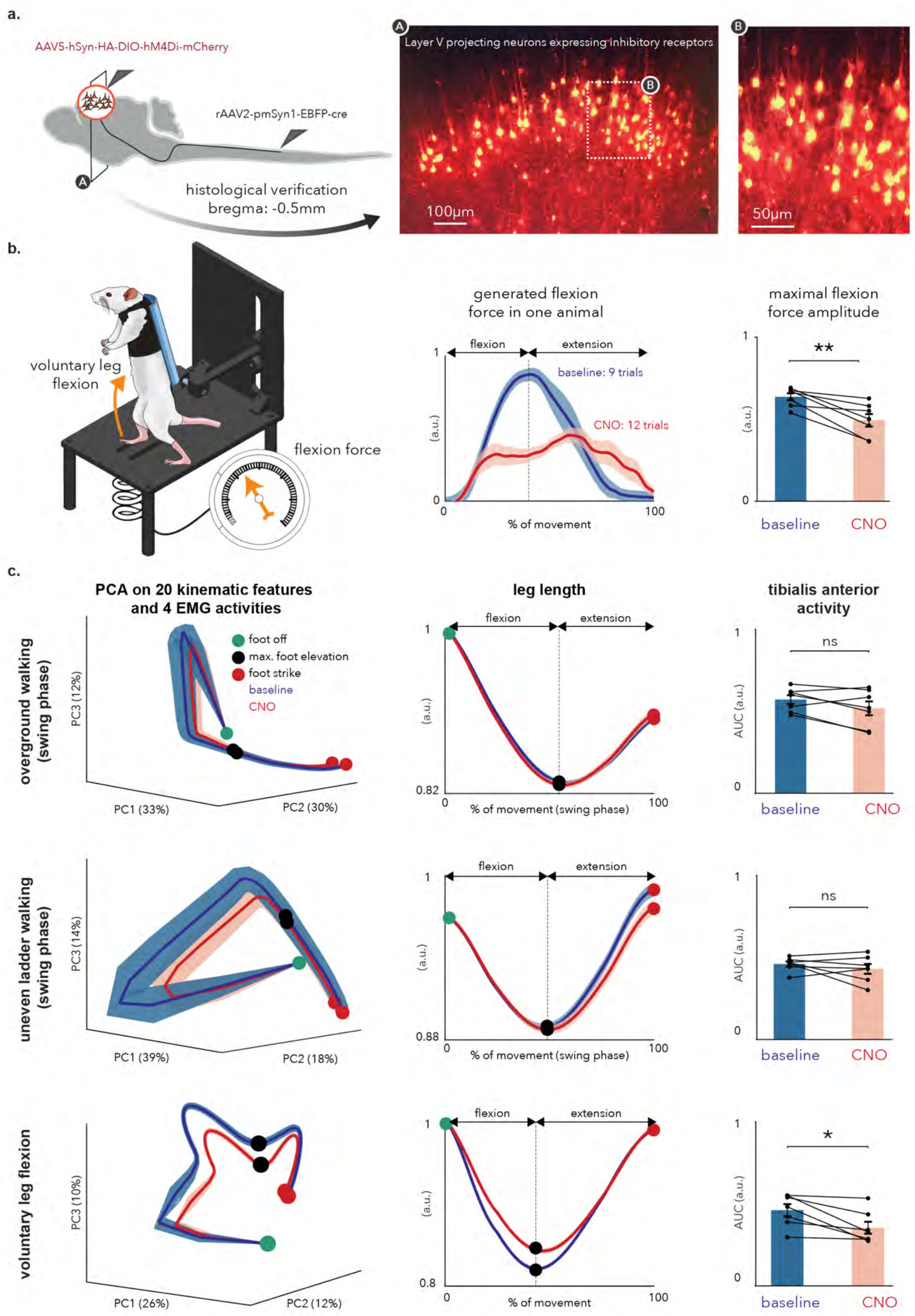

Figure 5.5 | Inhibition of the lumbar CST in rodents

a. Intersectional viral strategy targeting the lumbar corticospinal tract. **b.** Left panel: design of a voluntary leg flexion task in rodent. Middle panel: representative example in one animal after CNO administration. Right panel: decrease in generated force after CNO administration in 7 rats. **c.** Comparison of CNO administration effect in 3 different tasks, namely over-ground walking, uneven ladder and voluntary leg flexion task. Left panel: principal component analysis (PCA) performed on 20 kinematic features and activities of four muscles (tibialis anterior, medial gastrocnemius, iliopsoas and semitendinosus). Note that the stance phase was excluded in the locomotion tasks as there was none during the voluntary leg flexion task (see text). Middle panel: one representative kinematic feature (length of the leg) explaining the PCA variance in all the 7 rats. Right panel: one representative muscle activity explaining the variance in the PC space in all the 7 rats. All the plots show the mean ± sem. Statistically significance (Wilcoxon sign rank test) are shown with * for p-value ≤ 0.05, ** for p-value ≤ 0.01, "ns" meaning statistically non-significant (p>0.05).

The decrease in leg muscular activity during voluntary leg movement compared to locomotion could reflect higher cortical modulation through the layer V projecting neurons of lumbar spinal activity. However, this conclusion must be thoroughly validated, as this was a pilot study with only 7 rats. Indeed, many points have to be further addressed. First, the effect of CNO alone was not performed in control animals that did not receive DREADDs receptors, and CNO alone produces behavioral effects in healthy rats (MacLaren et al. 2016). A control study is thus crucial. An alternative to CNO is its metabolite clozapine (Gomez et al. 2017) or deschloroclozapine (Nagai et al. 2020). Therefore, the same experiment could be repeated by testing this drugs instead of the CNO. Second, the temporal precision of hM4Di activation might be too slow compared to the duration of the experiment. Therefore, optogenetics—at least in rats—seems more suitable to see an immediate effect of cells inhibition (Wiegert et al. 2017).

Translation of the DREADDs experiment in nonhuman primates was not successful (data not shown). The main reason was a poor expression of hM4Di receptors. This issue can be tackle by using a new engineered hM4Di non-fused with *mCherry* tag (Galvan et al. 2019). This technique allows a robust protein insertion into cell membrane comparable to rodents (Galvan et al. 2019). Nonetheless, the points addressed above still remain. Although local microinjection of CNO inhibits hM4Di-positive neurons in the primate basal ganglia (Deffains et al. 2020), systemic effects of CNO alone must be carefully assessed in primates (Raper et al. 2017). In our primate experiment, we saw a behavioral effect after CNO administration, whereas the hM4Di was almost not present (~3-4 cells per histological sections). The behavioral effects encompassed longer stance duration and smaller steps during over-ground walking as well as missing rungs in the ladder. This result emphasizes the careful experiment design involving CNO administration (MacLaren et al. 2016). Nonetheless, a recent study, in mice, shows that inhibition mediated by hM4Di of the layer V projecting neurons to the cervical spinal cord decreased correct paw placement (Wang et al. 2018). Overall, it is reasonable to assume that layer V neurons encode for fine adaptive locomotion (Serradj et al. 2014). Ideally, combination of selective inhibition with their corresponding neural activity would definitively help to extend our understanding of locomotion encoding at the cellular level.

5.1.4. Technological limitations in single cell encoding

Nature Journal defines '*neural encoding*' as: "*the study of how neurons represent information with electrical activity (action potentials) at the level of individual cells or in networks of neurons. Studies of neural encoding aim to characterize the relationship between sensory stimuli or behavioral output and neural signals*" [2]. Silencing neurons helps to characterizing the relationship between neural signals and behavioral output. Assuming that specific neural silencing perfectly works, does it mean that these particular neurons encode an output behavior? In my view, it does not. These neurons could be a relay layer. Ultimately, the combination of methodological investigation, such as silencing neurons, spiking activity and calcium-imaging, would definitively help for our understanding. To date, only few studies have performed *in-vivo* calcium imaging in primates (Heider et al. 2010; Seidemann et al. 2016; Trautmann et al. 2019). Only in the latter study were motor cortical areas assessed, and only at the dendritic level (not the soma). Moreover, technical issues and or challenges were reported in all three studies. Few of them are listed as followed: 1) chamber and microscopy geometry; (2) longevity of optical access; (3) image processing (blur images) and (4) neuron identification (O'Shea et al. 2017). Finally but yet importantly, viral transfection efficiency is a factor to be taken into consideration as for most of the primate studies. Few cells were transfected, possibly due to the presence of pre-existing neutralizing antibodies to the viral vectors (Galvan et al. 2017). Thus, screening the animals for neutralizing antibodies could minimize this problem. Future advances in biotechnology might tackle these issues, and we might be able to better define the identity (molecular, cellular, physiological) and function of the primate CST system. These advances include the possibility of selective neuron block via intersectional viral strategy (Kinoshita et al. 2012) combined with calcium imaging (Trautmann et al. 2019). Together, they might give further insights of the CST function (Lemon 2019). Supposing that we are able to precisely monitor and silence every type of neuron, will it finally answer the question of a causal link between neuronal behavior and movement ? In the next chapter, I will briefly describe a perspective about neural code. This perspective is proposed by Jazayeri and Afraz in 2017 (Jazayeri and Afraz 2017).

5.1.5. Searching for the neural code by exploring the neural manifold

Classically, direct perturbation of neural activity via micro-stimulation or neural silencing is qualified as causal, but conceptually, a causal inference must reside in randomization of the variables (neural inputs, perturbation, stimuli, etc); otherwise they are correlational. In the motor system, the layers in the causal chain are numerous, therefore limiting the inferences made from causal observation about the function of motor neurons. In an experiment where a random perturbation is applied to a given variable (e.g. neural activity of a particular neuron), their relationship is causal. However, the relationship between all the variables that are not randomized (e.g. brain activity in another region not directly perturbed) is still correlational. Therefore, the choice of correlation and causal inference depends on the variable of interest and not of the experimental methods. As primates show advanced sensorimotor attributes encompassing high-level interaction between neural population and circuits, a one-to-one causal map proves to be too challenging. Therefore, perturbations of the neural manifold might help the understanding of the neural code. However, this perturbation must respect the intrinsic patterns of activity. Next-generation of tools might thus go beyond targeting individual neurons types and/or neuronal population but should be able to (1) randomize correlated patterns of activity and (2) navigate into the neural space through controlled perturbations

---

[2] https://www.nature.com/subjects/neural-encoding

5.2. NEUROPROSTHETICS FOR SPINAL CORD INJURY

In the context of spinal cord injury (SCI), we designed personalized neuroprosthetics consisting of two soft epidural arrays (8 electrodes each) covering the lumbar spinal cord. Previous research conducted by the laboratory proposed a brain-spine interface (BSI) that converts the cortical neuronal activity from M1 to spatiotemporal spinal stimulation patterns that alleviate gait deficit after SCI (Capogrosso et al. 2016). Although the method showed remarkable effect, the spinal arrays were designed in an universal fashion and could trigger ‘only’ flexion or extension of the leg. BSI efficacy was thus not assessed in complex environment such as staircase or obstacles. We proposed thereby subject-specific imaging-based spinal arrays that target each individual dorsal roots in order to recruit multiple muscles, increasing therefore the selectivity {Greiner:jh}. The custom-made spinal arrays were implanted and tested in one anesthetized animal. Although the implants showed remarkable specificity, the challenges of long-term durability persist. I will thus briefly discuss future application of spinal epidural electrical stimulation (EES).

5.2.1. Epidural electrical stimulation: a long clinical story

Historically, spinal EES was already applied for the treatment of chronic pain in the 1960s but was recommended for treatment of motor disorders by Guillaume-Benjamin Duchenne in 1855 (Siegfried et al. 1978). Amelioration of quality of life was demonstrated after acute and chronic implantation of EES devices at cervical level in patients with multiple sclerosis, SCI and stroke in the late 1970s and early 1980s (Siegfried et al. 1978; Campos et al. 1981; Siegfried et al. 1981; Barolat-Romana et al. 1985; Waltz et al. 1987; Cioni et al. 1989). In 1998, spinal EES efficiency, reported in 1336 patients suffering from multiple motor disabilities (SCI, dystonia, cerebral palsy, etc), depends on the tuning parameters (polarity, frequency of stimulation and field configuration) (Waltz 1998). In paraplegic patients, continuous stimulations at the lumbosacral level (Harkema et al. 2011; Angeli et al. 2018) might show less beneficial outcomes than stimulation patterns coinciding with the intended movement (i.e. spatiotemporal stimulations) (Wagner et al. 2018).

5.2.2. Future directions: combinatorial therapies

The above study (Wagner et al. 2018) utilized commercial spinal arrays normally used for chronic pain treatment. Therefore, the efficiency of EES might be enhanced with subject-specific neuroprosthetics (Borton et al. 2013; Courtine and Bloch 2015). However, such neuroprosthetics must carefully be assessed and validated *in-vitro* and in animal models (Schiavone et al. 2020). Moreover, the commercialization process might take several years. Therefore, the SCI research community can combine different biological therapies with available clinical EES. Ultimately, the combinatorial therapy might include stem-cell grafts (Koffler et al. 2018; Rosenzweig et al. 2018), chemical components (Anderson et al. 2018; Kucher et al. 2018; Rosenzweig et al. 2019) and spatiotemporal EES (Wagner et al. 2018). This proposed approach will only be successful with a dedicated multidisciplinary team of neuroscientists, biologists, engineers, neurosurgeons, and neurologists (Courtine and Sofroniew 2019). Validation of such combinatorial approach must nevertheless be assessed in animal models from which the therapeutic strategy have emerged through fundamental research (Rouiller 2012).

5.3. BIBLIOGRAPHY

Anderson MA, Shea TMOX, Burda JE, Ao Y, Barlatey SL, Bernstein AM, et al. Required growth facilitators propel axon regeneration across complete spinal cord injury. Nature Publishing Group. Springer US; 2018 Aug 23;274(7723):1–21.

Angeli CA, Boakye M, Morton RA, Vogt J, Benton K, Chen Y, et al. Recovery of Over-Ground Walking after Chronic Motor Complete Spinal Cord Injury. N Engl J Med. 2018 Sep 27;379(13):1244–50.

Asboth L, Friedli L, Beauparlant J, Martinez-Gonzalez C, Anil S, Rey E, et al. Cortico–reticulo–spinal circuit reorganization enables functional recovery after severe spinal cord contusion. Nat Neurosci. Springer US; 2018 Mar 19;:1–19.

Barolat-Romana G, Myklebust JB, Hemmy DC, Myklebust B, Wenninger W. Immediate effects of spinal cord stimulation in spinal spasticity. J Neurosurg. 3rd ed. Journal of Neurosurgery Publishing Group; 1985 Apr;62(4):558–62.

Beloozerova IN, Sirota MG. The role of the motor cortex in the control of accuracy of locomotor movements in the cat. J Physiol (Lond). John Wiley & Sons, Ltd; 1993 Feb;461(1):1–25.

Borton D, Micera S, Millán JDR, Courtine G. Personalized neuroprosthetics. Sci Transl Med. American Association for the Advancement of Science; 2013 Nov 6;5(210):210rv2–210rv2.

Campos RJ, Dimitrijevic MM, Faganel J, Sharkey PC. Clinical evaluation of the effect of spinal cord stimulation on motor performance in patients with upper motor neuron lesions. Appl Neurophysiol. Karger Publishers; 1981;44(1-3):141–51.

Capogrosso M, Milekovic T, Borton D, Wagner F, Moraud EM, Mignardot J-B, et al. A brain–spine interface alleviating gait deficits after spinal cord injury in primates. Nature. Nature Publishing Group; 2016 Nov 10;539(7628):284–8.

Chaisanguanthum KS, Shen HH, Sabes PN. Neural Representation and Causal Models in Motor Cortex. J Neurosci. Society for Neuroscience; 2017 Mar 22;37(12):3413–24.

Cioni B, Meglio M, Zamponi A. Effect of spinal cord stimulation on motor performances in hemiplegics. Stereotact Funct Neurosurg. Karger Publishers; 1989;52(1):42–52.

Cisek P, Kalaska JF. Neural Correlates of Reaching Decisions in Dorsal Premotor Cortex: Specification of Multiple Direction Choices and Final Selection of Action. Neuron. 2005 Mar;45(5):801–14.

Courtine G, Bloch J. Defining Ecological Strategies in Neuroprosthetics. Neuron. 2015 Apr;86(1):29–33.

Courtine G, Sofroniew MV. Spinal cord repair: advances in biology and technology. Nat Med. Nature Publishing Group; 2019 Jun;25(6):898–908.

Deffains M, Nguyen TH, Orignac H, Biendon N, Dovero S, Bezard E, et al. In vivo electrophysiological validation of DREADD-based modulation of pallidal neurons in the non-human primate. Eur J Neurosci. John Wiley & Sons, Ltd; 2020 May 11;328:243–13.

DiGiovanna J, Dominici N, Friedli L, Rigosa J, Duis S, Kreider J, et al. Engagement of the Rat Hindlimb Motor Cortex across Natural Locomotor Behaviors. J Neurosci. Society for Neuroscience; 2016 Oct 5;36(40):10440–55.

Donoghue JP, Wise SP. The motor cortex of the rat: cytoarchitecture and microstimulation mapping. J Comp Neurol. John Wiley & Sons, Ltd; 1982 Nov 20;212(1):76–88.

Drew T. Motor cortical cell discharge during voluntary gait modification. Brain Research. 1988 Aug 2;457(1):181–7.

Evarts EV. Temporal patterns of discharge of pyramidal tract neurons during sleep and waking in the monkey. Journal of Neurophysiology. 1964 Mar;27:152–71.

Evarts EV. Relation of pyramidal tract activity to force exerted during voluntary movement. Journal of Neurophysiology. 1968 Jan;31(1):14–27.

Fitzsimmons NA. Extracting kinematic parameters for monkey bipedal walking from cortical neuronal ensemble activity. Front Integr Neurosci. Frontiers; 2009;3:1–19.

Friedli L, Rosenzweig ES, Barraud Q, Schubert M, Dominici N, Awai L, et al. Pronounced species divergence in corticospinal tract reorganization and functional recovery after lateralized spinal cord injury favors primates. Sci Transl Med. American Association for the Advancement of Science; 2015 Aug 26;7(302):302ra134–4.

Galvan A, Caiola MJ, Albaugh DL. Advances in optogenetic and chemogenetic methods to study brain circuits in non-human primates. J Neural Transm. Springer Vienna; 2017 Feb 25;112(Suppl 2):1–17.

Galvan A, Raper J, Hu X, Paré JF, Bonaventura J, Richie CT, et al. Ultrastructural localization of DREADDs in monkeys. Eur J Neurosci. 2019 May 7;:ejn.14429–20.

Gerfen CR, Economo MN, Chandrashekar J. Long distance projections of cortical pyramidal neurons. J Neuro Res. 2016 Nov 12;96(9):1467–75.

Gomez JL, Bonaventura J, Lesniak W, Mathews WB, Sysa-Shah P, Rodriguez LA, et al. Chemogenetics revealed: DREADD occupancy and activation via converted clozapine. Science. American Association for the Advancement of Science; 2017 Aug 4;357(6350):503–7.

Harkema S, PhD YG, MD JH, PhD PJB, PhD CA, PhD YC, et al. Effect of epidural stimulation of the lumbosacral spinal cord on voluntary movement, standing, and assisted stepping after motor complete paraplegia: a case study. The Lancet. Elsevier Ltd; 2011 Jun 4;377(9781):1938–47.

Heider B, Nathanson JL, Isacoff EY, Callaway EM, Siegel RM. Two-Photon Imaging of Calcium in Virally Transfected Striate Cortical Neurons of Behaving Monkey. Lowenstein PR, editor. PLoS ONE. Public Library of Science; 2010 Nov 4;5(11):e13829–13.

Jazayeri M, Afraz A. Navigating the Neural Space in Search of the Neural Code. Neuron. Elsevier Inc; 2017 Mar 8;93(5):1003–14.

Kaufman MT, Churchland MM, Ryu SI, Shenoy KV. Cortical activity in the null space: permitting preparation without movement. Nat Neurosci. Nature Publishing Group; 2014 Feb 2;17(3):440–8.

Kinoshita M, Matsui R, Kato S, Hasegawa T, Kasahara H, Isa K, et al. Genetic dissection of the circuit for hand dexterity in primates. Nature. Nature Publishing Group; 2012 Jul 3;487(7406):235–8.

Koffler J, Zhu W, Qu X, Platoshyn O, Dulin JN, Brock J, et al. Biomimetic 3D-printed scaffolds for spinal cord injury repair. Nat Med. Springer US; 2018 Dec 22;25(2):1–12.

Kucher K, Johns D, Maier D, Abel R, Badke A, Baron H, et al. First-in-Man Intrathecal Application of Neurite Growth-Promoting Anti-Nogo-A Antibodies in Acute Spinal Cord Injury. Neurorehabilitation and Neural Repair. 2018 Jun 29;32(6-7):578–89.

Lebedev MA, Ossadtchi A, Mill NA, Urpí NA, Cervera MR, Nicolelis MAL. Analysis of neuronal ensemble activity reveals the pitfalls and shortcomings of rotation dynamics. Sci Rep. Nature Publishing Group; 2019 Dec 12;9(1):18978–14.

Lemon R. Recent advances in our understanding of the primate corticospinal system. F1000Res. 2019;8.

Lemon R, Kraskov A. Starting and stopping movement by the primate brain. Brain and Neuroscience Advances. 2019 Mar 15;3(23):239821281983714–6.

Lemon RN. Descending Pathways in Motor Control. Annu Rev Neurosci. Annual Reviews; 2008 Jul;31(1):195–218.

MacLaren DAA, Browne RW, Shaw JK, Krishnan Radhakrishnan S, Khare P, Espana RA, et al. Clozapine N-Oxide Administration Produces Behavioral Effects in Long-Evans Rats: Implications for Designing DREADD Experiments. eNeuro. eneuro; 2016 Sep 8;3(5):1–39.

Mountcastle VB, of WTJ. Cortical neuronal mechanisms in flutter-vibration studied in unanesthetized monkeys. Neuronal periodicity and frequency discrimination. Journalsphysiologyorg 1969 May;32(3):452–84.

Mulliken GH, Musallam S, Andersen RA. Forward estimation of movement state in posterior parietal cortex. PNAS. National Academy of Sciences; 2008 Jun 17;105(24):8170–7.

Nagai Y, Miyakawa N, Takuwa H, Hori Y, Oyama K, Bin Ji, et al. Deschloroclozapine, a potent and selective chemogenetic actuator enables rapid neuronal and behavioral modulations in mice and monkeys. Nat Neurosci. Springer US; 2020 Jun 18;:1–18.

Ninomiya T, Inoue K-I, Hoshi E, Takada M. Layer specificity of inputs from supplementary motor area and dorsal premotor cortex to primary motor cortex in macaque monkeys. Sci Rep. Springer US; 2019 Nov 23;9(1):1–11.

O'Shea DJ, Trautmann E, Chandrasekaran C, Stavisky S, Kao JC, Sahani M, et al. The need for calcium imaging in nonhuman primates: New motor neuroscience and brain-machine interfaces. Exp Neurol. 2017 Jan;287:437–51.

Omlor W, Wahl A-S, Sipilä P, Lütcke H, Laurenczy B, Chen I-W, et al. Context-dependent limb movement encoding in neuronal populations of motor cortex. Nat Commun. Springer US; 2019 Oct 15;10(1):1–16.

Perich MG, Conti S, Badi M, Bogaard A, Barra B, Wurth S, et al. Motor cortical dynamics are shaped by multiple distinct subspaces during naturalistic behavior. bioRxiv. Cold Spring Harbor Laboratory; 2020 Aug 3;94:2020.07.30.228767.

Perich MG, Gallego JA, Miller LE. A Neural Population Mechanism for Rapid Learning. Neuron. Elsevier Inc; 2018 Oct 16;100(4):1–21.

Raper J, Daniels JS, Morrison RD, Howell L, Bachevalier J, Wichmann T, et al. Metabolism and Distribution of Clozapine-N-oxide: Implications for Nonhuman Primate Chemogenetics. ACS Chem Neurosci. 2017 Mar 21;:acschemneuro.7b00079–18.

Rathelot J-A, Strick PL. Muscle representation in the macaque motor cortex: an anatomical perspective. Proc Natl Acad Sci USA. National Acad Sciences; 2006 May 23;103(21):8257–62.

Rathelot J-A, Strick PL. Subdivisions of primary motor cortex based on cortico-motoneuronal cells. Proc Natl Acad Sci USA. National Acad Sciences; 2009 Jan 20;106(3):918–23.

Rosenzweig ES, Brock JH, Lu P, Kumamaru H, Salegio EA, Kadoya K, et al. Restorative effects of human neural stem cell grafts on the primate spinal cord. Nat Med. Nature Publishing Group; 2018 Feb 26;21:9334.

Rosenzweig ES, Salegio EA, Liang JJ, Weber JL, Weinholtz CA, Brock JH, et al. Chondroitinase improves anatomical and functional outcomes after primate spinal cord injury. Nat Neurosci. Springer US; 2019 Jun 15;14(8):1–13.

Roth BL. DREADDs for Neuroscientists. Neuron. 2016 Feb;89(4):683–94.

Rouiller EM. What can we learn from animal models? Routledge Handbook of Motor Control and Motor Learning. 2012.

Schiavone G, Fallegger F, Kang X, Barra B, Vachicouras N, Roussinova E, et al. Soft, Implantable Bioelectronic Interfaces for Translational Research. Adv Mater. John Wiley & Sons, Ltd; 2020 Mar 16;24:1906512–10.

Seidemann E, Chen Y, Bai Y, Chen SC, Mehta P, Kajs BL, et al. Calcium imaging with genetically encoded indicators in behaving primates. Elife. 2016 Jul 21;5:3771.

Semedo JD, Zandvakili A, Machens CK, Yu BM, Kohn A. Cortical Areas Interact through a Communication Subspace. Neuron. Elsevier Inc; 2019 Apr 3;102(1):249–259.e4.

Serradj N, Paixão S, Sobocki T, Feinberg M, Klein R, Kullander K, et al. EphA4-mediated ipsilateral corticospinal tract misprojections are necessary for bilateral voluntary movements but not bilateral stereotypic locomotion. J Neurosci. 2014 Apr 9;34(15):5211–21.

Sheikh IS, Keefe KM, Sterling NA, Junker IP, Eneanya CI, Liu Y, et al. Retrogradely Transportable Lentivirus Tracers for Mapping Spinal Cord Locomotor Circuits. Frontiers in Neural Circuits. Frontiers; 2018 Jul 25;12:2287–13.

Shenoy KV, Sahani M, Churchland MM. Cortical Control of Arm Movements: A Dynamical Systems Perspective. Annu Rev Neurosci. 2013 Jul 8;36(1):337–59.

Siegfried J, Krainick JU, Haas H, Adorjani C, Meyer M, Thoden U. Electrical spinal cord stimulation for spastic movement disorders. Appl Neurophysiol. Karger Publishers; 1978;41(1-4):134–41.

Siegfried J, Lazorthes Y, Broggi G. Electrical spinal cord stimulation for spastic movement disorders. Appl Neurophysiol. Karger Publishers; 1981;44(1-3):77–92.

Takei T, Crevecoeur F, Herter TM, Cross KP, Scott SH. Correlations Between Primary Motor Cortex Activity with Recent Past and Future Limb Motion During Unperturbed Reaching. J Neurosci. Society for Neuroscience; 2018 Sep 5;38(36):7787–99.

Trainito C, Nicolai von C, Miller EK, Siegel M. Extracellular Spike Waveform Dissociates Four Functionally Distinct Cell Classes in Primate Cortex. Current Biology. Elsevier Ltd; 2019 Sep 23;29(18):2973–5.

Trautmann E, O'Shea DJ, Sun X, Marshel JH, Crow A, Hsueh B, et al. Dendritic calcium signals in rhesus macaque motor cortex drive an optical brain-computer interface. 2019 Sep 23;6:1–53.

Wagner FB, Mignardot J-B, Le Goff-Mignardot CG, Demesmaeker R, Komi S, Capogrosso M, et al. Targeted neurotechnology restores walking in humans with spinal cord injury. Nature Publishing Group. Springer US; 2018 Oct 24;563(7729):1–29.

Waltz JM. Spinal Cord Stimulation: A Quarter Century of Development and Investigation. Stereotact Funct Neurosurg. Karger Publishers; 1998 Jul 3;69(1-4):288–99.

Waltz JM, Andreesen WH, Hunt DP. Spinal cord stimulation and motor disorders. Pacing Clin Electrophysiol. John Wiley & Sons, Ltd; 1987 Jan;10(1 Pt 2):180–204.

Wang L, Zhang J, Zhang Y, Yan R, Liu H, Qiu M. Conditional Granger Causality Analysis of Effective Connectivity during Motor Imagery and Motor Execution in Stroke Patients. BioMed Research International. Hindawi Publishing Corporation; 2016 Apr 20;:1–9.

Wang Z, Maunze B, Wang Y, Tsoulfas P, Blackmorea MG. Global connectivity and function of descending spinal input revealed by 3D microscopy and retrograde transduction. J Neurosci. Society for Neuroscience; 2018 Oct 19;:1196–18–40.

Wiegert JS, Mahn M, Prigge M, Printz Y, Yizhar O. Silencing Neurons: Tools, Applications, and Experimental Constraints. Neuron. Elsevier Inc; 2017 Aug 2;95(3):504–29.

- PART 6 -

APPENDIX

6.1. APPENDIX 1

This appendix describes the material and methods used in the pilot experiment presenting intersectional viral tracing and neural silencing using Designer Receptors Exclusively Activated by Designer Drugs (DREADDs) (technique in chapter 5.1.2). This work was performed at the laboratories of Prof. Grégoire Courtine at Campus Biotech, and Prof. Erwan Bezard at Motac neuroscience.

6.1.1. Animal models

Rodent experiments were conducted on adult female Lewis rats (180 to 240g). Housing, surgery, behavioral experiments, and euthanasia were performed in accordance with Swiss Veterinary Law guidelines. All the experimental procedures were approved by the Veterinary Office of the Canton of Geneva (Switzerland).

Nonhuman primate experiments were conducted on four adult macaque monkeys (two females, *Macaca fascicularis*, weighing between 3.3 and 4 kg, and two males, *Macaca mulatta*, weighing between 6.3 and 7.0 kg). Experiments were approved by the Institutional Animal Care and Use Committee of Bordeaux (CE50, France) and performed in accordance with the European Union directive on the protection of animals used for scientific aims in an AAALAC-accredited facility. Each monkey was housed in cages accepted by European guidelines (2m x 1.6m x 1.26m) with play items and soft music. The animals had free access to water and received food *ab libitum*.

6.1.2. Surgeries

The rats were anesthetized with isoflurane inhalation (1.0 - 2.0%). Prior to induction, the following medication was injected subcutaneously: 0.03ml of Dorbene and 0.5 ml NaCl 0.9% Rimadyl (Carprophen). The post-operative care consisted of analgesia (buprenorphine, Essex, 0.01 – 0.05 mg/kg, s.c.) and antibiotic (Baytril 2.5%, Bayer Health Care AG, Germany, 5-10 mg per kg, s.c. or Clamoxyl, Zoetis, France, 0.5mL per kg, s.c.) administration for 5 days following the surgeries. Similarly to chapter 2.3, bipolar intramuscular electrodes were implanted for electromyographic recording in the iliopsoas, medial gastrocnemius, semitendinosus, and tibialis anterior. The wires were connected to circular percutaneous Omnetics connectors cemented to the skulls of the animals. Virus delivery was performed through stereotaxic injections using glass pipettes, driven by a nanoliter pump (UMP3-1 injector and Micro4 Controller, WPI system) at a rate of 3nL/s. To prevent any reflux, the needle was withdrawn 2 minutes post-injection. Twelve 1mm rostro-caudal spaced injections (6 per side, 250nL per injection sites) of the retrograde cre vectors were performed in the spinal cord (-1.5mm dorsoventral; ±0.7mm mediolateral) at L1-L2 vertebral lumbar level. Twelve cortical injections (6 per hemisphere, 250nL per site) were performed (rostro-caudal: -0.5mm, -1.5mm and -2.5mm; mediolateral: ±2mm and ±3mm from bregma and -1.4mm dorsoventral). One hemisphere received the viral tracers (Syn-GFP and TdTomato), whereas the other received the DREADDs receptors (hM4Di).

In monkeys, all surgical procedures were performed under general anesthesia of 1-3% isolflurane, with hydration provided via continuous intravenous infusion of Ringer solution (5ml / kg / h). One day before the surgery, the animals received antibiotics (Duphamox, 15mg kg-1, subcutaneous injection). Prior to the surgery, monkeys were sedated with atropine (0.04 mg kg-1) and ketamine (10 mg kg-1, intramuscular injection). Anesthetic cream (Xylocain) was applied before the subjects were intubated. The post-op care consisted of daily administration of painkillers (Meloxicam, 0.2mg kg-1, subcutaneous injection) for 3 days, and 6 days of daily antibacterial administration (Enroflaxine, 5mg kg-1, subcutaneous injection and Ceftriaxone sodium 100mg kg-1, intramuscular injection). Microinjections were performed with the same material and protocol as for rodents. Apart from the glass pipette, we used 10µl Hamilton syringes and 33G needles. In the female macaque monkeys, ten unilateral spinal microinjections were performed at vertebral level L1, spaced by 1mm, at 1mm from the midline, and -3mm dorsoventrally to target the ventral horn of the spinal cord. About 30 cortical microinjections were performed (contralateral to the spinal injections) in the leg primary motor cortex, following (Rosenzweig et al. 2009) protocol. The syringe contained a mixture of the 3 viruses: tdTomato, Syn-GFP, and DREADDs receptors. In the male macaque monkeys, about 40 bilateral spinal microinjections (20 per side) were performed at vertebral level L1 and L2, spaced by 1mm, at 1mm from the midline, and at -3mm dorsoventral depth. About 30 microinjections were performed in one hemisphere with the viral tracer cocktail (Syn-Myc and tdTomato), while ~30 microinjections were performed in the other hemisphere with the DREADDs receptors.

6.1.3. Viral vectors

All the viruses are summarized in the following table:

	SEROTYPE	PROMOTER	NAME	TITER*	ANIMALS	ORIGIN
Cre	rAAV2	pmSyn1	EBFP - Cre	6.87 E12 GC/mL	rats	Addgene (51507)
	AAV9	CMV	Cre	1.15 E15 vg/mL	female macaque monkeys	Aebischer's laboratory (EPFL)
	rAAV2	CMV	Cre	2.68 E13 vg/mL	male macaque monkeys	Aebischer's laboratory (EPFL)
tdTomato	AAV1-5	CAG	DIO-tdTomato-WPRE	6.5 E12 vg/mL	rats	Aebischer's laboratory (EPFL)
	AAV1	CAG	DIO-tdTomato-WPRE	6.5 E12 vg/mL	female macaque monkeys	Aebischer's laboratory (EPFL)
	AAV5	CAG	DIO-tdTomato-WPRE	6.5 E12 vg/mL	male macaque monkeys	Aebischer's laboratory (EPFL)
Synapsin	AAV1**	CAG	DIO-Syn-GFP	6.5E12 vg/mL	rats and female macaque monkeys	Aebischer's laboratory (EPFL)
	AAV1	CAG	DIO-Syn-Myc	6.5E12 vg/mL	male macaque monkeys	Aebischer's laboratory (EPFL)
	AAV5	CAG	DIO-Syn-GFP	6.48 E12 vg/mL	rats	Aebischer's laboratory (EPFL)
DREADDs	AAV5	hSyn-HA	DIO-hM4Di-mCherry	1.12 E13 vg/mL	rats	Aebischer's laboratory (EPFL)
	AAV1	hSyn-HA	DIO-hM4Di-mCherry	4.9E12 VG/ml	female macaque monkeys	Aebischer's laboratory (EPFL)
	AAV5	hSyn-HA	DIO-hM4Di-mCherry	1.12 E13 vg/mL	male macaque monkeys	Aebischer's laboratory (EPFL)

Table 6.1 | **Viral vectors**

All viral vectors used are listed in this table. Most were supplied by the laboratory of Prof. Patrick Aebischer and Dr. Bernard Schneider from EPFL.

* Physical titer is a measurement of how much virus is present, and is expressed as the amount of viral genome per ml (vg/ml), or as genome copies per mL (GC/ml).

** Could be trans-synaptic.

6.1.4. DREADD-mediated inactivation experiments

Rat testing was performed 50 minutes after intraperitoneal injection of clozapine-N-Oxide (CNO) (5 mg/kg, diluted in saline). Prior to CNO testing, all the rats were recorded without any injection.

Monkey testing was performed 15 minutes, 60 minutes, 90 minutes and 180 minutes after CNO injection (5 mg/kg or 10mg/kg). The injection was performed either intravenously (saphenous vein) or subcutaneously.

6.1.5. Kinematic and muscle activity recordings

All rat procedures are detailed in (Dominici et al. 2012; Asboth et al. 2018). Briefly, during over-ground and ladder conditions, bilateral leg kinematics were captured using the Vicon high-speed motion capture system (Vicon Motion Systems, UK), consisting of 12 infrared cameras (200 Hz). Reflective markers were attached bilaterally at the iliac crest, the greater trochanter (hip joint), the lateral condyle (knee joint), the lateral malleolus (ankle), and the distal end of the fifth metatarsophalangeal joint. The same procedure was applied during voluntary hip flexion (custom-made CAD platform with force sensor (DFS-BTA sensor, Vernier) connected to Vicon system) but only on one leg. During the three tasks, the four muscles were recorded simultaneously with kinematics. The signals (2 kHz) were amplified, filtered (10–1,000 Hz butter worth bandpass), stored, and analyzed offline to compute the amplitude, duration, and timing of individual bursts.

The monkey kinematics were recorded as previously described in chapter 2.1.2.

6.1.6. Perfusion and histological preparation

Animals were deeply anesthetized with pentobarbital (50mg/ml; 0.5ml; intraperitoneal) and transcardially perfused with about 100ml PBS with heparin followed by 250ml of cold 4% paraformaldehyde (PFA) pH 7.4. The brains and spinal cords were dissected out and were treated with an overnight post-mortem perfusion in PFA4% at 4°C. The tissue was then transferred to a 30% sucrose solution in PBS, after which it was cut to a thickness of 40μm on a cryostat.

6.1.7. Immunohistochemistry

Free-floating sections were first washed 3x in 0.1M PBS and in 5% normal goat serum with 0.3% triton. Sections were then incubated with a primary antibody (mouse anti-NeuN (1:300, Chemicon #MAB5262, Millipore Corporation, USA) overnight at 4°C. Sections were then washed three times in 0.1 M PBS and incubated with a secondary antibody (Alexa Fluor 647, goat anti-mouse

#A21235; Molecular Probes, Life Technologies, USA). Then, the sections were washed for 10 minutes in PBS 0.1M, labelled over 15 minutes with DAPI (1:5000 in PBS 0.1M), and washed again in PBS 0.1M. Finally, the sections were mounted on histological slides and covered with a cover glass glued with Mowiol. All histological sections were acquired at 10x and 20x with a slide scanner microscope (Olympus VS120).

6.1.8. Synaptic connectome in the spinal gray matter analysis

We first used Fiji (version 2.0.0) to process the histological images. For each spinal segment, we then extracted the ten best-quality histological slices (not torn up, good staining) only in the green channel (Syn-GFP). We saved them in jpeg format. We then used a custom-made densitometry analyzer in MATLAB that allowed the computation of the synaptic density. We first converted the image into a binary format and manually selected a threshold (the same for all the images). A circularity criterion C ($C=4*\pi*A/P^2$, where C is the circularity, A the area of pixels that connect to each other, and P the perimeter of the same pixels) was used to minimize the noise, as the threshold was not sufficient (**Figure 6.1**).

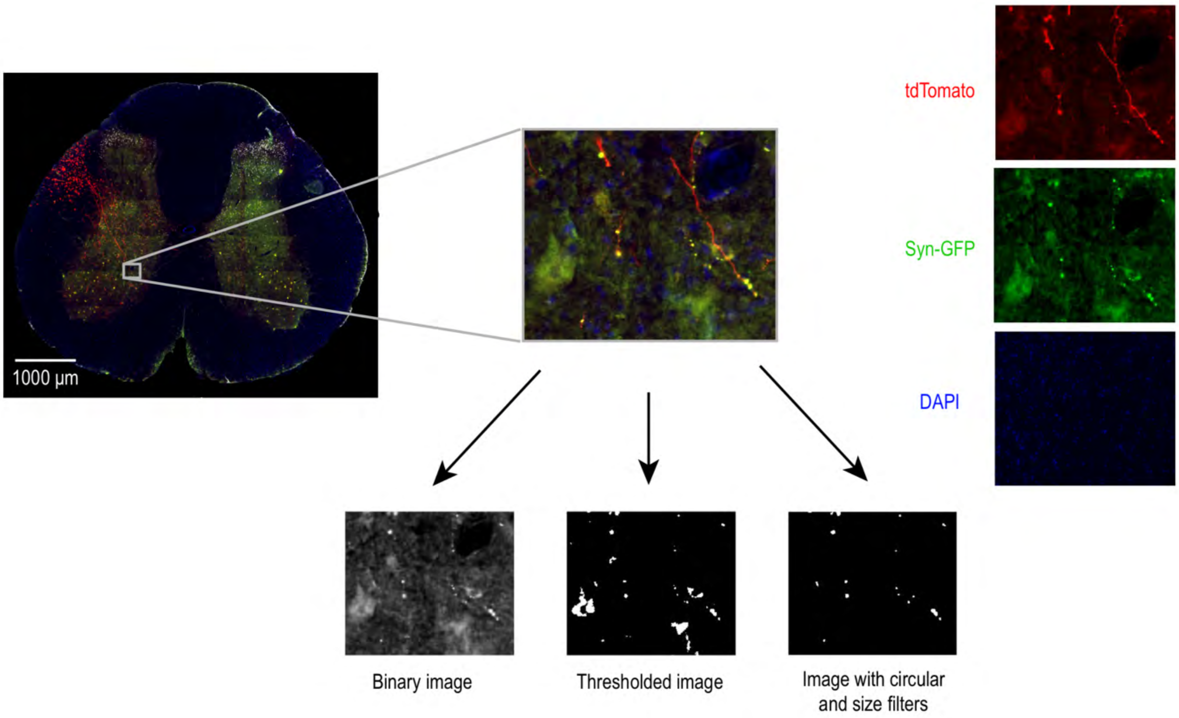

Figure 6.1 | **Synaptic density analysis pipeline**

The semi-automated image analyzer optimized the signal-to-noise ratio after applying a threshold and filters (size and circular).

6.1.9. Bibliography

Asboth L, Friedli L, Beauparlant J, Martinez-Gonzalez C, Anil S, Rey E, et al. Cortico–reticulo–spinal circuit reorganization enables functional recovery after severe spinal cord contusion. Nat Neurosci. Springer US; 2018 Mar 19;:1–19.

Dominici N, Keller U, Vallery H, Friedli L, van den Brand R, Starkey ML, et al. Versatile robotic interface to evaluate, enable and train locomotion and balance after neuromotor disorders. Nat Med. 2012 Jul;18(7):1142–7.

Rosenzweig ES, Brock JH, Culbertson MD, Lu P, Moseanko R, Edgerton VR, et al. Extensive spinal decussation and bilateral termination of cervical corticospinal projections in rhesus monkeys. J Comp Neurol. Wiley Subscription Services, Inc., A Wiley Company; 2009 Mar 10;513(2):151–63.

- PART 7 -

CURRICULUM VITAE

SIMON BORGOGNON

University of Fribourg, Department of Neuroscience and Movement Sciences,
Chemin du Musee 5, CH-1700 Fribourg, Switzerland
simon.borgognon@gmail.com

November 2020

EDUCATION

PhD in Medical Sciences, cluster in Neuroscience 2016 – 2020

- University of Fribourg, Department of Neuroscience and Movement Sciences Fribourg, Switzerland & Lemanic Neuroscience Doctoral School
- Thesis title: *Neural population dynamics in premotor, motor and somatosensory cortices during locomotion in primates*
- Directors: Prof. E.M Rouiller & Prof. G. Courtine

MSc of Science in Neuro & developmental biology 2013 – 2015

- University of Fribourg, Department of Medicine, Fribourg, Switzerland
- Thesis title: *Transplantation of autologous neural cell ecosystems as therapy for Parkinson's disease: a preclinical study*
- Director: Prof. E.M Rouiller

BSc of Science in Biology 2009 – 2013

- University of Fribourg, Department of Medicine, Fribourg, Switzerland
- Thesis title: *Brain plasticity following neonatal hippocampal lesion in monkeys : quantitative analyses of c-fos immediate-early gene expression throughout the medial temporal lobe*
- Director: Prof. P. Lavenex

RESEARCH EXPERIENCE

Defitech Center for Interventional Neurotherapies (NeuroRestore), Switzerland & 2020 – present
Swiss Federal Institute of Technology (EPFL), Lausanne, Switzerland &
University Hospital Lausanne (CHUV), Switzerland (CHUV)
Center for Neuroprosthetics and Brain Mind Institute (Prof. G. Courtine)
Department of Clinical Neurosciences (Prof. J. Bloch)
Head of the Translational Division

- Management of non-human primate experiments (mechanisms of recovery after subcortical stroke, cell auto-transplantation after cortical stroke and single cell RNA sequencing after spinal cord injury)
- Supervising PhD students
- Analysis of neural population dynamics during motor behaviors

University of Fribourg, Fribourg, Switzerland & 2016 – 2020
Swiss Federal Institute of Technology (EPFL), Lausanne, Switzerland
Department of Neuroscience and Movement Science (Prof. E.M. Rouiller) &
Center for Neuroprosthetics and Brain Mind Institute (Prof. G. Courtine)
PhD student in Neuroscience

- Aim 1: implementing an universal brain decoder for locomotion and design of personalized neuroprosthetic for spinal cord injury
- Techniques: macaque behavioral training, wireless electrophysiology, brain-spine interface design for spinal cord injury, laboratory surgical suite design
- Aim 2: understanding the neural encoding of locomotion in rodent
- Techniques: viral tracing (intra-spinal and intra-cortical microinjection), electrophysiology recordings during locomotion and voluntary leg movements, advanced histology analysis (CLARITY and automatized densitometry)
- Aim 3: assessing the connectome of the lumbar cortico-spinal tract in primate (work performed at Motac Neuroscience Ltd, Beijing, China)
- Techniques: viral tracing (intra-spinal and intra-cortical microinjection), electrophysiology recordings during locomotion and voluntary leg movements, surgical implantation of intra-cortical, epidural-spinal and intra-muscular electrode

University of Fribourg, Fribourg, Switzerland
Department of Medicine (Prof. E.M. Rouiller) 2015
Laboratory assistant

- Histological assessment of cell graft in the non-human primate striatum
- Fine manual dexterity assessments in non-human primate

Department of Medicine (Prof. C. Bourquin) 2014 - 2015
Animal welfare collaborator

- Management of a specific-pathogen-free (SPF)-like animal mice facility in a laboratory of cancer immunotherapy
- Weekly follow-up of animal well-being

University of Fribourg, Fribourg, Switzerland 2013 – 2015
Department of Medicine (Prof. E.M. Rouiller)
MSc of Science in Neuro & developmental biology

- Manual grasping and control of force in non-human primates before and after biopsy lesion in the prefrontal cortex
- *In-vivo* brain imaging (PET scan, MRI & CT) assessments in non-human primate model of Parkinson's disease after autologous neural cell ecosystem transplantation
- Cortico-bulbar projection following a lesion of the central nervous system in non-human primates
- Fine manual dexterity assessments in non-human primate model of Parkinson's disease after autologous neural cell ecosystem transplantation

University of Fribourg, Fribourg, Switzerland 2009 - 2013
Department of Medicine (Prof. P. Lavenex)
BSc of Science in Biology

- Brain plasticity following neonatal hippocampal lesion in non-human primates: quantitative analysis of immediate-early gene c-fos expression throughout the medial temporal lobe.

PEER-REVIEWED JOURNAL PUBLICATIONS AND PROCEEDINGS

[1] Badi, M.*, **Borgognon, S.*,** O'Doherty, J.E. & Shokur S. # (2020). *Cortical stimulation for somatosensory feedback: translation from nonhuman primates to clinical applications*. Book chapter in: 'Somatosensory Feedback for Neuroprosthetics', ed. Burak Güçlü. Elsevier/Academic Press. In press.

[2] Greiner, N.#, Barra, B., Schiavone, G., James, N., Fallegger, F., **Borgognon, S.**, Lacour, S.P., Bloch, J., Courtine, G. & Capogrosso, M.# (2020). *Recruitment of upper-limb motoneurons with epidural electrical stimulation of the primate cervical spinal cord*. Nature Communication. In press.

[3] **Borgognon, S.#**, Cottet, J., Badoud, S., Bloch, J., Brunet, J.-F. & Rouiller, E.M. (2020). *Cortical Projection From the Premotor or Primary Motor Cortex to the Subthalamic Nucleus in Intact and Parkinsonian Adult Macaque Monkeys: A Pilot Tracing Study.* Frontiers in Neural Circuits. 14, 1193 - 10.

[4] Schiavone, G., Kang, X., Barra, B., Fallegger, F., Vachicouras, N., Roussinova, E., Furfaro, I., Jiguet, S., Seañez, I., **Borgognon, S.**, Rowald, A., Qin, L., Qin, C., Bezard, E., Bloch, J., Courtine, G., M. Capogrosso, M. & Lacour, S.P.# (2020). *A translational framework for implantable soft bioelectronics*. Advanced Materials, , 24, 1906512–10.

[5] **Borgognon, S.***, Cottet, J.*, Moret, V., Chatagny, P., Carrara, L., Fregosi, M., Bloch, J., Brunet, J.-F., Rouiller, E.M.**,# & Badoud, S.** (2019). *Fine Manual Dexterity Assessment After Autologous Neural Cell Ecosystem (ANCE) Transplantation in a Non-human Primate Model of Parkinson's Disease.* Neurorehabilitation and Neural Repair, 33(7).

[6] Fregosi, M., Contestabile, A., Badoud, S., **Borgognon, S.**, Cottet, J., Brunet, J.-F., Bloch, J., Schwab, M.E., & Rouiller, E.M.# (2019). *Corticotectal Projections From the Premotor or Primary Motor Cortex After Cortical Lesion or Parkinsonian Symptoms in Adult Macaque Monkeys: A Pilot Tracing Study*. Frontiers in Neuroanatomy, 13, 1193.

[7] Fregosi M., Contestabile, A., Badoud, S., **Borgognon, S.**, Cottet, J., Brunet, J. F., Bloch, J., Schwab, M.E., Rouiller E.M.# (2018). *Changes of motor corticobulbar projections following different lesion types affecting the central nervous system in adult macaque monkeys.* The European Journal of Neuroscience, 591(suppl. 1), 5453–21.

[8] Badoud, S.*, **Borgognon, S.***, Cottet, J.*, Chatagny, P., Moret, V., Fregosi, M., Kaeser, M., Fortis, E., Schmidlin, E., Bloch, J., Brunet, J.-F. & Rouiller, E.M.# (2017). *Effects of dorsolateral prefrontal cortex lesion on motor habit and performance assessed with manual grasping and control of force in macaque monkeys.* Brain Structure and Function, 222(3), 1193–1206.

[9] **Borgognon, S.***, Cottet, J.*, Moret, V., Chatagny, P., Ginovart, N., Antonescu, C., Bloch, J., Brunet, J.-F., Rouiller, E.M.# & Badoud, S. (2017). *Enhancement of Striatal Dopaminergic Function Following Autologous Neural Cell Ecosystems (ANCE) Transplantation in a Non-Human Primate Model of Parkinson's Disease.* Journal of Alzheimer's Disease & Parkinsonism, 7(5), 1–11.

*co-first authors, #corresponding author, **co-senior authors

PRESENTATIONS

[1] Neural population dynamics are cortex-specific in premotor, motor, and somatosensory cortices during locomotion (2020) – oral – *The Day of Cognition* – Fribourg, Switzerland.

[2] Anatomical and functional properties of the lumbar corticospinal tract in rodent and non-human primate (2019) – poster – *Gordon Research Conferences (GRC), CNS injury and Repair* – Waterville Valley (NH), USA.

[3] Personalized brain-spine interfaces in freely-behaving non-human primates (2018) – poster – *Society for Neuroscience (SfN)* – San Diego (CA), USA.

[4] Personalized brain-spine interfaces for spinal cord injury rehabilitation in freely-behaving non-human primates (2018) – poster and oral – *Lemanic Neuroscience Annual Meeting* – Les Diablerets, Switzerland.

[5] Brain-spine interface (BSI) technology for restoration of locomotion in non-human primates – oral – *Lemanic primate meeting* – Fribourg, Switzerland.

[6] Autologous neural cells ecosystem (ANCE) transplantation as therapy for Parkinson's disease: a promising approach (2016) – poster - *IBSA Foundation* – Geneva, Switzerland.

[7] Autologous neural cells ecosystem (ANCE) transplantation as therapy for Parkinson's disease: a promising approach (2016) – oral – *Cognition day* – Fribourg, Switzerland.

[8] Adult neural progenitor cells autotransplantation in a non-human primate model of Parkinson's disease: a pre-clinical study (2016) – poster - *Federation of European Neurosciences Societies (FENS)* – Copenhagen, Denmark.

[9] Adult neural progenitor cells autotransplantation in a non- human primate model of Parkinson's disease: a pre-clinical study (2015) – poster - *XXI World Congress on Parkinson's disease and Related Disorders* – Milan, Italy.

[10] Contribution of dorsolateral prefrontal cortex (dlPFC) in fine motor tasks execution in non-human primates (2015) – poster - *Swiss Society for Neuroscience* – Fribourg, Switzerland.

AWARDS AND HONORS

[1] 1st place winner – Poster prize at Center for Neuroprosthetics EPFL Retreat 2020, Lavey-les-Bains, Switzerland

[2] 1st place winner - Abstract award competition 2016 (IBSA Foundation), Geneva, Switzerland

TEACHING EXPERIENCES

Teaching assistant at the University of Fribourg, Switzerland

Muscular responses after peripheral nerves stimulation – undergraduate medical students	2016-2018
Sensorimotor integration of reflexes – undergraduate medical students	2017-2018
Basic visual system - undergraduate medical students	2017-2018
Assessments of manual dexterity in primates – undergraduate bio-medical students	2016-2019
Bio-statistics courses – undergraduate biomedical students	2016-2019

Lecturer at the University of Fribourg, Switzerland

Ethical consideration in animal experimentation – students from the General Knowledge School of Fribourg (ECGF)	2017

Guest lecturer at the University of Fribourg, Switzerland

Translational Neuroscience – undergraduate neuroscience students	2018

RESEARCH SUPERVISIONS

Master students

Dylan Aymon, University of Fribourg, Switzerland	2019-2020
Rafael Ornelas Kobayashi, University of Groningen, The Netherlands	2018
Nicolò Macellari, Campus Biomedico di Roma, Italy	2018
Alexandra M. Hickey, University of Fribourg, Switzerland. Best Master Award	2017-2018

Undergraduate students

Margaux Di Natale, University of Fribourg, Switzerland	2020
Elisabetta Pagliara, Swiss Federal Institute of Technology (EPFL),, Switzerland	2019
Damian Jandrasits, University of Fribourg, Switzerland	2019
Lucas Zweili, Swiss Federal Institute of Technology (EPFL), Lausanne, Switzerland	2018
Julie Martignoles, summer intern from University of Poitiers, France	2018
Floriane Naef, University of Fribourg, Switzerland	2017
Annika Wegmann, University of Fribourg, Switzerland	2017
Audélia Mechti, University of Fribourg, Switzerland	2017
Zulkaida Mamat, summer intern from Massachusetts Institute of Technology, USA	2017
Yoshija Walter, University of Fribourg, Switzerland	2017

EXTRACURRICULAR ACTIVITIES

University of Fribourg, Switzerland 2015

Department of Medicine

Administration employee

- Organizers of annual exams for medical students
- Curriculum Vitae inspections for full-professorship applications for the head of the department of Medicine

LABORATORY AND COMPUTING SKILLS

Non-human primate model (long-tailed and rhesus macaque monkeys)

Behavioral training (locomotion, hindlimb and forelimb reach and grasp tasks), *in-vivo* imaging (computer tomography scan, magnetic resonance imaging, positron emission tomography scan), anesthesia, titanium mesh implantation, acute implantation of intrafascicular electrode in the median nerve, craniotomy, spinal and cortical virus injections, electromyographical electrode implantation, sterile assistance (laminectomy, intracortical multi-electrode array implantation, lumbar epidural spinal array implantation), post-operative follow-up, electrophysiological recordings (intra-cortical and electromyography), lumbar epidural electrical stimulation

Rat model

Anesthesia, craniotomy, laminectomy, spinal and cortical virus injections, behavioral training (locomotion and complex hindlimb tasks), electrophysiology recordings (intra-cortical and electromyography), perfusion

Histology

Non-human primate and rat central nervous system dissection, immunohistochemistry, CLARITY, confocal and epifluorescence microscopy

Programming and Data Analysis

Matlab, R, Python, TDT OpenEx, neural and muscular signal processing and filtering, spike sorting, neural population dynamics, motion tracking, kinematic analysis, statistical analysis, 3D brain and skeleton model extraction (OsiriX, 3D Slicers), ^{18}F-DOPA and FDG influx rate constant measurements (PMOD Technologies), synaptic densitometry (histological image processing)

Ethical reviews

Veterinary license authorization writing and trimestral report to the veterinary authorities

Administrative work

Researching, ordering and handling of toxic agents (neurotoxin and radioactive molecules), electrophysiological hardware (Blackrock and TDT), motion system hardware (SIMI, VICON and VigiePrimate) and human surgical equipment (Aesculap drill, KLS Martin coagulator, steam autoclaves, hydrogen peroxide sterilizer, Leica microscope and surgical tools)

Languages

French (mother tongue), English (fluent in writing, reading and speaking), German (professional competencies in writing, reading and speaking)

REFERENCES

Eric M. Rouiller, Professor Emeritus
Department of Neuroscience and Movement Sciences
University of Fribourg, Switzerland
eric.rouiller@unifr.ch

Grégoire Courtine, Full Professor
Center for Neuroprosthetics and Brain Mind Institute
Swiss Federal Institute of Technology Lausanne (EPFL), Switzerland
+41 21 693 07 62, gregoire.courtine@epfl.ch

Jocelyne Bloch, Professor and Associate Physician
Functional and Stereotactic Neurosurgery
Lausanne University Hospital (CHUV), Switzerland
+41 21 314 12 93, Jocelyne.bloch@chuv.ch

Marco Capogrosso, Assistant Professor
Department of Neurological Surgery
University of Pittsburgh, USA
+1 412 388 4017, mcapo@pitt.edu